EVOLUTION OF THE MARTIAN HIGHLANDS: IMPLICATIONS FROM DRAINAGE BASIN CHARACTERISTICS AND VALLEY NETWORK MORPHOLOGIES

by

Scott Charles Mest

B.S., West Chester University of Pennsylvania, 1995

M.S., University of Pittsburgh, 1998

Submitted to the Graduate Faculty of

Arts and Sciences in partial fulfillment

of the requirements for the degree of

Doctor of Philosophy

University of Pittsburgh

2004

UNIVERSITY OF PITTSBURGH

FACULTY OF ARTS AND SCIENCES

This dissertation was presented

by

Scott Charles Mest

It was defended on

October 1, 2004

and approved by

David A. Crown (Dissertation Director)

Mark A. Evans

John A. Grant

William Harbert

Michael S. Ramsey

EVOLUTION OF THE MARTIAN HIGHLANDS:
IMPLICATIONS FROM DRAINAGE BASIN CHARACTERISTICS
AND VALLEY NETWORK MORPHOLOGIES

Scott C. Mest, PhD

University of Pittsburgh, 2004

Geologic and geomorphic analyses reveal the effects of fluvial processes within Tyrrhena Terra, Promethei Terra and Libya Montes, Mars. High-resolution Mars Orbiter Camera (MOC), Thermal Emission Imaging System (THEMIS) visible and thermal infrared wavelength images, Viking Orbiter images, Thermal Emission Spectrometer (TES) and Mars Orbiter Laser Altimeter (MOLA) topographic data are used to qualitatively and quantitatively characterize highland fluvial systems and analyze the role of water in the evolution of these highland terrains. Highland materials--including rugged uplands, intermontane basin-filling materials, plains and impact crater ejecta deposits--are dissected by both widespread, well-integrated valley networks, such as Vichada Valles in Tyrrhena Terra, and small-scale isolated networks and single channels. The interior and exterior rims of impact craters, such as crater Millochau, are also dissected by gullies. Characterization of these features and the geologic units in which they occur is necessary to fully understand the nature of martian fluvial activity and the history of Mars' climate. High-resolution (128 pixels/degree) MOLA Digital Elevation Models (DEMs) are used with the Arc/Info GIS software (including GRID, ARCPLOT, and ArcView 3.2a) and GRIDVIEW to

quantitatively characterize the surface hydrology of Tyrrhena Terra, Promethei Terra and Libya Montes. Drainage basin divides and valley networks are modeled at different scales dependent on the depth to which anomalous pixel sinks are filled. Modeled drainage divides are defined by the distribution of highland peaks and impact crater rims. Hydrologic modeling results suggest that large areas of apparently undissected terrain in Tyrrhena Terra may have been influenced by fluvial processes. Compared to mapped networks, models of large-scale valley systems in Tyrrhena Terra accurately represent the locations of valleys down to at least second order. Smaller-scale systems observed in Promethei Terra and Libya Montes are more difficult to accurately represent with the model due to a combination of a large amount of topographic interpolation within the MOLA DEM and the close spacing of short, narrow valleys Rigorous comparison of the model results to image data is helping to produce accurate maps of martian drainage basins and their associated valley networks, which provide critical constraints for valley formation mechanisms and climate history.

TABLE OF CONTENTS

LIST OF TABLES

LIST OF FIGURES

ACKNOWLEDGEMENTS

I wish to thank David Crown, my dissertation advisor, for all of his support throughout this research. Thanks to Mark Evans, John Grant, Bill Harbert and Michael Ramsey for participating in this research as committee members and their continuing interest in this topic; the perspective each of them brought to this project was greatly appreciated. I would also like to thank Herb Frey and all of the Geodynamics Branch for giving me the opportunity to conduct my research at Goddard Space Flight Center. Thanks also to those Branch members (especially Herb, Jim Roark and Susan Sakimoto) for their help with GRIDVIEW and for many useful discussions. Lastly, I would like to thank Ken Tanaka, Tracy Gregg, Ken Herkenhoff, Edmond Grin, Jim Head and the Planetary Science Institute crew for their careful and insightful reviews of Chapters 2.0 and 3.0. This research was supported by grants from the NASA Graduate Student Researchers Program (NGT5-125), the Planetary Geology and Geophysics Program (NAG5-10529), and the Pennsylvania Space Grant Consortium.

DEDICATION

I would like to dedicate this work to my wife, Debbie, and to my daughter, Victoria, for all of their love, support and most of all patience over the last five years. Thanks guys.

1.0 INTRODUCTION

Since the Mariner 9 and Viking Orbiter 1 and 2 spacecrafts revealed the presence of extensive valley networks dissecting the ancient cratered highlands of Mars [McCauley et al., 1972; Masursky, 1973; Milton, 1973], it has been suggested that liquid water played a major role in modifying the surface of Mars via depositional and erosional processes. Current surface temperatures (average ≈ 210 K) and atmospheric pressure (~6 mbar) on Mars do not permit liquid water to exist at the surface; however, the presence of fluvial valleys indicates liquid water was likely present at some point in Mars' history. Most martian valley networks (~99%) are found in within highland terrains, and they are believed to be as old as the material they dissect [Pieri, 1976, 1980; Carr and Clow, 1981; Mars Channel Working Group, 1983; Baker and Partridge, 1986, Grant and Schultz, 1990; Craddock and Maxwell, 1993; Maxwell and Craddock, 1995; Carr and Chuang, 1997; Grant, 2000]. Terrestrial drainage networks typically form by a combination of surface runoff, driven by precipitation, and groundwater sapping [Ritter et al., 1995], and similar processes have been proposed to explain the origin of martian valley networks [e.g., Pieri, 1976, 1980; Carr and Clow, 1981; Gulick, and Baker, 1990; Craddock and Maxwell, 1993; Grant and Schultz, 1993, 1994; Maxwell and Craddock, 1995; Carr, 1995, 1996; Grant, 2000; Craddock and Howard, 2002; Grant and Parker, 2002], but these processes are not yet understood in relation to martian valley network development. The relative contributions of water from various fluvial processes involved in valley network formation on Mars are not known, and are especially important for understanding the evolution of Mars' climate and determining the relative roles of atmospheric versus subsurface volatiles.

Geologic and geomorphic mapping reveal the effects of fluvial processes within the Tyrrhena Terra (13°-30°S, 265°-280°W), Promethei Terra (27.5°-47.5°S, 245°-270°W) and

Libya Montes (5°N-5°S, 265°-280°W) regions of Mars (Figure 1.1). The Tyrrhena Terra, Promethei Terra and Libya Montes regions record complex histories of impact cratering and modification by fluvial and eolian activity [e.g., Schaber, 1977; Greeley and Guest, 1987; Crown et al., 1992; Craddock and Maxwell, 1993; Maxwell and Craddock, 1995; Tanaka and Leonard, 1995; Mest, 1998; Leonard and Tanaka, 2001; Mest and Crown, 2002a, 2003b, 2004a; Crumpler and Tanaka, 2003]. High-resolution Viking Orbiter, Mars Global Surveyor (MGS) Mars Orbiter Camera (MOC), and Mars Odyssey Thermal Emission Imaging System (THEMIS) images, Thermal Emission Spectrometer (TES) data, and Mars Orbiter Laser Altimeter (MOLA) topographic data are used to qualitatively and quantitatively characterize highland fluvial systems and analyze the role of water in the evolution of highland terrains. Fluvial features in these areas include widespread, well-integrated valley networks, small isolated networks and single channels, and gullies incised along the rims of impact craters. Characterization of these features and the geologic units in which they occur is necessary to understand the nature of Martian fluvial activity and the history of Mars' climate.

This dissertation presents the analyses, methodologies and results from geologic mapping and hydrologic modeling studies in four chapters. Chapter 2.0 discusses the geology of Mars Transverse Mercator Quadrangles -20272 and -27272 that cover part of Tyrrhena Terra, Mars, and provides a geologic history for this part of the highlands. Chapter 3.0 presents a focused geologic study of crater Millochau in Tyrrhena Terra, which characterizes the crater's interior deposits and assesses its erosional and depositional history in the context of Chapter 2.0. Hydrologic studies of the martian highlands are presented in Chapters 4.0 and 5.0. Chapter 4.0 outlines the methodology used to model drainage basins and valley networks in Tyrrhena Terra and presents the results. Finally, Chapter 5.0 shows the results of hydrologic modeling in the highland terrains of Promethei Terra and Libya Montes, Mars; comparisons are made with Tyrrhena Terra as well as with terrestrial watersheds. Each chapter included in this document is a stand-alone publication. Chapter 2.0 has been submitted to the United States Geological Survey [Mest and Crown, 2004a] to be published as part of the National Aeronautics and Space Administration's Planetary Geologic Mapping Program, and has passed the scientific review Chapter 3.0 has been submitted for publication in the journal Icarus [Mest and Crown, 2004b], and has gone through the scientific review. Chapters 4.0 and 5.0 will be submitted for publication as methodology and results papers, respectively.

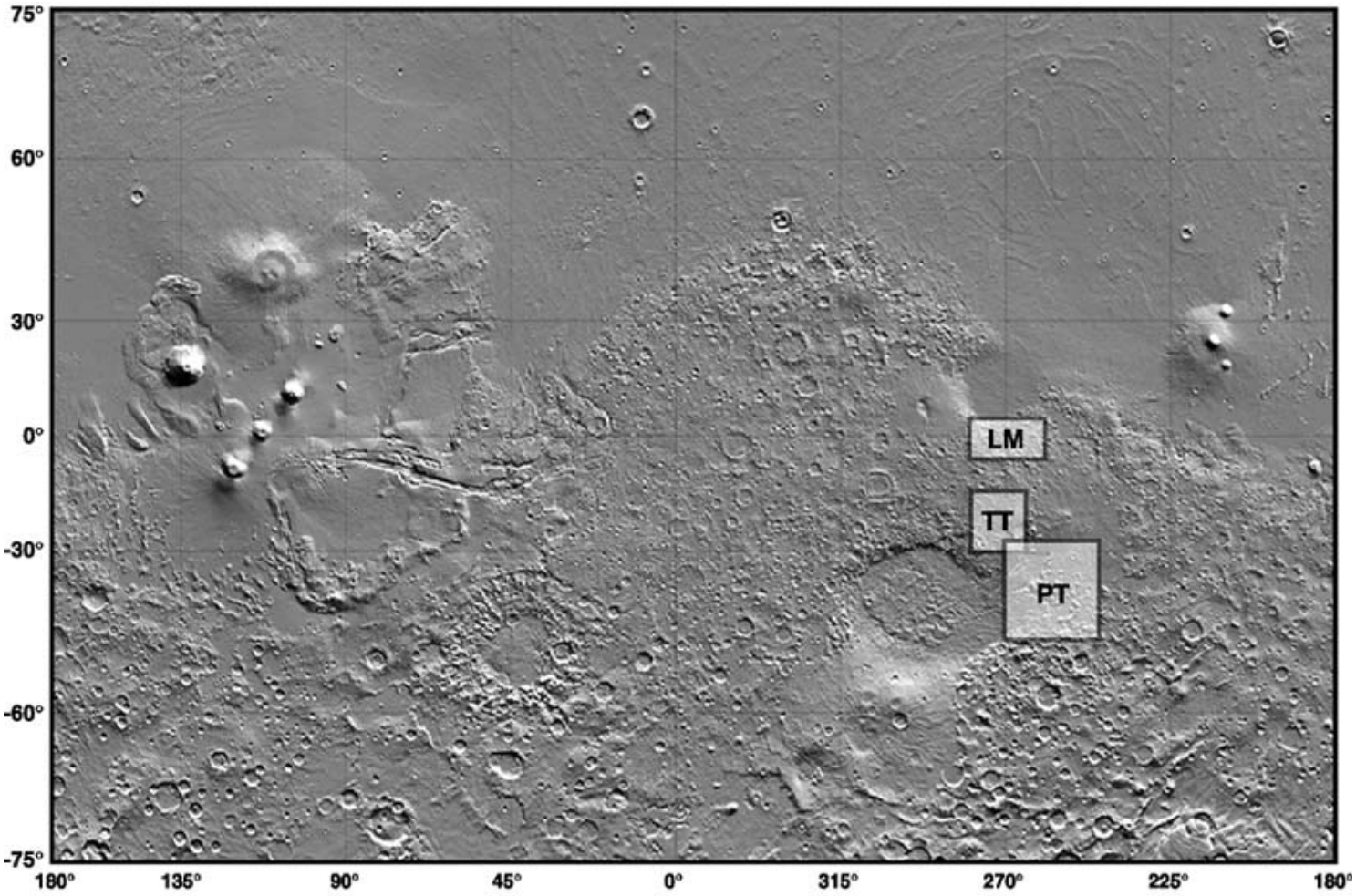

Figure 1.1. MOLA shaded relief map showing the locations of the Libya Montes (LM), Tyrrhena Terra (TT) and Promethei Terra (PT) study areas in the highlands adjacent to the Hellas and Isidis impact basins. DEM resolution is 256 pixels/degree; projection is Mercator; illumination from northeast. Shaded relief map created by Jim Roark, Geodynamics Branch, Laboratory for Terrestrial Physics, Goddard Space Flight and obtained from http://core2.gsfc.nasa.gov/mola_pub/mola_idl/mola_idl.html.

2.0 GEOLOGIC MAP OF MTM –20272 AND –25272 QUADRANGLES, TYRRHENA TERRA REGION OF MARS

2.1 INTRODUCTION

Mars Transverse Mercator (MTM) quadrangles -20272 and -25272 (latitude -17.5 to -27.5°, longitude 270° to 275°; Plate 1) cover part of the highlands of Tyrrhena Terra north of Hellas basin (Figure 2.1). The Tyrrhena Terra region records a complex history of impact cratering and modification by fluvial and eolian activity [Schaber, 1977; Greeley and Guest, 1987; Craddock and Maxwell, 1993; Maxwell and Craddock, 1995; Tanaka and Leonard, 1995; Leonard and Tanaka, 2001; Mest and Crown, 2002a, 2004a,b]. The map area consists primarily of intercrater plains, impact crater materials, and crater floor materials [Mest and Crown, 2002a, 2004a]. An extensive valley network, Vichada Valles[1], as well as several smaller networks, dissects the northern part of the map area. The abundance and widespread nature of fluvial features within the map area have significant implications for past martian environmental conditions. The degraded terrains surrounding Hellas basin provide constraints on the role and timing of volatile-driven activity in the evolution of the highlands [Mest and Crown, 2001a]. The geologic history of this area may have been influenced not only by the presence of Hellas basin but also by other buried impact basins as described by Frey et al. [2000].

[1] The name of 'Vichada Valles' is provisional until approved by the International Astronomical Union.

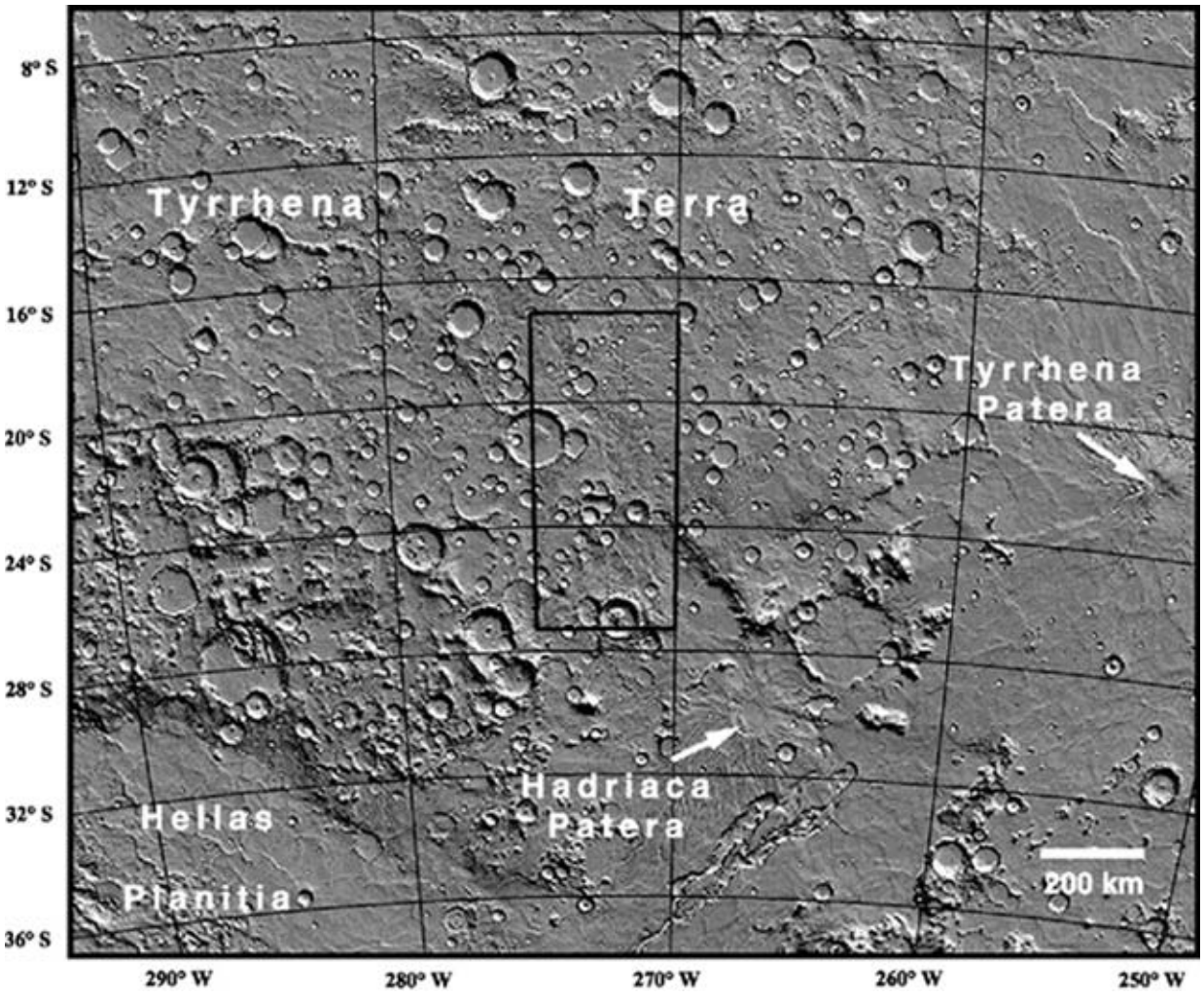

Figure 2.1. MOLA shaded relief image showing regional highland terrains north and east of Hellas impact basin. The map area (Mars Transverse Mercator quadrangles -20272 and -25272) is represented by the black box in the center of the image. Image produced using GRIDVIEW software [Roark et al., 2000; Roark and Frey, 2001] and MOLA 32 pixels/degree DEM. North is to the top in this and all subsequent images unless noted otherwise; projection is sinusoidal; illumination angle = 40°, azimuth = 30°.

The geologic units exposed in the Tyrrhena Terra region (Plate 2) have been analyzed using a combination of Viking Orbiter (VO), Mars Global Surveyor (MGS) Mars Orbiter Camera (MOC) and Mars Odyssey Thermal Emission Imaging System (THEMIS) images and Mars Orbiter Laser Altimeter (MOLA) data. VO image coverage of the map area generally ranges from 150-170 m/pixel around crater Isil (south-central MTM -25272) to ~230 m/pixel; however, the east-central part of the map area, which includes crater Millochau, is covered by high resolution VO images (~61m/pixel). High-resolution MOC coverage (~2-6 m/pixel) is sparse in the study area but has proven useful in characterizing geologic materials at small scales as well as analyzing the spatial extents of various units identified in the region. THEMIS daytime infrared (~95-100 m/pixel) and visible (~18-20 m/pixel) images cover most of the map area and provide adequate intermediate image resolutions to correlate units observed in both Viking Orbiter and MOC images. Crater size-frequency distributions have been compiled to constrain the relative ages of geologic units and determine the timing and duration of inferred geologic processes. MOLA topographic data have been used to identify relationships between valleys and impact craters, as well as to assess the distributions and stratigraphic positions of geologic materials.

2.2 REGIONAL GEOLOGY

MOLA data show that the map area has a shallow (~0.23°) southward-trending slope toward Hellas basin and is surrounded by large impact craters and rugged highland materials at higher elevations (Figure 2.2). The highlands surrounding Hellas basin include Noachian materials that are believed to represent some of the oldest rocks on Mars [Murray et al., 1971; Tanaka, 1986; Tanaka et al., 1988, 1992]. Erosion of highland materials characterized the Late Noachian Epoch and continued throughout the Hesperian Period, resulting in deposition of extensive plains

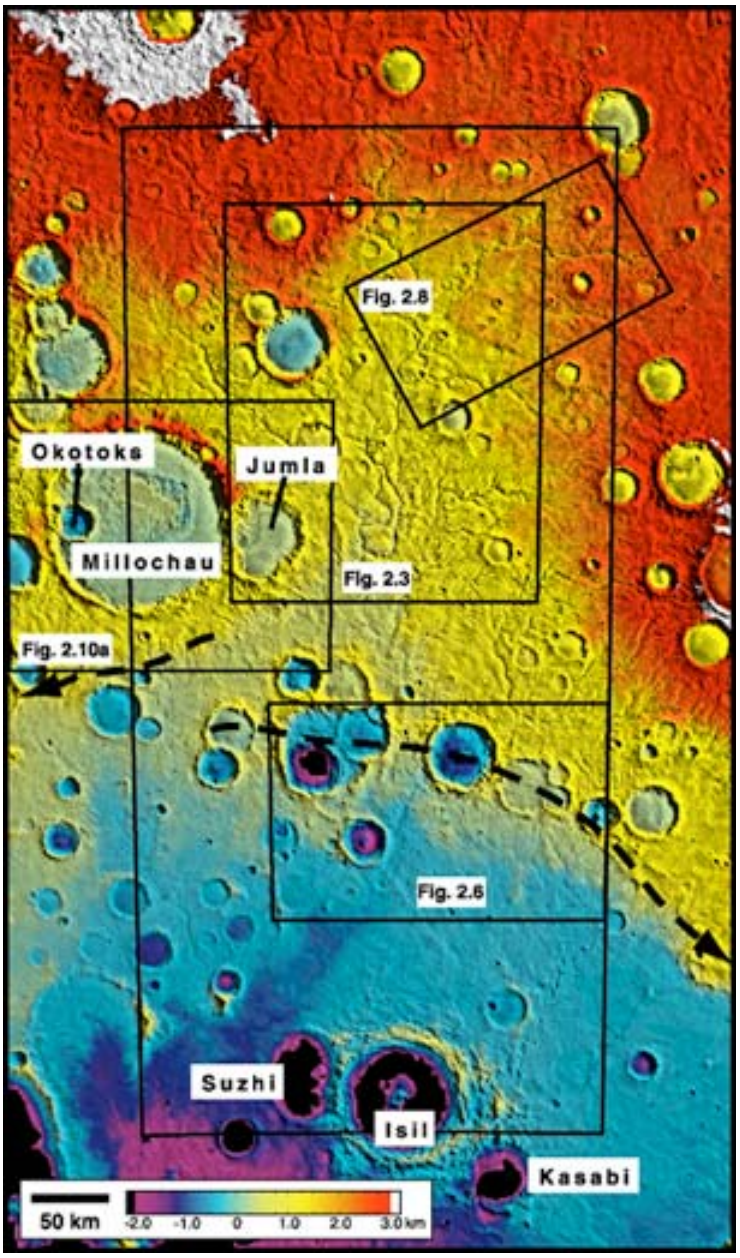

Figure 2.2. Viking MDIM 2.0 photomosaic merged with MOLA elevation data (latitude 16.5° S. to 28.5° S., longitude 268.0°W. to 276.0° W.; 32 pixels/degree DEM). The figure provides a regional view of the topography within and surrounding the map area (heavy black box). The map area slopes gradually to the south; however, the terrain drops ~600 m, located approximately by the dashed line, and this elevation change is traceable east and west of the map area. Most valleys observed in this study are within an elevation range of ~1.5 to 2.5 km, but some tributaries head at higher elevations. The locations of Figures 2.3, 2.6, 2.8 and 2.10a are shown. Image centered at 22.52°S, 271.61°W; projection is Mercator; illumination from upper right.

materials in and around Hellas basin [Greeley and Guest, 1987; Crown et al., 1992; Leonard and Tanaka, 2001; Mest and Crown, 2001a]. The geologic units along the north rim of Hellas basin were initially grouped into the plateau and high-plains assemblage, which consists of several rugged and cratered highland units, and various younger plains units, some of which contain channels, ridges, scarps, and mesas [Greeley and Guest, 1987]. Previous mapping studies at the 1:5M [Schaber, 1977] and 1:15M [Greeley and Guest, 1987] scales each described two main units in this region: the 'hilly and cratered highland material' and 'dark mottled plains material' [Schaber, 1977] and the 'dissected plateau material' and 'ridged plains material' [Greeley and Guest, 1987]. These researchers interpreted this area to be a mixture of volcanic materials and ancient impact breccias and ejecta that represent a heavily dissected part of the highlands [Schaber, 1977; Greeley and Guest, 1987]. Previous Viking-based analyses by Maxwell and Craddock [1995] in eastern Tyrrhena Terra (latitude -15 to -30°, longitude 260° to 270°) showed that formation of intercrater plains units, emplaced following extensive highland erosion, occurred in the Noachian Period. Erosion of impact craters and highland terrains in Tyrrhena Terra, as well as other equatorial (±30° latitude) highland regions, resulted primarily from fluvial processes, which were most likely precipitation-driven [Craddock and Maxwell, 1993; Craddock and Howard, 2002].

Central-vent volcanism in the Hellas region occurred in the Late Noachian/Early Hesperian Epochs with formation of the highland paterae [Greeley and Crown, 1990; Crown et al., 1992; Crown and Greeley, 1993; Tanaka and Leonard, 1995; Gregg et al., 1998]. Hadriaca and Tyrrhena Paterae, southeast and east of the map area, respectively, are interpreted to consist of pyroclastic deposits, possibly resulting from phreatomagmatic eruptions as magma rose through surface materials containing ground ice or water [Greeley and Spudis, 1981; Greeley and Crown, 1990; Crown and Greeley, 1993]. The presence of lava flow lobes within the ~1000-km-long Tyrrhena Patera flowfield and a smooth deposit filling the caldera of Hadriaca Patera suggest some effusive activity occurred late in the volcanoes' histories (presumably Late Hesperian/Early Amazonian) [Crown et al., 1992; Gregg et al., 1998; Mest and Crown, 2001b].

2.3 STRATIGRAPHY

Relative ages of geologic units mapped in MTM quadrangles -20272 and -25272 (Plate 2) were determined using observed stratigraphic relations in combination with crater size-frequency distributions (Table 2.1; Plate 3; see Appendix). Craters were identified and counted using a Mars Digital Image Mosaic of VO images (MDIM 2; 231.4 m/pixel; latitude -13° to -30°, longitude 265° to 280°), Mars Transverse Mercator photomosaics (1:500,000 scale; latitude -17.5 to -27.5°, longitude 270° to 275°), and individual VO frames. The highland terrain of the map area contains impact craters of all sizes with the largest crater being ~114 km in diameter. Based on VO images, the minimum crater diameter counted for valley floor material, highland materials (smooth plateau unit, intercrater plains material and mountainous material) and crater floor material was 500 m; craters with D>50 m were counted for talus material and the Millochau floor deposits (dune, etched, rugged and pitted materials) using a combination of VO, MOC, and THEMIS images. Only craters with D>3 km are shown on Plate 2.

2.3.1 Highland materials

The oldest geologic unit exposed in the area is mountainous material (unit Nm). Mountainous material forms a few small knobs believed to be the remnants of ancient crustal materials uplifted during formation of impact basins and large craters [Scott and Tanaka, 1986; Greeley and Guest, 1987] and is surrounded by younger plains material and impact ejecta. Crater size-frequency distributions for mountainous material show ages ranging from Early Amazonian to Middle Noachian for N(2). The degradational history, the especially small areal extent of unit exposures, and the small number of craters observed on mountainous material account for the anomalously young ages, and therefore do not allow relative ages to be accurately determined from crater statistics alone. Morphologically, the knobs of mountainous material in the map area are similar in appearance to exposures in other parts of the highlands and are most likely Middle

Table 2.1. Crater Size-Frequency Data and Relative Martian Ages

Craters contained within Mars Transverse Mercator quadrangles -20272 and -25272 (Plate 1). Areas equal total unit exposures within this map region (Plate 2). N(2), N(5), and N(16) represent the cumulative number of craters >2, >5, and >16 km in diameter/10^6 km^2. Error = $\pm$ [($N^{1/2}$)/A] x 10^6 km^2, where A is area (Crater Analysis Techniques Working Group, 1978). Epoch ranges are based upon crater counts using crater-density boundaries determined by Tanaka (1986): MA, Middle Amazonian; EA, Early Amazonian; LH, Late Hesperian; EH, Early Hesperian; LN, Late Noachian; MN, Middle Noachian; EN, Early Noachian. Epoch designations are based upon superposition and crosscutting relationships and crater counts (Plate 3). See text for names of geologic units.

Unit	Total craters[1] D < 2 km	Total craters D > 2 km	Area (km^2)	N(2)	N(5)	N(16)	Epoch range	Epoch designation
Amd	40	0	154	0	0	0	EH-MA	EA or above
AHt	96	2	956	2091 ± 1479	0	0	LN-LH	LH or above
Hpl_3	9	4	1,022	3915 ± 1958	2937 ± 1695	2937 ± 1695	MN-LN	EH-LH
HNvf	46	12	2,533	4738 ± 1368	1974 ± 883	1184 ± 684	EN-LN	LN or above
HNcf	86	8	13,803	580 ± 205	217 ± 126	72 ± 72	MN-LH	MN-LH
HNme	149	2	462	4329 ± 3061	2164 ± 2164	0	MN-EA	MN-EH
HNmr	799	4	3,400	1177 ± 588	883 ± 510	294 ± 294	EN-LH	MN-EH
Nmp	1603	3	1,160	2586 ± 1493	1724 ± 1219	862 ± 862	EN-EH	MN-LN
Npi	532	181	60,124	3011 ± 224	1663 ± 166	699 ± 108	EN-LN	MN-LN
Nm	4	1	466	2147 ± 2147	0	0	MN-EA	EN-MN
Millo. floor	2545	7	5,130	1365 ± 516	585 ± 338	195 ± 195	EN-EH	
Millo. rim	380	19	5,494	3458 ± 793	1456 ± 515	182 ± 182	EN-EH	
c_3	126	16	14,056	1138 ± 285	285 ± 142	71 ± 71	MN-EH	EH or above
c_2	23	5	1,472	3397 ± 1519	1359 ± 961	0	MN-EH	MN- EH
c_1	11	6	2,033	2951 ± 1205	1968 ± 984	1476 ± 852	EN-LN	EN-LN

[1]Craters D>0.5 km counted for Hpl_3, HNvf, HNcf, Npi and Nm; craters D>0.05 km counted for AHt and crater Millochau units (Amd, HNme, HNmr and Nmp).

Noachian in age, although regionally the unit began forming in the Early Noachian as a result of impact basin formation during the Period of Heavy Bombardment.

Impact craters and their ejecta cover much of the map area; about thirty craters larger than 10 km in diameter are seen with preserved ejecta blankets typically ~30-50 km across and up to 480 km across. The surrounding highland materials have been classified as intercrater plains material and the smooth plateau unit, which was previously described by Greeley and Guest [1987]. Intercrater plains material (unit Npi) contains well integrated networks of fluvial valleys and exhibits a surface that has been shaped predominantly by repeated impacts (Figure 2.3). In VO images, intercrater plains typically exhibit a smooth to irregular surface; closer investigation reveals that most irregularities within the plains result from a complicated mixture of crater materials (e.g., ejecta blankets) that can't be traced to specific source craters. Brightness changes very little across the surface of intercrater plains in both VO and THEMIS infrared daytime images, with the exception of subtle mottling or slight changes in grayscale, which are most likely due to the uneven distribution of ejecta and eolian deposits over the plains.

Both wide- and narrow-angle MOC images of the intercrater plains show a strikingly different surface than what is observed in VO images, due to higher spatial resolution and different illumination conditions. Wide- and narrow-angle MOC images show albedo changes that correlate with topography, and may provide evidence for the redistribution of dust or dark sand. For example, areas of low topography, such as plains adjacent to incised valleys, generally display lower albedos than the adjacent topographic highs; from MOLA data, the differences in relief for these topographically low (dark) and high (bright) areas are typically no more than a few tens of meters. These albedo patterns also allow identification and detailed mapping of valley network systems. High-resolution MOC images of intercrater plains show many small ($D<1$ km) poorly preserved craters that appear to have been eroded and (or) buried and are only visible as shallow rimless depressions (Figures 2.4 and 2.5). The most heavily dissected intercrater plains material occurs in the northern part of the map area and is separated from a narrow strip of less dissected intercrater plains material to the south by a cluster of about twenty large ($D>10$ km) craters. The northern exposure of intercrater plains material contains high concentrations of landforms believed to have formed by fluvial processes. The most obvious features are the numerous valleys that dissect the plains; the valleys tend to form dendritic or

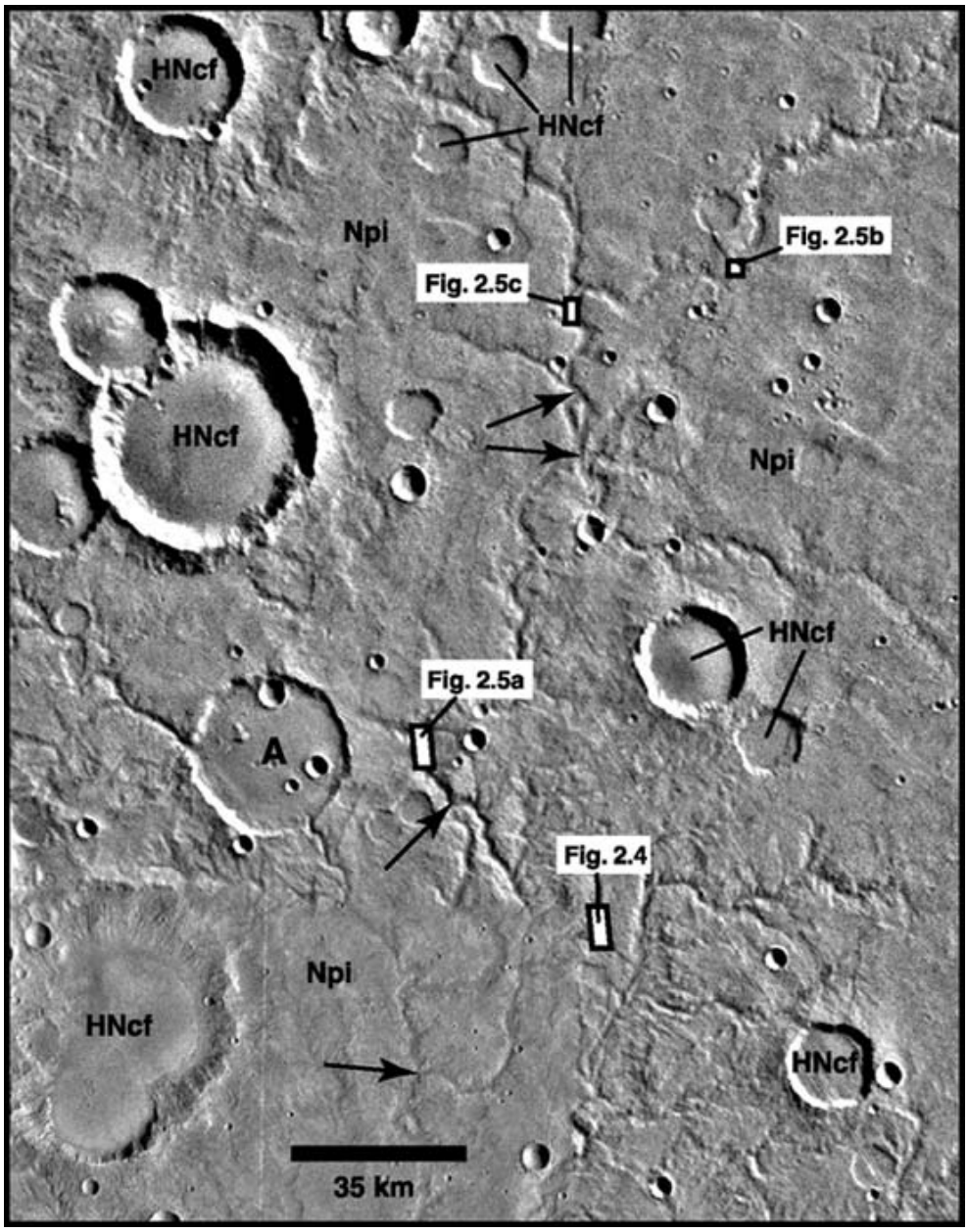

Figure 2.3. Part of Viking photomosaic of MTM quadrangle -20272 showing the intercrater plains (unit Npi), which is characterized by a smooth to irregular surface dissected by large-scale, well-incised valley networks and contains many impact craters exhibiting various degrees of preservation. In several places and at different scales, the main trunk valley of Vichada Valles splits and rejoins downstream (arrows). The image also shows a large crater (A; D = 34 km) that is breached along its western rim by an inlet valley and an outlet valley along its southeast rim. Most craters in the map area contain deposits of crater floor material (unit HNcf) presumably consisting of materials eroded from the crater rim, deposited by eolian processes, or deposited via fluvial/lacustrine processes as in the case of crater A. The locations of Figures 3.4 and 3.5a-c are shown. Image centered at 20.0°S, 272.2°W; illumination from upper right.

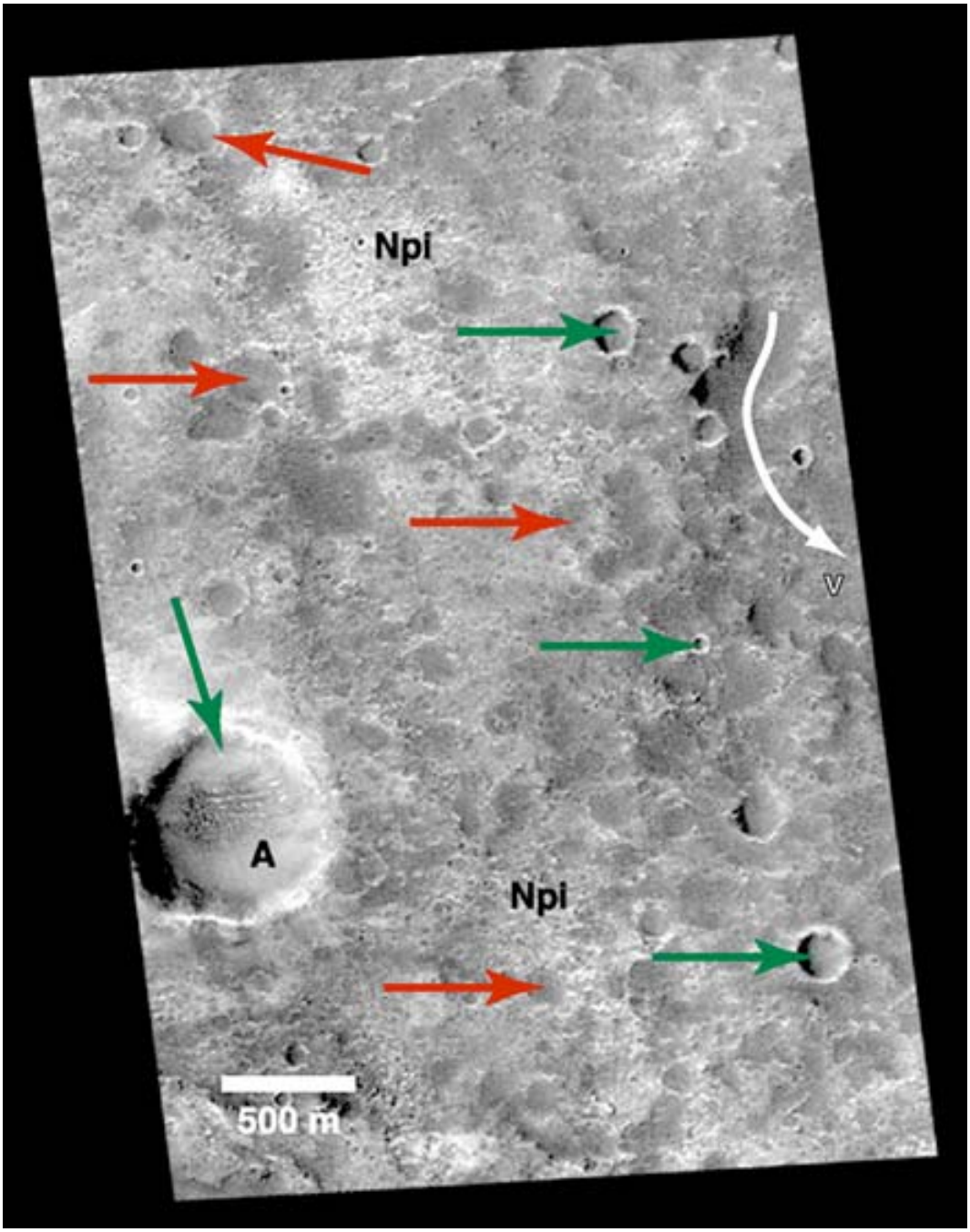

Figure 2.4. MOC image M04-00851 showing typical intercrater plains material (unit Npi). Here, the plains display a surface pock-marked with many small (D<1 km) degraded craters with morphologies ranging from visible rims and some infilling (green arrows) to little or no rims and almost completely filled interiors (red arrows). Most low-lying areas (craters, valleys (v), and other depressions) are filled with dark sediments that generally form dunes, such as in crater A. Image centered at 21.4°S, 272.1°W; image is 2.88 km across; resolution is 1.41 m/pixel; illumination is from left; NASA/JPL/MSSS.

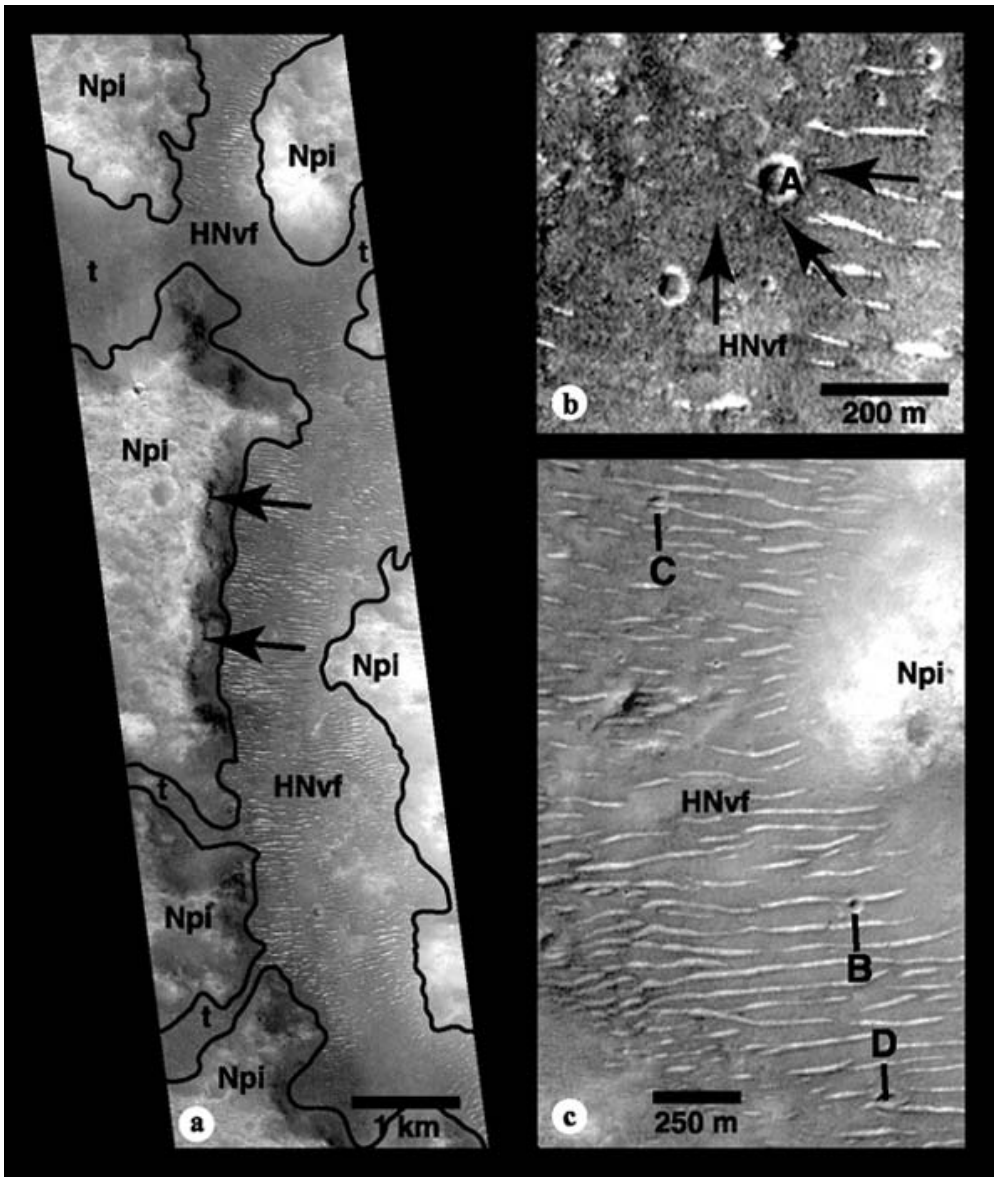

Figure 2.5. MOC image M08-02977 (a) shows part of the trunk valley and some tributaries (t) of Vichada Valles within the intercrater plains (unit Npi). Layers or terraces are exposed along the east-facing wall of the trunk valley (arrows) indicating stratigraphy within the plains material and (or) evidence of flow events. Most valleys in the map area contain valley floor material (unit HNvf), which commonly consists of sediments remobilized to form parallel sets of dunes oriented orthogonal to valley walls (a-c). Crosscutting relations between impact craters and dunes are shown in b and c. In b, ejecta (arrows) from an ~80-m-diameter crater (A) superposes dunes, and in c, crater B appears to bisect a dune, whereas craters C and D are superposed by dunes. M08-02977 (a): image centered at 20.7°S, 272.8°W, image is 2.88 km across, resolution is 2.81 m/pixel; M04-02305 (b): image centered at 19.1°S, 271.5°W, image is 2.16 km across, resolution is 2.82 m/pixel; M19-00428 (c): image centered at 19.2°S, 272.1°W, image is 1.44 km across, resolution is 2.82 m/pixel; illumination from left for a-c; NASA/JPL/MSSS.

parallel patterns (see 'Fluvial Valleys') that are related to local topography. Networks on steep slopes, such as south of crater Millochau or along the rims of other craters, tend to form parallel patterns, whereas networks within the more gradually sloping portions of the plains form open, dendritic patterns. For some of the larger valleys [Carr, 1995, 1996], their floor materials are able to be discerned and are mapped as a separate unit from intercrater plains material. In MOC images (Figure 2.5) the plains exhibit minor terracing where exposed along valley walls, indicating the plains may consist of Noachian-aged strata of various origins (i.e., impact materials and breccias, volcanics, or sediments), or the terraces may provide a record of past flow events.

The intercrater plains material contains an abundance of scarps, most of which are believed to be erosional in nature, but some may also have tectonic origins or indicate the locations of buried and (or) eroded impact craters. High-resolution MOC images show that several low-relief scarps are oriented orthogonal to valleys and generally intersect valleys at angles similar to tributary valleys; these scarps may be erosional and provide evidence for undeveloped valleys. It is also observed that the high-standing areas (Figure 2.4) generally consist of heavily pitted materials that appear competent in nature whereas lower areas (floors of large pits, eroded craters, small tributaries, etc.) are infilled with dark sediments. Roughly 13 linear to arcuate ridges are also observed within the plains or are buried by crater ejecta. The ridges are scattered throughout the map area and they do not appear to show any preferred orientation. They ridges are generally only a few tens of kilometers long, with the longest being ~50 km; all have degraded morphologies, and they do not display crenulations along their crests, which are typical of mare-type wrinkle ridges [Strom, 1972; Lucchitta, 1976; Fagin et al., 1978; Phillips and Lambeck, 1980; Saunders and Gregory, 1980]. No embayment relationships are observed with intercrater plains material indicating the ridges are composed of intercrater plains material. The ridges are believed to be erosionally modified tectonic landforms, or were formed entirely by erosional processes. The degraded nature of the ridges and lack of embayment relationships suggests they formed after the plains were emplaced and were eroded at the same time as the intercrater plains.

Parallel channels and valley networks dissect intercrater plains material immediately to the east and south of craters Millochau and Jumla[2]. These networks appear to be more finely

[2] The name of crater 'Jumla' is provisional until approved by the International Astronomical Union.

integrated and preserve finer scale detail than the larger networks, such as Vichada Valles, that dissect most of the intercrater plains. MOLA topography shows that the plains along the southern rim of Millochau are ~500 m higher in elevation and have steeper slopes (~1°) suggesting that this part of the plains most likely consists of eroded impact crater materials from Millochau and Jumla.

In VO images, the intercrater plains south of ~24°S appear significantly less dissected than the plains to the north (Figure 2.6)**.** MOLA data show that the southern plains are also ~600 m lower in elevation than the northern plains. This elevation change occurs at roughly 24°S where a cluster of about twenty large (D>10 km) craters stretches across the map area (east to west) (Figure 2.2), and is traceable into adjacent quadrangles, such as in MTMs -25262 and -30267 [Crown and Greeley, 2004] where the highlands meet the volcanic deposits of Tyrrhena Patera. The map shows the locations of five MOC images (M01-02558, M11-03386, M18-01026, M22-02342, and E09-00634), represented by red dots, that display the dune-covered nature of the southern part of the map area. MOC images show an abundance of dune features on the surface of this part of the intercrater plains (Figure 2.7), as well as on impact crater ejecta (M22-02342); however, small areas of the pitted and cratered surface diagnostic of the intercrater plains material in the northern part of the map area are visible among the dunes. This suggests that the intercrater plains material is quite extensive and appears to not only have been modified by fluvial processes, but have been buried in some areas by impact ejecta and wind-blown material as well. Greeley and Guest [1987] previously mapped the southern part of the intercrater plains as ridged plains material, although only 5 of the 13 ridges identified in the plains are found in this part of the map area, and almost all of those are completely to partially buried by impact ejecta. This part of the map area does not show the high density of wrinkle ridges typical of Hesperian ridged plains material. No lava flow features are visible within this unit in the map area.

Intercrater plains material is interpreted to be similar to the dissected plateau material of Greeley and Guest [1987], consisting of sequences of impact breccias, volcanic deposits and sediments deposited early in the region's history and covered in many places by ejecta from nearby craters. Erosion by fluvial processes produced extensive networks of valleys that dissected the plains and resulted in a variety of landforms discussed below. Portions of the

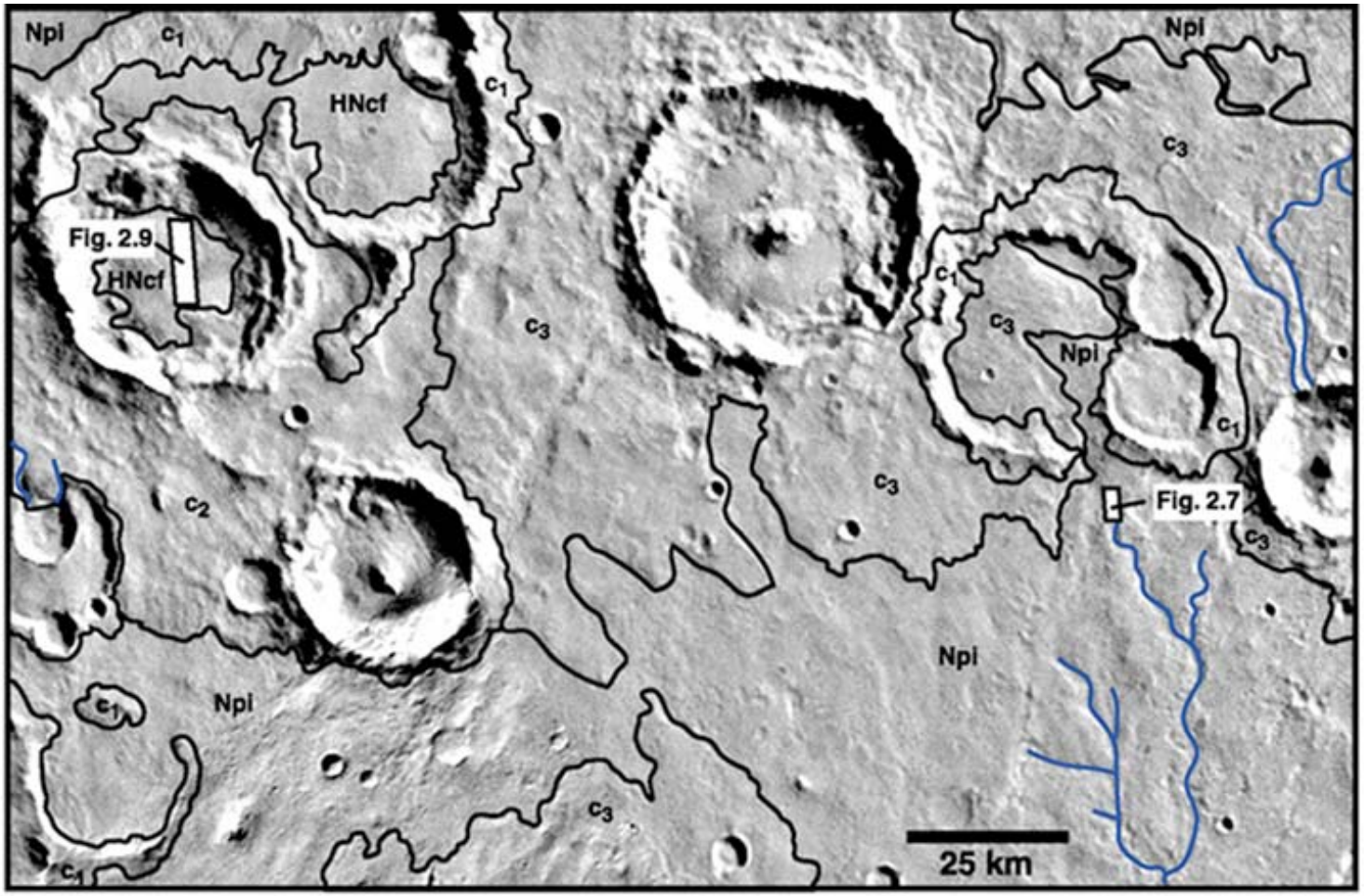

Figure 2.6. Part of Viking MTM quadrangle -25272 photomosaic with geologic sketch map of major contacts (black lines) and valleys (blue lines). Intercrater plains (unit Npi) in this part of the map area appear subdued compared to exposures in the north (Figure 2.3). The southeast corner of the image shows one of the best examples of fluvial activity preserved in the southern part of the map area. These valleys are shallower than those in the north, possibly due to a greater amount of eolian infilling (see Figure 2.7). The locations of Figures 2.7 and 2.9 are shown. Image centered at 24.5°S, 271.5°W; illumination from upper right for most of image and from upper left for bottom center of image.

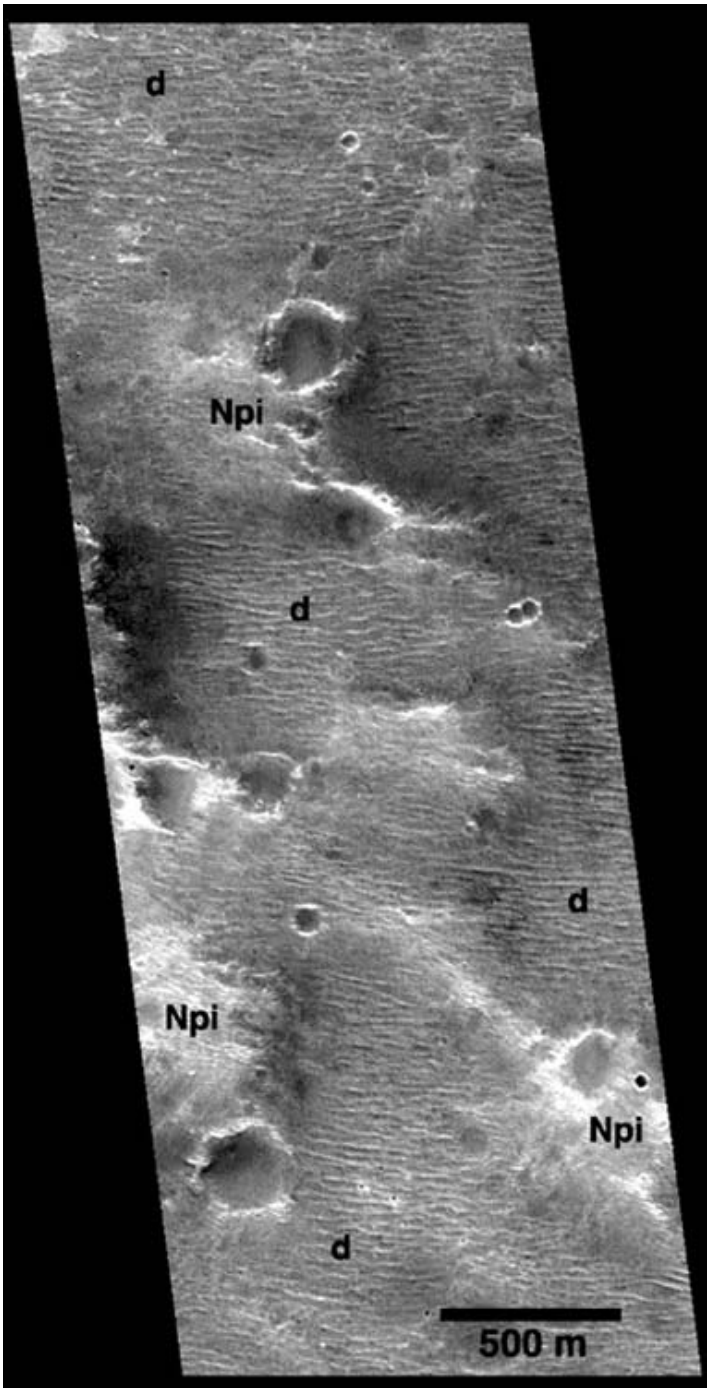

Figure 2.7. MOC image M11-03386 shows that the subdued appearance of the southern intercrater plains material (unit Npi) appears to be caused by a thin mantle of sediments. Here, dark sediments mantle and subdue the irregular surface texture formed by high-standing remnants of intercrater plains material typically seen to the north, bury many small craters and pits, and form dune fields (d). Image centered at 24.5°S, 270.6°W; image is 1.43 km across; resolution is 2.80 m/pixel; illumination from upper left; NASA/JPL/MSSS.

plains, as observed in MOC images, show that the upper few meters of material have been removed; small pockets of smoother, dark material fill low-lying areas as the heavily pitted surface is removed. Eolian activity has since buried the topographically lower southern portions of the plains and resulted in the formation of dunes.

Crater size-frequency distributions for intercrater plains material show ages ranging from Early to Late Noachian. Superposition relationships between craters and the plains are difficult to determine for many of the larger degraded craters where there is little to no ejecta preserved or the ejecta grades into the surrounding plains. Based on the dissected nature of the plains and observed variations in the distribution of fluvial valleys, it is believed that nonadjacent craters of similar size could also be of similar age despite significant differences in their preserved state. Morphologic differences could be due to underlying lithology, the characteristics of the ejected material, and the nature of the erosional process(es), any of which might result in different levels of resistance to erosion. The interpretation that intercrater plains material consists of interlayered deposits of impact materials, volcanic deposits and sediments that have been eroded by fluvial processes suggests a long history of emplacement. N(2), N(5), and N(16) crater statistics show a similar relationship between valley floor deposits and the intercrater plains, consistent with crosscutting relationships. Formation of the plains may have begun in the Early Noachian, but emplacement of most of the unit occurred during the Middle and Late Noachian Epochs.

The smooth plateau unit (unit Hpl_3; defined by Greeley and Guest [1987]) is found in the southeast corner of the map area. This location was initially mapped as pdm material by Schaber [1977] and Greeley and Guest [1987]; most recently the smooth plateau unit has been mapped in adjacent quadrangles by Crown and Greeley [2004], of which the exposure mapped in the current study is believed to be a part. This unit shows a smooth surface with a few wrinkle ridges and some channels that occur at the base of a scarp that forms the contact with the intercrater plains. Based on geologic mapping by Crown and Greeley [2004] in MTM -30267, the smooth plateau unit is believed to be composed of Hesperian-aged volcanic deposits and sediments, although there are no flow features visible in the map area of this study.

N(2) and N(5) crater size-frequency distributions for the smooth plateau unit show ages of Late Noachian and Middle Noachian, respectively. The exposure of this unit in the map area suggests older ages than shown by global mapping studies [Greeley and Guest, 1987]. Based on crater statistics determined for extensions of this exposure of the smooth plateau unit in adjacent

quadrangles [Crown and Greeley, 2004], this unit is interpreted to be Early to Late Hesperian in age. The anomalously high number of craters on Hpl_3 in the map area could be due to secondary craters associated with the large crater at the southern margin of the map and other large craters in the area.

2.3.2 Valley materials

Valley floor material (unit HNvf) appears to fill most of the valleys in the map area. These deposits are observed, and have been mapped, in the wider valleys based on characteristics in VO and MOC images; however, similar deposits are also believed to extend into smaller tributaries whose floors can't be studied with the available image resolution. Valley floor material appears smooth to pitted in VO images. High-resolution MOC images show the material to consist of sediments that have been mobilized to form dunes (Figure 2.5). The dunes are oriented perpendicular to the valley walls (transverse to the proposed direction of fluid flow within the valleys) and most of the larger dunes extend across the width of the valley; dune wavelengths range from 20-110 m (average ~50 m). From visual inspection of the dunes, it appears the backslopes of most dunes are oriented upstream suggesting the dunes are most likely transverse dunes with wind directions in most valleys oriented downstream. Numerous small craters are buried by valley floor material; however, MOC images (Figures 2.5b and c) show that several small craters are also observed to superpose dunes. Most of the craters that superpose dunes are small (D<1 km) and ejecta is difficult to observe, but Figure 2.5b shows 2 craters with ejecta that appears to drape dunes. Figure 2.5c shows examples of a crater that bisects a dune, as well as similar sized craters that are embayed by dunes. These relationships help to constrain the age of the floor deposits as well as the timing of fluid flow through the valleys. The fact that several craters superpose dunes suggests that the dunes are relatively stable and may indicate either (a) the sediments that comprise the dunes are difficult to mobilize, (b) the wind velocities required to form dunes within the valleys are no longer present, and (or) (c) the craters have acted to stabilize portions of the dunes and dunes are active in other areas.

We interpret valley floor material to consist of sediments derived from the surrounding highland materials that were deposited by a combination of water flowing through the valleys, mass-wasting of valley walls, and eolian processes. Crater size-frequency distributions for valley floor material show ages ranging from Early to Late Noachian. Crosscutting relationships with intercrater plains material indicate valley floor material must be younger than the plains material; therefore, valley floor material is designated to be Late Noachian or younger, consistent with N(2) and N(5) distributions. It is also possible that different exposures of valley floor deposits are of significantly different ages, spanning from Noachian to Amazonian times.

2.3.3 Crater materials

Crater materials within the map area display various states of preservation presumably resulting from different combinations of crater age, target lithology, and erosional environment, though crater morphology in general implies progressive degradation throughout the evolution of this region. Well preserved crater material (unit c_3) shows the least amount of degradation and is characterized by pronounced, continuous crater rims that are elevated relative to the surrounding materials, and also by well defined, continuous ejecta blankets. Numerous clusters and chains of small craters are observed within c_3 ejecta blankets and are likely secondary craters. Moderately degraded crater material (unit c_2) is characterized by crater rims that may be discontinuous, exhibiting minor relief above the surrounding materials, and by discontinuous and (or) poorly exposed ejecta blankets. Highly degraded crater material (unit c_1) shows discontinuous crater rims exhibiting little to no relief above the surrounding materials and ejecta blankets that have either been eroded or mantled by younger materials, or some combination of the two. The abundance of large highland craters with distinct ejecta materials allows superposition relationships between adjacent craters to be determined. In some cases, ejecta materials of similar preservation state cannot be traced to specific source craters and are mapped as single, large exposures containing several source craters. Martian ages are not formally assigned to impact crater materials in this work, but crater size-frequency distributions on three sample areas for c3 (crater Isil; 27.2°S, 272.1°W), c2 (20.3°S, 271.7°W) and c1 (19.6°S, 273.3°W) appear to

have relative ages of Early Hesperian or younger, Middle Noachian to Early Hesperian, and Early to Late Noachian, respectively.

Many craters of all designations (units c_3, c_2, and c_1) have smooth, flat floors and contain crater floor material (unit HNcf; discussed below) while still retaining their other characteristic morphologies. The fact that crater floor material may have various origins, and therefore ages, makes the presence (or lack) of this deposit an inappropriate method of characterizing craters within the map area. Ejecta blankets have also been modified to various degrees by fluvial processes, providing significant crosscutting relationships to constrain timing of fluvial activity. Several craters, such as the two shown in Figure 2.8, may have had their ejecta blankets dissected by valleys, although it is difficult to determine whether or not ejecta is present on the valley floor.

Many of the impact craters in the study area display low-relief rims and flat, relatively smooth floors; these craters contain distinct deposits that have been mapped as crater floor material (unit HNcf). Crater floor material is also mapped in some craters that have less degraded morphologies. Some crater interior deposits, such as in crater Millochau (see discussion below), have been mapped in more detail than other craters in the area due to greater coverage by MOC and THEMIS images [Mest and Crown, 2004b]. The study by Mest and Crown [2004b] is a first step in attempting to characterize crater interior deposits in the region in an effort to provide additional information on regional geologic evolution. MOC image E16-01803 shows that crater interior deposits within a 36-km-diameter crater, located at 23.5°S and 273.5°W (Figure 2.9), consists of several distinct layers that are in the process of being eroded, exposing what appears to be the remnants of a cratered plateau and buried impact craters. The very bright material surrounding the plateau, shown in Figure 2.9, could consist of materials deposited in a shallow lake.

Some crater floor deposits display lobate margins whereas others terminate gradually against the interior crater walls. Most of the filled craters have gullied interior walls, which suggests that some of the crater floor material observed in these craters consists of debris eroded from the crater walls and deposited on the crater floor. Some craters have been breached by valleys, such as shown in Figure2.3, indicating that a part of these deposits are most likely derived from materials eroded from the surrounding highlands. Some exposures of crater floor

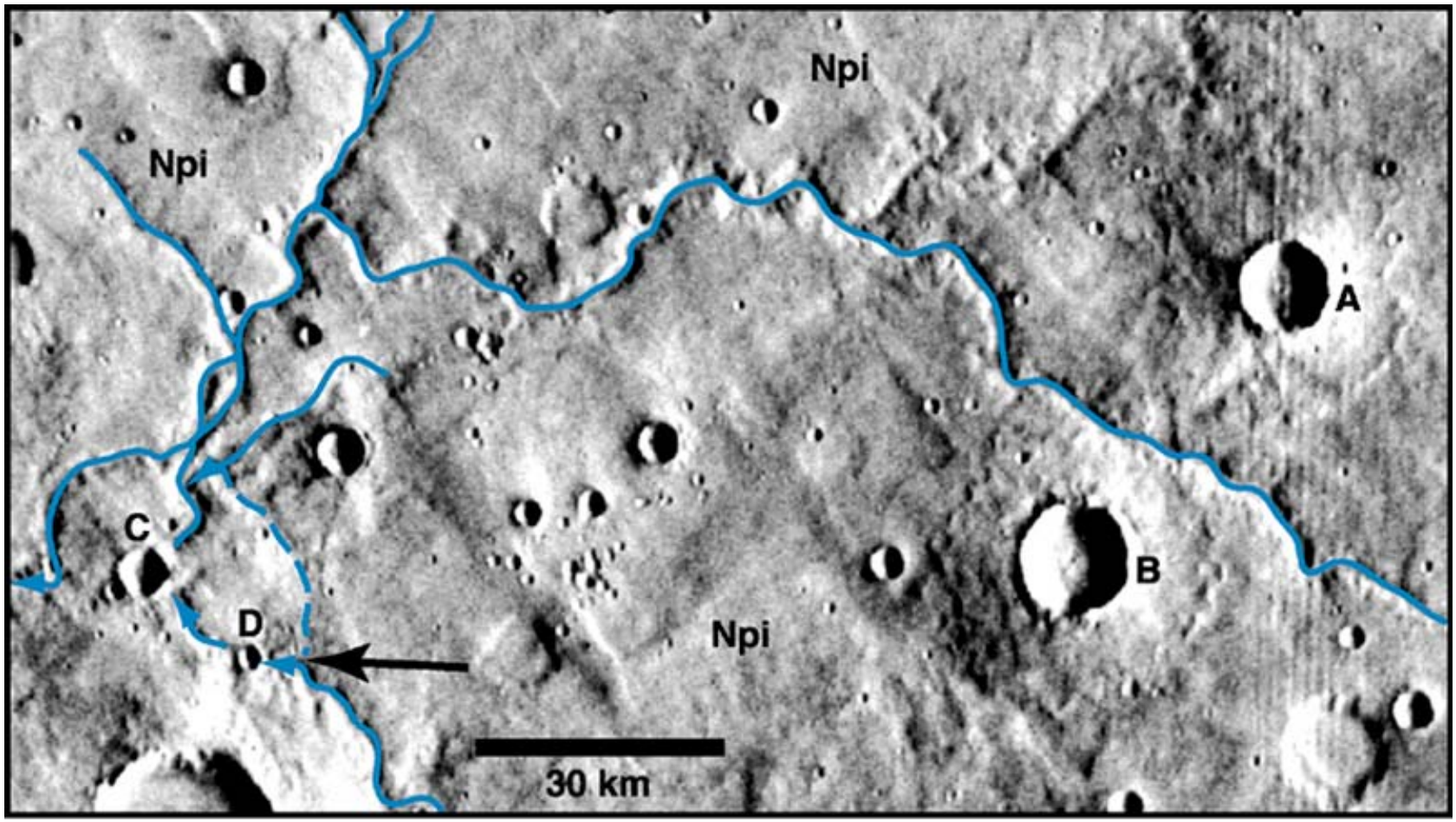

Figure 2.8. View of Vichada Valles and its tributaries (solid blue lines) showing cross-cutting relationships with impact craters in intercrater plains (unit Npi). Two large craters on the right side of the image (A and B) show ejecta blankets that are either 1) eroded by an incised valley or 2) mantle a preexisting valley. At the available image resolution it is not clear whether ejecta material is present on the valley floor. There is no evidence for ponding or diversion of this valley, suggesting fluvial processes were active before crater formation or that fluids moved easily through the valley following ejecta emplacement. Near the left edge of the image, craters C (D=6 km) and D (D=3 km) bisect a tributary of Vichada Valles. The presence of a shallow valley to the east that connects deeper segments of this tributary upstream and downstream of these craters suggests flow may have been diverted (at the arrow) via the course shown by the dashed blue line. VO image 625A25; north is to the upper right corner; image is centered at 18.5°S., 271.0°W; resolution = 239.82 m/pixel; illumination from right.

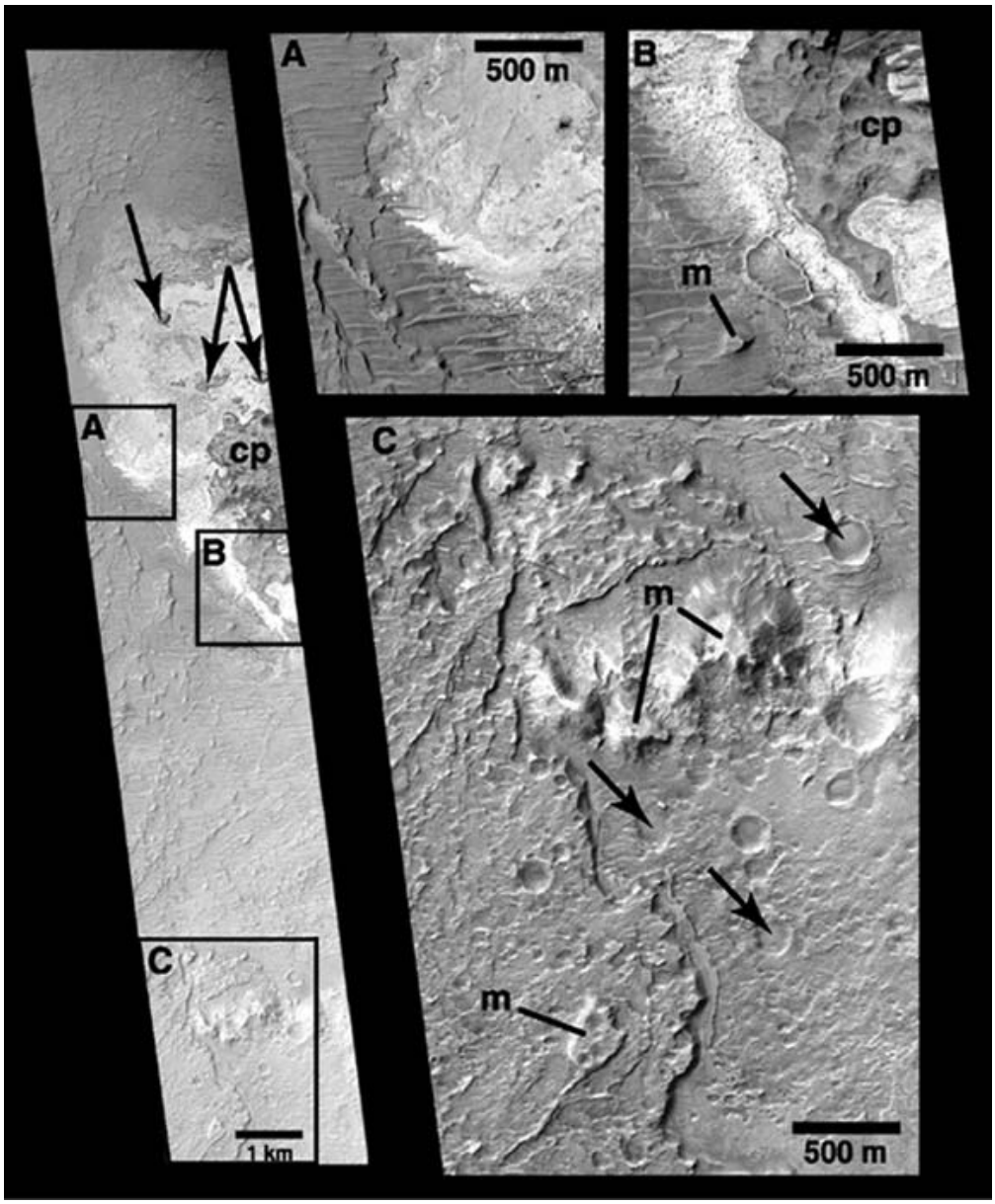

Figure 2.9. MOC image E16-01083 (left) showing crater floor materials (unit HNcf) within a 36-km-diameter crater at 23.5°S, 273.5°W. Crater floor material exhibits irregular surfaces and layering is visible in close-ups A-C. A rugged and cratered plateau (cp), located just northeast of this crater's center, is visible in B and is surrounded by very bright deposits (see A and B) that appear to embay the plateau or were exposed upon erosion of the rugged surface. Possible outliers of the plateau are also visible in the image at left (arrows). Surrounding and apparently overlying the bright material are layered deposits that display irregular surfaces (see A-C); some layers have been eroded to form mesas (m; see B and C) and reveal exhumed craters (arrows in C). Dunes, observed in A and B, superpose the bright and layered materials. Close-ups A-C are shown at the same scale. Image centered at 23.9°S, 273.3°W; image is 3.03 km across; resolution is 2.95 m/pixel; illumination from upper left; NASA/JPL/MSSS.

material may be lacustrine in origin, resulting from standing bodies of water contained in crater interiors. Also, some component of crater floor material may be composed of eolian deposits, derived both locally and from elsewhere. Previous studies of highland terrains [Grant and Schultz, 1993, 1994; Crown and Stewart, 1995; Grant, 1999; Mest and Crown, 2001b; Pierce and Crown, 2003] have shown that mass wasting of crater rim and wall materials can contribute significant amounts of material to crater floors. Although no evidence (lobes of debris extending from crater walls, transverse or longitudinal ridges, etc.) for discrete mass movements is observed on crater floors in this map area, some contribution from mass wasting cannot be ruled out. Deposits of crater floor material contain few large craters on their surfaces, but the moderately low total surface area of this unit yields relatively high crater densities. Crater size-frequency distributions (N(2, 5 and 16)) of these materials suggest they are Middle Noachian to Late Hesperian in age. Eolian deposition within craters could result in burial of many small craters thus skewing crater floor material toward younger ages. In addition, exposures of crater floor material with significantly different ages (Noachian to Amazonian) may be present in the study area.

Crater Millochau, centered at 21.4°S, 275°W (Figure 2.10a), is ~114 km in diameter, and based on MOLA data, is approximately 2 km deep. The floor of the crater shows a variety of terrains that record a complex geologic history. Millochau contains four distinct deposits, mapped as Millochau dune, etched, pitted, and rugged materials. Six high-resolution MOC images allow these deposits to be identified and characterized separately from the crater floor material (HNcf) that fills other large craters in the map area, which are not covered by MOC in as great detail. Seven THEMIS visible (two images) and infrared (four daytime IR and one nighttime IR) images provide almost complete coverage of Millochau's rim and interior deposits [Mest and Crown, 2004a]. Analysis of MOC and THEMIS images reveals numerous small exposures of these units in close proximity, more so than can be shown on this map. Mest and Crown [2004b] provide a detailed analysis of the Millochau floor deposits.

The floor of central Millochau forms a plateau that is raised as much as 400 m above the surrounding floor. This plateau is bounded on its northern and eastern edges by a scarp and a series of irregular depressions; the plateau slopes gently to the south and west where it grades into the surrounding deposits (Figure 2.10a). Numerous layers are exposed along the scarp

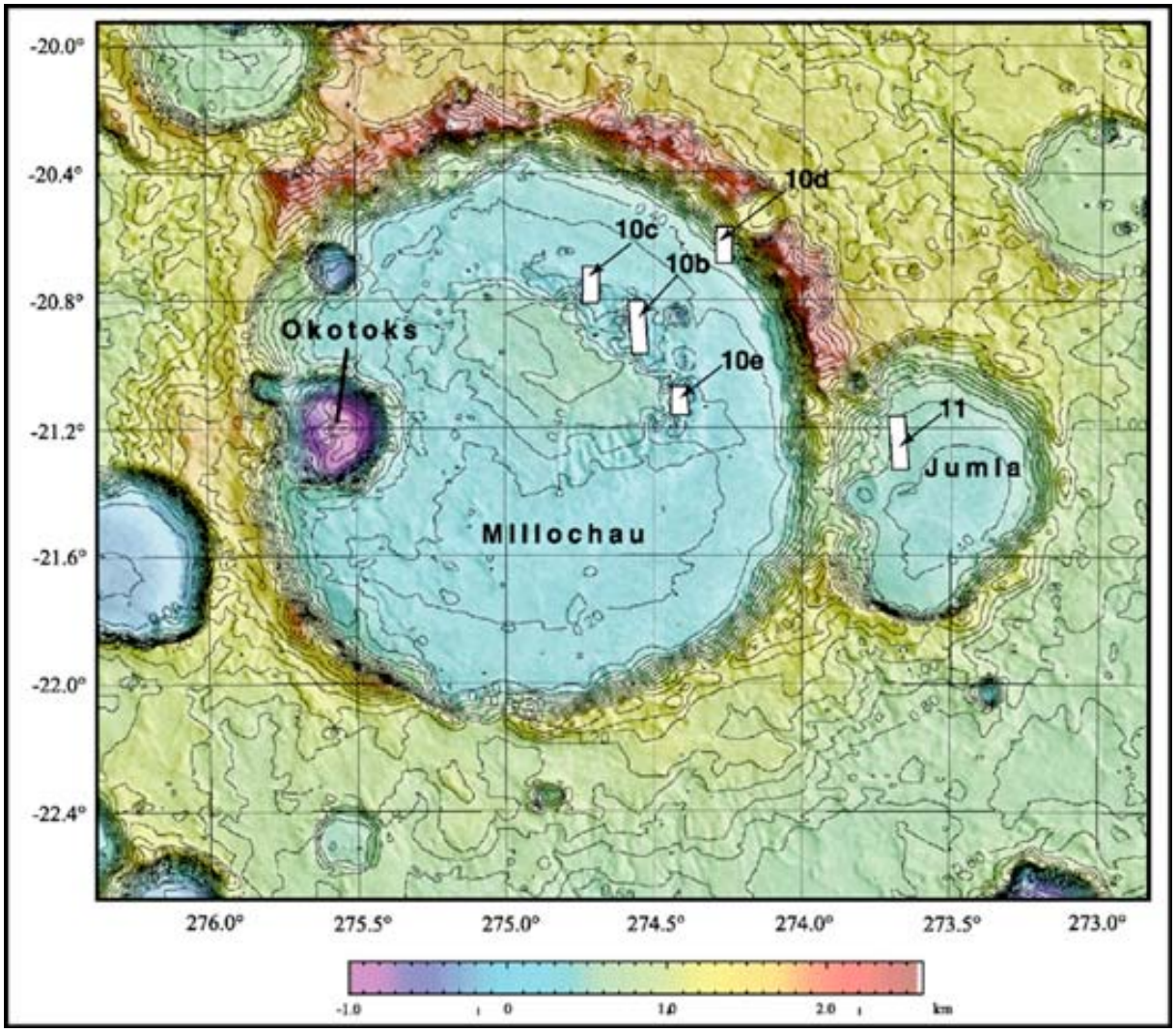

Figure 2.10a. Crater Millochau (D=114 km) and surrounding terrain shown here as merged Viking MDIM 2 and MOLA elevation data with contours (contour interval is 100 m). The northern and southern rims of Millochau display striking differences in relief with the northern rim being higher and steeper. Gullies along the southern rim are evidence for enhanced erosion in this part of Millochau. Also note the raised plateau in the north-central part of Millochau, which is bounded on the north and east by large depressions. The locations of Figures 2.10b-e and 2.11 are shown. Figure centered at 21.1°S., 274.5°W.

boundary of the plateau, as well as along knobs and mesas found in the depressions. These layers vary in thickness and are traceable across short distances (10's of km) in MOC images; outcrops observed in MOC images tend to exhibit a regular sequence of layering with a thick (150-250 m) and relatively massive layer overlying several thin (<10 m) layers [Mest and Crown, 2004a,b]. Martian craters of Millochau's size exhibit complex interiors [Wood, 1980; Pike and Spudis, 1987]. However, the size and position of the plateau (i.e. in the north central part of Millochau's floor) combined with the presence of layering, exposed in knobs and outcrops of the plateau, suggest that this feature is primarily a secondary feature unrelated to the Millochau impact event [Mest and Crown, 2004a,b]. The southern edge of the plateau contains several valleys, oriented roughly north-south, that have cut into the plateau. These valleys have fairly consistent widths and depths and they display amphitheater-shaped heads suggesting they may have formed primarily by groundwater sapping. Similar but smaller valley-like features are found cutting into the north-facing scarp of the plateau and the south-facing scarp of the surrounding floor materials. Valleys in the plateau tend to be contained entirely within the plateau; where the valleys meet the Millochau rugged material along the southern edge of the plateau, the mouths of the valleys stop at the Millochau rugged material, suggesting there may have been little to no downcutting into the rugged material.

Millochau pitted material (unit Nmp) covers and is found only on the central plateau and shows a heavily pitted and cratered surface (Figure 2.10b) in MOC images. Portions of this unit display subtle brightness variations in THEMIS images that correlate to surfaces exhibiting differences in degradation and possible mantling by ejecta from a 23-km-diameter crater in western Millochau [Mest and Crown, 2004a,b]. Dark surfaces appear more rugged and contain more craters and pits, than light surfaces. Light surfaces are rugged as well, but the craters and pits are more pristine. Light surfaces also appear to be higher standing suggesting this material may be in the process of being removed, thus exposing the underlying darker material, or low areas may contain a lag deposit or coarse sand. Although dark pitted material appears to contain more craters than the light material, the size ranges of craters are similar for all pitted material. TES thermal inertia data for Millochau pitted material ranges from ~275 to 350 $J/m^2Ks^{1/2}$ and corresponds to surface materials that contain fine materials and (or) few rocks [Jakosky et al., 2000; Mellon et al., 2000; Christensen et al., 2001; Putzig et al., 2003]. THEMIS infrared images

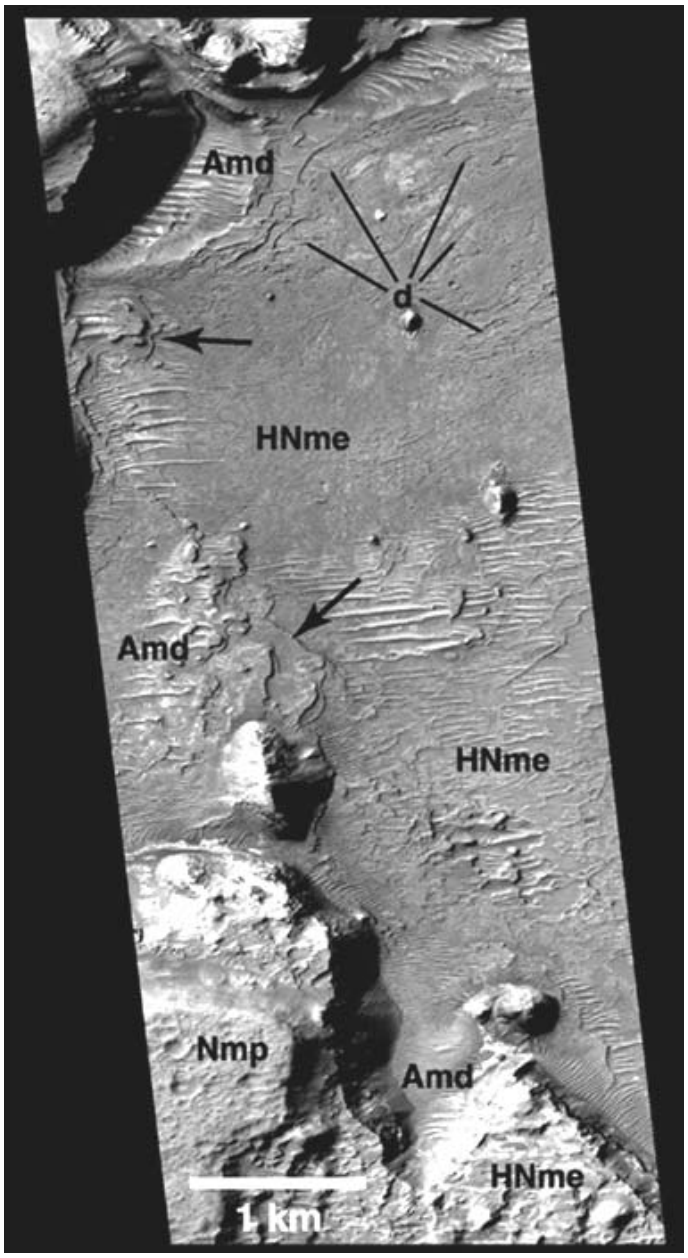

Figure 2.10b. Part of MOC image E01-01209 showing lineated (middle) and irregular (bottom) Millochau etched (unit HNme), pitted (unit Nmp), and dune (unit Amd) materials. Here, lineated etched material contains positive relief features that connect patches of smooth material with similar albedo. Orthogonal lineations form irregularly shaped polygonal depressions (d); some depressions are filled with bright material and (or) dune material. Step-like layers (arrows) are exposed in the center of this image suggesting portions of the Millochau interior deposits are composed of relatively thin layers of easily eroded material. Millochau dune material is found along the edges of scarps and knobs and mantles the etched material. Image centered at 20.9°S., 274.6°W; image is 2.9 km across; resolution is 2.82 m/pixel; illumination is from left; NASA/JPL/MSSS.

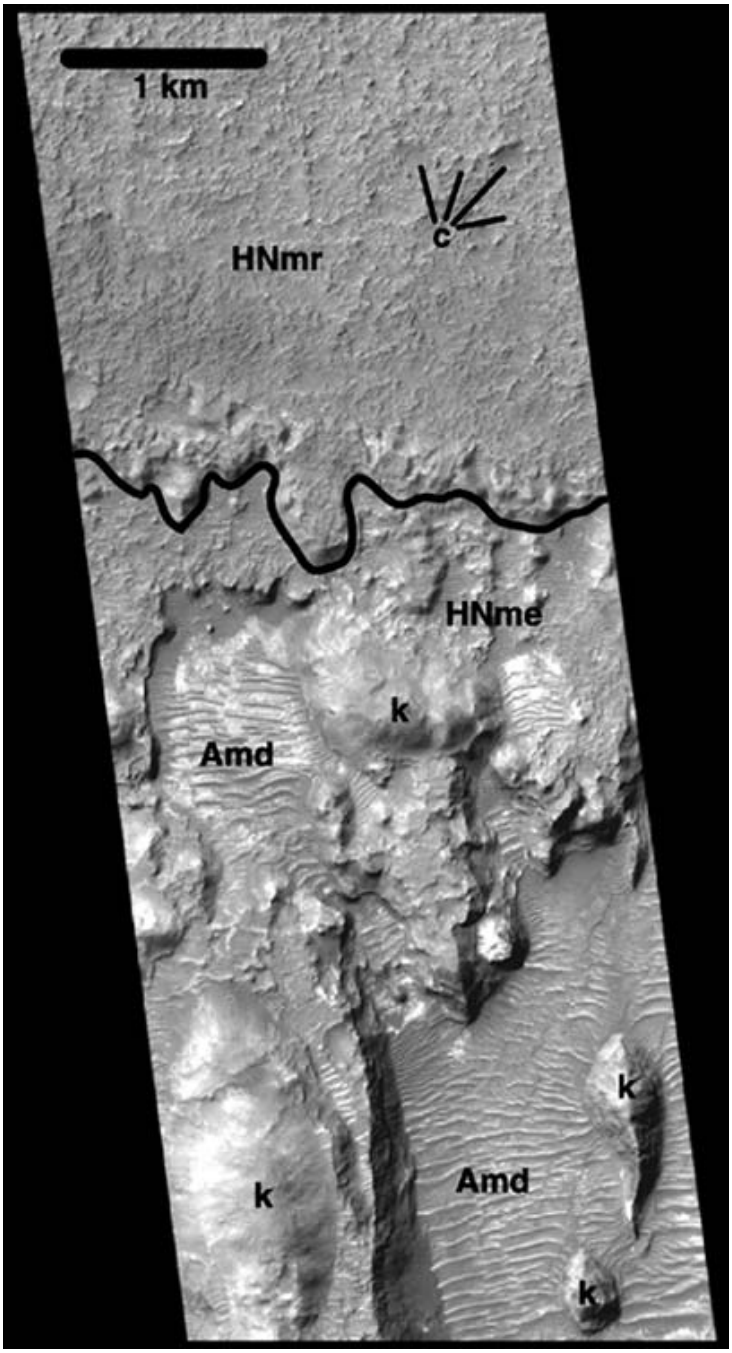

Figure 2.10c. Part of MOC image M19-01414 showing Millochau rugged (unit HNmr) and etched (unit HNme) materials; the contact between these units is shown by a heavy black line. Typical rugged material found within Millochau has a 'stucco'-like texture and contains impact craters (c) that are heavily degraded. In this image, etched material is irregular and contains several large knobs (k). Also, dune material (unit Amd) is observed filling in low areas of the etched material. Image centered at 20.7°S., 274.7°W; image is 2.8 km across; resolution is 2.81 m/pixel; illumination from upper left; NASA/JPL/MSSS.

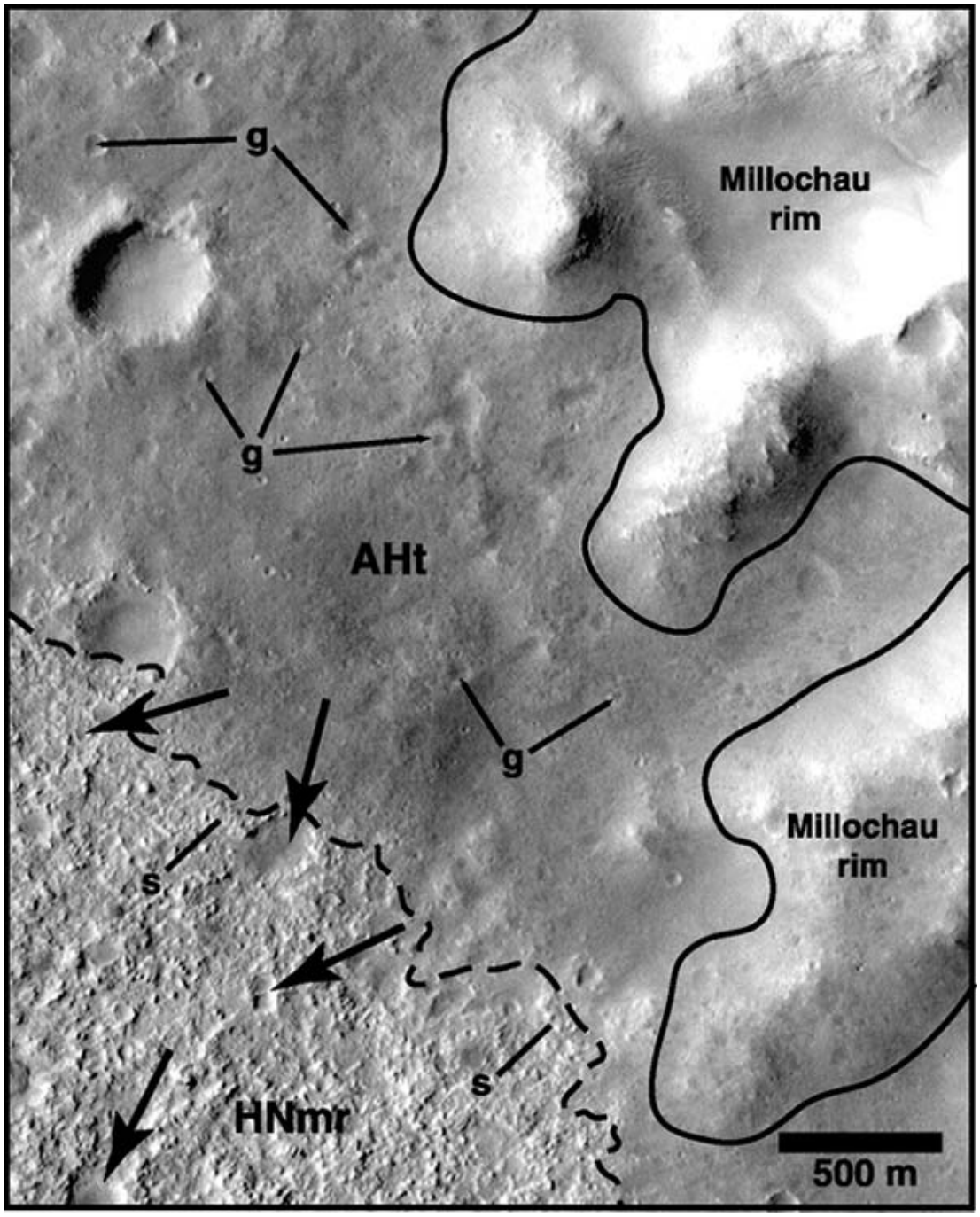

Figure 2.10d. Part of MOC image R04-01308 showing the contact (dashed line) between the smoother talus material (AHt) and the irregular rugged material (HNmr) near the base of Millochau's inner wall (right side of image). At some locations the contact is represented by a low-relief scarp (s), whereas in most places the contact is not discernible. Craters within rugged material are being exhumed as talus material is being removed; this is supported by the presence of numerous "ghost" craters (g) within the talus deposit. Illumination from left; image width = 3.02 km; resolution is 2.952 m/pixel; centered at 20.7°S, 85.8°E; NASA/JPL/MSSS.

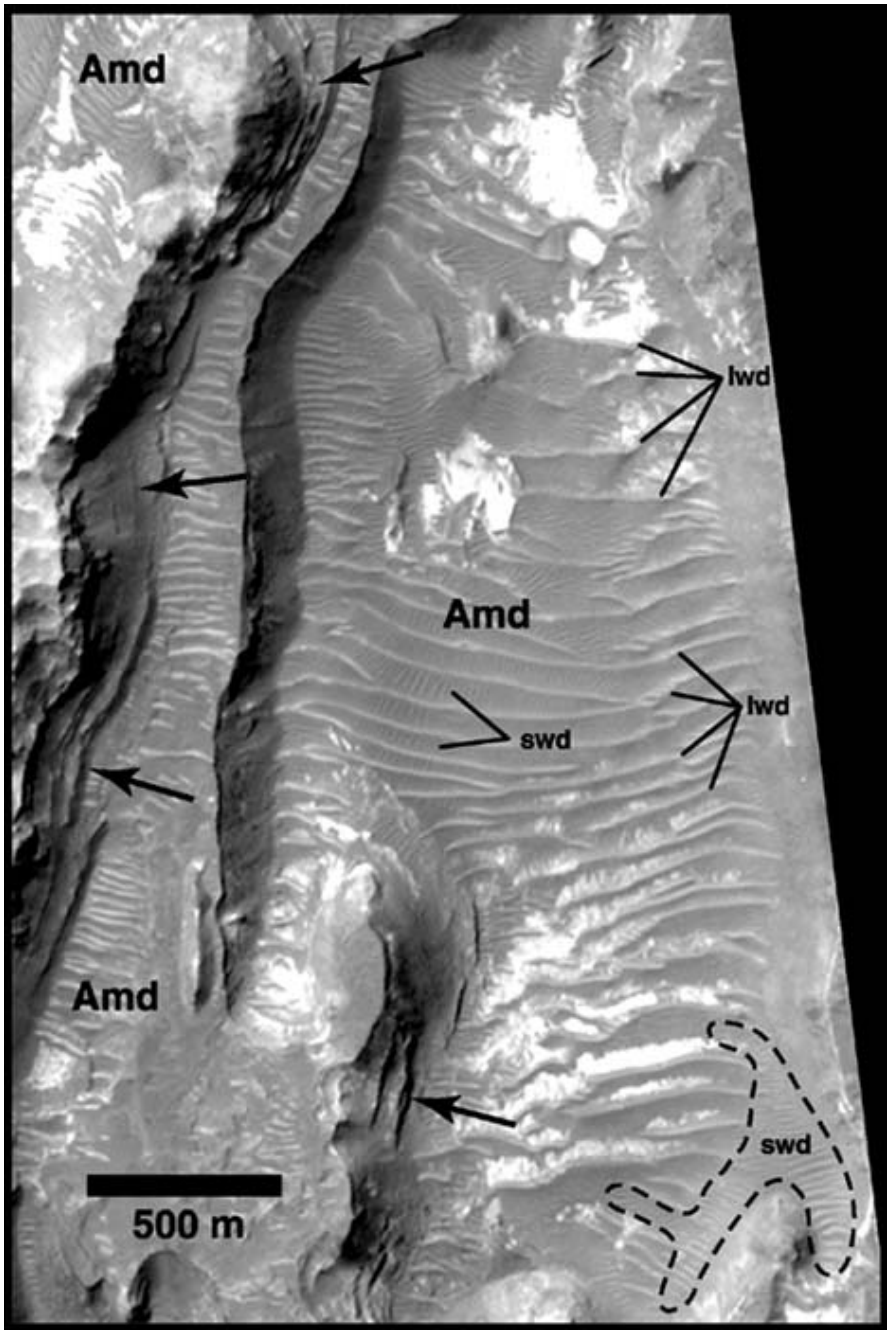

Figure 2.10e. Part of MOC image M18-00592 showing one of the larger exposures of dune material (unit Amd) in Millochau. Here, both long- and short-wavelength dunes are observed. Long-wavelength dunes typically trend east-west and span the widths of the depressions in which they occur. Short-wavelength dunes occur at all orientations, typically forming perpendicular to topographic highs, such as at the base of the layered knobs (arrows). Short-wavelength dunes also form perpendicular to the long-wavelength dunes as seen in the center of the image. Image centered at 21.1°S., 274.4°W; image is 2.8 km across; resolution is 2.81 m/pixel; illumination is from left; NASA/JPL/MSSS.

also show Millochau pitted material is bright during the day and dark at night, suggesting this unit consists of fine-grained deposits that heat up and cool down relatively quickly. The presence of many small (D<1 km) impact craters is similar to that which is observed in the northern intercrater plains and suggests these units may be similar in age. Millochau pitted material is believed to be composed partly of sedimentary deposits, but may also contain components of volcanic materials and impact-related (ejecta, impact melt) deposits, that may have extended across nearly the entire floor of Millochau and were subsequently eroded to their current extent. Capping the plateau, Millochau pitted material is topographically separated from the surrounding floor materials by nearly 400 m of relief. This separation, combined with the morphologic expression of its surface and TES and THEMIS data make it distinct from other units within Millochau. It is possible that some of the layering within the plateau, which includes the pitted material, could be lacustrine in nature, suggesting that crater Millochau may have contained large standing bodies of water. Pits on the surface of the deposit could be due to a large number of poorly preserved impact craters, collapse features, and (or) wind-modified depressions. Scarps within the deposit are most likely erosional in nature and may indicate the locations of immature sapping valleys as described above [Mest and Crown, 2004a,b].

Millochau rugged material (unit HNmr) forms irregular surfaces that exhibit a stucco-like texture (Figure 2.10c) and that slope down from the base of the interior wall to the central plateau. Most craters are poorly preserved showing highly degraded rims and little to no ejecta. Low areas within the unit typically contain dune material. High-resolution (8-11 m/px) VO images show low-relief (<20 m) scarps cutting through rugged material in the southern and eastern parts of Millochau; further analysis of THEMIS visible and daytime infrared images reveal these are not scarps, but mare-type wrinkle ridges [Mest and Crown, 2004a,b]. Millochau rugged material near the base of Millochau's eastern wall appears to have been exhumed in MOC image R04-01308 (Figure 2.10d) as overlying talus material (see below) was removed. Millochau rugged material exhibits TES-derived thermal inertia values of ~400 to 500 $J/m^2Ks^{1/2}$, suggesting rocky and (or) coarse-grained surface materials or cemented fine materials [Jakosky et al., 2000; Mellon et al., 2000; Christensen et al., 2001; Putzig et al., 2003]. THEMIS infrared images show that Millochau rugged material is dark during the day and bright at night, suggesting the materials that make up this unit is composed of materials that retain their heat into the night. Millochau rugged material is interpreted to consist of sedimentary and impact-related

(ejecta, impact melt) deposits; the fact that this unit slopes toward Millochau's center suggests a component of this unit may also be emplaced by mass wasting. The irregular surface of Millochau rugged material suggests this unit has experienced significantly more degradation or is less resistant to erosion than adjacent Millochau pitted material. It is believed that Millochau rugged material was at one time buried by Millochau pitted material, and has subsequently been exhumed [Mest and Crown, 2004a,b]. Wrinkle ridges within the deposit are most likely tectonic in nature [Strom, 1972; Lucchitta, 1976; Fagin et al., 1978; Phillips and Lambeck, 1980; Saunders and Gregory, 1980].

Millochau etched material (HNme) forms much of the terrain within the depressions that border the northern and eastern portions of the central plateau (Figures 2.10b and c). This unit displays a variety of surface textures (smooth, lineated and irregular) and brightness variations and encompasses surfaces not incorporated within other units mapped in Millochau. MOLA data show that Millochau etched material is consistently topographically lower than pitted material, but is found above and below rugged material [Mest and Crown, 2004a,b]. Some exposures of Millochau etched material are found within the depressions surrounding the plateau at roughly the same elevation as Millochau rugged material and may be eroded outliers of rugged material. Few fresh craters are observed within Millochau etched material; some exposures appear to contain craters that are being exhumed. Lineated Millochau etched material is shown in Figure 2.10e in which polygons filled with bright and dark materials are separated by narrow flat-topped ridges. It is unclear what the nature of this surface is, but one scenario is a thin layer that has been partially eroded. Lineated and irregular exposures of Millochau etched material are interpreted to be exhumed crater interior deposits; the thin layers observed in Figure 2.10e suggest these deposits are sedimentary in origin. Smoother exposures of Millochau etched material are believed to consist of eroded crater interior materials redistributed via fluvial and eolian processes and may be unconsolidated to loosely consolidated. Collapse of overlying materials and (or) erosion (fluvial and eolian) are believed to be the main processes operating to expose these deposits.

Millochau dune material (Amd) occurs in isolated patches that fill low-lying parts of pitted and etched materials (Figures 2.10b-c,e). The material that forms these deposits is generally darker than the underlying materials and forms long- and short-wavelength dunes, similar to those described by Edgett [2001a,b]. Dune wavelengths were measured on high-

resolution MOC images for thirty-four long-wavelength and twenty-one short-wavelength dunes. The long-wavelength dunes (~40-170 m; average ≈ 70 m) tend to be oriented east-west (long axis) and many span the widths of the depressions in which they occur. Short-wavelength (~10-30 m; average ≈ 20 m) dunes are shorter (long axis) and narrower than long-wavelength dunes. Short-wavelength dunes tend to be oriented parallel to the long-wavelength dunes, but some are perpendicular and are found between long-wavelength dunes; they are also typically oriented perpendicular to the dips of slopes of topographic highs (knobs and scarps). From MOC images, it appears that most short-wavelength dunes superpose the long-wavelength dunes, indicating they are younger and more mobile. Millochau dune material is interpreted to consist of sediments eroded from other interior floor deposits, as well as crater wall and rim materials, and redistributed within low-lying areas by wind.

The materials comprising the crater Millochau floor deposits have small areal extents and contain few large craters on their surfaces. The corresponding large statistical uncertainties suggest limited use of relative age determinations for these units. Crater size-frequency distributions for Millochau rugged, pitted and etched materials do not allow identification of a distinct progression in age for these units. Stratigraphic relationships between Millochau pitted and rugged material are unclear, but rugged appears to embay the pitted material, suggesting it is stratigraphically younger, and thus crater counts reflect formation age. Alternatively, rugged material could have been exposed when the plateau was eroded, yielding a younger surface than pitted material and thus the crater counts reflect surface retention age. However, Millochau pitted material shows higher crater densities for craters 2, 5, and 16 km in diameter, and has been designated as Middle to Late Noachian in age. Millochau rugged material shows lower densities (N(2) and N(5)), consistent with its more degraded appearance and the potential for more crater obliteration than the pitted material, and has been designated Middle Noachian to Early Hesperian in age. If Millochau pitted material did overlay Millochau rugged material, it would have effectively shielded the rugged material from impacts while continuing to accumulate impacts itself. Removal of Millochau pitted material to its current extent, along with erosion of Millochau rugged material and redistribution of sediments within this unit (and removal of small diameter craters) would yield the slightly younger ages that are observed [Mest and Crown, 2004a,b]. Thus the age determination for Millochau rugged material may be more representative of its exhumation and modification rather than its emplacement, which could be closer to Middle

Noachian. However, the margin of the plateau, and thus the contact of pitted material with rugged material, appears degraded and irregular in the THEMIS images available, and the possibility of rugged material embaying pitted material can not be discounted.

Determination of an age for Millochau etched material is difficult as only two craters with diameters greater than 2 km were identified in the image data sets. Given the interpretation that Millochau etched material is composed of a combination of old exhumed surfaces and younger redistributed unconsolidated debris, these data may more accurately represent surface retention ages rather than stratigraphic ages. Age determination for Millochau etched material is based on superposition relationships with Millochau pitted, rugged and dune materials. The base lithology composing the irregular, knobby and lineated outcrops of Millochau etched material likely formed a continuous surface that presumably extends beneath Millochau pitted and rugged materials. These exhumed materials are most likely Middle Noachian in age and older than Millochau pitted and rugged material; the depositional surfaces (smooth areas) formed after exhumation and could be as young as Early Hesperian, and their age is constrained by overlying Millochau dune material. As with Millochau rugged material, the ages designated for Millochau etched material are representative of an highly modified surface consisting of a mixture of reexposed older deposits and younger erosional debris.. Millochau dune material contains no superposed craters greater than 0.5 km in diameter and is therefore designated as being Amazonian in age.

Crater Okotoks[3] (D=22.6 km), in western Millochau, displays a well defined ejecta blanket [Mest and Crown, 2004a,b] that superposes Millochau rim, pitted and rugged materials, and provides an upper age constraint for the Millochau interior deposits, as well as for plateau formation and erosion. Crater size-frequency distributions for Okotoks (see Mest and Crown [2004a,b]) suggest an age of mid- to Late Hesperian. The ejecta from Okotoks appears relatively unmodified by the erosional processes that affected the pitted and rugged materials, suggesting emplacement and most of the erosion of these units occurred prior to formation of Okotoks within a window ranging from the Middle Noachian to Late Hesperian.

Talus material (unit AHt) forms narrow deposits along the interior walls of Millochau, Jumla and a large unnamed craters (17.2°S, 269.8°W) and generally overlies crater floor

[3] The name of crater 'Okotoks' is provisional until approved by the International Astronomical Union.

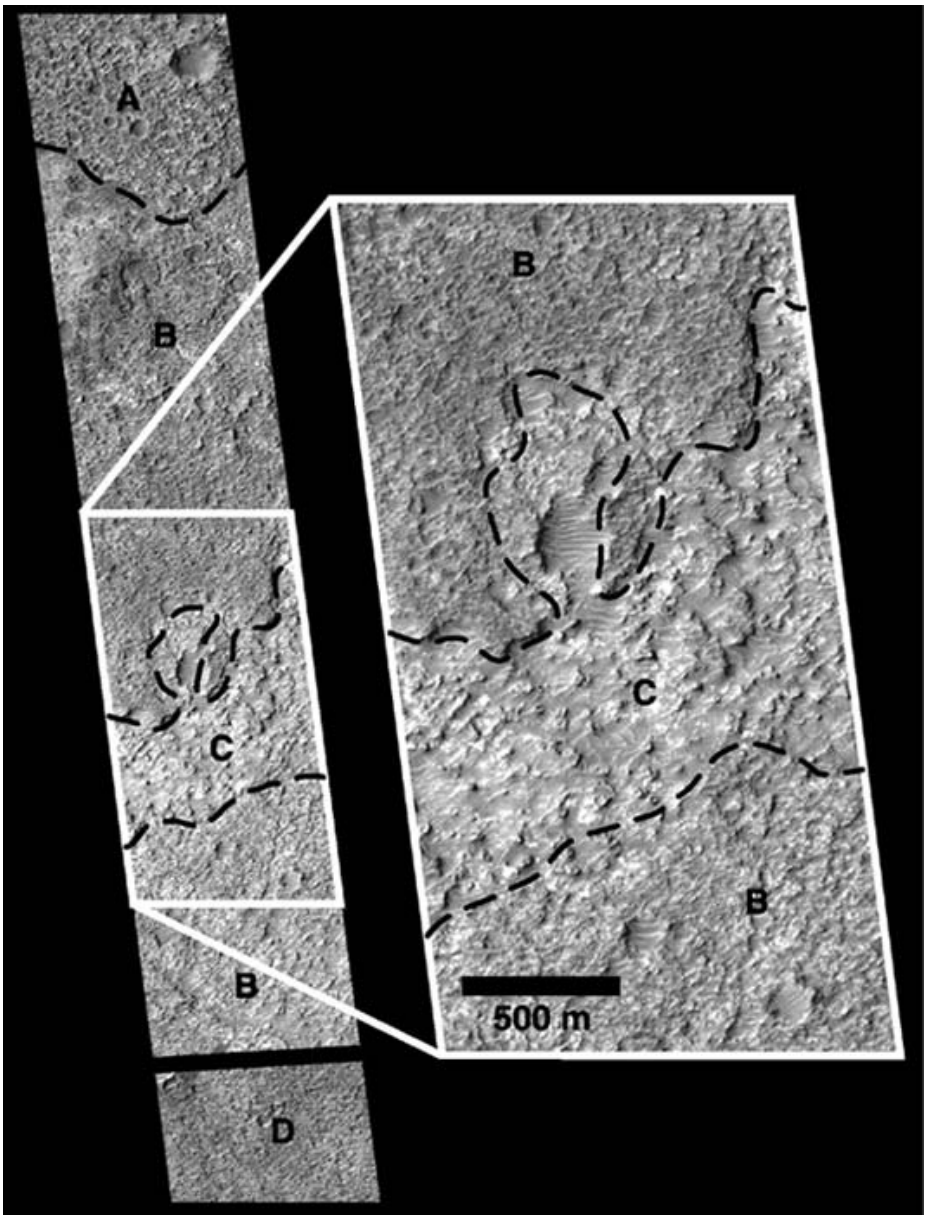

Figure 2.11. MOC image E04-02035 showing talus material (unit AHt) at the base of the inner rim of crater Jumla, a 43-km-diameter crater that adjoins Millochau's eastern rim. Here, talus material displays several surfaces, A-D, that appear to reflect different amounts of erosion. Surface A appears to be the uppermost layer in this sequence and displays distinct yet degraded crater forms. Surface B also displays degraded craters (see close-up), which are less distinct than on surface A. Surface C (see close-up) contains knobs and mesas that could be remnants of surface B or D. Surface D, separated by a data gap, contains mostly small degraded craters, and appears the least eroded of the surfaces pictured here. Dune forms, visible in the close-up, are found in the low-lying areas of surfaces B and C, suggesting eroded sediments have been remobilized within this crater. Image centered at 21.7°S, 273.9°W; image is 1.45 km across; resolution is 2.83 m/pixel; illumination is from left; NASA/JPL/MSSS.

material. These deposits are featureless in VO images, but show significant detail in MOC image E04-02035 (Figure 2.11), which covers part of crater Jumla that adjoins Millochau's eastern rim (Figure 2.10a). In this image surfaces A and B contain many recognizable craters despite a heavily degraded appearance, and portions of this surface resemble rugged material observed in Millochau, displaying irregular and degraded stucco-like surface textures. Figure 2.11 shows four distinct surfaces that have been subjected to different amounts of erosion, and it appears that surfaces A and B, and possibly D, are being removed to reveal underlying surface C. From this image it appears that the deposit shown in Figure 2.11 at the base of the crater wall is layered, suggesting that this particular deposit of talus could consist of sequences of material deposited in several mass wasting events. Talus material is interpreted to consist of unconsolidated debris shed from crater wall and rim materials by mass wasting and deposited along the interior walls of craters. The surface texture suggests talus material may have been extensively eroded in a manner similar to rugged material. Few large craters are observed on deposits of talus material, which show ages of Late Noachian to Late Hesperian for N(2) distributions. The low number of craters combined with the small surface area of this unit results in large age uncertainties. Based on the fact that talus material superposes crater floor material and Millochau rugged material, which are defined as Hesperian to Noachian in age, talus material is most likely Amazonian to Late Hesperian in age. Although only three exposures of talus material were large enough to be mapped, smaller deposits of talus may occur in other craters.

2.4 FLUVIAL FEATURES

The geologic evolution of the map area appears to have been greatly influenced by fluvial processes. The map area is dissected by large and small valley networks that display dendritic to sub-parallel patterns. The largest network, Vichada Valles, extends through much of the intercrater plains southward to the grouping of large craters at 24°S, and has tributaries that reach

outside of the map area. The drainage basin enclosing Vichada Valles, as well as several of the smaller networks, occupies an area of approximately 300,000 km^2 and is elongated in a north-south direction. From MOLA data, the basin exhibits roughly 4.5 km in relief with a maximum elevation near 3.5 km and a minimum near -1.0 km. At some point in the past, Vichada Valles presumably debauched into Hellas basin, but evidence of this extension has been obscured by later events. Most tributaries of Vichada Valles head within an elevation range of ~1.5-2.5 km.

Most of the networks in the map area display highly degraded morphologies (Figures 2.3 and 2.8). MOC images reveal that valleys have rounded banks, display terracing along valley walls, and have dunes covering their floors (Figure 2.5). MOLA profiles show that most of the trunk valleys and many of their smaller tributaries have v-shaped profiles in cross-section. Valley depths range from ~70 to 200 m and widths from ~0.9 to 10.5 km. Within the map area, the trunk valley of Vichada Valles branches and rejoins downstream several times along its length (Figure 2.3). Carr [1995, 1996] described one example of this phenomenon, attributing it to headward erosion of a sapping-type valley, where random headward extension led to intersection of the valleys upstream. However, the fact that valley widths and depths change significantly along their lengths, suggests another process of formation may be involved. In general, the larger valleys in the map area tend to vary in width along their lengths, possibly indicating areas of lateral flow or meandering, which is not characteristic of sapping-dominated valleys [Carr, 1995, 1996; Goldspiel et al., 1993; Goldspiel and Squyres, 2000].

Valleys and sub-parallel networks observed south of crater Millochau and east of the map area are smaller and appear less incised than Vichada Valles and other large systems. The tributaries of these smaller systems typically head at crater rim crests, at elevations between 1 and 2 km, and they are generally not more than a few hundred meters to a few kilometers long. The occurrence of these systems on steep slopes results in more closely spaced first-order tributaries. The valleys south of Millochau either merge with intercrater plains material with no sign of deposition at their mouths or they are truncated by craters and buried by ejecta. Some of the smaller networks east of the map area empty into an old buried crater basin that has subsequently accumulated large impact craters on its floor. None of these smaller networks are observed to intersect Vichada Valles. The morphologic differences between these smaller networks and Vichada Valles could be due to differences in age, lithology, slope, and (or) the effects of broad-scale versus localized erosion. In a synopsis by Carr [1995, 1996], the smaller

and more dense networks of valleys just east of the current map were not attributed to sapping alone because many valleys head at crater rim crests. It was therefore suggested that some component of surface runoff was required to form these valleys, perhaps by overflow of craters that were filled to their rims with percolating groundwater combined with mass wasting of water-saturated materials.

Identification of clear crosscutting relations between fluvial valleys and impact craters is difficult due to coverage by low resolution VO images of much of the map area. Much of the dissection of the local plains material appears to have been contemporaneous with or post-date impact crater formation. For example, several of the moderately degraded craters in the northern and east-central parts of the map area have ejecta dissected by well incised valleys (Figure 2.8). In addition, a valley dissects the terrain between two fairly pristine craters (craters A and B in Figure 2.8) in the northeastern part of the map area. VO images do not clearly resolve whether impact ejecta is found on the floor of this valley, but MOLA profiles across the valley show very little difference in its depth where the valley crosses the ejecta compared to upstream and downstream from the ejecta. It is also possible in this case that any ejecta on the valley floor(s) has been removed by subsequent flow events, or redistributed by eolian processes.

Impact craters exhibiting breached rims are also observed in the map area, but are not common. Two of the more prominent examples of breached craters are found at 20.7°S, 273.1°W (crater 'A' in Figure 2.3) and -17.7°S, 272.5°W; although the latter example is not mapped as an impact crater, its circular planform morphology suggests this feature is a crater that has been severely degraded, more so than most degraded craters in this area. The first crater, shown in Figure 2.3, displays a relatively flat interior containing several small impact craters, an inlet valley breaching the western rim and an outlet valley breaching the southeast rim. A sequence of fluvial erosion and deposition may be derived based on the morphologies of the inlet and outlet valleys. MOLA data show that the mouth of the inlet valley is approximately 200 m wider and 50 m deeper than the head of the outlet valley (widths = 1100 m and 900 m and depths = 100 m and 50 m, respectively), and the floor of the outlet valley is ~100 m higher in elevation than the floor of the inlet valley. These differences suggest that the inlet valley may have breached this crater first, resulting in ponding of water and deposition of sediments eroded from the surrounding highlands. The smaller outlet valley suggests that incision of this valley probably did not occur until this crater was filled with water at which time it overtopped the crater rim and

began downcutting. There is not clear evidence (in images or MOLA) within this crater to indicate water level (such as shorelines or benches), therefore it is also possible that the outlet valley grew headward from the southeast until intersecting and breaching the crater rim. The valleys that breach this crater and the crater at -17.7°S, 272.5°W likely carried materials derived from upstream exposures of intercrater plains and impact materials. The interiors of these breached impact craters therefore should contain a suite of fluviolacustrine deposits representative of the local highlands.

Impact craters that superpose valleys are also observed, showing that some large craters post-date valley formation. Observations indicate that there was little to no flow following the impact. For example, some craters that intersect valley segments do not appear to have caused any visible "damming" and (or) diversion of water upstream from the crater due to the structure of the crater itself or emplacement of its ejecta within the valley. If significant flow within these valleys was present at the time of impact, some evidence of ponding and deposition of sediments, or diversion of the water and incisement of a new channel should be present. Figure 2.8 shows one possible example for diversion of flow around a crater, but no evidence for ponding upstream from the crater is observed. These features are rarely observed in the available data sets.

The relationships mentioned above suggest that most of the fluvial activity in the map area appears to have occurred prior to or soon after the majority of large impact craters formed, as evidenced by their eroded rims and ejecta blankets. These relationships, combined with crater size-frequency distributions for valley floor material, indicates that most of the valley formation in this part of the highlands was relatively old, with most fluvial activity ceasing in the Late Noachian to Early Hesperian. Geologic mapping by Maxwell and Craddock [1995] in Tyrrhena Terra (15°-30°, 260°-270°W) showed similar results. In their study, dissected highlands and intercrater plains were found to range from Middle to Late Noachian and Late Noachian to Early Hesperian in age, respectively; and dissection of these materials occurred in the Late Noachian to Early Hesperian.

As mentioned earlier, previous researchers [e.g., Carr, 1995, 1996] have interpreted highland valleys, such as those mapped here, to have formed by combinations of surface runoff-induced mass wasting and sapping processes. However, questions regarding the ability of sapping to be sustained in local environments (i.e., along crater rims) have been raised

[Craddock and Maxwell, 1993; Maxwell and Craddock, 1995]. Furthermore, the ability to sustain an interconnected aquifer system in the highlands might be problematic over regional scales where the subsurface materials may not be conducive for flow of groundwater. Hydrologic modeling is currently being used to examine these problems to further constrain the fluvial evolution of the Tyrrhena Terra region [Mest et al., 2002].

2.5 GEOLOGIC HISTORY

Geologic mapping in the Tyrrhena Terra region of the martian highlands reveals a surface that has undergone significant degradation and modification by impact, fluvial, and eolian processes. Most of the materials mapped in this study are very old, ranging from Middle Noachian to Early Hesperian in age. Only surficial deposits such as dune material and talus, which have very limited exposure in the area, show evidence for activity in the Amazonian Period. The map area shows complex relationships between impact craters and the valley networks that dissect the intercrater plains. Lack of consistent high-resolution coverage across the entire map area complicates interpretation of age relationships. However, using stratigraphic relationships combined with crater size-frequency distributions, general constraints on the geologic evolution of the region have been developed.

Dominant events in the geologic development of this part of the highlands include the formation of Hellas and other large basins early in Mars' history. The impacts forming these basins deposited ejecta over much of the surface and altered the topography of the highlands, forming large low-lying areas that later served as sediment sinks. During the Early and Middle Noachian Epochs, widespread intercrater plains formed by accumulation of some combination of sedimentary (fluvial and eolian), volcanic (may include flow sequences and (or) pyroclastic deposits), and impact-related (melt and ejecta) materials. The materials composing the plains are layered but not consistently so across the highlands in the map area. The lack of evidence for

volcanic flow features and the eroded nature of the plains material suggests the uppermost layers most likely consist of sedimentary and impact deposits.

Heavy bombardment during the Noachian Epoch produced numerous (28) large (D>10 km) impact craters, including crater Millochau, in the map area. At the same time, fluvial processes shaped the intercrater plains, forming well incised networks of valleys and degrading plains surfaces. In addition to dissecting the plains, the valleys cross-cut ejecta deposits of some craters. As fluvial activity waned, numerous impacts continued to affect Tyrrhena Terra; evidence for this is shown by craters that truncate and (or) bury valley segments, such as the cluster of several large craters at about 24°S latitude. These craters did not appear to cause redirection of flow or ponding of water and sediments indicating there was little to no flow within these channels at the time of impacts. The nature of the fluvial activity that formed extensive valley networks has been questioned in this and other areas of the highlands [e.g., Craddock and Maxwell, 1993; Carr, 1996, Maxwell and Craddock, 1995; Grant, 2000; Craddock and Howard, 2002; Grant and Parker, 2002]. Carr [1995, 1996] attempted to explain their formation by groundwater sapping combined with mass wasting induced by surface runoff, such as by collapse of surface materials by fluvial undercutting or incorporation of water into surficial materials to form wet debris flows. However, in this study variations in valley widths and depths along the lengths of the valleys, which is uncharacteristic of sapping valleys, and the fact that several valleys head near crater rim crests, suggest a significant component of surface runoff not derived from groundwater was involved, such as from direct precipitation or water derived from melting snow or ice. This scenario has been proposed for the Margaritifer Sinus area [Grant, 2000; Grant and Parker, 2002] and for other areas within the martian highlands [Craddock and Maxwell, 1993; Maxwell and Craddock, 1995; Craddock and Howard, 2002]. The size and nature of Vichada Valles provide further information from which to address the styles of fluvial activity that may have shaped the Martian highlands. Vichada Valles is an extensive, integrated drainage system. Although, high-resolution imaging datasets have allowed identification of small tributaries not observed earlier [Carr, 1995, 1996], there are still large undissected interfluve regions associated with it. A drainage system of this magnitude and morphology would seem to require either 1) mobilization of volatiles contained within an extensive subsurface reservoir or 2) widespread precipitation. High infiltration rates presumably characterize the surface and near-surface materials, and the formation of valley segments likely includes a combination of sapping

and runoff processes, with larger valley segments shaped in run-off dominated phases or as greater volumes of groundwater collected in the surface drainage system.

During the Late Noachian and Early Hesperian Epochs, impact craters were being degraded as well. In addition to eroded ejecta blankets and rims, impact craters in the map area show interior walls incised with numerous gullies and floors containing deposits of relatively smooth fill material. Crater Millochau is one example where detailed analysis and mapping of the floor deposits could be accomplished because of available MOC and THEMIS images [Mest and Crown, 2004a,b]. Millochau floor deposits display surface textures similar to those of the intercrater plains, containing degraded pits and craters and low-lying areas filled with darker sediments. The geology of Millochau is complex, revealing a history of emplacement of sequences of sedimentary, volcanic and (or) impact materials that subsequently experienced degradation, possibly involving collapse and fluvial erosion. Sedimentation within Millochau appears to be related in part to erosion of the interior crater rim by numerous gullies, but may also include contributions from eolian and lacustrine activity [Mest and Crown, 2004a,b]. Although the areas for most of the units within Millochau are small, which produces rather large uncertainties in their unit ages, crater Okotoks in western Millochau displays a fairly unmodified ejecta blanket with relatively large area. Crater size-frequency distributions for Okotoks' ejecta provide upper age constraints (mid- to Upper Hesperian) on the emplacement and erosion of Millochau's interior deposits and the central plateau [Mest and Crown, 2004a,b]. Crater size-frequency distributions and superposition relationships indicate emplacement and most of the erosion of Millochau floor deposits occurred prior to formation of Okotoks within a window ranging from the Middle Noachian to Upper Hesperian. Although Millochau is the only crater in the map area that has been imaged with such detail, other large craters in the map area are believed to contain similar floor deposits and may have had similar histories.

The Late Noachian and Early Hesperian Periods also involved emplacement of the smooth plateau unit in the southeast corner of the map area as well as deposition and remobilization of valley floor material. Valley floor material, believed to consist of materials eroded from the highlands and deposited in the channels via fluvial and eolian processes, shows dune-forms in high-resolution MOC images, suggesting that they are composed of easily mobilized material. Eolian transport and deposition of material also occurred in the southernmost exposures of the intercrater plains material. The plains material in this part of the map area is

subdued in nature. MOC images show that high-standing outcrops of the pitted and degraded material characteristic of the plains in the northern part of the map area are surrounded by smooth, darker materials that fill low-lying areas of the plains and form dune features. Dark material and dune features are also found on the high-standing outcrops of the intercrater plains material, but the overall pitted and irregular surfaces characteristic of the plains are visible through this material, suggesting the mantling layer is relatively thin. Sources of this fine-grained sediment could include material deposited by the valley networks that characterize the area, ejecta of several large and fairly young impact craters, and material blown from Hellas basin and the surrounding highlands. With the exception of crater Millochau and valley floors, these high-density dune fields are only observed with this kind of clarity by MOC images in the southern part of the map area.

The most recent activity in the area involves eolian processes that formed the dune material in Millochau and the valley floor material, eroded the uppermost layers of the intercrater plains, and redistributed material throughout the map area. Some of this activity may have been geologically very recent and may currently be active. Also, mass wasting processes, such as formation of talus deposits in Millochau and other large craters appears to have been geologically recent.

Investigation of highland degradation in this and other areas of the circum-Hellas highlands provides important insights into the potential variability of geologic processes and climatic conditions. For comparison, geologic mapping in eastern Hellas [Crown et al., 1992; Mest and Crown, 2001b, 2002b, 2003a] has shown that much of the fluvial activity there is younger relative to that in Tyrrhena Terra. Valley networks in the highlands adjacent to Reull Vallis formed in the middle to Late Hesperian because they dissect Late Noachian to Early Hesperian intermontane sedimentary deposits and these systems re believed to have contributed sediments to the adjacent plains materials that are Early to middle Hesperian in age. These networks are an order of magnitude smaller in scale than those in Tyrrhena Terra and tend to be confined to low-lying areas among highland massifs. The large events that formed Reull Vallis also most likely occurred in the Hesperian; this type of activity is not observed in the Tyrrhena Terra study area. In addition to the evidence for fluvial processes, the highlands east of Hellas contain numerous Amazonian debris aprons that are interpreted to result from downslope movement of volatile-rich debris [Crown et al., 1992; Crown and Stewart, 1995; Mest and

Crown, 2001b, 2002b, 2003a; Pierce and Crown, 2003]. The significant differences between the ages, scales and morphologies of fluvially-produced features suggests (a) the climate history of the two regions differ significantly, (b) the distribution of volatiles around the Hellas basin varies greatly, even within a few hundred kilometers, and (or) (c) the effects of fluvial processes on the landscape were greatly dissimilar in the two areas. Mars Orbiter Laser Altimeter and THEMIS data are being used in conjunction with geologic mapping to document the styles and timing of the degradational processes. Specifically, watershed modeling is being conducted to further constrain fluvial activity in these highland terrains.

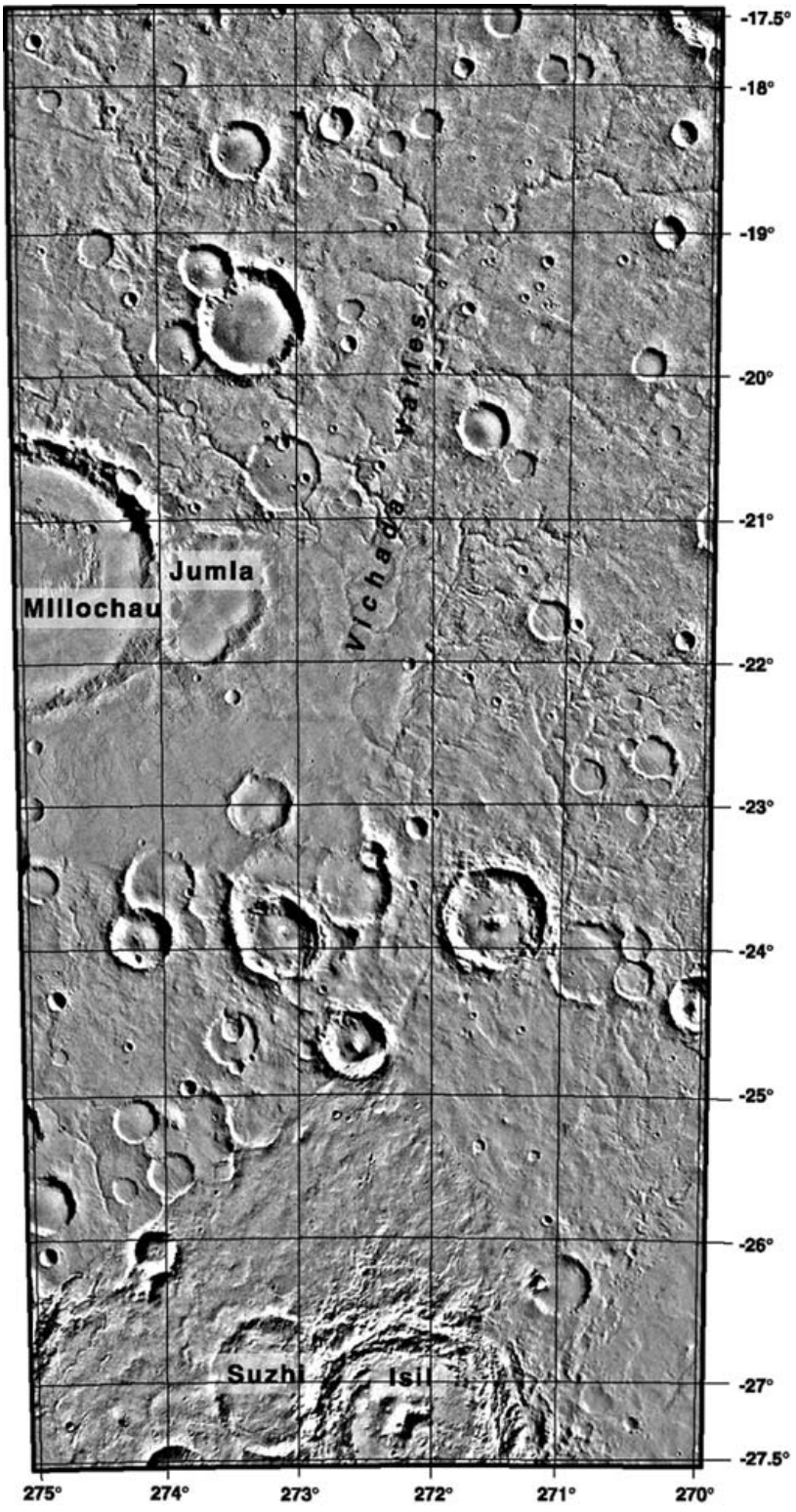

Plate 2.1. Viking Orbiter image Mosaic of Mars Transverse Mercator quadrangles -20272 and -25272. Image resolution ranges from 60 to 237 m/pixel. Location of mosaic shown in Figure 2.1.

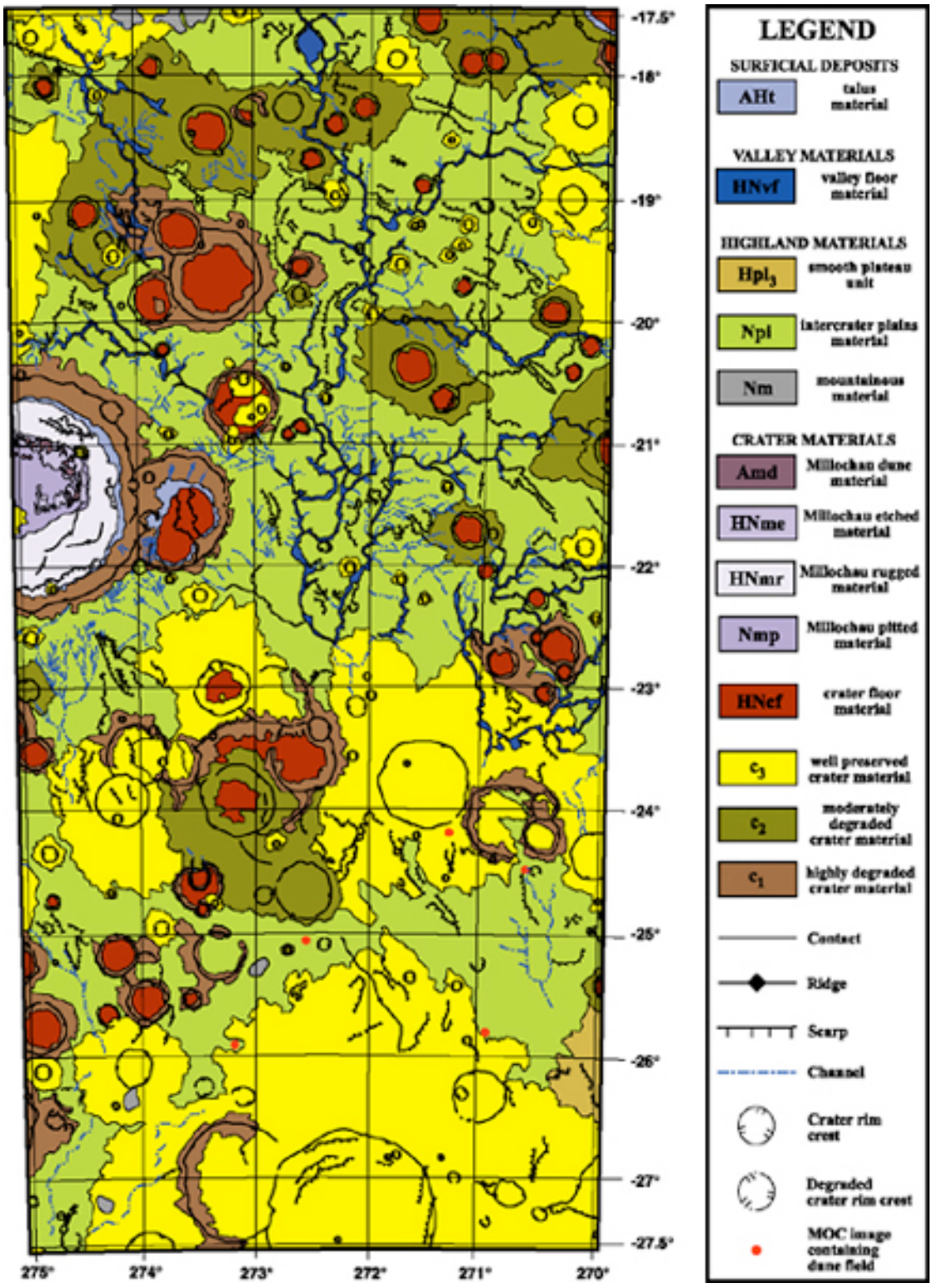

Plate 2.2. Geologic map of Mars Transverse Mercator quadrangles -20272 and -25272. Location of map shown in Figure 2.1.

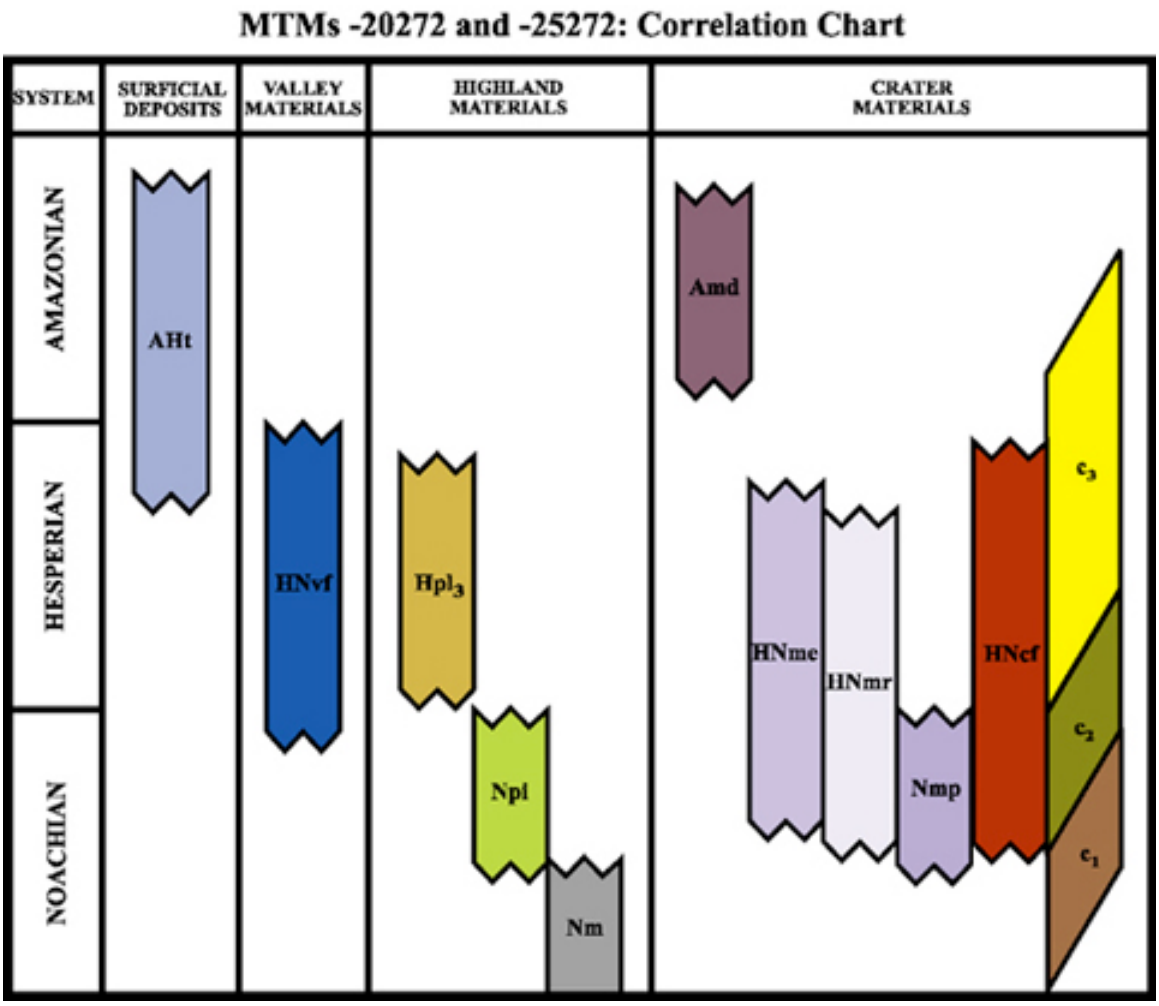

Plate 2.3. Correlation chart showing relative stratigraphic positions of units defined in text and Description of Map Units (Appendix 2), and shown in Plate 2.2.

3.0 CRATER MILLOCHAU, MARS: HESPERIAN-AGED EROSION OF AN ANCIENT HIGHLAND IMPACT CRATER

3.1 INTRODUCTION

The martian highlands preserve a long and complex record of degradation dominated by fluvial, eolian, and mass-wasting processes. The effects of these processes are displayed in various degrees within the ejecta blankets, on the rims, and on the floors of many impact craters that characterize ancient parts of the martian surface. Studies of the Tyrrhena Terra region in the southern cratered highlands [Murray et al., 1971; Schaber, 1977; Tanaka, 1986; Greeley and Guest, 1987; Grant and Schultz, 1991a,b, 1993, 1994; Tanaka and Leonard, 1995; Craddock et al., 1997a,b; Leonard and Tanaka, 2001; Mest and Crown, 2002a, 2004a] suggest significant amounts of fluvial erosion and deposition occurred during the Noachian Period, followed by remobilization of sediments by eolian activity. The highland terrain surrounding crater Millochau within Tyrrhena Terra is dissected by numerous valley networks that are believed to have formed by fluvial [Grant and Schultz, 1993, 1994; Mest and Crown, 2003b, 2004a] and (or) groundwater sapping [Carr, 1995, 1996] processes. Cross-cutting relationships between valleys and impact craters provide relative age information and help to evaluate the timing of valley formation and the degradation styles and sequences for highland features (such as craters) and surfaces.

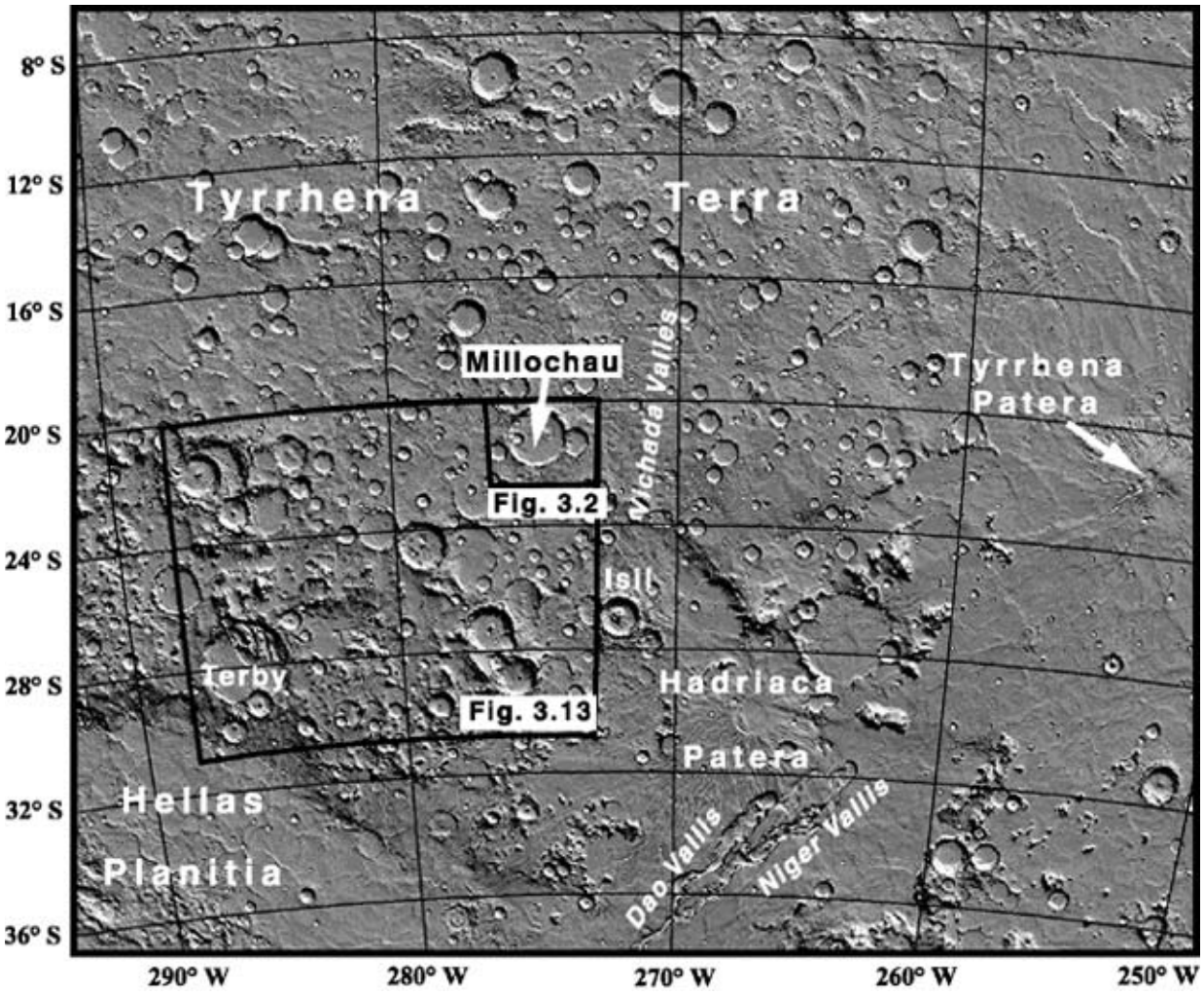

Figure 3.1. MOLA shaded relief image showing regional highland terrains north and east of Hellas basin. Regional names and the locations of features local to crater Millochau (diameter = 114 km) are indicated. Boxes indicating the locations of Figures 3.2 and 3.13 are shown. Projection is Mercator; north is to the top in this and all subsequent Figures, except where noted; illumination altitude = 40°; azimuth = 30°.

Crater Millochau (21.4°S, 275°W) is a large (D=114 km) crater in Tyrrhena Terra north of the Hellas impact basin (Figure 3.1). Its complex geology is representative of many of the above-mentioned processes. Due to its size, degraded morphology, and apparent ancient age, the geologic record of crater Millochau could represent a large part of martian history, recording changes in degradational style(s) and the effects of climatic changes. Millochau also serves as a proxy for craters of similar age to understand the regional degradational history. The presence of valley networks along the exterior rim of Millochau and numerous gullies along its interior rim indicate fluvial activity played a large role in the crater's modification and may have contributed significantly to deposition on the crater floor. The geological (e.g., composition, distribution, and strata thicknesses and horizontal continuity) and physical (e.g., grain size) characteristics of the deposits that fill Millochau, as well as other craters in the region, can provide significant insights into the past martian environments. Furthermore, if Millochau contained a paleolake, heat from the initial impact dissipating through hydrothermal vents could have provided the necessary environment for sustaining life, signs of which may be preserved in the rocks and sediment that cover the floor of Millochau. Through geologic mapping, analyses of Viking Orbiter, Mars Orbiter Camera (MOC), and THEMIS-visible (Thermal Emission Imaging System) and -thermal infrared wavelength images, TES (Thermal Emission Spectrometer) data, and Mars Orbiter Laser Altimeter (MOLA) topographic data, this study (1) characterizes the geologic and geomorphic terrains within Millochau, (2) assesses potential origin(s) and the ages of the Millochau floor deposits, and (3) investigates the degradation processes that might have affected Millochau and other craters in the region. Detailed analysis of crater Millochau is part of a larger project being undertaken to document the history and characterize the geology of Tyrrhena Terra [Mest and Crown, 2004a].

3.2 BACKGROUND

Many impact craters on Mars are thought to have contained standing bodies of water. Forsythe and Blackwelder [1998] and Cabrol and Grin [1999, 2001a] compiled extensive databases of the locations, classification, and ages of impact craters (D>5 km) that show evidence for interior lakes. Mars displays three types of postulated crater-lake systems: (a) closed, (b) open, and (c) lake-chains [Forsythe and Blackwelder, 1998; Cabrol and Grin, 1999]. Closed systems (e.g., craters Schiaparelli, Henry, Galilaei, and Becquerel) are characterized by a valley or network of valleys that flow into a crater and no outflow valley, and appear to be the most common. Open impact crater systems, such as craters Galle, Gale, Barabashov, and Da Vinci, are characterized by rims breached by both an inflow valley(s) and an outflow valley; outflow valleys form either by headward erosion of an interior valley or overflow of water from a crater lake. Holden crater (26°S, 34.2°W; D~140 km), part of the Ladon/Uzboi Valles system, contains eroded layered deposits (with thicknesses down to the limit of MOC image resolution) that are laterally continuous for several kilometers, consistent with emplacement in a standing body of water [Grant and Parker, 2002; Malin and Edgett, 2003]. Lake-chain systems on Mars may be open or closed systems consisting of a series impact craters linked by a channel or series of channels [Cabrol and Grin, 1999]. Lake chain systems include Gusev crater, and several unnamed craters along Mangala and Mamers Valles.

Inflow and outflow valleys that breach crater rims and flat, relatively smooth deposits on the floors of these craters have been used as evidence for the existence of paleolakes on Mars. In addition, a suite of other geomorphic features that further support the existence of paleolacustrine environments has been identified. These include lacustrine deltas, sedimentary terraces, and shorelines [Cabrol et al., 1996; Grin and Cabrol, 1997; Forsythe and Blackwelder, 1998; Ori et al., 2000; Cabrol and Grin, 1999, 2001a; Moore and Wilhelms, 2001; Irwin et al., 2002a,b]. Analyses of these features can provide insight into the environment(s) in which they might have formed. Furthermore, compiling impact crater statistics on the surfaces of the geologic materials and the geomorphic features that form the crater lake system can provide relative age constraints for the existence and duration of paleolacustrine environments. N(2) and N(5) crater size-frequency distributions for most (~70%) of the crater lake systems observed indicate activity

from the Early to Late Hesperian Epochs, with the remaining 30% being as young as Middle Amazonian [Cabrol and Grin, 1999, 2001a].

Other researchers, such as Grant [1999] and Grant and Schultz [1993], observed drainage networks and gullies on crater rims and ejecta blankets, crater rims breached by valleys, and crater walls sloped at the angle of repose for fine-grained material. They have attributed many crater interior deposits, especially within highland craters, to combinations of fluvial, mass wasting (talus and debris aprons), and eolian processes. Through morphologic analysis of highland impact craters and characterization of drainage features superposing those craters, Craddock and Maxwell [1993] proposed that fluvial erosion from exogenic processes (precipitation or snowmelt) produces most interior deposits whereas mass wasting and eolian provide minor contributions of material. However, it has been shown in the highlands east of Hellas basin that a significant amount of crater floor material is emplaced via mass wasting in the form of prominent lobate debris aprons [Crown et al., 1992; Mest, 1998; Mest and Crown, 2001b, 2002b, 2003a; Pierce and Crown, 2003]. The presence of dune fields and dark splotches indicates that eolian deposition within martian craters may also contribute significant quantities of sediments to crater interior deposits as shown by Edgett and Malin [2000] in crater Trouvelot and other craters in western Arabia Terra. Lastly, lunar craters are observed to contain fractured or chaotic interior deposits (‘floor-fractured’ craters described by Schultz, [1976]) that have been attributed to tectonic modification by volcanic intrusions localized within the heavily brecciated zone beneath the craters. Similar volcano-tectonic processes are believed to have affected some martian impact craters [Schultz and Glicken, 1979]. The martian examples contain a wider variety of features than the lunar counterparts due to incorporation of volatiles and include fractures, concentric graben, and knobs, plateaus and furrows. The martian process of endogenic modification also differs from the lunar process in that significant erosion and removal of material is a factor for martian craters [Schultz, 1976; Schultz and Glicken, 1979].

Crater Millochau has not been studied in great detail in the past and does not appear in either the Forsythe and Blackwelder [1998] or Cabrol and Grin [1999, 2001a] databases. This is most likely due to the classification schemes used by the aforementioned authors, as well as a lack of adequate high-resolution data to identify possible small-scale lacustrine features. A wealth of new mission data, particularly the MOC, MOLA, and THEMIS datasets, allows the

geology of crater Millochau to be characterized in detail, the nature and history of deposition on the crater floor to be evaluated, and a potential lacustrine component in its history to be assessed.

3.3 GEOLOGIC SETTING

The region of the highlands of Tyrrhena Terra containing crater Millochau displays an overall south-trending slope of approximately 0.33°, which is toward, and has presumably been established by, Hellas basin. The highlands adjacent to Millochau are characterized by a high density of impact craters that range in size from the limits of MOC resolution to over 100 km in diameter [Mest and Crown, 2004a]. These craters also vary in degrees of preservation; most craters are moderately to highly degraded, but even many of the 'fresh' craters with well-defined rims and ejecta blankets have experienced some degree of modification. Most craters in this area, regardless of their preservation state, contain deposits that cover their floors. These deposits are believed to be Late Noachian to Early Hesperian in age and have several likely origins, such as (a) eroded crater rim and wall materials deposited via gullies and(or) by mass wasting, (b) highland materials deposited via a valley that breached a crater rim, and(or) (c) sediments deposited via eolian processes [Mest and Crown, 2004a].

The terrain surrounding Millochau also shows abundant evidence for erosion and deposition by fluvial and eolian processes. Surrounding Millochau are a series of dendritic to (sub)parallel valley networks [Mest and Crown, 2004a] that dissect an extensive Noachian-aged intercrater plains unit. The largest network in the area, Vichada Valles[4], drains a large portion of this part of the highlands (~3.0×10^5 km^2), but several smaller networks and individual channels are also found. Much of the erosion that formed these valley networks and degraded most of craters in this area is believed to have occurred in the Late Noachian Epoch and continued into

[4] The name of 'Vichada Valles' is provisional until approved by the International Astronomical Union.

the Early Hesperian Epoch [Greeley and Guest, 1987; Tanaka and Leonard, 1995; Leonard and Tanaka, 2001; Mest and Crown, 2004a]. The geology of Tyrrhena Terra shows distinct temporal and process-related differences compared to other parts of the southern highlands. In particular the highlands east and northeast of Hellas basin contain a more diverse suite of geologic features than in Tyrrhena Terra and a significant amount of the volatile-driven activity (fluvial and mass wasting) is younger than in Tyrrhena Terra, some of which has been shown to extend into the Amazonian Period [Crown et al., 1992; Mest, 1998; Mest and Crown, 2001b, 2002b, 2003a].

3.4 GEOLOGY OF CRATER MILLOCHAU

This section summarizes geologic observations for crater Millochau made using multiple data sets (Viking Orbiter, MOC, THEMIS, TES, and MOLA) (Figure 3.2). Crater Millochau is ~114 km in diameter and 2.3 km deep (d/D ≈ 0.020); diameter was measured from the point on the rim with the maximum elevation across the center of the crater, and depth was measured from the maximum rim elevation to the lowest point in the crater. Using the Craddock et al. [1997b] calculation for Type B/C degraded craters[5], which Millochau most closely resembles, Millochau should be ~3.1 km deep (d/D ≈ 0.027). Similarly, recent calculations by Garvin et al. [2003] for simple and complex fresh and degraded impact craters show that Millochau should be ~3.6 km deep (d/D ≈ 0.032). Craddock et al. [1997b] also noted that martian craters could undergo 5 to 9% enlargement in diameter due to backwasting, with smaller diameter craters (i.e., ~20 km) being close to 5% enlargement and increasing to 9% at larger diameters. Because Millochau is a large crater, we assume here that its diameter underwent 9% enlargement, which yields a fresh crater diameter (D_f) of ~103 km. Based on the depth versus diameter diagram in Strom et al.

[5] Type B/C craters display eroded ejecta blankets, low-relief sharp to rounded rim crests, flat floors and typically no central peak [Craddock et al., 1997b].

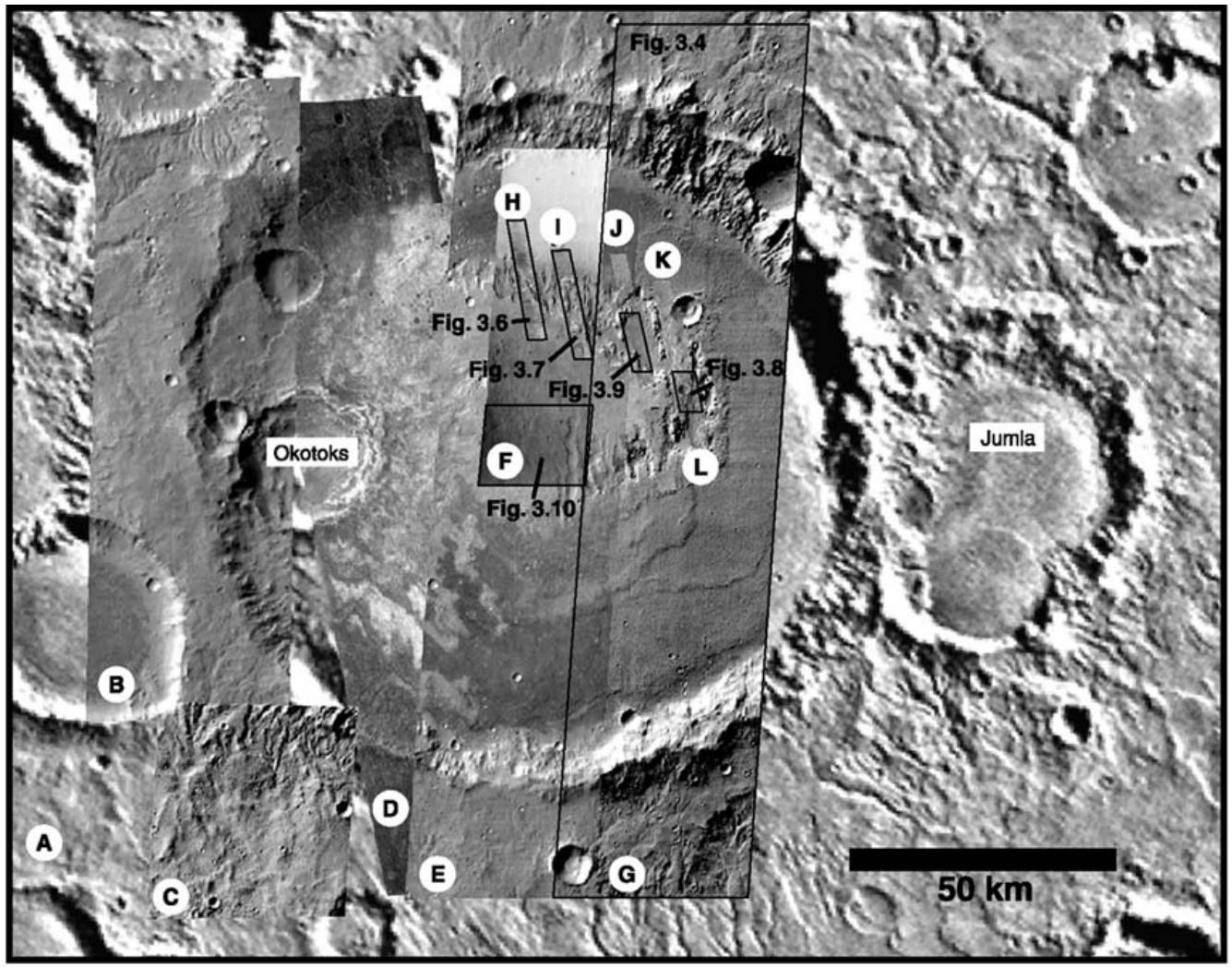

Figure 3.2a. Mosaic of Viking, THEMIS, and MOC images that cover Millochau. (A) Viking MDIM (v2), and parts of (B) THEMIS I02045002 (day), (C) THEMIS I05041002 (day), (D) THEMIS I02001002 (night), (E) THEMIS I02020002 (day), (F) THEMIS V02020003, (G) THEMIS I04629003 (day), (H) MOC M08-06402, (I) MOC M19-01414, (J) MOC E01-01209, (K) MOC M04-03384, and (L) MOC M18-00592. The locations of Figures 3.4, 3.6-3.10 are shown.

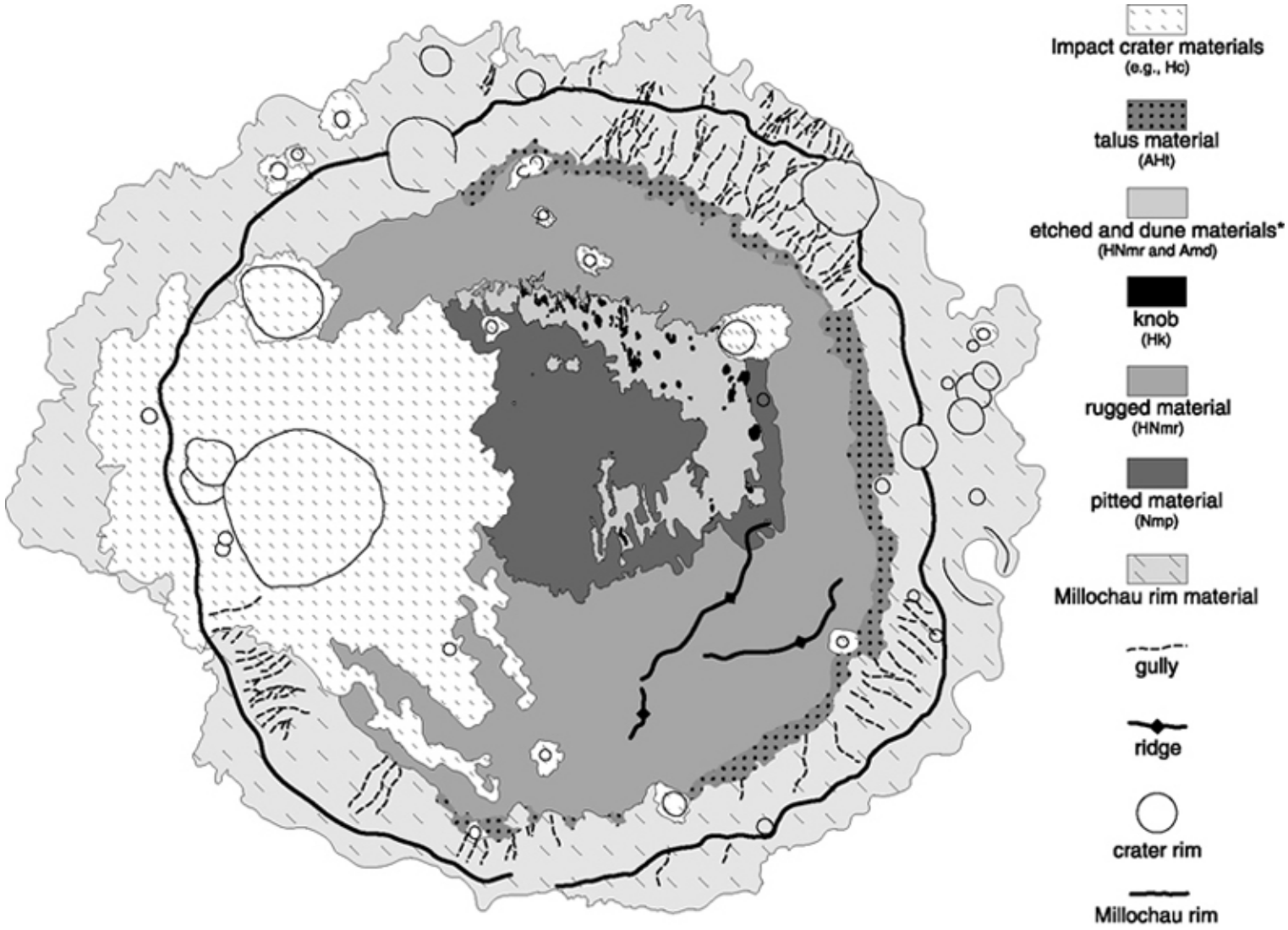

Figure 3.2b. Geologic map of crater Millochau and associated Correlation Chart (following page). Impact craters exhibit pristine to highly degraded morphologies. *Due to scale, etched and dune materials are shown together on the map, but are distinguished in the Correlation Chart and other Figures.

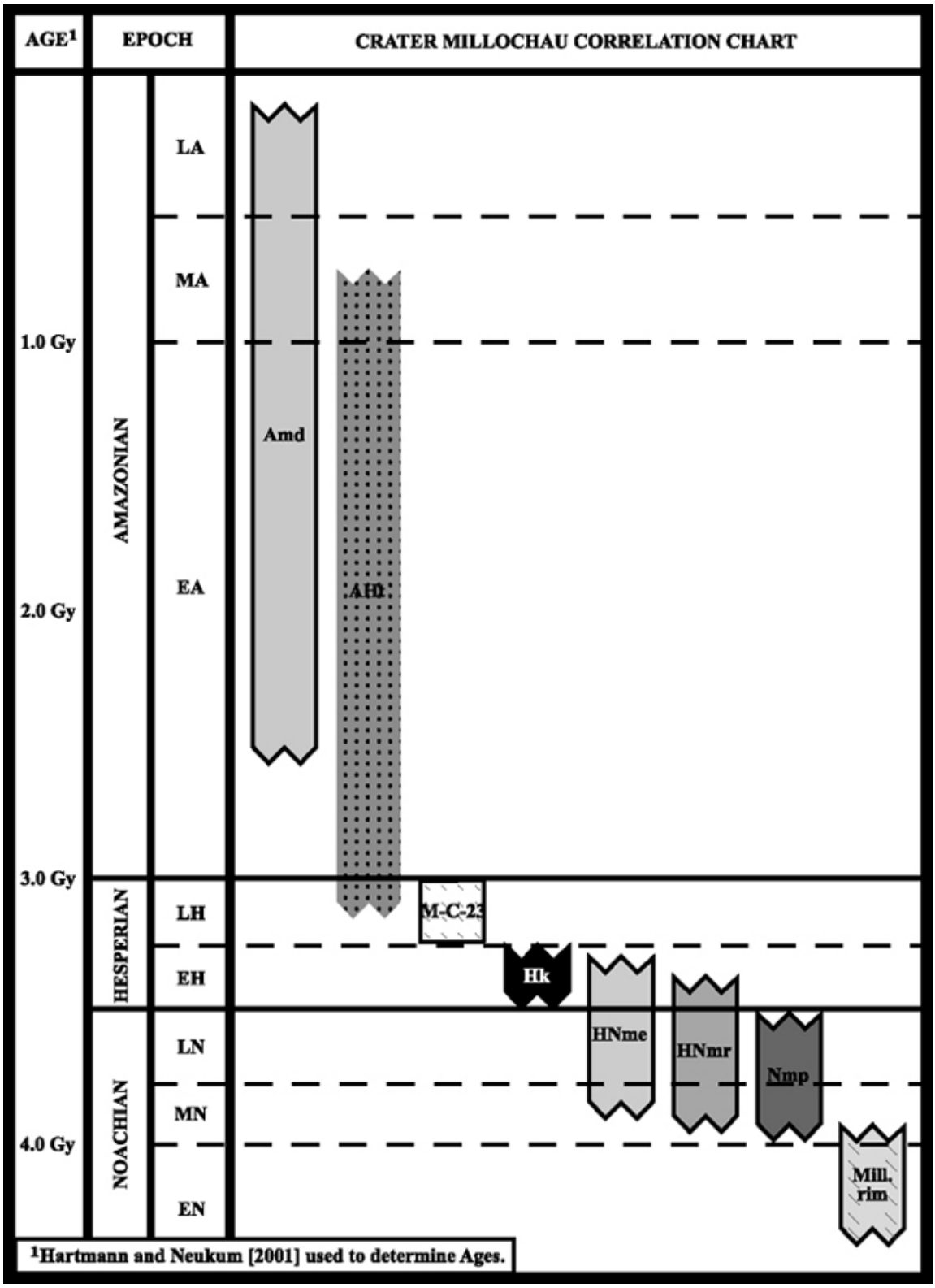

Figure 3.2b (continued). Correlation chart for the geologic map of crater Millochau.

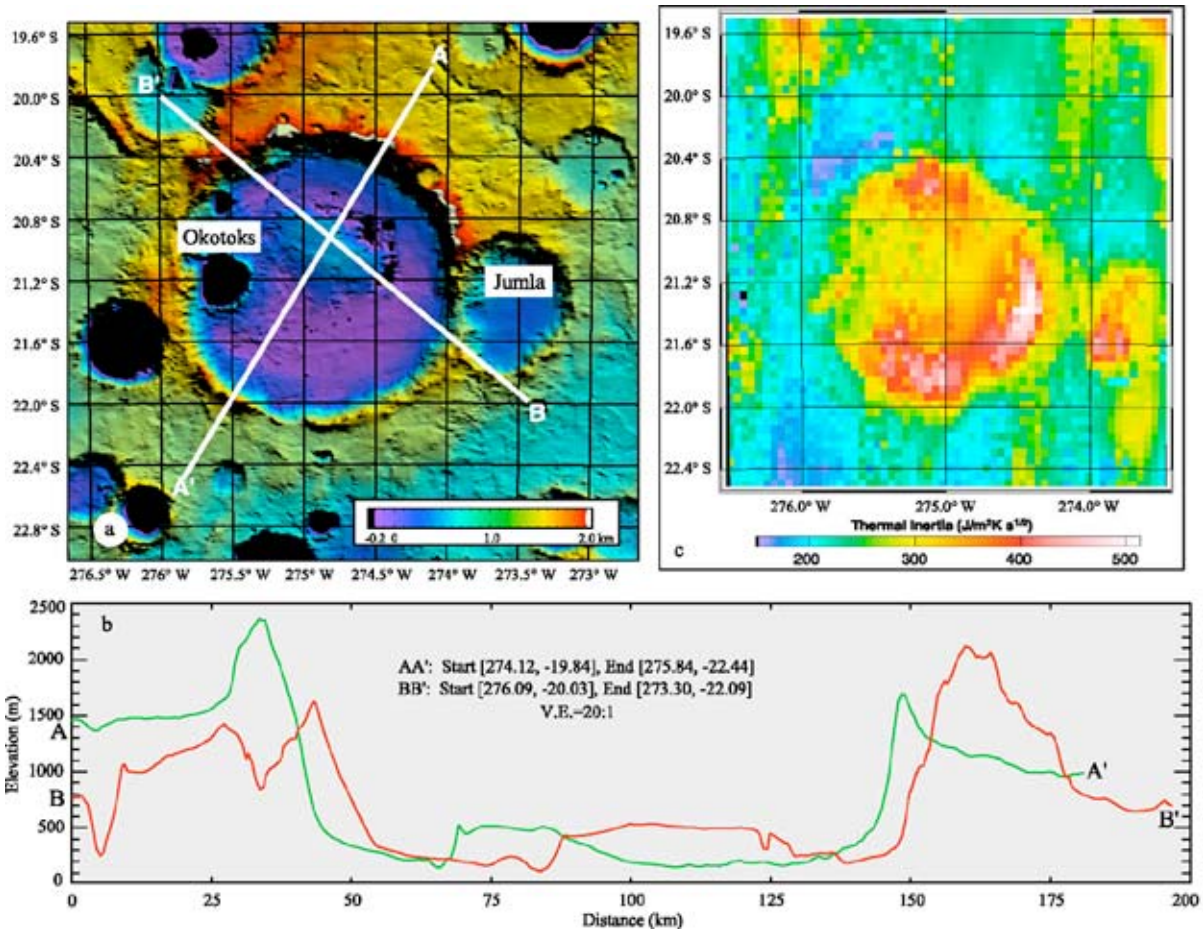

Figure 3.3a-c. Topography of Millochau is shown in the MOLA shaded relief map (a) and two profiles (b). The central plateau and surrounding depressions are the most prominent features within Millochau; the ejecta from crater Okotoks in western Millochau also exhibits a topographic signature on Millochau's floor. Note the difference in elevation between the northern and southern rims of Millochau, due in part to the prevailing north-south regional slope but also to differential erosion across Millochau. Profiles A and B show the relative asymmetry of Millochau's rim. Profile A shows a more conical plateau and profile B shows that the plateau is much broader along its northwest-southeast axis. The floor materials surrounding the plateau slope gradually (~0.8°) toward the center of the crater. (c) TES thermal inertia map (generated using the Mars Data Conglomerator (v. 1.6) [Laboratory for Atmospheric and Space Physics, University of Colorado, Boulder, http://lasp.colorado.edu/cgi-bin/ion-p?page=/lasp3/html/mars/MDC_input.html] shows variability in the interior deposits within Millochau. The impact structure and ejecta of Okotoks are clearly distinguishable from the remainder of the interior deposits; from this map it appears that ejecta was emplaced on the southwest part of the plateau. This map also shows that the plateau and surrounding floor deposits have distinct thermal inertias. Topographic map and profiles produced from 256 pixel/degree DEM using GRIDVIEW software [Roark et al., 2000; Roark and Frey, 2001]; projection is Mercator; illumination altitude = 40°; azimuth = 30°.

[1992], a 100-km-diameter crater should have a depth of ~2.5 to 3.0 km, which yields d/D ratios of 0.025 and 0.030, respectively. For Millochau, these d/D ratios provide fresh depths of 2.59 to 3.11 km, encompassing the degraded depth calculated from Craddock et al. [1997b] and within 500 m of the depth calculated from Garvin et al. [2003]. Based on the above calculations and Millochau's observed depth, 2.3 km, roughly 300 m to 1.3 km of fill material could currently reside in Millochau. It should be noted that crater shapes were measured using photoclinometry in Craddock et al. [1997b] and with MOLA topographic profiles in Garvin et al. [2003]. The study presented here made topographic measurements using high-resolution MOLA Digital Elevation Models (DEMs) and topographic profiles[6].

3.4.1 Crater Millochau Ejecta Deposit

Crater Millochau displays no distinct ejecta blanket (Figure 3.2a) indicating it was eroded and (or) mantled by local plains or eolian materials. However, given the degraded nature of this part of the highlands, it is possible that unidentifiable deposits of Millochau ejecta may exist within the intercrater plains that make up much of Tyrrhena Terra. Topographically, the plains immediately south of Millochau are steeper (~5°) and roughly 500 m higher in elevation than the more gradually sloping plains east of Millochau (Figures 3.3a and b), and it is here that dendritic and (sub)parallel valley networks and channels are incised. The plains surrounding Millochau generally terminate abruptly against Millochau's rim materials; however, along the southern rim the plains gradually slope up to the crater. The higher plains adjacent to Millochau may represent uplifted topography produced when Millochau formed as well as possible ejecta materials that were welded to a higher degree than distal ejecta, thus making them more resistant to erosion.

[6] Topographic profiles and volume calculations were made from a 256 pix/deg MOLA DEM using the IDL module GRIDVIEW [Roark et al., 2000; Roark and Frey, 2001].

3.4.2 Crater Millochau Rim

The rim of Millochau varies in morphology suggesting processes affecting the rim may not be spatially consistent. The northern rim of Millochau shows the highest relief (~2.6 km), is the most rugged, and is the steepest with interior slopes of ~18° (Figures 3.3a and b, and 3.4a). The height of the rim above the surrounding terrain is generally 50 to 400 m along the southern rim and 300 to 700 m along the northern and western rims (Figure 3.3a). Topographic profiles (Figure 3.3b) show the rim crest occurs at elevations of ~1.0 to 2.3 km. Previous researchers [Pike and Davis, 1984; Craddock et al., 1997b] have shown that rim heights above the surrounding terrain for complex craters are highly variable and little correlation exists between rim height and crater diameter, indicating that the local pre-impact datum can not be determined. This is especially true in areas around Millochau where significant post-impact modification of the crater rim and landscape have occurred. The current elevation of the plains surrounding Millochau ranges from ~1.0 km south of Millochau to almost 3.0 km north and east of the crater (Figures 3.3a and b); this reflects the regional, north-to-south slope toward Hellas. Immediately adjacent to Millochau the plains range from ~500 m to 1.7 km in elevation. Most of Millochau's rim has been degraded by impact craters and fluvial and eolian processes (Figures 3.2a and 3.3a, and 3.3a and c). The eastern rim is shared with crater Jumla[7] (D=45 km; Figure 3.3a) that forms a gap in Millochau's rim (~600 m above floor and 1700 m below max rim height) (Figure 3.3a). The southern rim of Millochau also shows a gap (700 m above floor and 1800 m below max rim height) (Figure 3.3a Valley networks on the southern exterior flank of Millochau and gullies along the interior wall (Figures 3.2a and 3.3a; Plate 1 (Chapter 2.0)) indicate this gap may have been formed or modified by fluvial processes; one valley in particular on the exterior flank appears to head fairly near the gap. A few small exterior valleys also head near Millochau's western rim and most likely caused the lowering and degradation of this part of the rim. Portions of the interior wall of Millochau contain numerous gullies that have contributed to the erosion of the crater rim. The steepest parts of the interior wall, mostly along the northern rim but also along parts of the southern rim, show the highest concentrations of gullies within Millochau

[7] The name of crater 'Jumla' is provisional until approved by the International Astronomical Union.

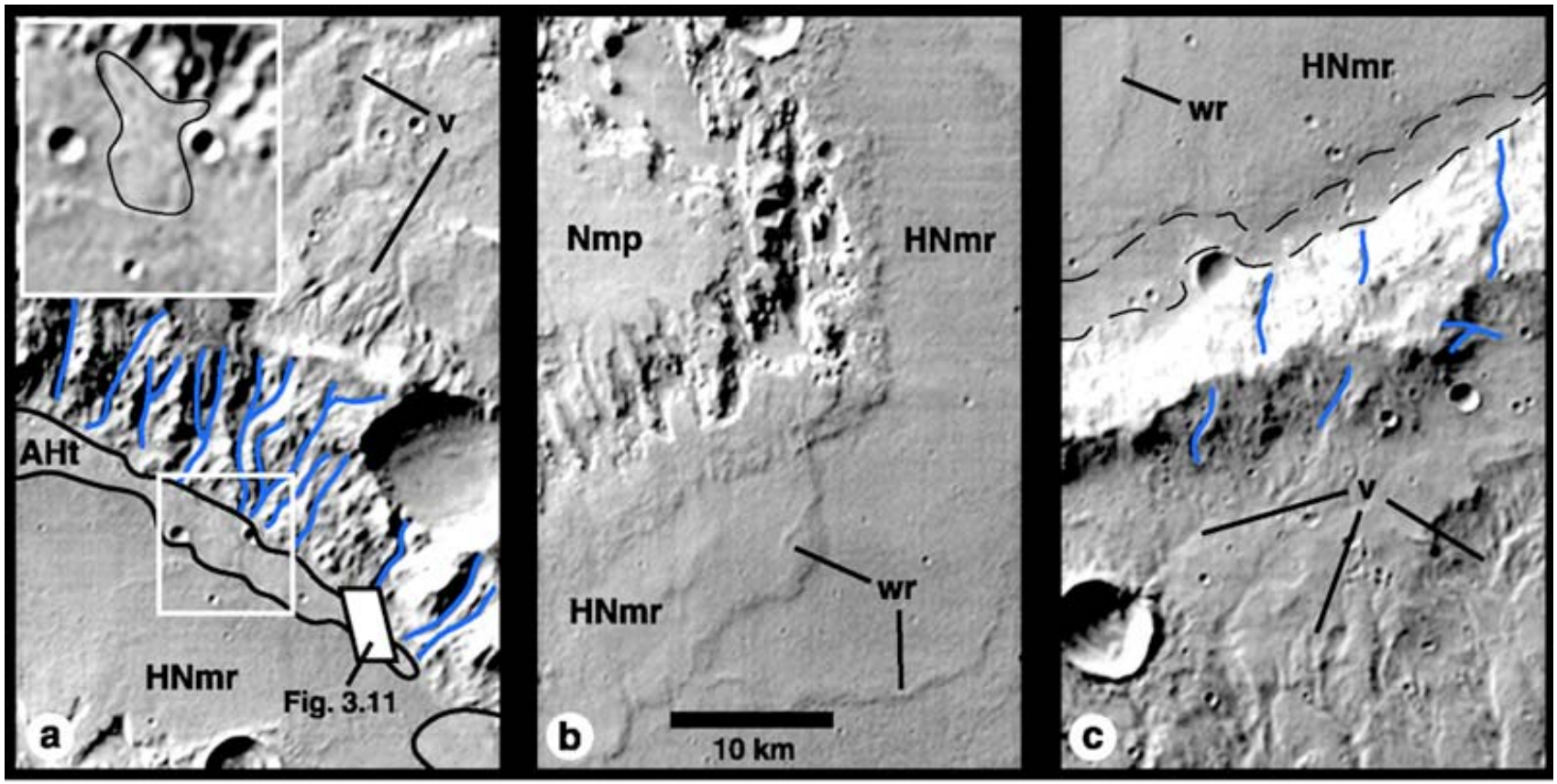

Figure 3.4. Part of THEMIS daytime infrared image I04629003 (G in Figure 3.2a) covering crater Millochau and adjacent highland materials. Rim morphology is noticeably different between the north (a) and south (c) rims, with the former being more rugged and containing more interior gullies than the latter. Many interior gullies (blue lines) visible in (a) and (c) head at or near Millochau's rim crest. Some gullies appear to have transported debris to form lobate features at their termini (a - insert). In (a), talus material (AHt) forms a bright band a the base of Millochau's wall. Rugged material (HNmr) is dark in THEMIS daytime infrared images, contains wrinkle ridges (wr in (b) and (c)), and forms a trough (within dashed lines in (c)) along the southern crater wall. Millochau's plateau (b) is capped with pitted material (Nmp), which is bright in THEMIS daytime infrared images, displays an irregular scarp boundary embayed by rugged material and is dissected by a series of depressions. Most depressions are irregular, but some, such as along the central western edge of (b), are linear and have a clear northwest-southeast trend, similar to the valley shown in Figure 9. Valley networks (v) are visible in the plains outside of Millochau (a and c). The location of Figure 3.11 is shown. Illumination from upper left; image is ~31 km across; resolution is 97 m/pixel; centered at 22.9°S, 85.5°E.

(Figure 3.2a). The western wall is mantled by ejecta from crater Okotoks[8] (D=22.6 km); if gullies formed here they are likely buried by ejecta as well or were destroyed by this impact event along with part of Millochau's rim. Most gullies are morphologically simple. Gully heads are not restricted to a single layer but range in elevation along Millochau's rim, and generally they do not display alcove headwalls or debris fans at their termini. However, Figure 3.4a (inset) shows a lobe of debris near the termini of several large gullies. Some gullies head at or near Millochau's rim, clearly indicating they were not formed by slow seepage or rapid outbursts of liquid from a confined aquifer, which has been suggested for many of the recently discovered martian gullies [Malin and Carr, 1999; Malin and Edgett, 2000]. The gullies observed in Millochau most likely formed by a process involving surface runoff of water and possibly some component of mass wasting. In a study of crater degradation, Grant [1999] noted that crater Jumla displayed an inner wall heavily dissected by 'debris chutes' (or gullies) similar to those observed in Millochau, and attributed them to a combination of mass wasting and fluvial processes. Unlike other large martian craters proposed to have contained paleolakes, Millochau's rim is not breached by any obvious inflow or outlet valleys. Therefore, any water that may have accumulated within Millochau most likely entered via gullies, through the subsurface, or by direct precipitation.

3.4.3 Crater Millochau Plateau

MOLA Digital Elevation Models (DEMs) and topographic profiles show that the central part of Millochau's floor contains a 'plateau' as much as 400 m above the surrounding floor (Figures 3.3a and d, and 3.5-3.7) and could consist of over 330 km^3 of material (Figure 3.5). Volume estimates in this study were made using a 256 pix/deg MOLA DEM in the IDL module GRIDVIEW [Roark et al., 2000; Roark and Frey, 2001]. Volume calculations involve defining (a) the planform area of the plateau (the lateral extents of the plateau are represented by vertical bars in cross section view), and (b) the upper and lower bounding elevations representing the

[8] The name of crater 'Okotoks' is provisional until approved by the International Astronomical Union.

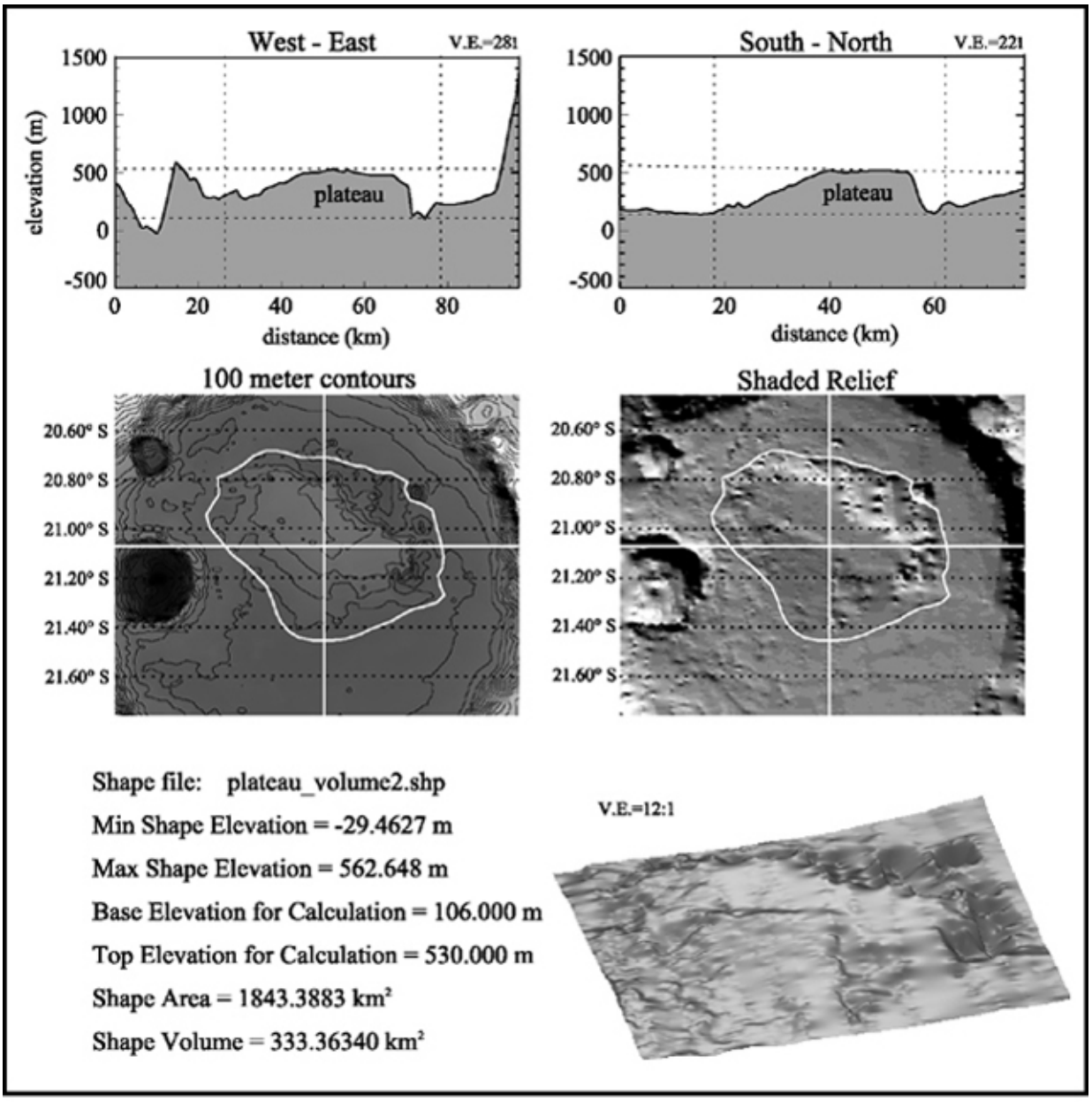

Figure 3.5. Output from the Area/Volume calculation tool in GRIDVIEW. The plateau is outlined in white on the contour and shaded relief maps. The white crosshairs in each map represent the west-east and north-south profiles shown at the top, drawn through the plateau's approximate planimetric center. The dashed vertical lines in each profile window represent the position of the plateau's outline where it crosses the profile track. The dashed horizontal lines represent the upper and lower bounds of the plateau. Results are shown in the lower left and a 3-dimensional representation of the plateau is shown in the lower right (view is to the northeast).

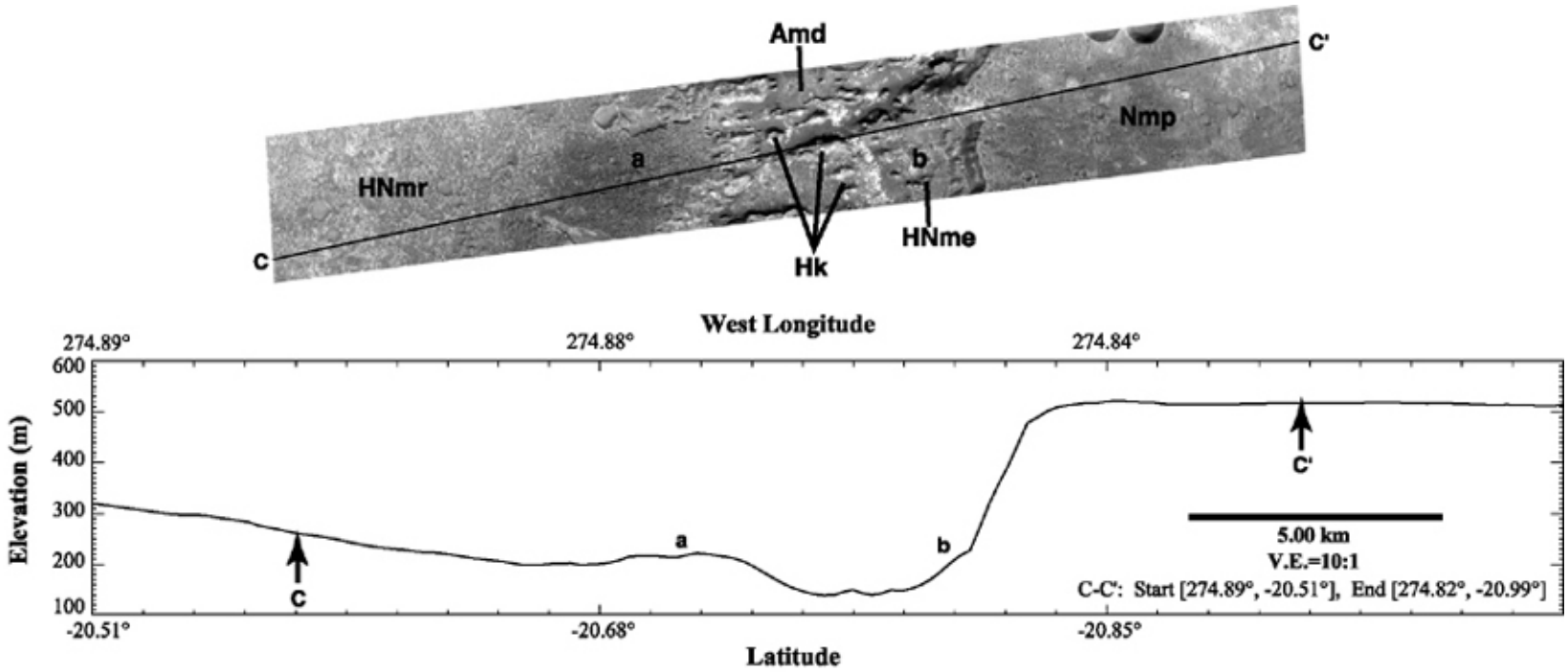

Figure 3.6. MOC image M08-06402 (H in Figure 3.2a) showing - from north to south - rugged material (HNmr), depressions containing etched (HNme) and dune (Amd) materials and knobs (Hk), and pitted material (Nmp). Rugged material slopes gradually (0.8°) toward Millochau's center, but rises ~30 m (a) where adjacent to depressions bounding the plateau (see profile C), and appears darker than rugged material to the north. Etched material, exposed at (b), occurs at roughly the same elevation as the 30-m-high hill at (a). In profile C, the plateau is bounded by a steep (~12.5°) north-facing scarp that rises ~330 m above rugged material and shows a relatively flat surface. Most knobs and outliers of etched material are elongated along a north-south trend. North is to the left; illumination from bottom; image width = 2.88 km; resolution = 2.8 m/pixel; image center is 20.75°S, 274.85°W; NASA/JPL/MSSS. Profile generated in GRIDVIEW from 256 pixel/degree MOLA DEM; profile extends beyond MOC image

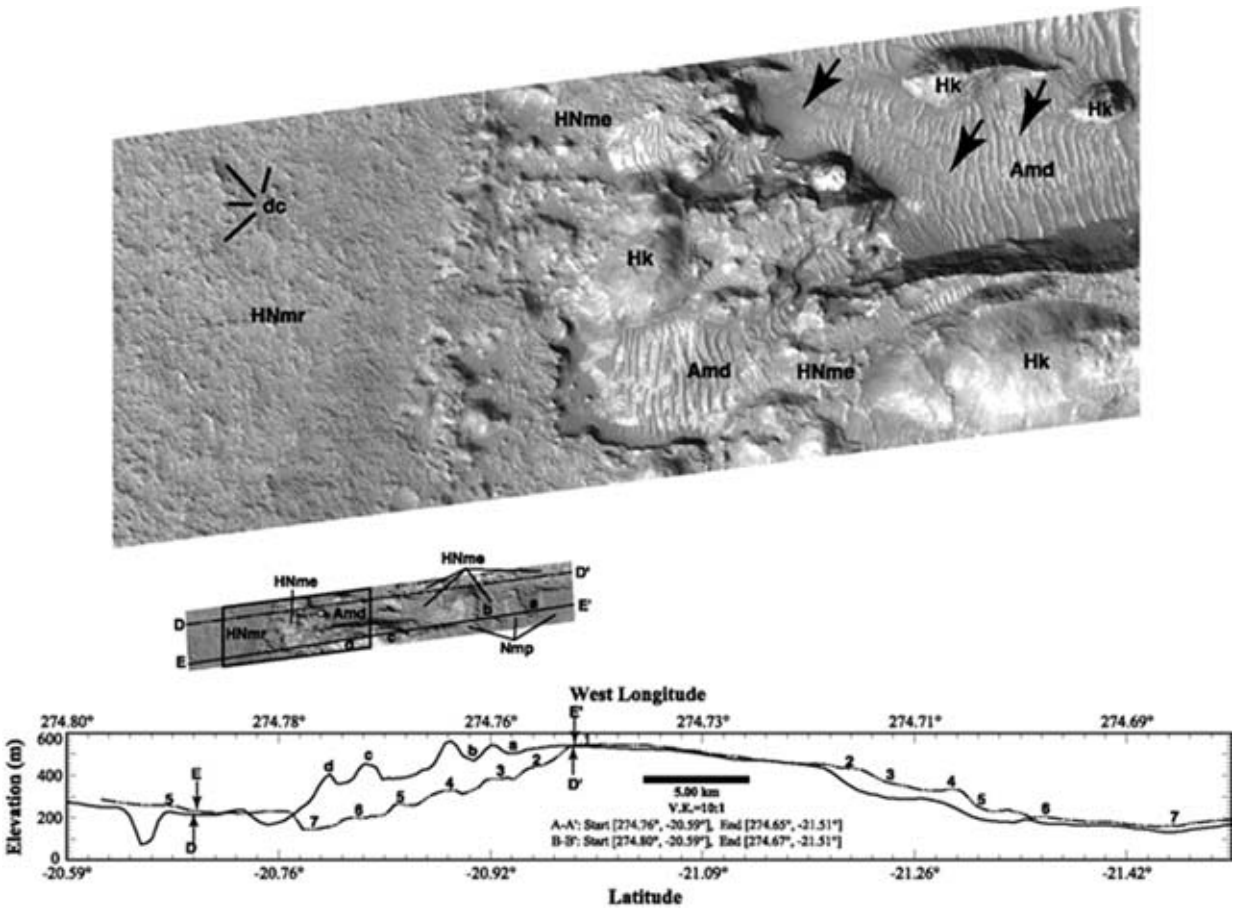

Figure 3.7. Full MOC image M19-01414 (I in Figure 3.2a) shows a north-south sequence of rugged material (HNmr), etched (HNme) and dune (Amd) materials within depressions, and pitted material (Nmp; a small mesa (c) is also capped with pitted material). Profiles D and E, generated using GRIDVIEW from 256 pixel/degree MOLA DEM, extend beyond the MOC image to show the topography of the plateau relative to the adjacent floor materials. Similar to profiles shown in Figures 3.3b and 3.6, rugged material slopes gradually (~0.8°) and rises ~20 m adjacent to the northern plateau-bounding depressions. However, unlike in Figure 3.6, the plateau displays several distinct breaks in slope (D1-7, E1-6) along the northern and southern plateau edges. Two valleys (a and b) are characteristic of several valleys that erode the edges of the plateau. The close-up of M19-01414 shows the depressions along the northern part of the plateau contain hummocky etched material adjacent to rugged material, rounded knobs (such as "d" in the full image and profile B), and dune material filling low areas. Several thin layers (arrows) are observed within the dune material suggesting the cover is relatively thin in this depression. Rugged material (HNmr) displays a 'stucco'-like texture and contains degraded impact craters (dc). North is to the left; illumination from bottom; image width = 2.8 km; resolution is 2.81 m/pixel; centered at 21.9°S, 85.3°E; NASA/JPL/MSSS.

surface and subsurface, respectively, extents of the volume to be measured (see Figure 3.5). The plateau is bounded on its northern and eastern edges by a scarp and a series of irregular depressions (Figures 3.4b, and 3.5-3.7) and slopes to the south and west where it grades into the surrounding floor materials (Figures 3.3a). The plateau is capped with pitted material (Nmp - described below), which appears unique to the plateau. The topographic expression of the plateau could in part reflect a buried crater structure. Millochau's size is well beyond the onset diameter for central peak formation on Mars and also exceeds the transition diameter (50-70 km) from complex craters to basins [Wood, 1980; Pike and Spudis, 1987]. However, the plateau is not centered on the center of Millochau's planform, which is not typical for interior crater structures such as central peaks and peak rings. Millochau's interior plateau could also consist of some component of impact melt. A crater of Millochau's size (~100 km) is expected to produce a melt volume of ~1000 km^3 (assuming Mars is an intermediate case between the Earth and Moon, a chondritic impactor, and crystalline target) [Grieve and Cintala, 1992]. For Millochau's diameter, this is equivalent to a ~130 m layer covering the crater floor. However, the layering exhibited within materials of the plateau is inconsistent with the interpretation that the plateau is either a crater structure (central peak or ring) or impact melt sheet, and minimum estimates of the volume of the plateau exceed the expected value for an impact melt sheet. It is therefore likely that the plateau is principally a secondary feature unrelated to the impact event that formed Millochau.

Evidence for layering within the plateau is exposed along the scarps that define the irregular depressions that border the plateau on its northern and eastern edges, along part of the plateau's southern boundary, and along knobs and mesas within the depressions. Some layers display regular thicknesses and morphologies that allow them to be traced laterally for several kilometers in MOC images (Figures 3.7-3.9). For example, MOC image M08-06402 shows a north-facing scarp exposing a thick (150-250 m) and massive layer capped with pitted material (Figure 3.6). The ~50-m-high south-facing scarp defining the edge of the rugged material also shows what appears to be a relatively massive layer and represents a minimum thickness for this layer. Underlying the massive unit of the plateau occurs a series of thin layers (~10 m or less). This sequence - massive layer overlying thin layers - is also observed in knobs and is represented in all MOC images that cover the Millochau floor deposits. Furthermore, thin layers are also seen

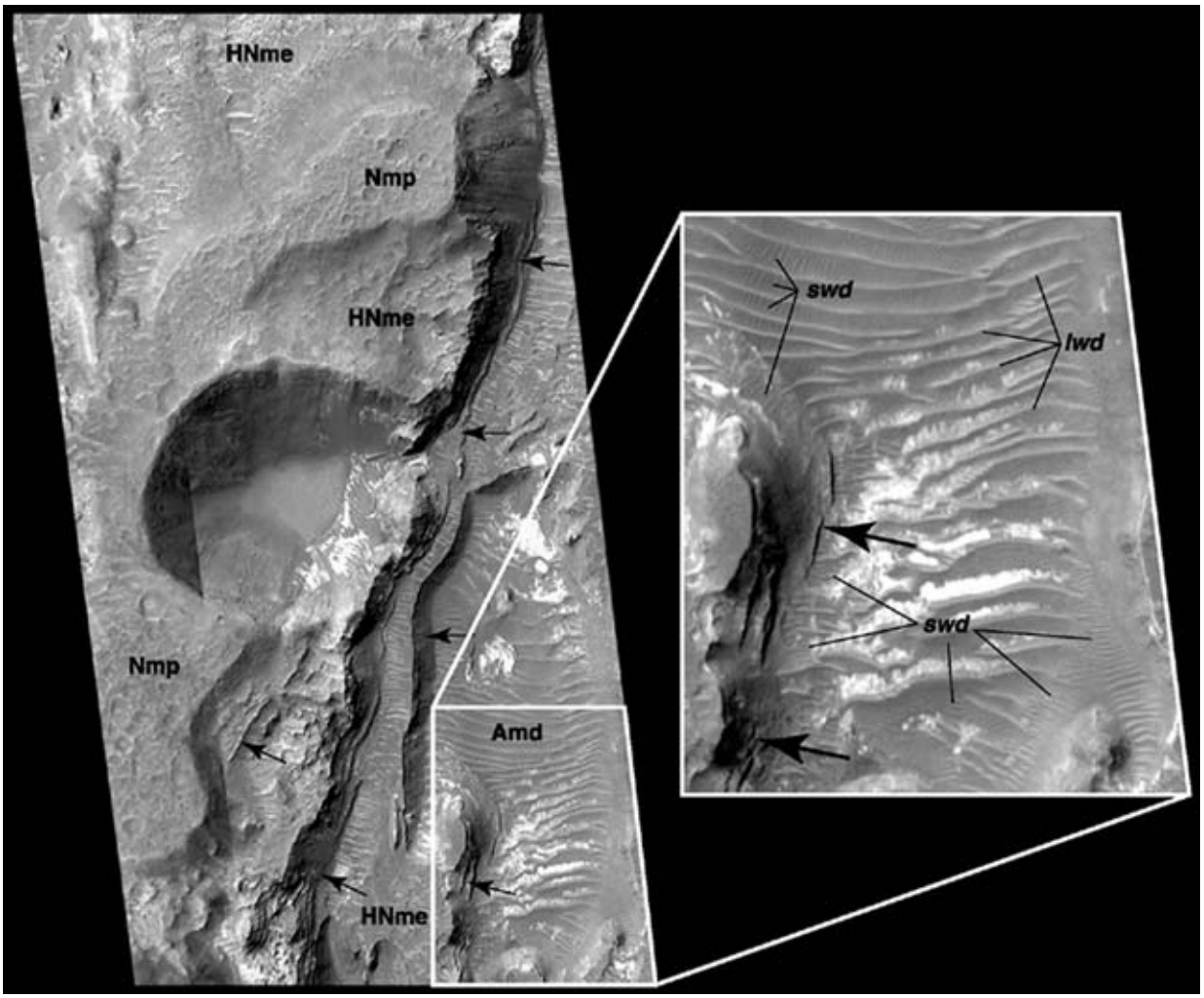

Figure 3.8. Mosaic of parts of MOC images M04-03384 (K in Figure 3.2a) and M18-00592 (L in Figure 3.2a) showing the depressions along the eastern edge of the central plateau. A portion of the plateau, visible in the lower left, and a mesa (upper right) are capped with pitted material (Nmp). Portions of this unit have collapsed and (or) been eroded to expose etched material (HNme). The walls of the depressions and slopes of knobs commonly show layering (arrows). Sediments within Millochau have been mobilized to form dune material (Amd) that commonly covers the floors of the depressions, as well as other low-lying areas. Long-wavelength dunes (lwd) generally trend east-west and span a depression. Small-wavelength dunes (swd; see close-up) tend to form perpendicular to topographic highs (depression walls, knobs, mesas, and long-wavelength dunes), but some form parallel to long-wavelength dunes. Illumination from left; image width = 4.08 km; resolution is 2.81 m/pixel; centered at 21.3°S, 85.6°E; NASA/JPL/MSSS.

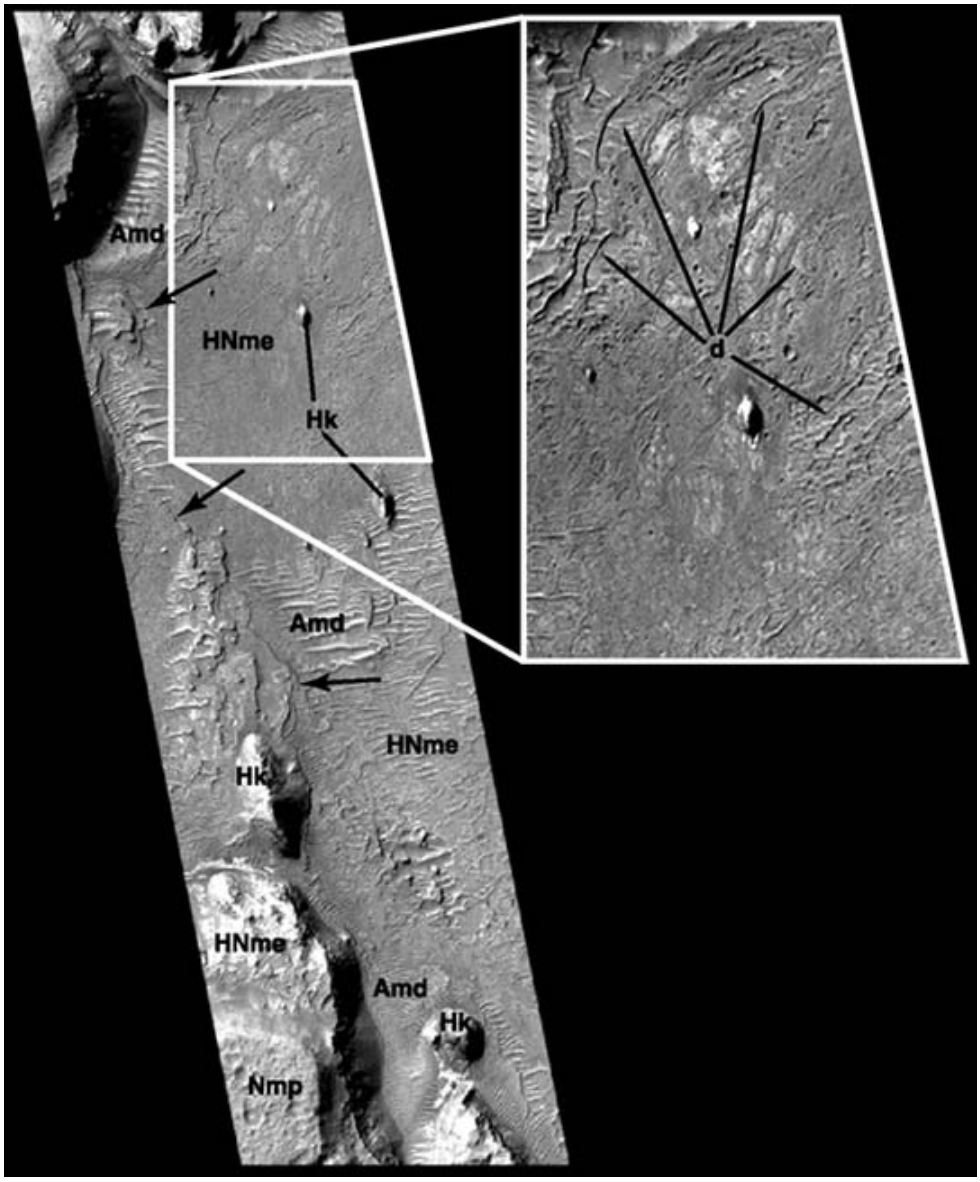

Figure 3.9. Part of MOC image E01-01209 (J in Figure 3.2a) showing lineated (middle) and irregular (bottom) etched material (HNme), pitted material (Nmp), dune material (Amd), and knobs (Hk). Here lineated etched material contains numerous positive relief features that connect patches of smooth material of similar albedo (see close-up). Orthogonal lineations form irregularly shaped polygonal depressions (d); some depressions are filled with brighter albedo material and (or) dune material. It is unclear what the nature of this surface is, but it may form as a thin layer is being eroded, with the erosional pattern reflecting heterogeneities in the physical properties of the layer. Also, note the presence of staircase-like layering (arrows) exposed in the center of this image suggesting portions of the Millochau interior deposits are composed of relatively thin and easily eroded material. Dune material is found along the edges of scarps and knobs and forms exposures that mantle the etched material. Illumination from left; image width = 2.9 km; resolution is 2.82 m/pixel; centered at 22.2°S, 85.4°E; NASA/JPL/MSSS.

outcropping on the floors of the depressions from underneath dune material, such as in Figure 3.9, and typically form staircase-like patterns. The depressions, as well some of the knobs within them, appear to show a trend of elongation in a north-south direction (Figures 3.6-3.9), suggesting development of the depressions may be due to an underlying series of structures within the floor materials. This trend is also clearly observed along the southern edge of the plateau where several valleys, elongated north-south, have cut into the plateau (Figures 3.4b and 3.10). These valleys have roughly uniform widths and depths from head to mouth, and they display amphitheater-shaped heads consistent with formation primarily by groundwater sapping. Similar but smaller and less developed examples of possible sapping features are found cutting into the north-facing scarp of the plateau and the south-facing scarp of the surrounding floor materials. Valleys tend to be contained entirely within the plateau (Figure 3.4b and 3.10) and where these valleys meet the rugged material, such as along the southern edge of the plateau, the mouths of the valleys stop at the rugged material, suggesting there may have been little to no downcutting into the rugged material.

3.4.4 Crater Millochau Interior Deposits

Crater Millochau contains 6 distinct interior deposits: pitted, rugged, etched, dune and talus materials, and knobs (Figure 3.2b). The youngest and easily identifiable materials in Millochau are surficial deposits of dune and talus materials. The stratigraphically older units - pitted, rugged and etched materials and knobs - display less clear relationships, such as embayment or superpostion, despite the high-resolution quality of MOC and THEMIS images available for Millochau. Nevertheless, these units have been able to be separated from each other based on surface texture and impact crater densities (Table 3.1). Descriptions of the geomorphic characteristics and stratigraphic relationships are also included in the mapping study of Mest and Crown [2004b]. High-resolution MOC and THEMIS images also allow the Millochau interior deposits to be described in greater detail than deposits that fill many other craters in the region.

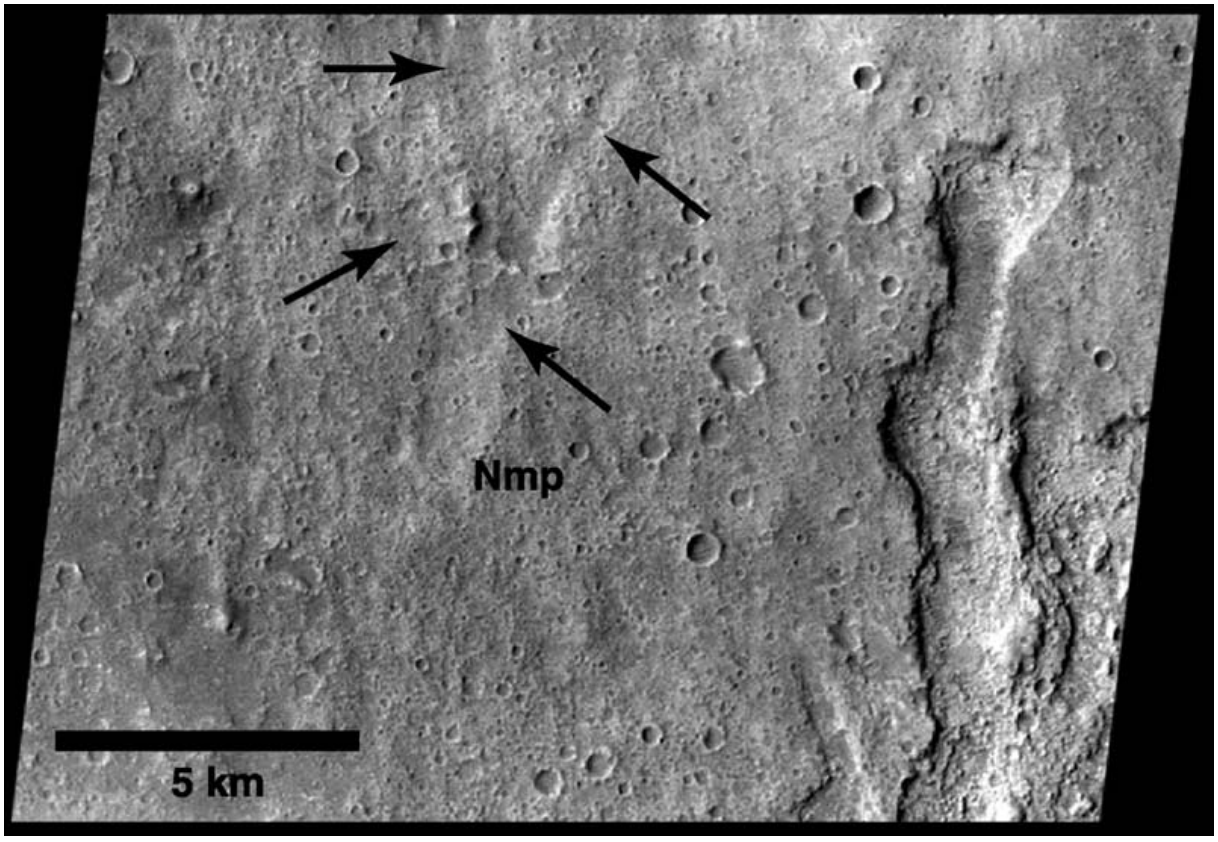

Figure 3.10. Part of THEMIS image V02020003 (F in Figure 3.2a) showing the southern part of Millochau's plateau. The plateau is covered by pitted material (Nmp) that here displays a mottled surface, which could be due in part to a mantle of ejecta from crater Okotoks to the west, especially in the southwest corner of this image. It also appears that the lighter materials are being removed to expose underlying darker materials. The linear feature in the east part of the image is one of several "valleys" that cut into the plateau. These valleys show potential layering in their walls, relatively flat floors (in some places dune-covered), and are believed to be sapping valleys. Undulations in the center of this image (arrows) may indicate the locations of less developed valleys. Illumination from left; image is ~18.4 km across; resolution is 18 m/pixel; centered at 22.5°S, 85.2°E.

Table 3.1. Crater Size-Frequency Data Relative Martian Ages

Impact craters were counted using the Viking Orbiter, THEMIS, and MOC images shown in Figure 3.2a; areas equal total unit exposures within the map area shown in Figure 3.2b. See Appendix C for a more detailed description of crater counting methodology. N(2), N(5), and N(16) represent the cumulative number of craters >2, >5, and >16 km in diameter per 10^6 km^2; error = $\pm$ (($N^{1/2}$)/A) x 10^6 km^2, where A is area [Crater Analysis Techniques Working Group, 1978]. Epoch ranges are based upon crater counts using crater-density boundaries determined by Tanaka [1986]: MA, Middle Amazonian; EA, Early Amazonian; LH, Late Hesperian; EH, Early Hesperian; LN, Late Noachian; MN, Middle Noachian; EN, Early Noachian. Epoch designations are based upon superposition and crosscutting relationships and crater counts. See text for names of geologic units.

Unit	Total craters[1] D < 2 km	Total craters D > 2 km	Area (km^2)	N(2)	N(5)	N(16)	Epoch range	Epoch designation
Amd	40	0	154	0	0	0	EH-MA	EA or above
AHt	96	2	956	2091 ± 1479	0	0	LN-LH	LH or above
Hc (Okotoks)	86	2	2,820	709±502	355±355	0	MN-EA	LH
Hk	10	0	41	0	0	0	EH-MA	EH
HNme	149	2	462	4329 ± 3061	2164 ± 2164	0	MN-EA	MN-EH
HNmr	799	4	3,400	1177 ± 588	883 ± 510	294 ± 294	EN-LH	MN-EH
Nmp	1603	3	1,160	2586 ± 1493	1724 ± 1219	862 ± 862	EN-EH	MN-LN
Millo. floor	2545	7	5,130	1365 ± 516	585 ± 338	195 ± 195	EN-EH	
Millo. rim	380	19	5,494	3458 ± 793	1456 ± 515	182 ± 182	EN-EH	

[1]Includes areas and counts for all units composing the Millochau floor assemblage (includes pitted, rugged, etched and dune materials and knobs).

Pitted material (Nmp) covers the central plateau and shows a heavily pitted and cratered surface (Figures 3.4b, and 3.6-3.10) in THEMIS and MOC images. Subtle brightness differences in this unit observed in THEMIS images tend to coincide with different erosional surfaces. THEMIS image V02020003 (Figure 3.10) offers a detailed view of these differences. (a) Lighter areas across this image are rugged and contain more "pristine" craters than darker surfaces. (b) Darker areas, except in the southwest corner of V02020003, show smooth and rugged surfaces, and contain more degraded craters than lighter surfaces. (c) Lighter areas appear higher-standing (MOLA resolution is too coarse to distinguish these surfaces), except in southwest corner of V02020003, and form scarps adjacent to darker areas. (d) The southwest corner of V02020003 shows apparently high-standing, rugged and dark surfaces (darker than the low-lying dark areas) that contain craters with similar morphologies to those within lighter areas elsewhere in this image. The above observations imply lighter material is being removed, thus exposing the low-lying darker material, which could be an underlying unit and (or) include lag deposits or coarse sand that accumulates in local low-lying areas. The high-standing darker areas in the southwest corner of V02020003 coincide with the location of ejecta from crater Okatoks in western Millochau, which is most likely relatively thin in this distal part of the ejecta deposit, and probably covers both lighter and low-lying darker surfaces. TES thermal inertia data (Figure 3.3c) show that pitted material ranges from ~275 to 350 $J/m^2Ks^{1/2}$, which corresponds to surface materials that contain fine materials and (or) few rocks [Jakosky et al., 2000; Mellon et al., 2000; Christensen et al., 2001; Putzig et al., 2003]. THEMIS infrared images show pitted material to be bright during the day and dark at night, consistent with fine-grained deposits that heat up and cool down relatively quickly. The presence of many small (D<1 km) impact craters is similar to that observed in the plains surrounding Millochau and suggests these units may be similar in age. Low areas within the unit tend to contain dune material. Pitted material could include sedimentary (fluvial, lacustrine or eolian) and volcanic (loosely consolidated pyroclastics). Pits on the surface of the deposit could be due to a large number of poorly preserved impact craters, collapse features, and (or) eolian-modified depressions.

Rugged material (HNmr) forms irregular surfaces with a stucco-like surface texture (Figures 3.4, 3.6 and 3.7) and extends from the plateau to the base of Millochau's interior crater wall (Figure 3.4 and 3.11). TES data and THEMIS images show this material to be distinct from

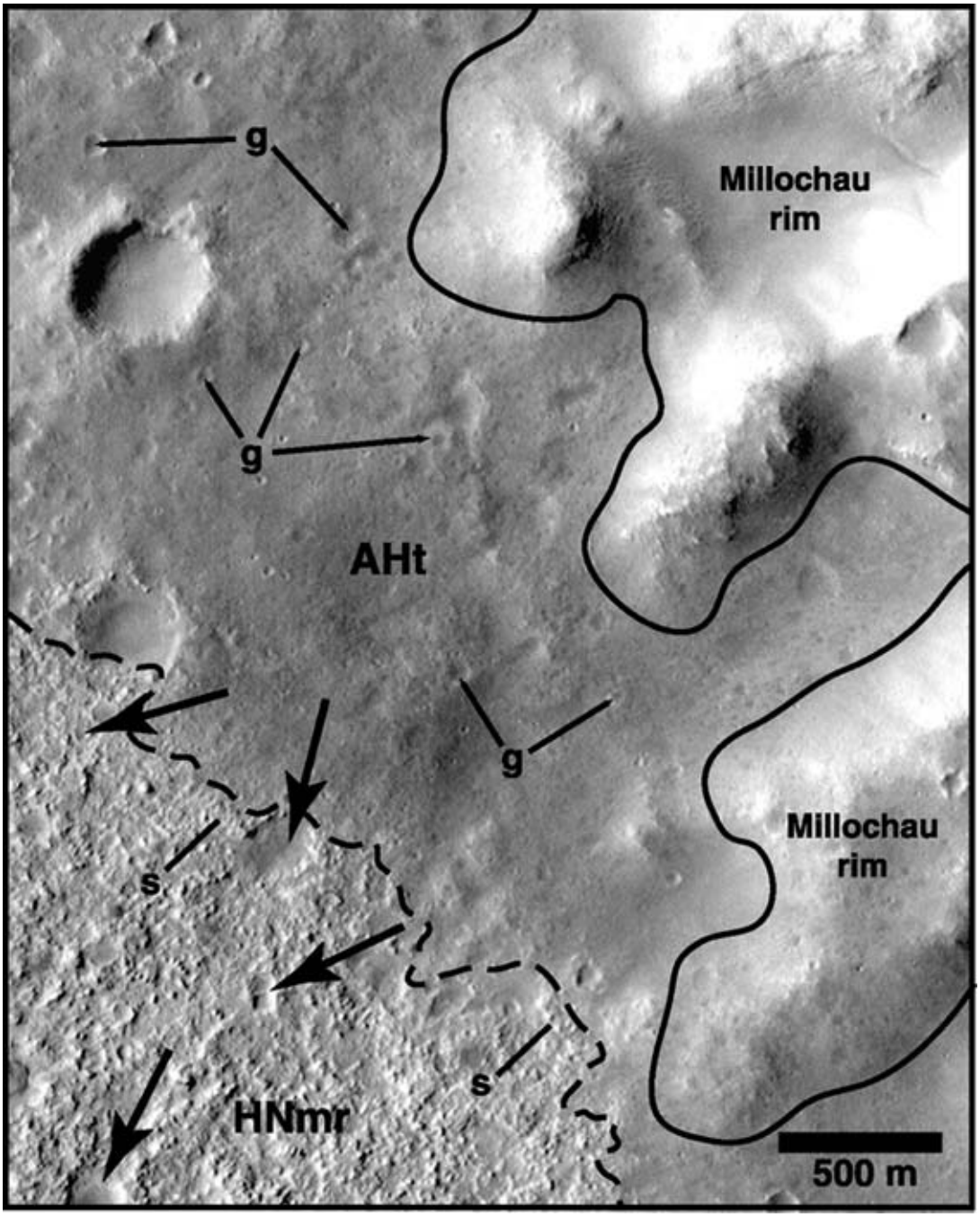

Figure 3.11. Part of MOC image R04-01308 showing the contact (dashed line) between the smoother talus material (AHt) and the irregular rugged material (HNmr) near the base of Millochau's inner wall (right side of image). At some locations the contact is represented by a low-relief scarp (s), whereas in most places the contact is not discernible. Craters within rugged material are being exhumed as talus material is being removed; this is supported by the presence of numerous "ghost" craters (g) within the talus deposit. Illumination from left; image width = 3.02 km; resolution is 2.952 m/pixel; centered at 20.7°S, 85.8°E; NASA/JPL/MSSS.

pitted material. Rugged materials exhibit TES-derived thermal inertia values of ~400 to 500 $J/m^2Ks^{1/2}$ (Figure 3.3c), consistent with rocky and (or) coarse-grained surface materials or cemented fine materials [Jakosky et al., 2000; Mellon et al., 2000; Christensen et al., 2001; Putzig et al., 2003]. THEMIS infrared images show that rugged material is dark during the day and bright at night. This suggests the materials that make up the rugged unit is composed of materials that retain their heat into the night. THEMIS images (Figure 3.4a and c) also show the unit to contain several mare-type wrinkle ridges [Strom, 1972; Lucchitta, 1976; Fagin et al., 1978; Phillips and Lambeck, 1980; Saunders and Gregory, 1980], which implies compressional tectonism resulting from folding or thrust faulting of layered sedimentary or volcanic deposits [e.g., Lucchitta, 1977; Plescia and Golombek, 1986; Watters, 1988, 1991, 1993].

Rugged material appears to embay Millochau rim material where they are in contact, such as in the southwest part of Millochau, but the embayments are not pronounced. Here it appears that rugged material covers several gullies incised within Millochau rim material. There are no discernable fluvial deposits visible at the mouths of these gullies superposing rugged material, which indicates fluvial activity within these gullies may have ended prior to emplacement of rugged material. Alternatively, as the steeper rim meets floor deposits, the combination of lower slope and potentially unconsolidated and porous materials on Millochau's floor may not allow valley incision to extend inward from the crater rim. Most of the rugged material that is presumably in contact with Millochau rim material is buried by talus in the north, east and parts of the south, and impact ejecta from Okatoks in the south and west (Figure 3.2b). Figure 3.11 shows rugged material along the eastern interior wall of Millochau is being exhumed from beneath a relatively thin cover of talus material (discussed below). Along the southeast part of Millochau's wall the darker rugged material displays a lobate scarp edge (Figure 3.4c); between this scarp and the rim material occurs a narrow trough or moat (~50 m deep) that retains the surface characteristics of rugged material. This moat could represent an area of deflation or erosion similar to the moats identified on debris aprons in eastern Hellas [Pierce and Crown, 2003].

Most craters in rugged material are poorly preserved showing highly degraded rims and little to no ejecta, and low areas within the unit tend to contain dune material. Profiles across Millochau (Figures 3.3a, 3.6 and 3.7) show that rugged material slopes gradually (~0.8°) toward the center of Millochau. Rugged material appears to have experienced significantly more

degradation of its upper surface than pitted material. Given the consistent sloping nature of this unit, rugged material likely includes a component of material shed from Millochau's walls by mass wasting; however, unlike typical martian debris aprons, this material does not display any features (such as elongated craters or pits, or transverse ridges) suggestive of ice-rich, gravity-driven flow [e.g., Carr and Schaber, 1977; Squyres, 1978; Lucchitta, 1984; Colaprete and Jakosky, 1998; Pierce and Crown, 2003]. The precise nature of rugged material is unclear, but it could include sedimentary (fluvial, lacustrine or eolian), volcanic and impact related deposits. MOC image E04-02035 (Figure 3.12) covers part of the floor materials in the crater that adjoins Millochau's eastern rim and displays the same stucco-like surface texture characteristic of rugged material, but is identified as "talus material" in Mest and Crown [2004b].

The contact between pitted and rugged material is for the most part unclear. Most of the western contact is buried by ejecta from Okatoks and the northern contact is complicated by numerous depressions that separate the units. The eastern and southern edges of the plateau provide the best stratigraphic relationships between pitted and rugged material. THEMIS images I02020002 and I04629003 (Figure 3.4b) show that although the margin of the plateau is degraded and irregular, rugged material appears to embay the pitted material. Topographic profiles (Figures 3.3c, 3.6 and 3.7) show that the plateau, and thus pitted material, rise 300 to 400 meters above the rugged material in contact with the plateau or adjacent to depressions. However, rugged material slopes toward the plateau yielding a relative relief of ~250 m between the plateau and rugged material adjacent to Millochau's inner wall. If pitted material extended beyond its current boundary, the deposit must have thinned out nearer to Millochau's inner wall.

Etched material (HNme) is exposed within depressions that border the northern and eastern portions of the plateau (Figures 3.2a and b). This unit displays a variety of surface textures (smooth, lineated, and irregular) and albedos (Figures 3.6-3.9), and encompasses surfaces not incorporated within other units mapped in Millochau. In short, the unit mapped as etched material is more of a geomorphic surface than a true geologic unit and may represent many different lithologies. Few fresh craters are observed within etched material, and some exposures appear to contain craters that are in the process of being exhumed. Irregular and lineated etched material is interpreted to be exhumed crater interior deposits, which are most likely composed of the same sedimentary, volcanic, and (or) impact materials as the pitted and

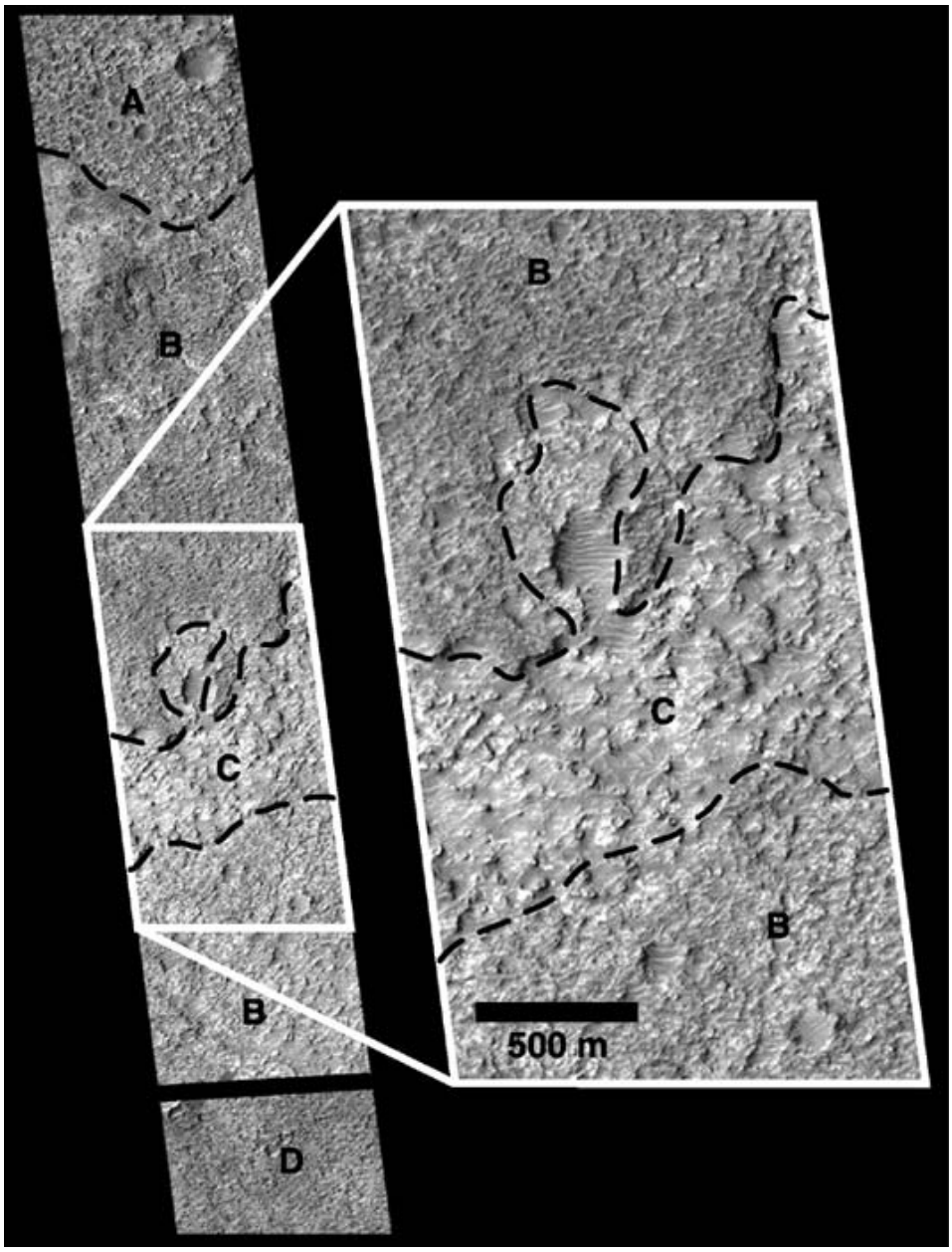

Figure 3.12. MOC image E04-02035 showing talus material (AHt) at the base of the inner rim of crater Jumla that adjoins Millochau's eastern rim. Here, talus material displays four surfaces, A-D, that appear to reflect different amounts of erosion. Surface A is the uppermost layer in this sequence and displays degraded craters. Surface B also displays degraded craters (see close-up), but they are less distinct than on surface A. Surface C (see close-up) contains knobs and mesas that could be remnants of surface B or D. Surface D (separated by a data gap) contains mostly small degraded craters, and appears the least eroded of the surfaces pictured here. Dune forms (see close-up) are found in the low-lying areas of surfaces B and C, suggesting eroded sediments have been redistributed. Image centered at 21.7°S, 273.9°W; image is 1.45 km across; resolution is 2.83 m/pixel; illumination is from left; NASA/JPL/MSSS.

rugged units. Collapse of overlying materials and (or) erosion (fluvial and eolian) are believed to be the main processes operating to expose these deposits. Etched material that displays relatively smooth surfaces is believed to consist of eroded crater interior materials that have been redistributed via erosional processes (fluvial and eolian) and may be unconsolidated to loosely consolidated. Given the catchall nature of etched material in that it represents many types of exposed surfaces within the depressions, it can not be used as a stratigraphic determinant. Lastly, etched material always occurs topographically below pitted material, but is found both above and below the rugged material it contacts (Figure 3.6 and 3.7). It is observed in Figure 3.6 that locations 'a' (rugged material) and 'b' (etched material) are at roughly the same elevation (~220 m). This suggests that some exposures of etched material and perhaps knobs (described below) might be outliers of rugged material, and that this material may extend laterally beneath the plateau.

Numerous knobs (Hk) are found within the depressions that separate the plateau from surrounding rugged material (Figures 3.6-3.9). Most knobs are rounded and are found at elevations lower than the surface of the plateau, but some knobs are capped with pitted material suggesting they are outliers of the plateau (Figure 3.9 and 3.7). Identification of these capped knobs may help constrain the extent of the plateau and pitted material prior to collapse and erosion of the floor deposits. There are no knobs visible, rounded or capped, within rugged material, which implies that if pitted material extended over most of Millochau's floor, it was completely removed from these distal areas. Alternatively, the lack of knobs in rugged material could also suggest that the extent of pitted material was not much greater than it is now. Layers of variable thickness are exposed in some knobs indicating deposition of sedimentary materials and (or) volcanic activity in Millochau's history.

Dune material (Amd) occurs in isolated patches that fill low-lying parts of pitted, rugged, and etched materials (Figures 3.6-3.9). In MOC images, the material that forms these deposits is generally darker than the underlying materials, but in some MOC images very bright deposits, possibly frost, are found between dunes. The materials composing this unit form large sets of long- and short-wavelength dunes, similar to those described by Edgett [2001a,b]. Long-wavelength dunes (wavelengths ~40-170 m, avg. ≈ 70 m), are oriented east-west (long axis) and they typically span the widths of the depressions in which they occur. Short-wavelength dunes (wavelengths ~10-30 m, avg. ≈ 20 m) occur between long-wavelength dunes and at the bases of

knobs and the scarps of massifs and the plateau. The orientations of short-wavelength dunes tend to be strongly influenced by adjacent topography in that they are oriented perpendicular to the knob, scarp or long-wavelength dune with the highest relief, which is why short-wavelength dunes form both perpendicular and parallel to adjacent long-wavelength dunes (see close-up in Figure 3.8). From MOC images, it appears that most short-wavelength dunes superpose long-wavelength dunes indicating they are either younger and (or) more mobile. In MOC images, most impact craters observed in dune material are found between dunes and do not superpose the dunes. Most craters counted in dune material were identified using THEMIS and Viking images where dune forms are not visible. Dune material is interpreted to consist of sediments eroded from other interior floor deposits, as well as crater wall and rim materials, and redistributed within low-lying areas by eolian processes.

Viking Orbiter, THEMIS and MOC images show Millochau also contains a narrow band of material located along the base of its interior wall (Figures 3.2a and b). This material has been mapped as talus (AHt) and most likely consists of sediments shed from the crater wall by rock slides and falls, but may also include sediments eroded by fluvial processes and transported via gullies, as well as other volatile-related mass movements, such as the lobate feature observed in Figure 3.4a (inset). Talus material buries the outer edge of rugged material in many places along the base of Millochau's wall, thus obscuring their contacts. The fronts of some talus deposits, especially in the northeast of Millochau (Figure 3.11), have very irregular edges and appear to have been eroded. Here, removal of talus has exposed underlying rugged material and numerous degraded impact craters. Several "ghost" craters are visible within this exposure of talus indicating the deposit may be relatively thin, possibly only a few 10's of meters thick. Talus material is also exposed in crater Jumla, east of Millochau [Chapter 2.0; Mest and Crown, 2004b] and is shown in Figure 3.12. In this adjoining crater, talus material displays four surfaces, which are presumably erosional in nature. Surfaces B and (or) C appear similar and may be related to the exhumed surface of rugged material visible in Figure 3.11.

3.5 IMPACT CRATER STATISTICS AND GEOLOGIC HISTORY

Geologic mapping and geomorphic analyses using Viking, MOC, TES, THEMIS, and MOLA datasets have shown that crater Millochau contains several distinct deposits and that the crater interior has undergone a complex history of post-emplacement modification that may have included collapse, erosion, and redistribution of fine-grained sediments by the wind. Superposition and cross-cutting relationships, combined with crater size-frequency distributions (see Table I and Appendix C), have been used to determine the relative stratigraphic positions of the units identified within Millochau. It should be noted that the areal exposures and overall abundances of craters on some units examined in this work are small causing large statistical uncertainties in some cases. Given the erosional nature and potential for redistribution of significant amounts of material within these units, such as rugged and etched materials where interpretations suggest there has been exhumation, these data may more accurately represent surface retention ages rather than stratigraphic ages. Crater size-frequency distributions for Millochau rim materials indicate that the crater is Early to Middle Noachian in age. Millochau is older than the surrounding intercrater plains, which has been determined to be Middle to Late Noachian in age in the region between 17.5°-27.5° S and 270°-275° W [Mest and Crown, 2004b]. Crater size-frequency distributions for valley floor deposits and cross-cutting relationships indicate that much of the fluvial activity that eroded the ejecta and rim materials of Millochau and many other craters, and formed extensive valley networks within surrounding plains, occurred during the Late Noachian and Early Hesperian Periods [Mest and Crown, 2004a,b]. Many of the craters in the region also have gullied interior walls and relatively flat floors, indicating the erosional and depositional processes were similar and widespread; gully formation most likely represents some of the latest fluvial activity in this part of the highlands [Mest and Crown, 2004b]. Stratigraphic relationships and crater size-frequency distributions also show that the bulk of the geologic record within Millochau spans from the Middle Noachian Period (post-Millochau formation) through the Early to mid-Hesperian Period.

It was during the Middle Noachian to Early Hesperian that erosion of Millochau's rim materials and gully formation along the inner crater wall were active. Deposits of sediments eroded by the gullies are not present at the mouths of the gullies indicating that talus or rugged

material buried these deposits, these materials have been removed, or they were incorporated into the interior deposits. Contributions of crater wall debris to the floor deposits are consistent with the inward sloping surfaces of rugged materials. Water introduced to Millochau via the gullies may have ponded for short periods within low-lying areas of Millochau's floor and could have percolated into the subsurface to be stored in aquifers (or frozen) and later released via sapping processes to form the valleys bordering the plateau.

Crater Okatoks in western Millochau displays a well defined ejecta blanket (Hc) that superposes Millochau's rim, pitted and rugged materials, and provides a stratigraphic referent for the Millochau interior deposits, as well as for gully formation. Crater size-frequency distributions for this crater suggest an age of mid- to Late Hesperian (uncertainties suggest a range of Middle Noachian to Early Amazonian) (Table 3.1). The ejecta from Okatoks appears relatively unmodified by the erosional processes that affected the pitted and rugged materials, indicating emplacement and most of the erosion of these units occurred prior to formation of Okatoks within a window ranging from the Middle Noachian to Late Hesperian. Crater size-frequency distributions for pitted (N(5) and (16)), rugged (N(16)) and etched (N(2) and (5)) materials show ages that are anomalously older than Millochau rim materials (Table 3.1); however, the uncertainties in counts for these units are significantly greater and their lower limits always plot younger than Millochau rim materials. Millochau's lack of an ejecta blanket, and thus a larger area from which to derive a more accurate crater population, as well as erosion of craters on Millochau's rim could partly account for this discrepancy. For this study all craters that could be resolved down to MOC resolution (D=50 m) were counted regardless of their preservation state, except in Okatoks' ejecta. Secondary craters from Okatoks inadvertently included in the statistics may account for the anomalous old ages relative to the Millochau rim (see Appendix C). Within Okatoks' ejecta blanket, 'highly degraded' craters were not counted because it was difficult to determine whether these craters are mantled by the ejecta or are eroded craters that superpose the ejecta.

Crater size-frequency distributions show consistently older but similar ages for pitted material relative to rugged material. This can be explained in one of two scenarios. The first scenario suggests the deposits identified as pitted and rugged material were emplaced across much of the crater floor, with the material now exposing rugged surfaces being the basal layers of a sequence capped by the material with pitted surfaces. Portions of the pitted materials were

subsequently eroded back into the plateau currently observed, exposing deposits, which over time produced the rugged surfaces observed. The rugged material was therefore shaped by removal of the upper layers and subsequent erosion. The second scenario suggests that pitted and rugged materials were emplaced such that their current extents closely reflect their extents at the time of emplacement. Both units were able to accumulate craters at similar rates, and thus the rugged material would be a younger geologic unit rather than a younger surface as in the first scenario. Superposition relationships between these units are difficult to discern and either scenario, or some variation, could be valid. The degraded nature of the pitted material is similar in appearance to the surface of the intercrater plains surrounding Millochau, suggesting either similar materials compose the plains and some Millochau interior deposits and (or) similar processes have acted to degrade these units.

Layering observed within the depressions surrounding Millochau's central plateau might provide further insight into the origin of these deposits. The thin stratigraphically lower layers appear fairly horizontal and flat indicating deposition in a large standing body of water or playa, by eolian processes, or by pyroclastic volcanism. The thicker and more massive layers, observed to be capped by pitted and rugged surfaces, most likely accumulated over a longer period of time. Given that the surfaces of neither of these units is far from horizontal required a method of deposition that was widespread (within the confines of Millochau) and involved near-surface lithification of thick sequences of material. This could involve emplacement of sediments that were subsequently cemented together, welded or cemented pyroclastic deposits, or some combination of these. Although active volcanism occurring within the confines of Millochau's walls seems unlikely given the lack of source vents or flow structures typically observed in volcanic environments, volcanic deposits derived from outside of Millochau may have contributed to Millochau's floor materials.

Gullies along the interior wall of Millochau show water was transported into the crater, and the presence of several sapping-type valleys incised in the plateau indicate water was released from Millochau's interior deposits. It is possible that parts of the water-rich, or at least unconsolidated, pitted and rugged materials could have collapsed as a result of the Okatoks impact event to form the depressions along the northern and eastern edges of the plateau. These collapse zones exposed layered deposits beneath pitted and rugged materials and as a result of post-collapse erosion and redistribution of sediments formed exposures of etched material. It is

believed that exposure of this unit probably occurred during the Hesperian Epoch with subsequent fluvial and eolian modification in the mid- to Late Hesperian Epoch to Amazonian Period. Major valley formation along the southern plateau edge and minor formation along the northern and eastern scarp boundaries of the plateau and collapse zones might have been initiated following the formation of the collapse zones; the scarp face would have been a free surface from which subsurface water could escape.

The most recent activity within Millochau includes eolian deposition of sediments in low-lying areas of the collapse zones and pitted and rugged materials to form dune fields, and mass wasting of crater wall material to form deposits of talus along Millochau's wall. Both units contain few craters and yield relatively young ages of Early to Middle Amazonian for dune material and Late Hesperian to Middle Amazonian for talus (Table 3.1). It is also possible that eolian activity and mass wasting are still active and are presently modifying these deposits.

3.6 DISCUSSION

Crater Millochau in the highlands of Tyrrhena Terra contains a suite of intriguing geological units and features that have not been examined in detail prior to this study. Previous studies of martian impact craters, particularly those that categorize craters as paleolake basins [e.g., Forsythe and Blackwelder, 1998; Cabrol and Grin, 1999, 2001a], do not include Millochau and many other craters that show features such as layered floor deposits or gullied walls. These features do not definitively indicate that Millochau contained a crater lake, and they could very well have a variety of different origins, but the presence of layered deposits in Millochau and other large craters warrants investigation and may lead to a better understanding of impact crater degradation, and perhaps martian paleolake formation.

Millochau displays a rim that has been worn down by fluvial, eolian and mass wasting processes and an interior wall that has been eroded by water to form gullies. The lack of

identifiable ejecta deposits associated with Millochau and the presence of extensive valley networks within the plains surrounding Millochau, of which some tributaries dissect Millochau's rim, indicate fluvial erosion was an important process in regional degradation.

The floor of Millochau has been filled in with materials that form laterally continuous layered deposits with thicknesses down to the limits of MOC resolution. Portions of the interior deposits have undergone collapse and erosion forming a series of depressions north and east of a central plateau and revealing much of the layering along scarps and knobs. Layering exposed within Millochau is consistent with deposition in transient, shallow bodies of water, as proposed for other martian craters (e.g. Holden, Gusev, Gale, and Schiaparelli) [Cabrol et al., 1996; Newsom et al., 1996; Grin and Cabrol, 1997; Forsythe and Blackwelder, 1998; Ori et al., 2000; Cabrol and Grin, 1999, 2001a; Grant and Parker, 2002; Malin and Edgett, 2003], although landforms diagnostic of lacustrine environments (e.g., deltas, terraces) have not been identified and contributions by mass-wasting, eolian, and volcanic processes cannot be ruled out. If the layered deposits of the plateau are lacustrine or partially lacustrine in nature, the associated body of water would have been ancient, given the degree of degradation observed, the absence of lacustrine landforms, and the lack of connection between the plateau and the crater walls. The exposed surfaces of at least two of these deposits--pitted and rugged material--are clearly distinct in THEMIS and TES datasets. Although their origins are uncertain, fluvial and eolian processes have subsequently modified these units. Pitted and rugged materials have been shown to be Middle Noachian to Early Hesperian in age, indicating that the layered deposits underlying these units were emplaced earlier. If these layered deposits are fluvial and (or) lacustrine in nature, consistent with the presence of interior gullies, the ages of the interior deposits indicate that most fluvial activity within Millochau was in the Noachian Period. Further constraints on gully formation can be made by ejecta from Okatoks superposing rugged material and possibly burying gullies along Millochau's western wall, and the fact that rugged material buries gullies in the southwestern part of Millochau. Emplacement of pitted and rugged materials via fluvial, lacustrine, eolian or pyroclastic volcanism would tend to produce relatively flat-lying deposits that drape pre-existing topography. The sloping nature of rugged material toward the center of Millochau could indicate emplacement via mass wasting; however, the presence of the central plateau, its several hundred meters of relief, and the current southward slope of pitted material

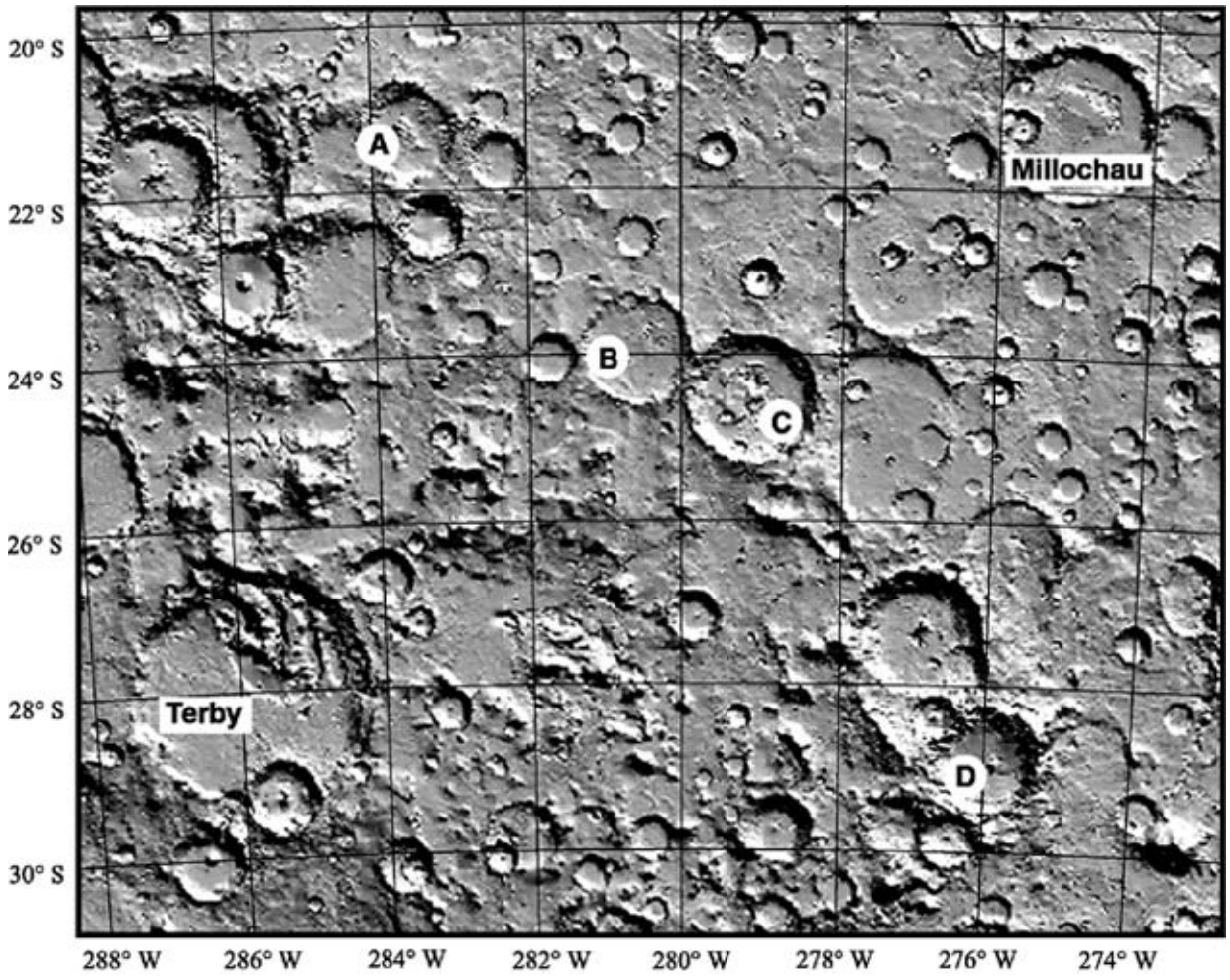

Figure 3.13. MOLA shaded relief showing highlands southwest of crater Millochau (D=114 km). Crater Terby and several unnamed craters (A-D) contain deposits that display layers and (or) depressions visible in MOC and THEMIS images, similar to Millochau. The degraded morphologies of these craters suggest they are of similar age, and their proximity to each other suggests they may contain similar deposits and (or) they underwent similar processes of infilling and erosion. Projection is Mercator; illumination altitude = 40°; azimuth = 30°.

plateau, its several hundred meters of relief, and the current southward slope of pitted material are not easily explained by any of the above processes. The topography of this unit, for the most part, likely has resulted from significant post-emplacement modification of a thick sequence of near-horizontal layers. Small dune fields within low-lying areas of Millochau's interior deposits suggest mobilization and redistribution of sediments by eolian processes is among the most recent activity within Millochau, and dune formation by eolian activity may be ongoing. Volume estimates of the interior deposits (using the method shown in Figure 3.5) imply ~10,000 km^3 of material currently reside within Millochau. If pitted materials at one time completely covered the entire floor, prior to emplacement of rugged material, this would yield ~12,000 km^3 of material with ~2000 km^3 of material removed from the crater interior. For comparison, from earth-based radar Grin and Cabrol [1997] estimated ~7,300 km^3 of compacted sediments reside in Gusev crater (D=150 km). A bench or terrace along Millochau's inner wall at an elevation corresponding to the elevation of the plateau might indicate that plateau materials extended to the crater wall, but there is no evidence of this.

High resolution MOC and THEMIS data sets have allowed similar enigmatic crater interior deposits to be identified, specifically within large degraded craters southwest of Millochau, such as Terby and several unnamed craters, that contain layered interior deposits and depressions similar to Millochau (Figure 3.13). This suggests that these craters may have undergone similar processes of degradation, infilling, and erosion. There is a clear need for detailed analyses of individual highland craters and regional comparisons of the emplacement and modification of crater interior deposits. If the crater interior deposits are volcanic in origin, then significant volumes of volcanic material need to be accounted for and their source(s) needs to be identified. If a large part of these deposits are lacustrine, and it should be noted that many of these craters are not breached by large valleys but merely display gullied walls, then a process for directly filling these large craters with water, such as widespread and voluminous precipitation, is required. If eolian deposition is the source for these interior deposits, this is consistent with a location north of Hellas basin, one of the largest sediment traps on Mars; however, a method of lithifying these deposits into layers tens of meters or more in thickness and the timescale for accumulating thick, layered sequences needs to be understood. Subsurface water or ice could cement the sediments together, but this requires large volumes of water to be introduced into the sediment. Regional mantling deposits associated with climate fluctuations, as

suggested by Mustard et al. [2003], but of significantly greater thicknesses than proposed may also be a source. Alternatively, if these crater filling deposits are not related genetically, then multiple origins are required to explain deposits that are layered similarly and have been eroded similarly in a specific region of the martian highlands. Detailed analyses of other craters in the Martian highlands using the methods described in this study will provide further understanding of impact crater degradation during the early part of Mars' history and of the types and sequences of processes that have shaped Martian highland surfaces.

4.0 WATERSHED MODELING IN THE TYRRHENA TERRA REGION OF MARS

4.1 INTRODUCTION

Since the Mariner 9 and Viking 1 and 2 spacecrafts showed intricate systems of valleys dissecting the ancient cratered highlands [McCauley et al., 1972; Masursky, 1973; Milton, 1973], these valley networks have become some of the most intriguing features on Mars, suggesting water may have played a major role in modifying the martian highlands. Although liquid water can not exist at the surface under current conditions, the presence of fluvial valleys indicates liquid water was likely present at some point in Mars' history. Most martian valley networks (~99%) are found in the highlands, and they may be as old as the material they dissect [Pieri, 1976, 1980; Carr and Clow, 1981; Mars Channel Working Group, 1983; Baker and Partridge, 1986, Grant and Schultz, 1990; Craddock and Maxwell, 1993; Maxwell and Craddock, 1995; Carr and Chuang, 1997; Grant, 2000]. Although many hypotheses have been proposed regarding their formation, the origin(s) and processes of development of martian valley networks are not yet understood. Terrestrial drainage networks typically form by a combination of surface runoff, driven by precipitation, and groundwater sapping [Ritter et al., 1995]. Similar processes have been proposed to explain the origin of martian valley networks [e.g., Pieri, 1976, 1980; Carr and Clow, 1981; Gulick, and Baker, 1990; Craddock and Maxwell, 1993; Grant and Schultz, 1993, 1994; Maxwell and Craddock, 1995; Carr, 1995, 1996; Grant, 2000; Craddock and Howard,

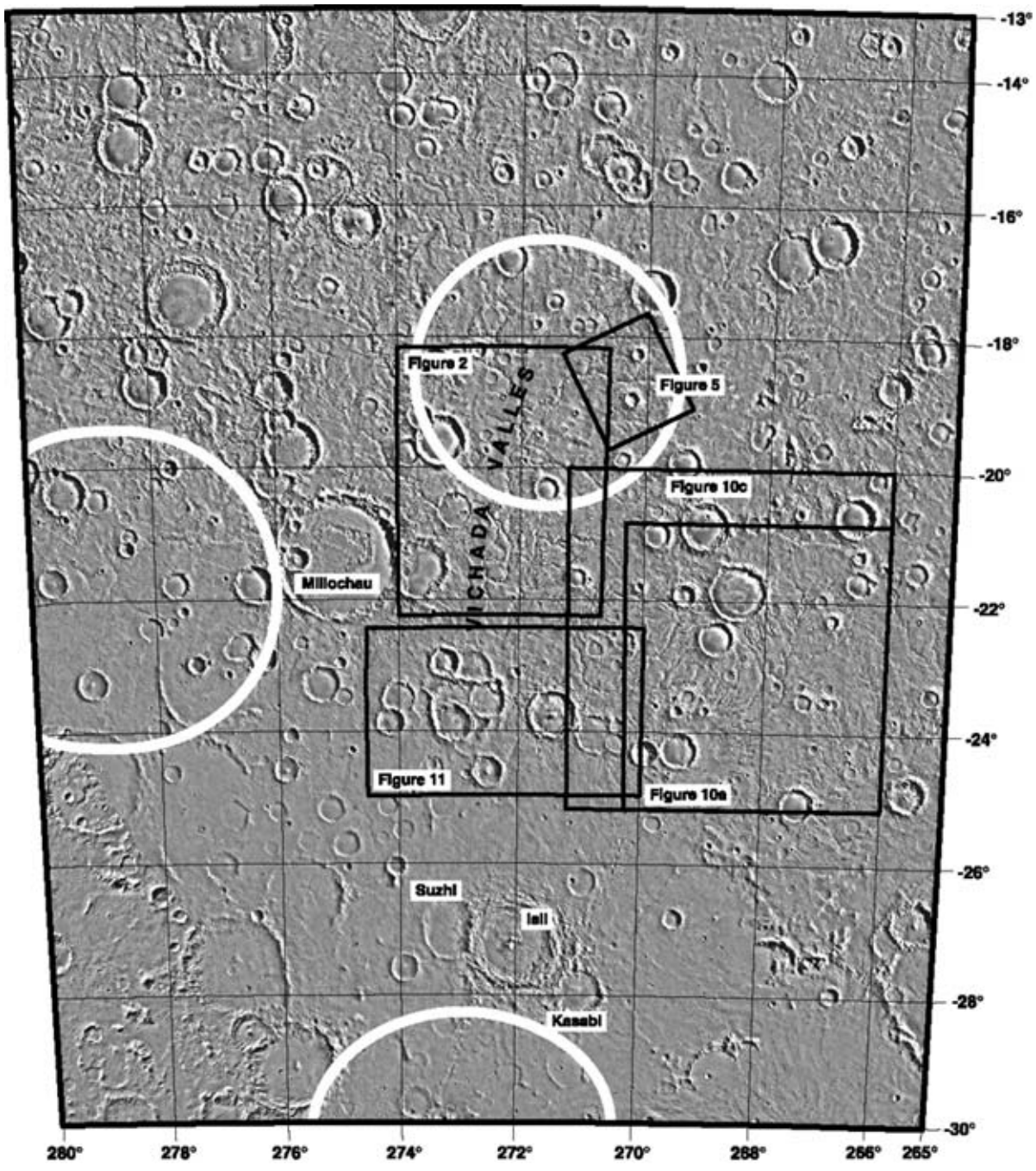

Figure 4.1. Viking MDIM 2.0 photomosaic showing the highland terrain of the Tyrrhena Terra study area north of Hellas impact basin. The locations of three possible impact basins identified using MOLA by Frey et al. [2000] are shown (white circles. The locations of Figures 4.2, 4.3, 4.10 and 4.11 are shown. North is to the top in this and all subsequent images unless noted otherwise; projection is Mercator.

2002; Grant and Parker, 2002]; however, the relative contributions of runoff and sapping to valley network formation on Mars are not known. This is an especially important issue for understanding Mars' evolution, given ongoing debates about climate change and whether the fluvial history of the surface is dominated by atmospheric or subsurface cycling of volatiles.

Geologic mapping and geomorphic analyses in Tyrrhena Terra along the north rim of Hellas basin (13°-30°S, 265°-280°W) (Figure 4.1) have revealed a complex history of impact cratering and modification by fluvial and eolian activity [Schaber, 1977; Greeley and Guest, 1987; Tanaka and Leonard, 1995; Mest and Crown, 2004a]. High-resolution Mars Orbiter Camera (MOC), Thermal Emission Imaging System (THEMIS), and Viking Orbiter images and Mars Orbiter Laser Altimeter (MOLA) topographic data have been used to qualitatively and quantitatively characterize highland fluvial systems and analyze the role of water in the evolution of the highlands of Tyrrhena Terra. Fluvial features in this area include widespread, well-integrated valley networks, such as Vichada[9] Valles, smaller networks and single channels, and gullies incised along the rims of impact craters [Mest and Crown, 2004a,b]. Arc/Info Geographical Information System (GIS) software has been used in conjunction with MOLA Digital Elevation Models (DEMs) to model drainage basin divides and valley networks and derive basin and network morphometric parameters useful in characterizing basin "maturity" and the processes of watershed development. This paper describes the methodology used in the modeling process, as well as present the results obtained from modeling watersheds in Tyrrhena Terra. The modeled networks and the parameters calculated from these data are compared to data derived from fluvial systems mapped by Mest and Crown [2004a]. The abundance and widespread nature of fluvial features within Tyrrhena Terra have significant implications for past martian environmental conditions, and characterization of these fluvial features by mapping and hydrologic modeling is necessary to fully understand the nature of martian fluvial activity and the history of Mars' climate.

[9] The name of 'Vichada Valles' is provisional until approved by the International Astronomical Union.

4.2 BACKGROUND

Martian valley networks consist of channels with few tributaries to complex, well-developed stream patterns, and are interpreted to have formed by flowing water [e.g., Milton, 1973; Pieri, 1976, 1980; Mars Channel Working Group, 1983; Carr, 1996; Malin and Carr, 1999; Craddock and Howard, 2002]. Many previous studies have suggested that Mars' climate has remained relatively unchanged (i.e., cold and dry), with most valley networks formed predominantly by groundwater sapping or seepage-fed runoff [Pieri, 1976, 1980; Carr and Clow, 1981; Mars Channel Working Group, 1983, Baker and Partridge, 1986 (pristine valleys); Kochel and Piper, 1986; Carr, 1995, 1996; Carr and Chuang, 1997; Malin and Edgett, 2000; Cabrol and Grin, 2001b; Stepinski and Collier, 2004; Stepinski and Coradetti, 2004]. To accommodate the instability of water on the surface of Mars due to low atmospheric pressure, some models invoke geothermal heating to drive groundwater sapping processes [Brakenridge et al., 1985; Clifford, 1993; Gulick, 1998, 2001; Tanaka et al., 1998; Malin and Carr, 1999; Carr and Malin, 2000; Goldspiel and Squyres, 2000]. However, Craddock and Howard [2002] noted that many of the studies advocating sapping-dominated valley network formation do not account for the fact that many valleys head at or near the tops of massifs and the rims of impact craters. As a result, other studies have proposed a hybrid process whereby precipitation dominates valley formation via surface runoff, as well as recharges subsurface aquifers, which contribute to network formation by sapping [Baker and Partridge, 1986 (degraded valleys); Craddock and Maxwell, 1993; Craddock et al., 1997a,b, 1999; Grant, 2000; Hynek and Phillips, 2001; Mest and Crown, 2001a, 2004a; Craddock and Howard, 2002; Grant and Parker, 2002; Irwin and Howard, 2002; Stepinski et al., 2002; Irwin et al., 2004]. Recent studies have also suggested that snowmelt, resulting from a warmer climate or geothermal heating, could have formed many of the valleys observed in the highlands and on the flanks of most martian volcanoes [Gulick et al., 1997; Stepinski et al., 2002; Carr and Head, 2004; Fassett and Head, 2004].

According to Pieri [1976, 1980], unlike terrestrial valleys, martian valley networks lack dendritic patterns and tributaries, and show reticulate patterns (suggesting structural control) more indicative of a sapping dominated system; however, Carr [1995, 1996] stated most highland valley networks form open, branching networks with tributaries that converge

downstream. Martian valleys with steep-walled, U-shaped cross-sections and stubby tributaries with theatre-headed terminations are morphologically similar to sapping valleys on the Colorado Plateau [Pieri, 1976, 1980; Carr and Clow, 1981; Mars Channel Working Group, 1983; Carr, 1995, 1996; Malin and Carr, 1999]. However, topographic profiles across highland valleys [Goldspiel et al., 1993] were shown to have "smoothly curved" cross-sections and lack the steep walls typical of terrestrial sapping valleys; morphologically, these highland valleys more closely resemble valleys formed or modified by surface runoff. Goldspiel et al. [1993] suggested that cross-sections of valleys formed by sapping and runoff processes on Mars could be similar due to (1) valley formation in highly fractured megaregolith or unconsolidated ash versus competent rock, and (2) the extensive period of time that weathering, mass-wasting, and erosion has modified the valleys.

Craddock and Maxwell [1993] observed that many highland craters have etched or dissected ejecta deposits or lack ejecta altogether, have smooth floors, and (or) contain parallel interior valleys that terminate at the crater floor indicating highland craters may preserve a record of extensive crater erosion and degradation. Both endogenic (sapping) and exogenic (precipitation) processes may have eroded impact craters and the surrounding highlands. Precipitation would have eroded, and in some cases removed ejecta by sheetwash; channels along the exterior and interior of the craters could have been formed by combinations of runoff and sapping, provided aquifers were recharged by precipitation and an adequate hydrostatic head was available. Over time, precipitation would have decreased at higher elevations resulting in less erosion at higher elevations and less recharge to aquifers (sapping would cease at higher elevations) [Craddock and Maxwell, 1993; Craddock et al., 1997a,b, 1999]. Grant [2000] and Grant and Parker [2002] have shown that valley networks in the Margaritifer Sinus region of Mars have lower drainage densities than terrestrial basins formed by runoff. However, groundwater sapping can not be inferred either, as these densities do not reflect resurfacing of some valleys and the resolutions at which the measurements were taken are not comparable to terrestrial mapping resolutions. Further analysis by Grant [2000] suggested valley formation in this region might be due to a "hybrid" process of sapping recharged by surface water with lesser contributions to valley formation by runoff.

4.3 GEOLOGIC SETTING

The highlands of Tyrrhena Terra display a shallow (0.23°) southward-trending slope toward Hellas basin. The impact event forming Hellas basin established a regional slope and structural patterns that have influenced the geologic history of this region. The geologic history may have also been affected by three buried and degraded impact basins identified by Frey et al. [2000] (Figure 4.1). These basins would have acted as sinks in which water, and alluvial and eolian sediments could have accumulated. From MOLA data, the Hellas basin exhibits more than 9 km of relief [Smith et al., 1999] with a maximum elevation near 3 km along the north and west rims of the basin, and a minimum elevation near -7 km along the western floor of Hellas. The geologic units in Tyrrhena Terra, initially included in the Plateau and High-plains assemblage [Greeley and Guest, 1987], are believed to consist of a suite of interlayered sedimentary, volcanic, and impact-related (ejecta, impact breccia, etc.) materials [Schaber, 1977; Greeley and Guest, 1987; Mest and Crown, 2004a]. This area is characterized by a high density of impact craters that range in size from the limits of MOC resolution to over 100 km in diameter [Schaber, 1977; Greeley and Guest, 1987; Mest and Crown, 2004a,b] and vary in preservation state (Figure 4.1). Most craters are moderately to highly degraded, and even many 'fresh' craters with well-defined rims and ejecta blankets have experienced some degree of modification. Many craters in Tyrrhena Terra, regardless of their preservation state, contain deposits that cover their floors. These deposits, mostly Late Noachian to Early Hesperian in age, have several likely origins, such as (a) eroded crater rim and wall materials deposited via gullies and (or) by mass wasting, (b) highland materials deposited via a valley that breached a crater rim, and (or) (c) sediments deposited via eolian processes [Mest and Crown, 2004a].

The terrain of Tyrrhena Terra shows abundant evidence for erosion and deposition by fluvial and eolian processes. These highlands contain a series of dendritic to (sub)parallel valley networks that dissect an extensive Noachian-aged intercrater plains unit [Mest and Crown, 2004a]. Vichada Valles, which is composed of at least thirteen subbasins (discussed below), is the largest network in the area and drains a large portion of this part of the highlands (~3.0×10^5 km^2), but several smaller networks and individual channels are also found [Craddock and Maxwell, 1993; Carr, 1996; Carr and Chuang, 1997; Cabrol and Grin, 2001b]. Much of the

erosion that formed these valley networks and degraded craters in this area is believed to have occurred in the Late Noachian Epoch and continued into the Early Hesperian Epoch [Greeley and Guest, 1987; Tanaka and Leonard, 1995; Leonard and Tanaka, 2001; Mest and Crown, 2004a]. Previous researchers [e.g., Carr, 1995, 1996] have interpreted highland valleys, such as those found in Tyrrhena Terra, to have formed by combinations of surface runoff-induced mass wasting and sapping processes. However, questions regarding the ability of sapping to be sustained in local environments (i.e., along crater rims) have been raised [Craddock and Maxwell, 1993; Maxwell and Craddock, 1995] and are applicable here. Furthermore, the ability to sustain an interconnected aquifer system in the highlands of Tyrrhena Terra is problematic; interlayered sequences of volcanic, sedimentary and impact materials, proposed in Mest and Crown [2004a], would likely restrict groundwater flow. The most recent geologic activity in the area is eolian mobilization of sediments and deposition of wind-blown material in most low-lying areas.

4.4 GEOMORPHOLOGY OF TYRRHENA TERRA VALLEY NETWORKS

From analysis of Viking Orbiter, MOC and THEMIS images, valley networks in the Tyrrhena Terra study area display dendritic to sub-parallel patterns and dissect large portions of these highlands. At some point in the past, Vichada Valles (Figure 4.2) presumably debauched into Hellas basin, but evidence of this extension is obscured by a group of large craters at 24°S (Figures 4.1). In addition, several smaller networks are incised around Vichada Valles, some of which are separated from Vichada Valles by impact craters or ejecta. These networks have been modeled as separate subbasins (discussed below), but most are believed to have been connected to Vichada at one time. Most tributaries of Vichada Valles identified in image data head within an elevation range of ~1.5-2.5 km. MOC images reveal that valleys in the study area display

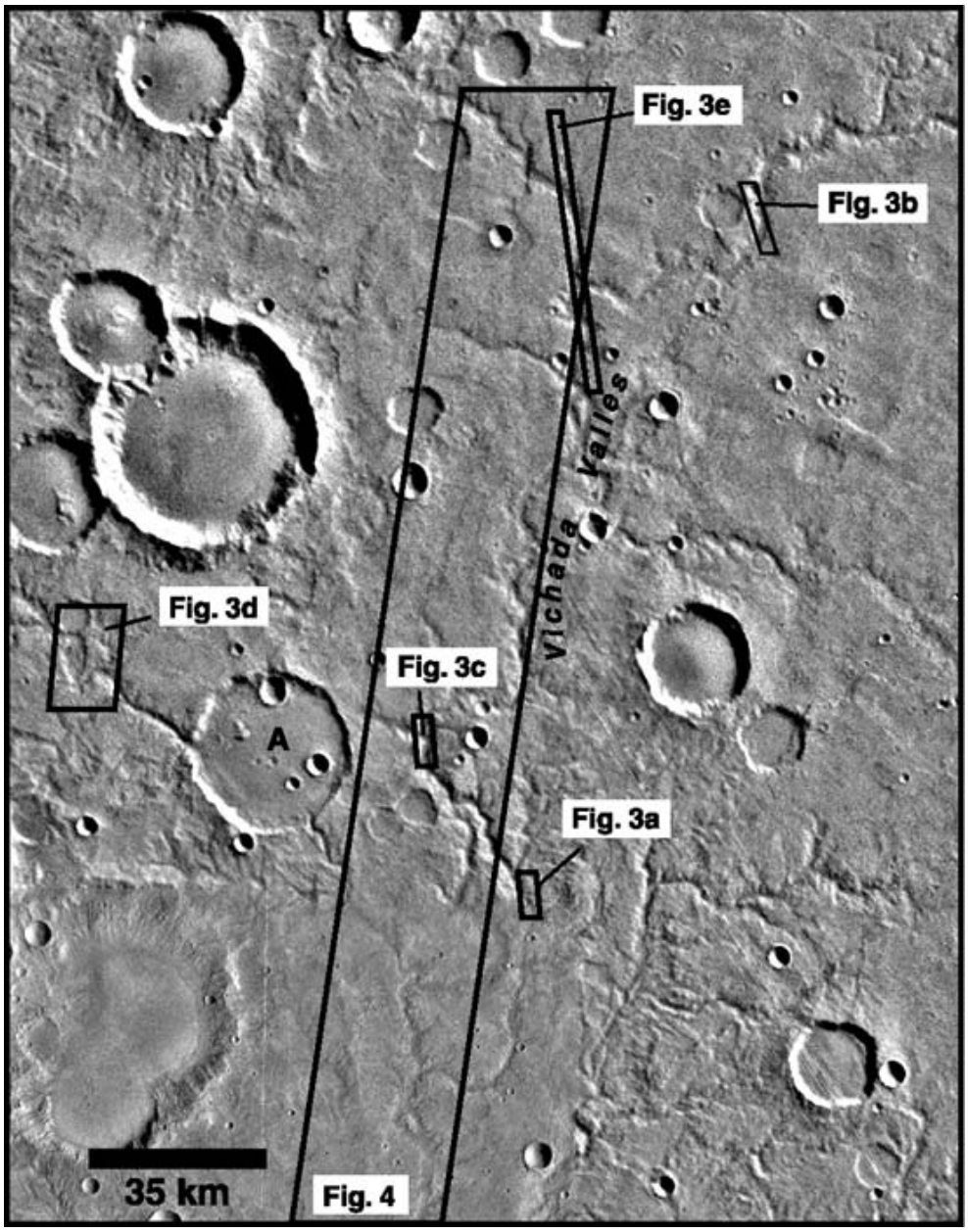

Figure 4.2. Part of Viking Mars Transverse Mercator quadrangle -20272 showing the local intercrater plains material [Mest and Crown, 2004a]. Here the plains are dissected by large-scale, well-incised systems of valley networks, including Vichada Valles, and contain many impact craters exhibiting various degrees of preservation. The image shows a large crater (A; D = 34 km) that is breached along its western rim by an inlet valley and an outlet valley along its southeast rim. Most craters in the map area contain smooth (at Viking Orbiter resolutions) deposits presumably consisting of materials eroded from the crater rim, deposited by eolian processes, or deposited via fluvial/lacustrine processes as in the case of crater A [Mest and Crown, 2004a]. The locations of Figures 4.3 and 4.4 are shown. Image centered at 20.0°S, 272.2°W; illumination from upper right.

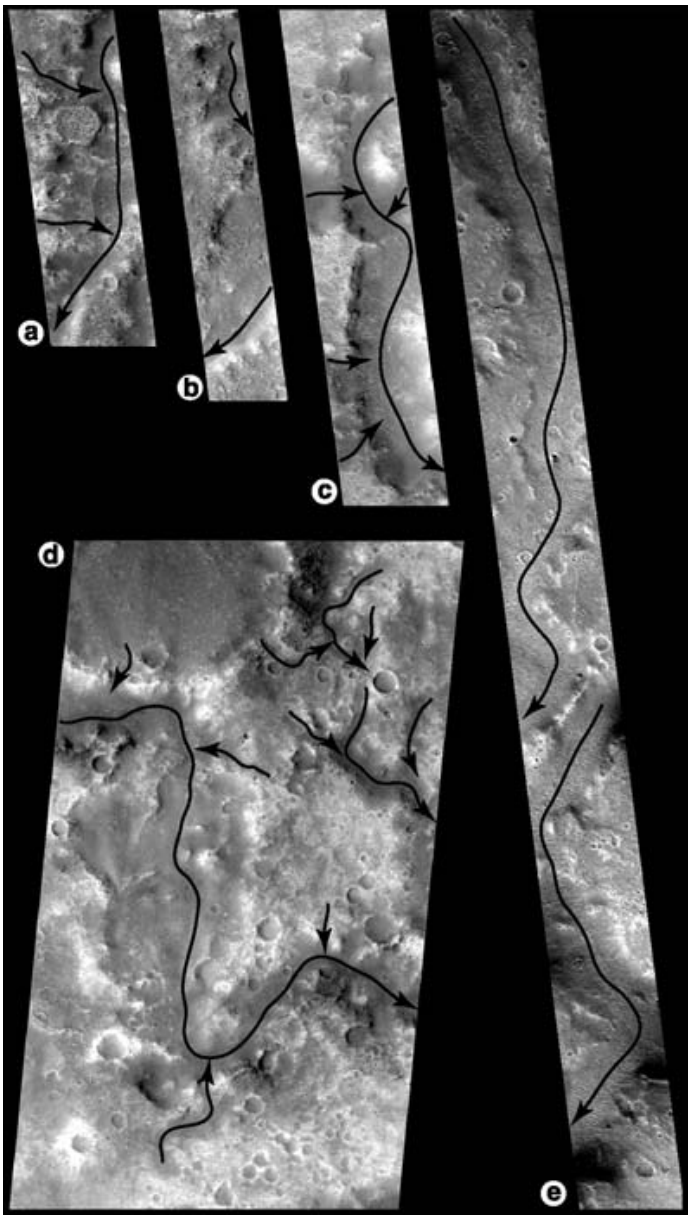

Figure 4.3. MOC narrow-angle images showing parts of the Vichada Valles system - including sections of the main channel (a, c and e) and tributaries (b, d and e) - incised within intercrater plains material in Tyrrhena Terra. The sections of valleys shown in all of the images are filled to some degree with alluvial and eolian sediments; parallel sets of dunes oriented orthogonal to valley walls are visible in a, b, c and e, suggesting this material has been mobile [Mest and Crown, 2004a]. Black arrows point in downstream direction. (a) M03-03481; centered at 21.0°S, 272.2°W; image width = 2.88 km; resolution = 2.81 m/pixel. (b) M04-02305; centered at 18.7°S, 271.5°W; image width = 2.16 km; resolution = 2.82 m/pixel. (c) M08-02977; centered at 20.7°S, 272.8°W; image width = 2.88 km; resolution = 2.81 m/pixel. (d) AB1-09306; centered at 20.4°S, 273.9°W; image width = 10.79 km; resolution = 5.27 m/pixel. (e) E12-00204; centered at 19.0°S, 272.0°W; image width = 3.04 km; resolution = 5.94 m/pixel. NASA/JPL/MSSS.

highly degraded morphologies with rounded banks, layers or terraces along valley walls, and dunes covering their floors (Figure 4.3). MOLA profiles show that most trunk valleys have fairly flat or gently sloping floors and many tributaries are v-shaped in cross-section; valley depths range from ~70 to 200 m and widths from ~0.9 to 10.5 km. The trunk valley of Vichada Valles branches and rejoins downstream several times along its length (Figure 4.4). Carr [1995, 1996] attributed this phenomenon to headward erosion of a sapping-type valley, where random headward extension led to intersection of the valleys upstream. Terracing, branching and rejoining of larger valleys, and varying downstream widths and depths suggest valley formation and modification may be more complex than by sapping alone, and requires a process involving higher, and generally fluctuating, discharges to cause lateral erosion of valley walls or meandering. These features are generally not characteristic of sapping-dominated systems in which discharges are relatively constant and valley width and depth would remain relatively constant from head to mouth [Carr, 1995, 1996; Goldspiel et al., 1993; Goldspiel and Squyres, 2000]. It has also been suggested by Carr and Malin [2000] that a section of one of Vichada Valles' tributaries, shown in Figure 4.3d, resembles thermokarst terrain where alases (irregularly shaped, flat-floored, steep-sided hollows) grow and merge due to combined processes of surface drainage and melting ground ice. They also state that although Viking images show much of this system is well-integrated, this MOC image (AB1-09306) shows that subsequent processes that formed this potential thermokarst terrain, "dominate" Vichada Valles and other highland valley networks. Our analysis of MOC and THEMIS images of Vichada Valles (Figures 4.2, 4.3, 4.4 and 4.5) indicates that the morphology observed in MOC image AB1-09306 is not typical of the system as a whole. This potential thermokarst morphology is not observed either up- or downstream of the particular reach shown in AB1-09306, or in valleys elsewhere within the Vichada Valles system. This suggests that this thermokarst terrain is localized to this stretch of the system and does not dominate Vichada Valles as suggested by Carr and Malin [2000]. Rather the morphology of Vichada Valles and its tributaries can be attributed to a combination of fluvial erosion and minor amounts of mass wasting, as well as different degrees of subsequent eolian infilling. Eolian infilling is observed throughout the Vichada Valles and extensive infilling can explain regions that appear to be poorly integrated.

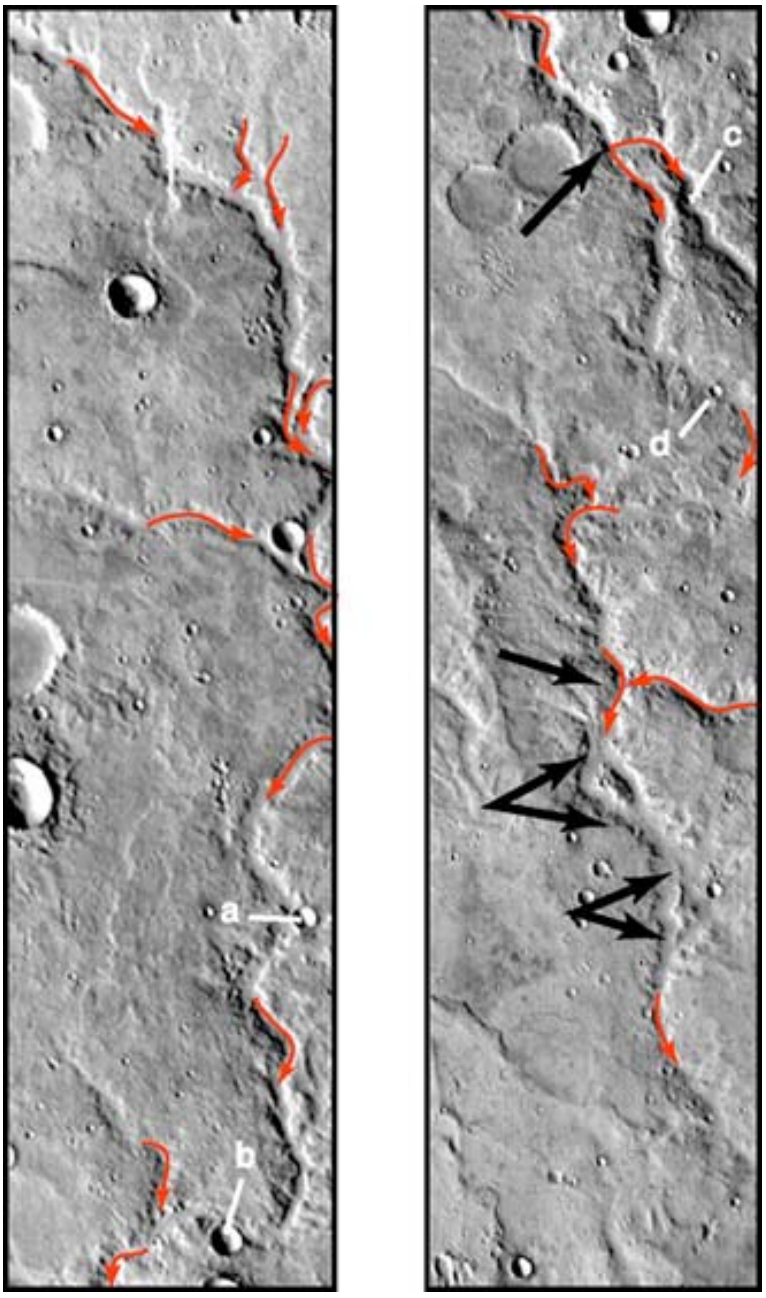

Figure 4.4. Part of THEMIS daytime IR image I07550002, split into upper (left) and lower (right) sections, showing the main valley of Vichada Valles. The lower section shows three locations where the main valley of Vichada Valles splits and rejoins downstream (black arrows). There are no obvious obstructions, such as an impact crater, along the valley that would cause diversion or redirection of flow to form these splits. Furthermore, several craters (a-d) are located either fully or partially within the main valley of Vichada Valles, but there is no evidence for ponding upstream or diversion of water around the obstruction, suggesting flow within the system was low or had ceased prior to formation of these impacts. Red arrows point in the downstream direction.

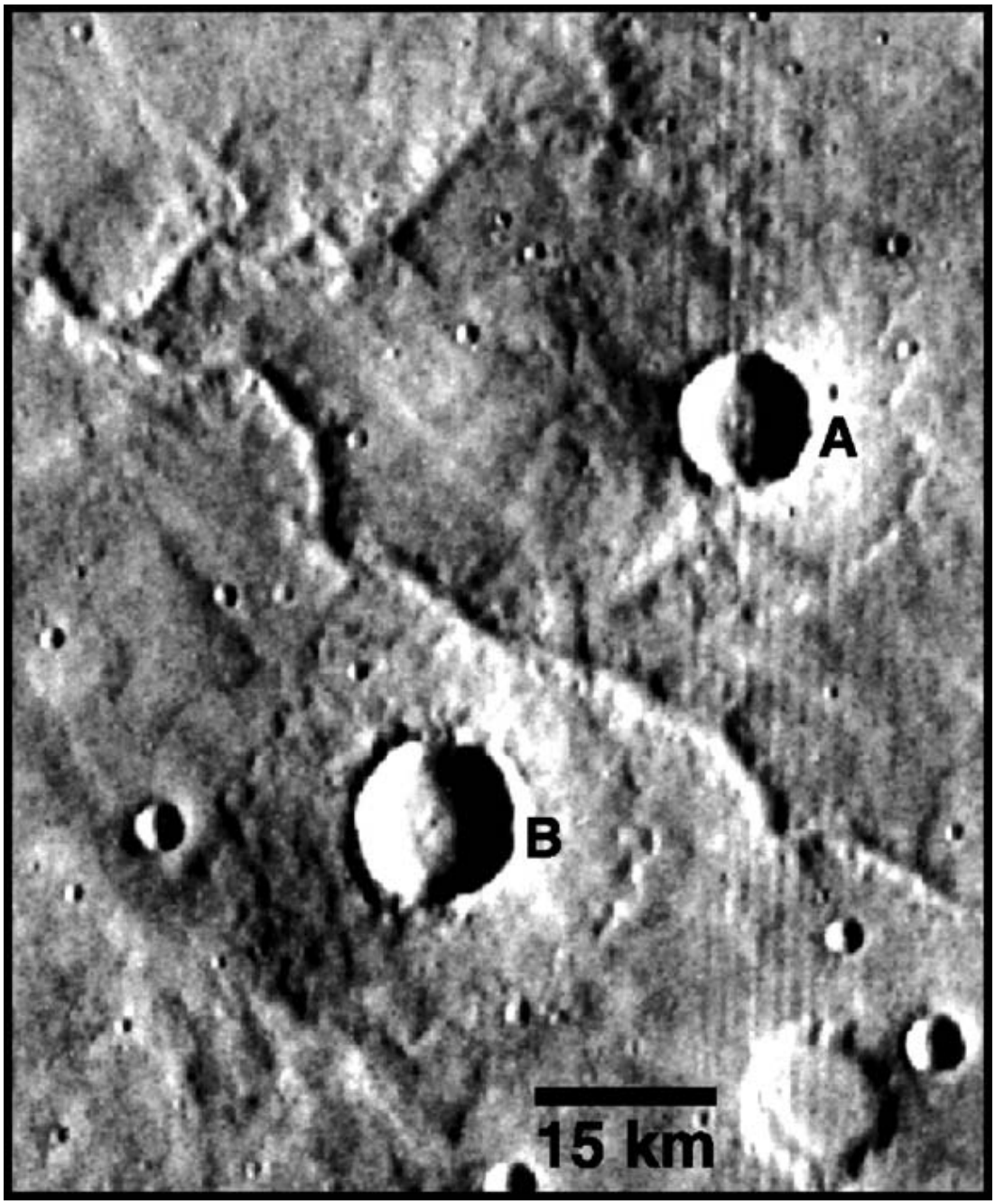

Figure 4.5. Part of Viking Orbiter image 625A25 showing a tributary of Vichada Valles incised within the plains between two large craters (A and B). The craters show ejecta blankets that are either 1) eroded by a incised valley or 2) mantle a preexisting valley. At the available image resolution it is not clear whether ejecta material is present on the valley floor. There is no evidence for ponding or diversion of this valley, suggesting fluvial processes were active before crater formation or that fluids moved easily through the valley following ejecta emplacement. North is to the upper right corner; image is centered at 18.5°S., 270.0°W; resolution = 239.82 m/pixel; illumination from right.

Some valleys within the study area, particularly those that have no tributaries or form sub-parallel networks, are smaller and appear less incised than Vichada Valles and other large dendritic systems. The tributaries of these smaller systems typically head at crater rim crests and they are generally not more than a few hundred meters to a few kilometers long. The occurrence of these systems on steep slopes results in more closely spaced first-order tributaries. For example, smaller networks in the eastern part of the study area empty into an old buried crater basin (centered at 24.4°S, 269.0°W; Figure 4.1) that has subsequently accumulated large impact craters on its floor. None of these and other smaller networks are observed to intersect the trunk valley of Vichada Valles. Because many of these dense networks of valleys head at crater rim crests, Carr [1995, 1996] attributed their formation to sapping combined with minor components of surface runoff derived from water that overtopped the crater rims in which the valleys are incised and mass wasting of water-saturated materials. The morphologic differences between these smaller networks and Vichada Valles could also be due to differences in age, lithology, and (or) slope.

4.5 VALLEYS-IMPACT CRATER CROSS-CUTTING RELATIONSHIPS

Impact craters are the dominant local topographic features in Tyrrhena Terra and also presumably have a large influence on subsurface permeabilities; therefore, craters have potentially significant effects on flow of both surface and subsurface water. Coverage of Tyrrhena Terra by mostly low-resolution Viking Orbiter and few high-resolution MOC images makes identification of clear crosscutting relations between fluvial valleys and impact craters difficult. However, recent coverage by THEMIS images, such as in Figure 4.4, allows stratigraphic relationships to be characterized in detail in specific locations, and helps to evaluate spatial and temporal relationships between fluvial activity and cratering.

Impact craters observed to superpose valleys do so typically by truncation or bisection by the impact structure or the ejecta blanket. If water actively flowed within these valleys after the time of the impact event, water would have ponded behind the obstruction, resulting in deposition of sediments. Or if the obstruction were small enough, water might have been diverted, resulting in incision of a new channel. Similarly, if an obstruction, such as an ejecta blanket, were thin enough and (or) highly permeable, water could pond behind the obstruction until it eventually percolated through and eroded the obstruction such that a "new" channel was incised within the obstruction and flow continued along its course through the original channel. Figure 4.5 shows a potential example of this relationship, but clear evidence for ejecta from the two ~10-km-diameter craters on the floor of the valley can not be discerned. Most examples in the study area in which an impact structure truncates or bisects a valley show no clear evidence for ponding behind the crater or diversion of water around the crater (Figure 4.4). This suggests that there was little to no flow within these valleys following the impact events [Mest and Crown, 2004a]. These examples show that some valley formation predates emplacement of many of the impact craters in this part of the highlands.

Some dissection of the local plains material [Mest and Crown, 2004a] appears to have been contemporaneous with or postdate impact crater formation. The clearest examples that show valley formation postdates crater formation are those where the valleys actually originate within the crater materials, such as gullies and tributaries that head near crater rims. Less distinct examples, in part due to low-resolution image coverage, are those where valleys dissect the ejecta blankets of pristine and moderately degraded craters. In Figure 4.5, Viking Orbiter images do not clearly resolve whether impact ejecta is found on valley floors, but MOLA profiles across the valleys show very little difference in their depth where the valleys cross the ejecta compared to upstream and downstream from the ejecta [Mest and Crown, 2004a]. It is possible in many of these cases that any ejecta on the valley floor(s) has been removed by subsequent flow events, or redistributed by eolian processes.

Impact craters exhibiting breached rims are also observed, but are not common. One example, found at 20.7°S, 273.1°W (crater 'A' in Figure 4.2), displays a relatively flat interior containing several small impact craters, an inlet valley breaching the western rim and an outlet valley breaching the southeast rim [Mest and Crown, 2004a]. MOLA data show that the mouth of the inlet valley is approximately 200 m wider and 50 m deeper than the head of the outlet

valley (widths = 1100 m and 900 m and depths = 100 m and 50 m, respectively), and the floor of the outlet valley is ~100 m higher in elevation than the floor of the inlet valley. These differences suggest that the inlet valley may have breached this crater first, resulting in ponding of water and deposition of sediments eroded from the surrounding highlands. The smaller outlet valley suggests that its incision probably occurred after the crater was filled with water that overtopped the crater rim and began downcutting. This crater shows no clear evidence (in images or MOLA data) to indicate water level (such as shorelines or benches); therefore, it is also possible that the outlet valley grew headward until it intersected and breached the crater rim. Alternatively, it is possible that a valley in this location existed prior to formation of impact crater 'A' in Figure 4.2. Formation of this crater disrupted flow within this earlier valley, but perhaps flow was significant enough to breach the northwest rim of crater 'A' to form the present "inlet" valley. The fluvial evolution of crater 'A' could have then followed the scenario described above, and formation of the "outlet" valley would have either followed pre-impact drainage or developed in a new location.

The relationships mentioned above suggest that most fluvial activity in the study area occurred prior to or soon after the majority of large impact craters formed. The eroded rims and ejecta blankets of many craters provide evidence for fluvial erosion post-dating their formation. These relationships, combined with crater size-frequency distributions for valley floor material [Mest and Crown, 2004a], indicates that most valley formation in this part of the highlands is relatively old, with most fluvial activity ceasing in the Late Noachian Epoch to Early Hesperian Epoch. Similarly, Maxwell and Craddock [1995] showed in Mare Tyrrhenum (15°-30°, 260°-270°W) that dissected highlands and intercrater plains were found to be Middle to Late Noachian and Late Noachian to Early Hesperian in age, respectively; and valley formation occurred in the Late Noachian Epoch to Early Hesperian Epoch.

In terms of the hydrologic modeling discussed below, knowledge of the relationships described above is necessary to accurately interpret the model results. If most impact craters in the area formed prior to fluvial activity and valley incision, then the craters would create local topography that would control subsequent surface flow. In this scenario, the current observed decameter-scale topography (i.e., at the scale of 10-km-diameter craters and larger) closely represents the surface prior to most fluvial incision. Valleys delineated using the model described below should accurately follow the topography, as water would have on the post-impacted

martian surface, and correlate well with valleys observed in the image data sets. If most impact craters in the area formed after fluvial activity and valley incision, then the pre-impact surface in which most valleys were incised was significantly different than what is currently observed. Modeled valleys would follow the topography created by the craters and would correlate with observed valleys only in areas where the effect of impact-generated topography was minimal. If impact cratering and valley incision were largely contemporaneous or significant numbers of craters both pre- and post-dated fluvial activity, then fluvial systems would be more difficult to reconstruct [Irwin and Craddock, 2001; Irwin and Howard, 2001, 2002; Irwin and Maxwell, 2003; Irwin et al., 2002a,b]. If clear temporal relationships between impact craters and fluvial valleys can be assessed from photogeologic analyses, it is therefore also possible to evaluate the topographic effects of impacts that post-date fluvial activity and reconstruct the pre-impact topography.

4.6 METHODOLOGY

Hydrologic mapping (described in previous sections) and modeling of valley networks in the Tyrrhena Terra region of Mars are being used in an attempt to derive the hydrologic history of this part of the martian highlands. This section first provides a general description of the image and topographic data sets used in this study and their usage within the Arc/Info Geographical Information System. The hydrologic modeling technique, specifically the Arc/Info GRID functions, is then described in detail. In order to evaluate the robustness of the model, several different DEM resolutions and sink-fill depths (described below) were tested and their results were compared. The results of these evaluations are shown.

4.6.1 Data sets

Viking Orbiter (10-90 m/pixel), THEMIS infrared (day) and visible (~100 and 20 m/pixel, respectively) and MOC narrow angle (1-8 m/pixel) and wide angle (~237 m/pixel) images were used to identify valleys and produce a detailed hydrologic map of the Tyrrhena Terra study area on a Mars Mosaiked Digital Image Model (MDIM) version 2.0 base (231 m/pixel) in Adobe Illustrator (v. 9.1). The high-resolution data sets now available for this region have allowed significantly more tributaries to be identified than in previous studies [e.g., Carr and Chuang, 1997]. The valley map and MDIM base were imported as individual raster files into ESRI Arc/Info (v. 8.1.2) software and converted to an arc coverage and GRID, respectively. A high-resolution MOLA DEM (128 pixel/degree) of the study area, generated from MOLA gridded topographic data, was also imported into Arc/Info in ascii format and converted to an Arc/Info GRID. The MDIM, mapped valley and DEM data layers were projected into a sinusoidal coordinate system using Mars1990 (IAU1990) as the martian spheroid, where the semi-major and semi-minor axes equal 3,393,400 m and 3,375,730 m, respectively (this spheroid is used for all subsequent martian data layers) [Trent Hare, personal communication; 'spheroids.dat' file available by downloading 'planetary_projection4_1.zip' from ftp://ftpflag.wr.usgs.gov/dist/pigpen/arcview_extensions/]. Sinusoidal projection was used because it is adequate for small-scale usage and for low- to mid-latitude regions, and it is an equal-area projection, appropriate for calculation of such parameters as drainage basin area [Snyder, 1982].

4.6.2 Hydrologic modeling

Drainage divides and valley networks were modeled using standard techniques that have been successfully used to model terrestrial drainage networks [e.g., O'Callaghan and Mark, 1984; Jenson, 1991; Tarboton et al., 1991; Thieken et al., 1999; Turcotte, et al., 2001; Vogt et al., 2003]. Four Arc/Info GRID functions (FILL, FLOWDIRECTION, WATERSHED AND

FLOWACCUMULATION) were used to derive drainage basin divides and valley networks from a high-resolution MOLA DEM (128 pixel/degree = 0.0078125 degree/pixel) of the Tyrrhena Terra study area. A drainage basin is defined here as the area surrounded by a continuous topographic divide within which all water (surface and subsurface) flows downslope to a point where the water crosses the divide.

The FILL function is used to remove sinks (or pits), generally assumed to be artifacts resulting from DEM generation, in the topographic data set; removal of these anomalous pixels ultimately improves the accuracy of the model results [O'Callaghan and Mark, 1984; Jenson and Domingue, 1988; Fairfield and Leymarie, 1991; Tarboton et al., 1991; Martz and Garbrecht, 1998]. In terms of hydrologic modeling, a sink is a pixel with undefined drainage direction as all pixels surrounding it are higher; thus water might flow into a sink, but would have no point from which to continue flowing downslope. Sinks are filled to a depth called the z-limit, referred to as the 'sink-fill depth' (SFD) in this study, which represents the specified maximum depth of a sink that will be filled. In Arc/Info, all sinks with a depth less than the SFD, relative to their lowest adjacent pixel, which is the pour point, are filled to that pour point pixel. The pour point is the point where water would continue to flow downslope. Conversely, sinks with a depth greater than the SFD, relative to the pour point, will not be filled at all. Table 4.1 shows the percent of sinks filled for ten iterations of the model. Part of the modeling technique has been to determine the appropriate SFD to model drainage basins at a scale adequate to approximate basins identified from mapped valley distributions.

The FLOWDIRECTION function creates a grid of flow direction (or slope grid) from each pixel to its steepest downslope neighbor in a 3x3 pixel neighborhood [O'Callaghan and Mark, 1984; Jenson and Domingue, 1988; Vogt et al., 2003]. This function indicates the direction in which surface water will flow from one pixel to another by calculating the direction of steepest descent from each cell.

The WATERSHED function is used to calculate the locations of watersheds, or more simply delineate drainage divides. Arc/Info uses a complex process based on the sink-fill depth to identify the pixels representing the topographically highest points that will be delineated as part of drainage divides. This function also identifies pour points, which differ slightly from the pour point for the FILL function, in that here pour point refers to the lowest point along the

Table 4.1. Sink data for 15 model runs in Tyrrhena Terra.

Sink-fill depth (meters)	Number of sinks filled*	Percent of sinks filled
0.0	0	0.0
100.0	15,900	95.3
322.7	16,371	98.1
400.0	16,437	98.5
450.0	16,461	98.7
500.0	16,487	98.8
540.0	16,509	98.9
550.0	16,514	99.0
560.0	16,520	99.0
570.0	16,530	99.1
575.0	16,533	99.1
580.0	16534	99.1
600.0	16,539	99.1
639.4	16,553	99.2
960.0	16,633	99.7

*Total number of sinks identified in the Tyrrhena Terra DEM = 16,682.
Note: Tyrrhena Terra DEM (128 pixels/degree) is 2177 rows by 961 columns (2,092,097 pixels).

drainage flow path. In ideal cases the pour point is the drainage mouth but in many instances in this study, pour points are the floors of craters contained within the drainage basin. Identification of pour points allows Arc/Info to determine the set of contributing pixels that occur above the pour point to the drainage divide, thus calculating the contributing area or drainage basin.

Lastly, the FLOWACCUMULATION function is used to calculate an accumulation grid, which is a grid of accumulated flow to each 'downstream' pixel [Jenson and Domingue, 1988; Tarboton et al., 1991; Vogt, et al., 2003]. Accumulated flow is based upon the number of upstream pixels that contribute to each subsequent downstream pixel. Arc/Info accumulates the weight for all pixels in the grid that flow into each downslope cell and in general, pixels with zero flow are determined to be topographic highs and pixels with high accumulation are areas of concentrated flow and are used to determine the locations of stream channels. It is important to note that calculation of the accumulation grid assumes that all water is surface runoff and there is no interception, evaporation or infiltration.

The introduction of the near-global MOLA topographic data set for Mars has enabled other researchers to conduct hydrologic modeling studies similar to the one presented here. Howard [1994] developed one of the first models that simulated erosion and deposition on the martian surface (pre-MOLA) [Howard and Craddock, 1998] to study impact crater degradation. This model incorporated impact cratering of the surface thereby simulating the competition between surface processes and cratering. Despite the lack of accurate topographic data, the simulations of Howard and Craddock [1998] fairly accurately reproduced martian landscapes displaying degraded craters, gullied crater rims, and dissected intercrater terrain. Craddock et al. [2001a,b, 2003] used GIS techniques similar to the current study to extract drainage networks and divides from the MOLA data set and to compare them to mapped valleys between ±30° latitude. Results showed that streams with orders ≤3 were not accurately identified or located, a finding attributed to DEM resolution, but streams with order >3 were more accurately identified. Average drainage densities were found to be 0.193 km^{-1} [Craddock et al., 2001a,b, 2003]. In studies of Terra Cimmeria, Irwin and Craddock [2001], Irwin and Howard [2001, 2002], Irwin and Maxwell [2003], and Irwin et al. [2002a] used a combination of MOLA-derived drainage divides, mapped valleys and geologic analyses to show a complex fluvial history involving competition with impact cratering, breaching of divides, and redirection of flow by large craters. They showed cratering processes overcame valley formation in the Early Noachian Epoch,

preventing networks from developing. By Middle to Late Noachian, cratering had slowed and valley formation dominated; thus, fluvial erosion was able to erode and breach smaller craters and form networks in intercrater areas of the highlands.

Hypsometric properties of martian drainage basins have been characterized with the availability of higher resolution MOLA DEMs. Hypsometric analysis is a valuable geomorphic tool that is used to estimate the degree of erosion within a watershed, or simply the basin's "maturity" [Strahler, 1952]. This is measured with the hypsometric integral or hypsometric index (HI), which is the proportion of the volume of the original basin that remains above a specified elevation [Strahler, 1952; Ritter et al., 1995], and may be used to determine the dominant process of valley formation. Initial hypsometric analyses, conducted by Luo [2001, 2002] in the Margaritifer Sinus region of Mars, showed that hypsometry can be useful to infer processes of valley formation if used in conjunction with other morphometric analyses. Hypsometric indices for Margaritifer Sinus and several other martian terrains were found to span the range typical of terrestrial drainage basins (0.2 to 0.8) [Luo, 2001, 2002; Grant and Fortezzo, 2003a,b; Fortezzo and Grant, 2004] HI<0.5 indicates a runoff dominated drainage, and HI>0.5 indicates a sapping dominated drainage [Luo, 2000, 2002]. The broad range of martian hypsometric indices indicates both runoff and sapping characteristics are evident [Luo, 2001, 2002; Grant and Fortezzo, 2003a,b; Fortezzo and Grant, 2004]. This suggests that more than one fluvial process was likely responsible for valley formation and is consistent with precipitation-recharged groundwater sapping [Luo, 2002].

Although other studies use similar techniques as this study to extract valley networks and drainage divides, few of their results account for the effects of local and regional geology. The results of some studies are based solely on modeling and ignore both the underlying geology as well as the valuable corroborating evidence from image data sets. Simple drainage basin analyses, such as Banerdt and Vidal [2001] and De Hon [2002], used MOLA DEMs to model drainage basins on a global scale. Banerdt and Vidal [2001] identified eight regional basins (Argyre, Cimmeria Terra, Hellas, Isidis, Sirenum Terra, Solis Planum, Utopia and the Northern Plains), whereas De Hon [2002] identified eleven (Aeolis, Amazonis, Argyre, Australe, Borealis, Chryse, Elysium, Hellas, Icaria, Isidis and Solis Planum). Both studies identified basins based on a "pit-filling" technique in which water is continuously introduced to the surface until basin divides are identified essentially by forming a large lake. They also showed that many of these

regional basins could have been interconnected, assuming these regional hypothetical lakes filled to the point of overtopping their divides.

Other studies [Stepinski et al., 2002a,b, 2003; Collier et al., 2003; Stepinski, 2003, Stepinski and Collier, 2003, 2004] have conducted strictly quantitative analyses of valley networks extracted from MOLA DEMs in an attempt to characterize the processes responsible for the "roughening" of the martian surface, as well as valley formation. Stepinski et al. [2002a,b, 2003], Collier et al. [2003] and Stepinski [2003] compared the fractal nature of twenty martian networks with nineteen terrestrial basins and found strong correlations for contributing area and stream length, suggesting rainfall was possible. However, overwhelmingly weak correlations for drainage density and dissipated potential energy, suggesting erosion by sustained and uniformly distributed rainfall was not likely. Their results showed that the observed surface reflects roughening by the competing processes of rainfall-driven erosion and impacts, or that rainfall was minimally important and processes such as sapping or glacial/snow pack melt were the dominant erosional forces. In a continuation of the above studies, Stepinski and Collier [2003, 2004] found drainage densities for twenty-six areas to be 0.06 to 0.22 km^{-1}, comparable to densities calculated in the current and other studies for martian drainage basins (discussed below).

4.6.3 Resolution of MOLA gridded data

During the course of this project, higher resolution MOLA DEMs were used as they were made available from NASA's Planetary Data System and the MOLA team, and the results from these data were incorporated into the project. This has proven to be quite useful as these data provided a valuable tool in gauging the effects of DEM resolution on the hydrologic modeling technique. Comparisons of DEM resolution have been applied in numerous terrestrial hydrologic modeling studies [e.g., Wang and Yin, 1998; Gyasi-Agyei et al., 1995; Kenward et al., 2000] and have shown that DEMs with higher spatial and vertical resolution more accurately determine flowpaths within watersheds. Figure 4.6 shows a comparison of modeled drainage divides and

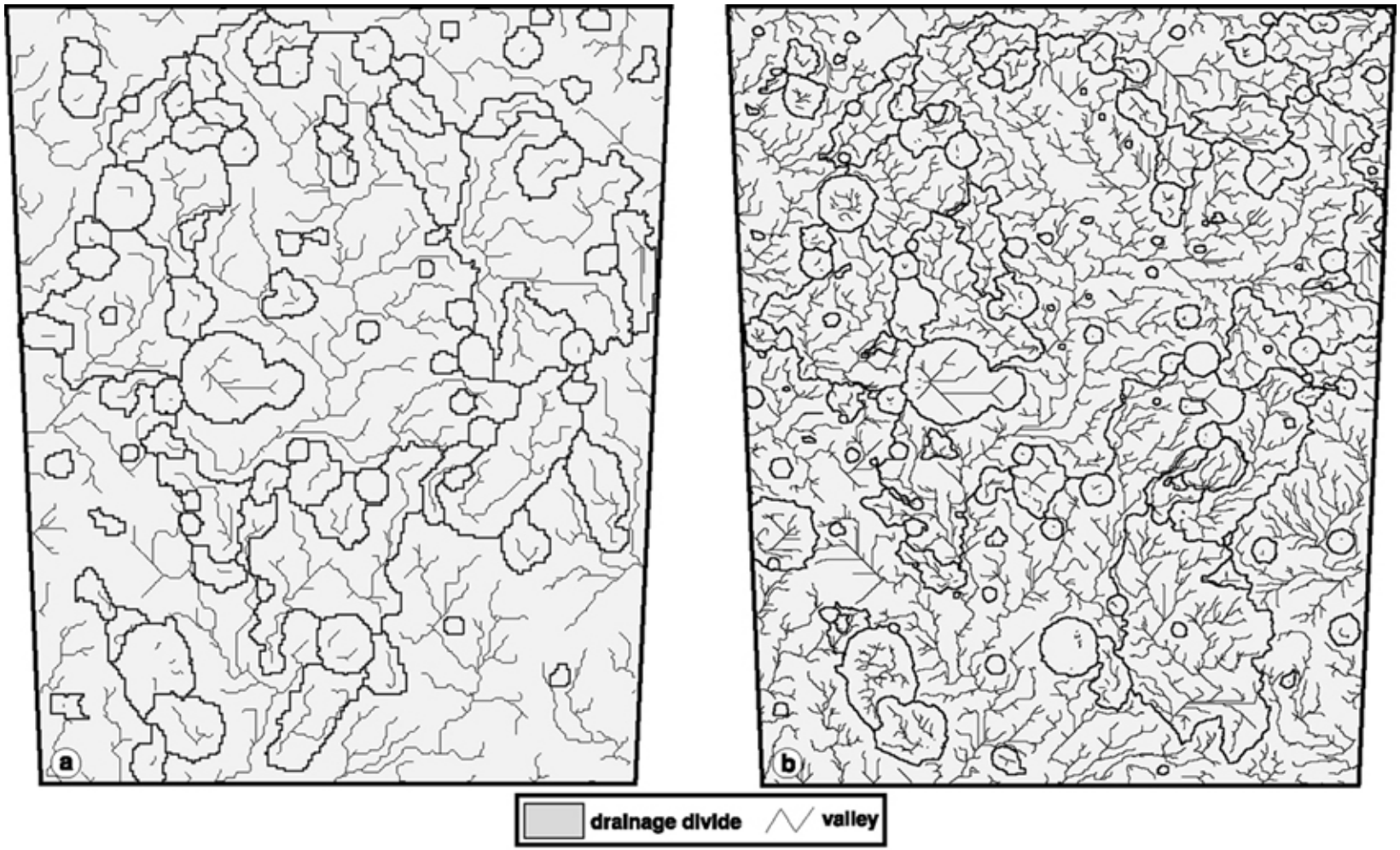

Figure 4.6. Modeled watersheds in Tyrrhena Terra (13°S to 30°S, 265°W to 280°W) demonstrating the effects of MOLA DEM resolution on the numbers of watersheds produced and the amount of detail mapped for each network. Here watersheds were modeled at a sink-fill depth of 20 meters for 16 and 128 pixels/degree MOLA DEMs [Mest et al., 2001]. The higher resolution DEM delineates more drainage divides per the same area and valley networks display more tributaries.

valley networks using a sink-fill depth of 575 m (see 'Comparison of sink-fill depth') for the 16 and 128 pixels/degree (3.7 km/pixel and 460 m/pixel, respectively) MOLA DEMs. Both DEMs have a vertical resolution of ~10 m [Smith et al., 2001]. Given these spatial and vertical resolutions, both datasets would be expected to most accurately predict features greater than 10 meters deep, and greater than 4 km and half a kilometer wide, respectively. The FILL, FLOWDIRECTION, WATERSHED and FLOWACCUMULATION GRID functions were applied to each DEM to determine slope, aspect, flow direction, watershed and flow accumulation grids. The resulting watershed grids delineated 91 and 151 drainage basins for the 16 and 128 pixels/degree DEMs, respectively. Table 4.2 provides statistics for these two model runs. This comparison clearly shows that DEM resolution makes a significant difference in the accuracy of modeling drainage basin size and networks representative of those observed in image data sets. In general, as the spatial resolution of the DEM improves, the ability of the model to accurately delineate watersheds also improves. The coarseness of the 16 pixels/degree (3.7 km/pixel) DEM reduces the ability of lower order valleys to be extracted. The affects of resolution are further compounded by the number of MOLA data tracks used to make a DEM versus the degree of interpolation required between the tracks; interpolation of topography between tracks results in a "smoother" surface. For example, the 128 pixels/degree DEM contains more data tracks than the 16 pixels/degree DEM and requires less interpolation between tracks, and therefore provides a more accurate and detailed representation of the surface topography. As shown in Figure 4.6 and Table 4.2, the 16 pixels/degree data set delineates fewer basins than the 128 pixels/degree, but most of the larger basins share, at least in part, the same divides and most of the differences arise in identification of smaller-scale basins, such as craters. Similarly, the amount of dissection shown in Figure 4.6 is significantly different between the 16 and 128 pixels/degree data sets; the larger trunk valleys are identified reasonably well between the two data sets. However, smoother topography in the 16 pixels/degree DEM results in delineation of fewer small-scale tributaries and lengths between tributaries (link lengths) are greater (Table 4.2). This shows that although lower-resolution data sets could be used to delineate larger-scale drainage divides and high-order valleys with reasonable accuracy, the coarseness of the topography plus the excessive interpolation between MOLA tracks results in omission of many small-scale basins and low-order tributaries.

Table 4.2. Comparative area and length statistics for 16 and 128 pixels/degree MOLA DEMs in Tyrrhena Terra.*

		16 pixels/degree DEM	128 pixels/degree DEM
Number of basins		91	151
Area (km^2):	maximum	137,008.8	177,557.1
	minimum	12.8	0.80
	mean	5318.6	3181.9
	total	483,992.3	480,464.7
Number of links		323	3,632
Link Length (km):	maximum	224.9	104.1
	minimum	3.6	0.5
	mean	37.3	14.1
	total	12,036.7	51,015.1

*Sink-fill depth = 575 m used for both DEM resolutions.

4.6.4 Comparison of sink-fill depth:

One of the most critical aspects in the modeling was to determine the sink-fill depth (SFD) that generated drainage divides containing the networks observed in image data sets and produced stream systems that approximated the positions of individual valleys and the scales of the networks observed. Another way of testing the robustness of the model was to run the model for several SFDs. Given any MOLA-derived DEM, the SINK function was run on the data set to identify sinks, and a histogram was produced to observe the distribution of sinks versus sink-fill depth. A standard procedure was used for the first few iterations of the model and includes running the FILL function for SFDs equal to 0 (zero) m, the mean sink depth, and ± one-half the mean. For the 128 pixels/degree MOLA DEM, SFDs used for the first iterations of the model were equal to 0.0 m, 639.4 m, 322 m and 960 m, respectively. The resulting watershed and network GRIDs were overlain on the network map compiled from Viking Orbiter, THEMIS, and MOC images to compare the accuracy of the modeled watersheds. Two criteria were used to determine which model iteration(s) most closely approximated the mapped networks: (1) do the number of drainage basins equal the number of mapped networks and do the drainage divides enclose the mapped networks, and (2) are the locations and numbers of the modeled valleys roughly equivalent to the mapped valleys. Analyses of these criteria for the 128 pixels/degree (and previous) MOLA DEMs determined whether additional iterations should be run. For the 128 pixels/degree DEM, the mapped networks most closely matched the 322-m and mean SFDs. To further improve accuracy, this study used an iterative procedure of running the model for several additional sink-fill depths, shown in Table 4.1. These results for each of these runs were compared to the mapped networks as described above. It was observed that the 575-m SFD generated drainage divides that adequately enclosed mapped networks, and extracted networks most accurately approximated both the positions of mapped valleys and the scales of mapped networks. This iteration (SFD = 575 m) was selected to characterize the morphometric parameters of the watersheds of interest.

As an additional test of accuracy, iterations using SFDs of 540, 560, 570 and 580 m were conducted and their results are shown in Tables 4.1 and 4.2. For watersheds of the scale observed in Tyrrhena Terra and the resolution of the MOLA DEM (128 pixels/degree), the results are

shown to be more sensitive to large changes in SFD (> 10 m; e.g., SFD = 570 m versus 600 m). Small-scale SFD adjustments (< 10 m; e.g., SFD = 570 m versus 575 m versus 580 m) do not significantly change the numbers of drainage basins and the positions of drainage divides, and the locations of modeled valleys remain relatively unchanged. Tables 4.3a and 4.3b show some of the areal and length data, respectively, derived from modeling for fourteen iterations with sink-fill depths ranging from 0 to 960 m, and Table 4.1 shows the percent of sinks filled in the Tyrrhena Terra MOLA data set. Figure 4.7 shows differences in the numbers and sizes of drainage basins identified in the Tyrrhena Terra study area and the lengths and morphology of networks calculated by the model. This test shows that increasing the sink-fill depth will yield fewer drainage basins (basins are merged) with larger areas (Tables 4.3a and b; Figure 4.7). Link lengths (the distances between valley junctions) increase, but the number of exterior links decreases as watersheds are combined and networks are delineated to fill the watersheds; the modeling technique more effectively uses the topography of the DEM to delineate valleys and despite the increase in link length, drainage density decreases.

Terrestrial drainage basins are generally delineated by divides that include ridges formed tectonically, volcanically, or by continued erosion. However, on Mars there is an abundance of impact craters that although they make effective divides by collecting and distributing water and sediment to crater floors, they also tend to disrupt drainage patterns, as noted earlier, or they form drainage basins within drainage basins. Previous researchers have used various techniques to identify martian drainage divides, including stereo pairs [Boothroyd and Grant, 1985; Grant, 2000] and the most headward extension of tributaries [Kochel et al., 1985; Baker and Partridge, 1986]. Figure 4.7 shows many of the modeled drainage divides for both sink-fill depths correspond to the locations of impact craters, which further demonstrated the need for correction of the associated single pixel sink anomalies. Ideally a sink-fill depth was chosen that not only approximated the locations of mapped networks, but also effectively eliminated drainage divides delineated by the rims of single or nested impact craters.

Table 4.3a. Drainage basin area and length statistics for 15 model runs in Tyrrhena Terra.

SFD (m)	Number of Basins[2]	Min Area[3] (km^2)	Max Area[4] (km^2)	Mean Area[5] (km^2)	Total Area[6] (km^2)	Total Stream Length[7] (km)	D_d[8] (km^{-1})
0.0	17737	0.20	1251.4	46.2	819701.7	363497.5	0.444
100.0	803	0.40	16397.9	831.8	667965.9	100669.2	0.151
322.7	319	0.40	90097.6	1812.9	578311.9	72406.0	0.125
400.0	251	0.40	128382.0	2139.3	536950.8	60900.3	0.113
450.0	227	0.40	131074.9	2352.4	533988.2	60919.6	0.114
500.0	200	0.40	146558.4	2598.3	519652.9	56487.3	0.109
540.0	177	0.40	152195.7	2885.5	510681.3	56711.9	0.111
550.0	171	0.80	152242.8	2906.2	496952.8	55376.9	0.111
560.0	165	0.80	170065.5	3007.5	496236.7	53573.6	0.108
570.0	155	0.80	170364.5	3099.8	480464.7	53230.2	0.111
575.0	151	0.80	177557.1	3181.9	480464.7	51015.1	0.106
580.0	150	0.80	177557.1	3203.1	480464.7	52250.0	0.109
600.0	145	0.80	180896.5	3300.4	478563.2	49667.5	0.104
639.0	130	0.80	215158.8	3339.1	434078.3	48347.2	0.111
960.0	50	0.80	17944.0	2210.6	110531.2	40343.0	0.365

[1]SFD = sink-fill depth
[2]Number of Basins = total number of drainage basins delineated by the model.
[3]Min Area = area of smallest basin delineated by the model.
[4]Max Area = area of largest basin delineated by the model.
[5]Mean Area = average basin area calculated from the Total Area / Number of Basins.
[6]Total Area = sum of the areas of all basin delineated by the model.
[7]Total Stream Length = sum of the lengths of all streams delineated by the model; only streams enclosed within a drainage basin are summed.
[8]D_d (drainage density) = Total Stream length (km) / Total Area (km^2).

Table 4.3b. Stream link length statistics for 15 model runs in Tyrrhena Terra.

SFD[1] (m)	Number of Links[2]	Min Length[3] (km)	Max Length[4] (km)	Mean Length[5] (km)	Total length[6] (km)
0.0	138791	0.45	33.85	2.52	363497.46
100.0	14294	0.45	59.00	7.04	100669.22
322.7	7287	0.45	93.23	9.94	72406.02
400.0	5169	0.45	93.23	11.78	60900.25
450.0	5135	0.45	93.23	11.86	60919.63
500.0	4491	0.45	92.60	12.58	56487.29
540.0	4478	0.45	92.60	12.66	56711.93
550.0	4278	0.45	104.12	12.94	55376.89
560.0	4006	0.45	104.12	13.37	53573.63
570.0	3949	0.45	104.12	13.48	53230.22
575.0	3632	0.45	104.12	14.05	51015.14
580.0	3785	0.45	104.12	13.80	52249.95
600.0	3440	0.45	104.12	14.44	49667.51
639.0	3250	0.45	104.12	14.88	48347.16
960.0	2200	0.45	109.09	18.34	40343.00

[1]SFD = sink-fill depth
[2]Number of Links = total number of valley segments delineated by the model in all of the drainage basins; links are unbroken valley segments between successive nodes (sources, junctions or outlets) [Knighton, 1998].
[3]Min Length = length of smallest link delineated by the model.
[4]Max Length = length of longest link delineated by the model.
[5]Mean Length = average link length calculated from the Total Length / Number of Links.
[6]Total Length = sum of the lengths of all streams delineated by the model; only streams enclosed within a drainage basin are summed.

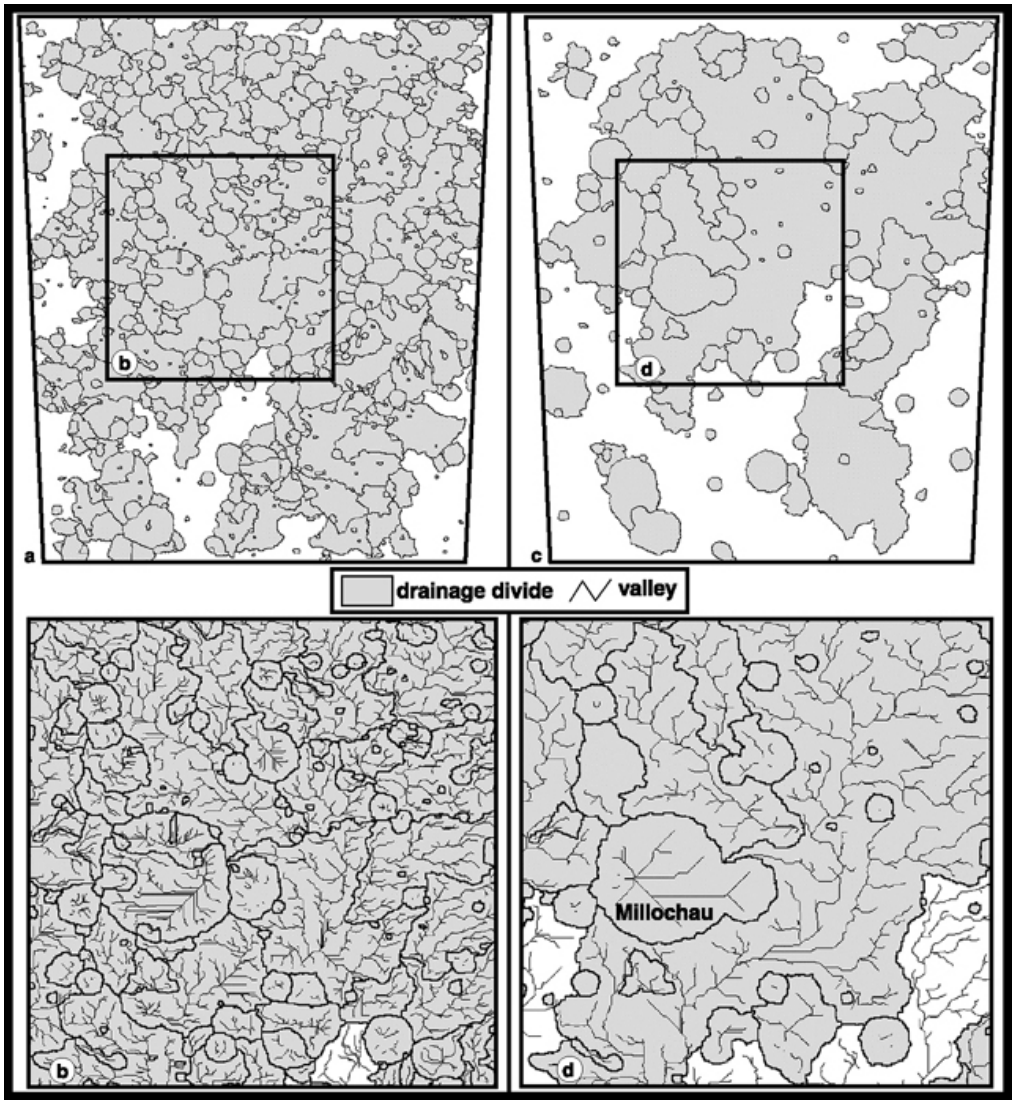

Figure 4.7. Modeled watersheds in the Tyrrhena Terra study area demonstrating the effects of different sink-fill depths on the numbers of watersheds produced and the amount of detail mapped for each network. Here watersheds are modeled for sink-fill depths of 100 m (a and b) and 575 m (c and d). In general, the larger sink-fill depth yields fewer, but less detailed, watersheds; 784 and 151 basins generated for SFD = 100 and 575 m, respectively. In the regional views (a and c), significant watersheds are observed that correlate with impact craters that denote sinks; as watersheds are modeled at higher sink-fill depths, more of these impact-crater-watersheds are eliminated and incorporated into larger systems. In close up view b, many of the larger craters, such as crater Millochau, are subdivided into multiple watersheds that contain intricate, though nonexistent, networks. It is important to note that these networks do not reflect the numerous gullies incised within the interior walls of many craters in this region, but miscellaneous topographic features (scarps, ridges, unit contacts, etc.) that Arc/Info misidentifies as valleys. At higher sink-fill depths, these subdivisions are removed as expected, but unobserved networks remain in some craters.

4.7 RESULTS

The following results are based on (a) valley networks mapped from Viking Orbiter, THEMIS and MOC images and (b) basin divides and networks modeled using a SFD = 575 m, which, as discussed above, is deemed the optimal model run. After analysis of zonal elevation statistics associated with single pixel sinks, which identified 0.79 percent of the DEM points as having undefined surface water flow directions (Table 4.1), sinks with depths of 575 meters or less were filled. The sink filling correction applied to the 128 pixels/degree MOLA DEM, which identified ~0.8 percent (16,682 pixels) of the total pixels in this scene (~2 million pixels), is comparable to corrections made to terrestrial DEMs that contain 0.9 percent to 4.7 percent of cells that are sinks [Tarboton et al., 1991]. Modeling at SFD = 575 m yielded 151 drainage basins and several modeled networks with no associated divides that extend beyond the limits of the study area (Figure 4.8a). Image analysis shows that drainage divides consist of combinations of impact crater rims, ridges associated with upland terrains, and degraded, discontinuous craters. Of the 151 basins identified, 119 correspond to impact craters (79%), of which 111 are single craters (93%) and 8 are clusters of two or more craters (7%). Of the 119 crater basins, 58 of these (49%) correspond to impact craters (single and clusters) that postdate fluvial activity in Tyrrhena Terra (56 are single craters and 2 correspond to clusters (1 doublet and 1 triplet cluster), of which only one crater in each cluster postdates fluvial activity). Surface materials in drainage basins in Tyrrhena Terra are believed to be laterally and vertically variable [Mest and Crown, 2001a]. This variability occurs on both a regional scale and within individual basins, and would likely affect the permeability and erodibility of these surface materials.

Mapped and modeled networks were rigorously compared to test the validity of the hydrologic modeling technique. The results discussed here focus on 13 basins (Figure 4.9a) and their associated networks that adequately encompass the mapped networks shown in Figure 4.9b. Morphometric parameters, listed in Table 4.4, were calculated for both mapped and modeled networks. These parameters are valuable in geomorphic analysis and classification of terrestrial terrestrial drainage basins, and have been used to relate the measureable properties of a drainage

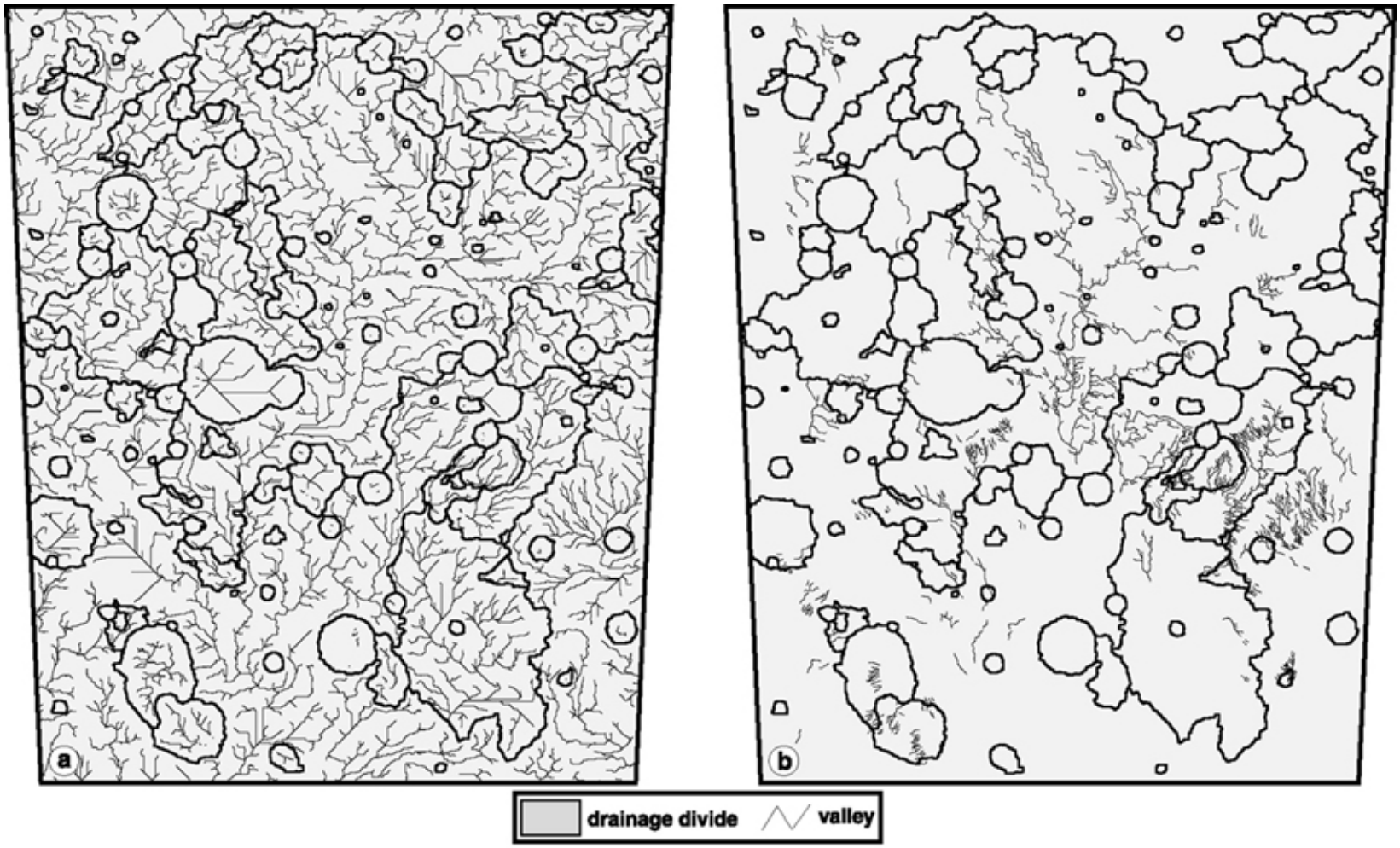

Figure 4.8. Regional view and comparison of modeled (a; SFD = 575 m) and mapped (b) watersheds. At this sink-fill depth, watersheds are modeled such that drainage divides do not extend to the edge of the study area, but only completely enclosed drainage basins are displayed. However, networks are modeled so that they are able to extend beyond the study area boundary. In this comparison, the model produces significantly more networks, especially in the unbound parts of the study area, than are mapped from Viking Orbiter, MOC and THEMIS images.

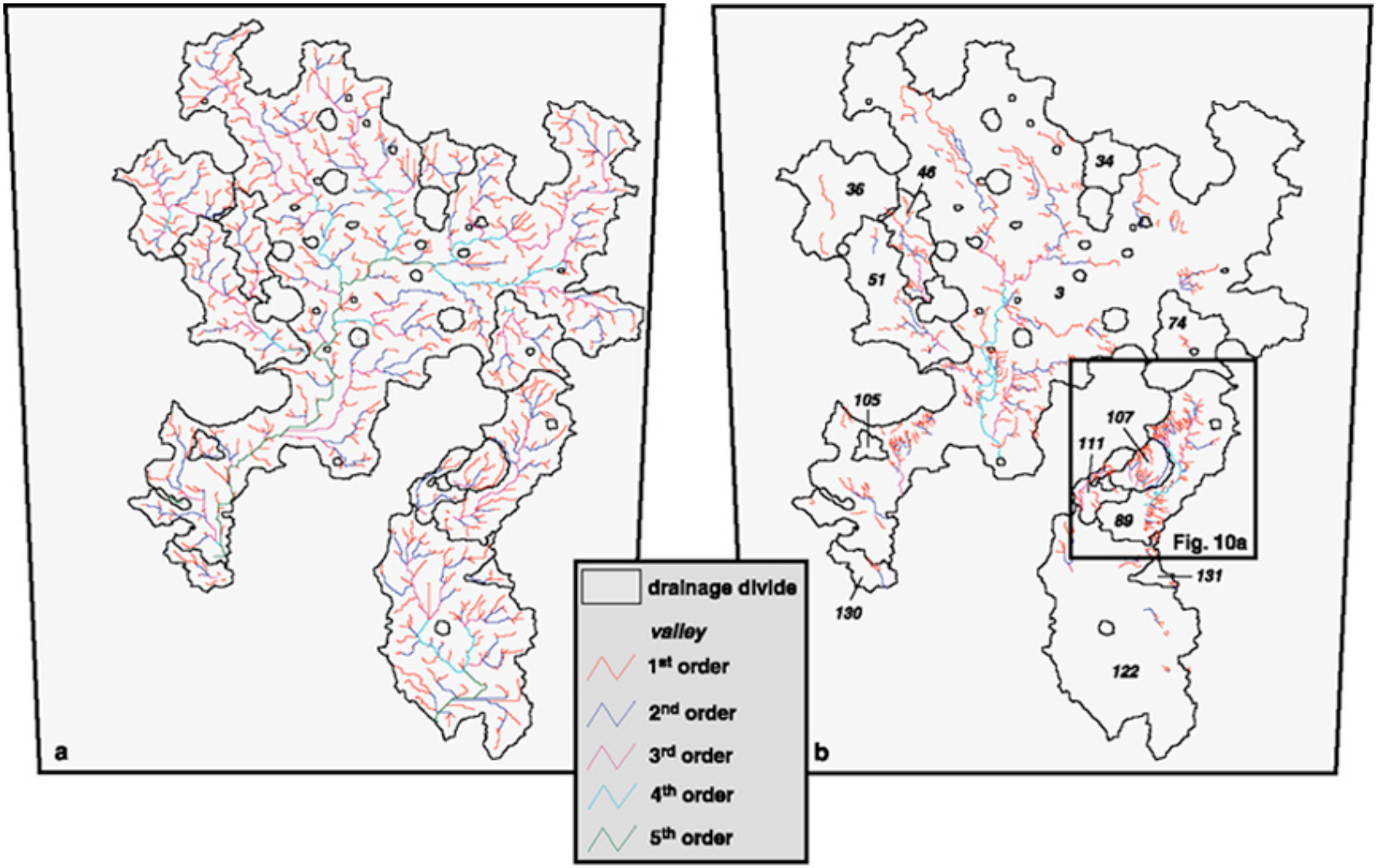

Figure 4.9. Comparison of modeled (a) and mapped (b) watersheds for thirteen drainage basins (labeled) that are believed to compose the Vichada Valles system; drainage basins within and amongst the thirteen are shown for reference, but are not labeled (see Appendix A). Drainage basins display a range of sizes and shapes, including circular (#107), elongate (e.g., #'s 46, 51 and 89) and irregular (#3). Networks are shown as a function of Strahler stream order. One of the most significant differences between the modeled and mapped networks is the model produced two networks of order 5 (#'s 3 and 122), whereas the highest order determined for mapped networks is 4th order (#'s 3 and 89). The location of Figure 4.10a is shown.

Table 4.4. Hydrologic morphometric parameters used in this study.

Parameter	Units	Symbol	Relationship	Reference
Stream order		*u*		Strahler, 1952, 1954
Number of streams of order *u*		N_u		Strahler, 1952, 1954
Stream length	km	L		
Bifurcation ratio		R_b	N_u / N_{u+1}	Horton, 1945 Strahler, 1952, 1954 Ritter et al., 1995
Length ratio		R_L	Avg L_u / Avg L_{u+1}	Horton, 1945 Ritter et al., 1995
Drainage basin area	km^2	A		
Drainage density	km^{-1}	D_d	$\Sigma L / A$	Horton, 1945
Maximum basin relief	m	H	max basin elevation - min basin elevation	Strahler, 1952 Schumm, 1956
Basin length	km	L_b		
Relief ratio		R_h	H / L_b	Schumm, 1956
Ruggedness Number		R	$H * D_d$	Melton, 1957 Strahler, 1958, 1964

basin to geology and streamflow patterns [Horton, 1932, 1945; Strahler, 1957, 1958, 1964; Gregory and Walling, 1973; Baker and Partridge, 1986], as well as climate and precipitation patterns [Gregory, 1976; Gyasi-Agyei et al., 1995; Ritter et al., 1995; Vogt et al., 2003].

4.7.1 Comparison of mapped and modeled watersheds

Visual inspection of mapped and modeled watersheds for the 13 selected basins shows an overall good match for the locations of valley networks, but an overall poor match for the amount of dissection produced by the model and the drainage density (discussed below). Regional differences between mapped and modeled networks can be seen in Figures 4.8 and 4.9, and some sample areas of disagreement are shown in Figure 4.10a for basin #89. Higher order (third to fifth order) modeled valleys are good approximations of the equivalent mapped valleys in terms of both the numbers and locations of valleys, but the numbers and locations of modeled valleys are less accurately predicted for lower order valleys (first and second order). For example, basin #89 (Figure 10a) shows third and fourth order mapped valleys correspond rather well with second and third order modeled valleys that occur on the relatively lowest slopes (0.2-0.4°) within this basin. However, first order modeled valleys in basin #89 rarely have a corresponding mapped valley, which tend to occur on the steeper slopes in the basin, and are not predicted to have the same density as the mapped valleys. In addition, the coarseness of the MOLA DEM could also have an affect on delineation of the more closely spaced parallel valleys observed on the steeper slopes of basin #89. The spatial resolution of the MOLA DEM (~460 m/pixel) is apparently not able to delineate systems of valley that here have spacings of roughly 10's of meters. In all 13 basins, lithology and unit age appears to play a minor role in discrepancies between mapped and modeled networks. The most obvious lithologic differences in the study area are between the plains material and impact crater ejecta. Mapped and modeled valleys appear to dissect the older craters equally well, however modeled valleys also dissect the fresh ejecta blankets of all of the young craters where mapped valleys are rarely observed. This observation suggests that during the peak of fluvial activity, both plains and ejecta materials

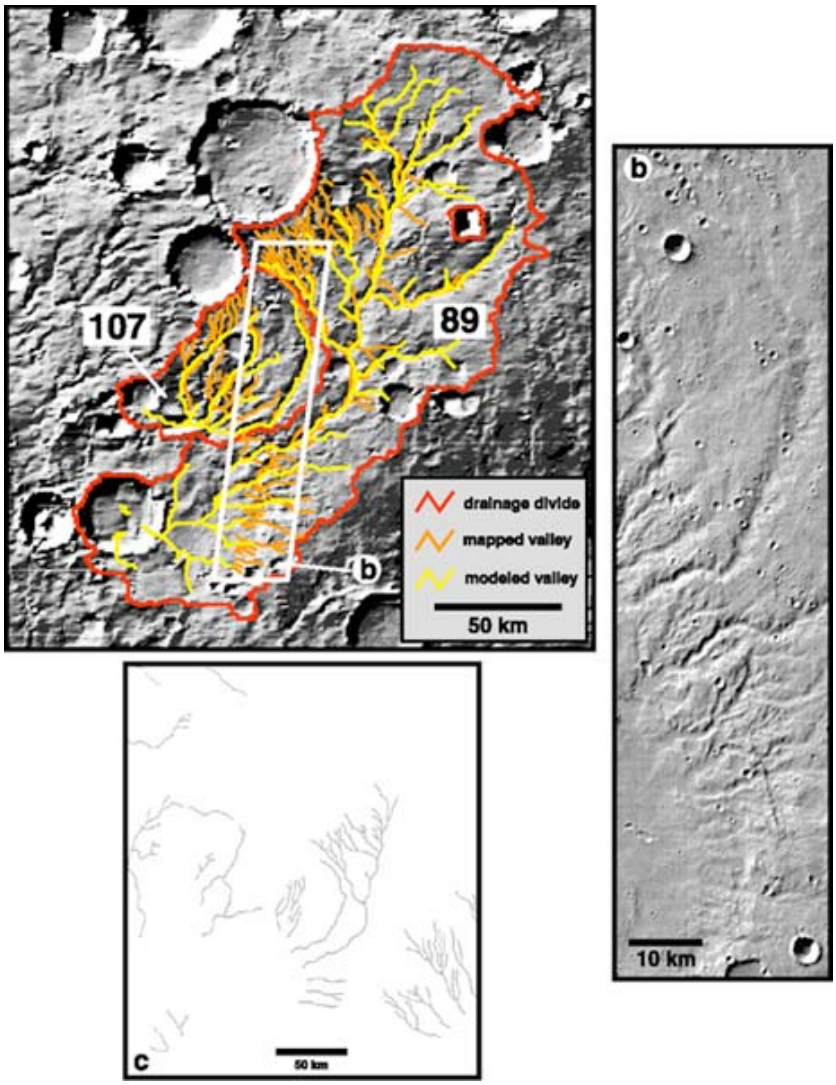

Figure 4.10. (a) Modeled drainage basins #89 and #107 and associated modeled and mapped networks; MOLA shaded relief base (centered at 23.0°S, 268.2°W; illumination angle = 40°, azimuth = 30°). The positions of most mapped and modeled trunk valleys in basin #89 are in agreement, as are most of the next lower order tributaries. The model does not identify most of first- and second-order mapped tributaries in both basins. Numerous first-order valleys in basin #89 are incised along the rim of a degraded and filled impact crater, and terminate on the floor of this crater; these are seen in THEMIS daytime infrared image I03680002 (b) (image width ~31 km; resolution ~99 m/pixel; illumination from upper left). The trunk valley in basin #89 continues across the floor of the degraded crater, joining with several tributaries, and terminating on the floor of an ~32-km-diameter crater. No valleys are visible on the floor of the degraded crater and the 32-km-diameter crater displays no visible breach in its rim as the model suggests. (c) shows a map of valley networks produced by Carr and Chuang [1997] (location shown in Figure 4.1; centered at 22.5°S, 268.5°W) at 1:2 M from Viking Orbiter image analysis. The branching network in the center of (c) corresponds to basin #89 in the current study.

appear to have been dissected equally and the physical characteristics (permeabiltity, porosity, etc.) of both materials were not different enough to cause variations in dissection.

The FLOWDIRECTION and FLOWACCUMULATION functions in Arc/Info, and other hydrologic modeling algorithms (e.g. RiverTools distributed by IDL), inherently attempt to place valleys everywhere where the topography is sufficient to concentrate flow. For terrestrial modeling, of typically precipitation-dominated systems, this is less of a problem because a fluvial valley is most likely present. However, given the coarse nature of the MOLA DEM, the presence of a variety of geologic and geomorphic features that can be misidentified by Arc/Info for fluvial valleys (graben, crater and pit chains, coalescing ejecta blankets and debris aprons), and the likelihood that a martian climate did not permit valley-forming processes to persist long enough to effectively erode all parts of the highlands, comparisons of the mapped and modeled networks are necessary and may shed light on the nature of the network-forming processes. Unfortunately, high-resolution image data is not consistent across Mars and unless various spacecraft parameters are ideal (sun angle, etc.) visual inspection of images does not always reliably identify all valleys. For this study despite some obvious differences between the mapped and modeled data sets, all modeled valleys were retained and the following morphometric parameters used to characterize watersheds were calculated based on these data.

As mentioned previously, impact craters are the dominant local topographic features in Tyrrhena Terra. In order to better constrain temporal relationships between impact cratering and fluvial activity within the 13 identified drainage basins, the basins were categorized according to the relative amount of pre- and post-fluvial activity cratering that appear to have affected each basin. Quantifying the degree of impact cratering that occurred prior to and subsequent to most of the fluvial activity in a basin can be used to evaluate the degree of topographic change within a basin relative to the fluvial activity. For example, a significant amount of impact cratering following the main period of fluvial activity within any particular basin would produce topographic changes unaffected by fluvial erosion, but could yield vastly different results from hydrologic modeling than the pre-impacted surface. In order to assess the relative affect pre- and post-fluvial impact craters have on topography and network development, crater size must be considered. Impact craters identified within the 13 basins are grouped into D>3 and D>10 km bins (Table 4.5), and only include craters whose rims are confined entirely within the drainage

Table 4.5. Distribution of impact craters* within 13 Tyrrhena Terra watersheds.

Basin	Pre-fluvial craters (PrFC)		Post-fluvial craters (PoFC)		Total craters (PrFC + PoFC)		% PrFC		% PoFC	
ID	D > 3 km	D > 10 km	D > 3 km	D > 10 km	D > 3 km	D > 10 km	D > 3 km	D > 10 km	D > 3 km	D > 10 km
3	56	30	46	4	102	34	55	88	45	12
34	1	0	1	0	2	0	50	0	50	0
36	6	1	4	0	10	1	60	0	40	0
46	1	0	1	0	2	0	50	0	50	0
51	1	0	6	0	7	0	14	0	86	0
74	2	1	4	0	6	1	33	100	67	0
89	7	2	3	1	10	3	70	67	30	33
105	0	0	0	0	0	0	0	0	0	0
107	2	1	1	0	3	1	67	100	33	0
111	0	0	2	0	2	0	0	0	100	0
122	8	3	8	1	16	4	50	75	50	25
130	0	0	1	0	1	0	0	0	100	0
131	1	0	0	0	1	0	100	0	0	0

*Includes craters whose impact structure is enclosed entirely within a drainage divide **and** does not form part of the drainage divide.

divides and do not form any parts of the divides. Craters whose rims form part of the drainage divide were not selected because their topographic signatures have already been recognized by the model and will affect the locations of delineated valleys. In addition, the topographic affects of craters with D<3 km, are believed to be insignificant. These small-diameter craters would generally not hinder valley development, but valleys could easily adjust their pathways around them. Also, Hartmann [1971] showed craters on Mars with diameters less than ~3 km could be removed from the geologic record rather quickly, over a period of 0.2 to 0.4 million years by burial and erosion, an order of magnitude less than larger craters, which are more persistent and could thus influence valley development more significantly.

Table 4.5 shows the number and relative percentages of pre- and post-fluvial craters (PrFC and PoFC, respectively) greater than 3 and 10 km in diameter determined for each of the 13 basins. For craters with D>3 km, five of the 13 basins contain more pre-fluvial craters than post-fluvial craters, four of the 13 basins show the opposite relationship, and three basins show equivalent numbers of pre- and post-fluvial craters. However, the >10-km-diameter data shows five basins (five) contain overwhelmingly more pre-fluvial craters than post-fluvial craters. From Table 4.5, basins 34, 46, 51, 111, 130 and 131 contain no pre- or post-fluvial craters larger than 10 km in diameter. It can be stated that the topography of these basins is dominated by craters between 3 and 10 km. For basin #74, Table 4.5 shows that the basin contains 3 PrFCs and 4 PoFCs, most of which are less than 10 km in diameter. If we assume the topographic effects of these <10-km-diameter craters is negligible, then the topography of basin #74 would have been dominated by one pre-fluvial crater larger than 10 km in diameter. With the exception of basins 105 and 131, the basins 3, 34, 36, 46, 89, 107 and 122 show equivalent or less modification by post-fluvial craters. Finally, only basins 3, 89 and 122 contain craters larger than 10 km in diameter (4, 1 and 1 craters, respectively), suggesting only these basins have topography that has been significantly modified by post-fluvial impact craters, which would affect the results of the Arc/Info model. In the following data tables (Tables 4.6 and 4.7) basins 3, 89 and 122 are separated from the other basins (by a double line) to show differences between the morphometric properties of these basins and the other 10 basins. However, it can be seen that the morphometric statistics of basins 3, 89 and 122 do not differ from other basins in which pre-fluvial craters dominate the topography.

All of the mapped valleys in basin #89 clearly postdate the surface materials in which they occur (Figure 4.10a), that is none of the valleys appear to be mantled by impact ejecta or other deposits, and all of the larger craters (D > 10 km) found within basin #89 and those that form portions of the drainage divide clearly postdate valley formation. Conversely, in basin #3 (Figure 4.9), many of the modeled valleys do not reflect observed cross-cutting relationships with craters, but rather Arc/Info uses the topography to predict non-existent valleys in order to "avoid" topographic obstructions. For example, the fourth order mapped trunk valley of Vichada Valles in basin #3 is clearly truncated by a cluster of at least 16 large (D > 10 km) fresh, moderately and highly degraded craters (Figures 4.1 and 4.11). From the above analysis of basin categorization by pre- and post-fluvial craters, there are seven craters (A, D, G, J, K, P and O in Figure 4.11) that appear to be post-fluvial in age. Given the location and orientation of Vichada Valles at the point of its truncation, only craters J (D~8 km), K (D~36 km) and possibly P (D~24 km) were most likely involved in its truncation. The path that Vichada Valles took beyond the truncation point prior to emplacement of craters J, K and P is unclear. Although no distinct valleys remain to provide evidence for a southern extension of Vichada Valles, due to destruction and (or) burial by craters J, K, P and crater Isil (south of Figure 4.11), as well as widespread eolian deposits identified by Mest and Crown [2001a], several subtle scarp-bounded troughs have been identified within the ejecta of crater K [Mest and Crown, 2004a]. Furthermore, the model has accurately predicted valleys within these troughs (Figure 4.11). However it should be noted that prediction of other valleys within the ejecta of craters J, K, P and Isil are likely to be inaccurate due to the post-fluvial emplacement of these craters and the significant topographic changes these craters made on the post-fluvial surface in this part of the study area. The valley predicted by the model does not reflect this cross-cutting relationship, rather the model continues the trunk valley around the western margin of the cluster of craters, and delineates valleys within the ejecta of some of the craters that clearly postdate fluvial activity in this area. Not only do the image datasets show no evidence for diversion of Vichada Valles, but there also is no evidence for ponding of water north of these craters, suggesting fluvial activity for the most part had ceased in this part of Tyrrhena Terra, even prior to formation of craters J, K and P in Figure 4.11. Crater O, along the eastern edge of Figure 4.11, appears to have truncated the mapped valleys in basin #111, and the modeled valleys terminate on the floor of

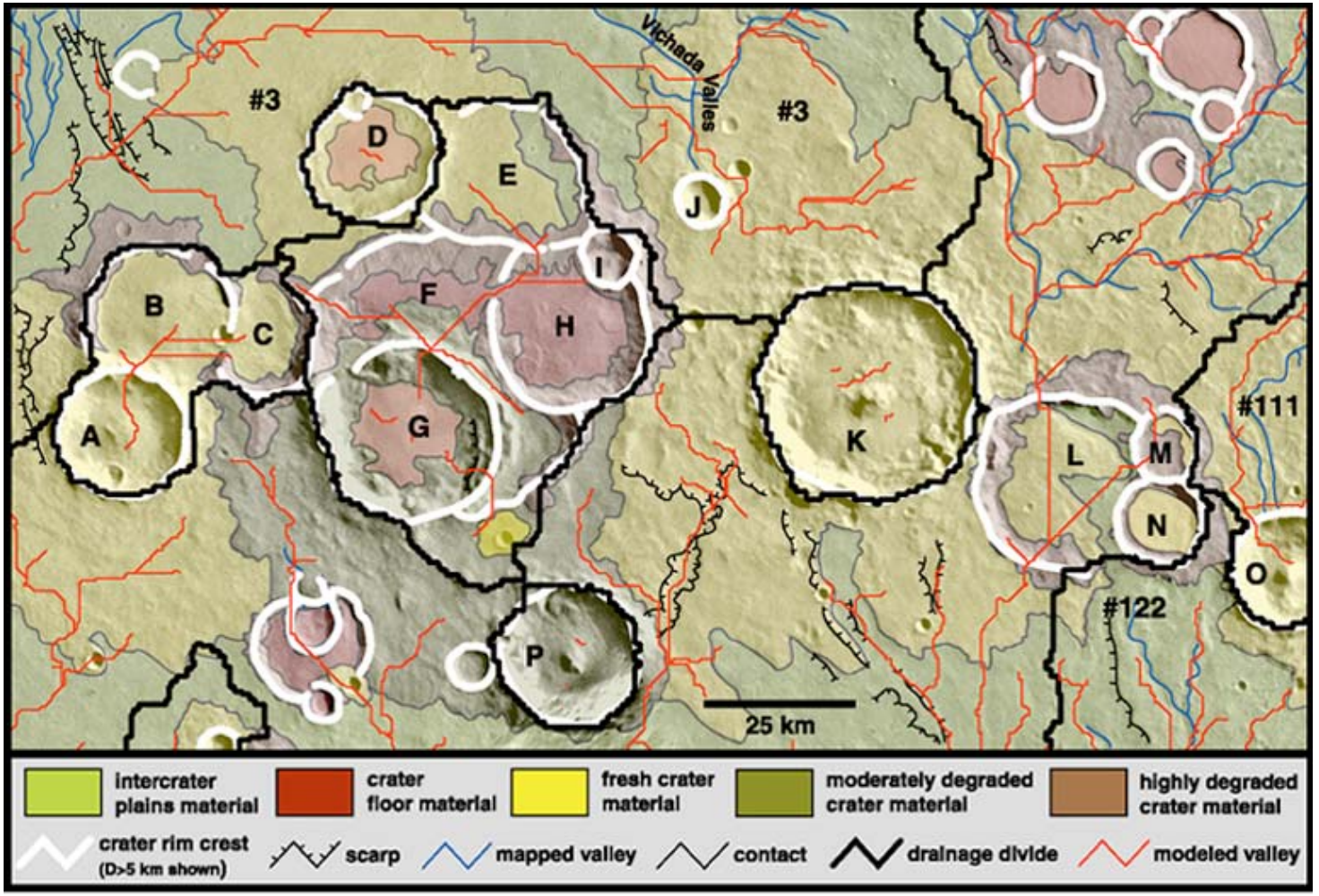

Figure 4.11. Map of geology (Chapter 2.0; Mest and Crown [2004a]), impact crater rims (D>5 km), mapped and modeled valleys, and drainage divides covering part of Tyrrhena Terra study area. Here a cluster of 16 large craters (A-P) truncates Vichada Valles (top of map) and other southerly-flowing valleys. The model however, delineates the path of Vichada Valles to the west of the cluster, which is not observed in images. Using a SFD=575 m, the sinks representing some craters (e.g., craters L and M) have been filled and valley pathways are delineated through them. Viking MDIM 2.0 photomosaic base; centered at 23.5°S, 272.8°W.

crater O. The remaining craters in this cluster (B, C, E, F, H, I, L, M and N) appear to be pre-fluvial in nature and have had no effect on Vichada Valles after its course had been established. In this and other parts of the study area, the model clearly does not account for the topography created by post-fluvial craters to reflect observed cross-cutting relationships, and the model alone can not be used to assess martian valley network development.

Drainage patterns are consistent between mapped and modeled data (Figure 4.9). Mapped networks in Tyrrhena Terra consistently show dendritic (e.g., basin #3) and (sub)parallel (e.g., basin #89) patterns, but the mapped networks within some basins (e.g., basin #3) appear less integrated than the corresponding modeled networks. Subparallel patterns appear to be favored on steeper slopes. Regional slopes in the study area are low (0.23°), which is consistent with the large dendritic pattern of the Vichada Valles system. At smaller scales, steeper, local slopes, such as along the rims of impact craters, produce (sub)parallel drainage patterns. Variations in the geology (lithology, structure, etc.) of the substrate in which valleys are incised could have also influenced drainage patterns. For example, basin #3, which drains the greatest area of the thirteen basins identified in this study, contains valleys that dissect what are believed to be interlayered sedimentary, volcanic and impact-related materials [Mest and Crown, 2004a]. Spatial variations in these layered sequences within basin #3 would influence infiltration and thus the amount of runoff produced [Ritter et al., 1995]. For instance, an area overlain by brecciated and fractured (and therefore relatively porous) impact ejecta could have higher infiltration, lower runoff, and thus less dissection than loosely consolidated sediments overlying bedrock [Kelson and Wells, 1989; Ritter et al., 1995]. The latter would tend to promote continued headward and lateral growth of channels, as well as initiation of new tributaries as channels erode down to the resistant bedrock.

4.7.2 Drainage Density

Drainage density (D_d), defined as the total length of streams in a drainage basin divided by the area of the basin [Horton, 1945], is one of the most important morphometric parameters used to

Table 4.6a. Length and area morphometric data for mapped watersheds.

Basin ID	A (km^2)	N	Total L (km)	Min L (km)	Max L (km)	Mean L (km)	St. Dev. (km)	D_d (km^{-1})	u	N_u	Total L_u (km)	Min L_u (km)	Max L_u (km)	Mean L_u (km)	St. Dev. $_u$ (km)	R_b	R_L
34	contains no mapped valleys																
105	contains no mapped valleys																
36	13902	3	155	37	75	52	20	0.011	1	3	155	37	75	52	20	-	-
46	6070	21	473	2	83	23	20	0.078	1	16	286	2	49	18	14	3.8	0.6
									2	4	104	12	57	26	21	4.0	0.3
									3	1	83	-	-	-	-	-	-
51	14557	23	386	4	68	17	16	0.027	1	18	175	4	19	10	4	4.5	0.2
									2	4	166	22	68	42	22	4.0	0.9
									3	1	45	-	-	-	-	-	-
74	9015	4	33	2	17	8	6	0.004	1	3	31	5	17	10	6	3.0	4.9
									2	1	2	-	-	-	-	-	-
107	3480	34	452	3	96	13	16	0.130	1	26	277	3	30	11	7	4.3	0.4
									2	6	151	3	96	25	35	3.0	2.1
									3	2	24	8	16	12	6		
111	3401	23	273	3	81	12	16	0.080	1	18	162	3	30	9	7	4.5	1.2
									2	4	30	6	12	8	3	4.0	0.1
									3	1	81	-	-	-	-	-	-
130	2752	3	68	15	28	23	7	0.025	1	2	39	15	25	20	7	2.0	0.7
									2	1	28	-	-	-	-	-	-
131	1218	5	56	5	30	11	11	0.046	1	4	50	5	30	12	12	4.0	2.0
									2	1	6	-	-	-	-	-	-
3	177557	332	6358	0.86	416	19	41	0.036	1	270	3223	0.86	84	12	13	5.6	0.4
									2	48	1348	1	160	28	35	4.8	0.5
									3	10	546	10	120	55	44	3.3	0.2
									4	4	1240	82	416	310	158		
89	17106	114	1358	2	128	12	16	0.079	1	90	799	2	30	9	5	4.4	0.6
									2	20	305	2	96	15	21	6.7	0.4
									3	3	127	25	74	42	28	3.0	0.3
									4	1	128	-	-	-	-	-	-
122	43041	33	437	2	47	13	12	0.010	1	27	280	2	36	10	9	5.0	0.4
									2	5	144	3	47	29	17	5.0	2.2
									3	1	14	-	-	-	-	-	-

Note: In Tables 4.6a and b, double line separating basin #'s 3, 89 and 122 indicates most impact craters (D>10 km) in these basins are post-fluvial.

Table 4.6b. Length and area morphometric data for modeled watersheds.

Basin ID	A (km^2)	N	Total L (km)	Min L (km)	Max L (km)	Mean (km)	St. Dev. (km)	D_d (km^{-1})	u	N_u	Total L_u (km)	Min L_u (km)	Max L_u (km)	Mean L_u (km)	St. Dev. $_u$ (km)	R_b	R_L
34	4264	11	260	0.63	74	24	21	0.061	1	8	173	8	44	22	12	4.0	0.6
									2	2	75	0.63	75	37	52	2.0	3.0
									3	1	13	-	-	-	-	-	-
36	13902	48	1016	0.89	76	21	18	0.073	1	34	577	0.89	64	17	15	3.5	0.7
									2	10	244	10	76	24	20	3.3	0.5
									3	3	162	31	73	54	21	0.8	1.7
									4	1	33	-	-	-	-	-	-
46	6070	18	388	0.45	108	22	24	0.064	1	15	239	0.45	40	16	10	8.0	0.3
									2	2	113	5	108	57	73	2.0	1.6
									3	1	36	-	-	-	-	-	-
51	14557	53	1000	0.45	126	19	22	0.069	1	41	497	0.45	43	12	9	4.6	0.4
									2	9	247	4	74	28	22	4.5	0.3
									3	2	183	57	126	91	48	2.0	1.3
									4	1	73	-	-	-	-	-	-
74	9015	27	574	1	80	21	18	0.064	1	20	310	1	50	16	12	5.0	0.5
									2	4	117	26	33	29	3	2.0	0.5
									3	2	129	50	80	65	21	2.0	3.5
									4	1	18	-	-	-	-	-	-
105	1091	4	75	6	27	19	9	0.069	1	3	51	6	27	17	11	3.0	0.7
									2	1	24	-	-	-	-	-	-
107	3480	11	323	5	90	29	24	0.093	1	6	230	7	90	38	29	2.0	3.0
									2	3	38	5	29	13	14	3.0	0.5
									3	2	54	27	27	27	0	-	-
111	3401	9	227	4	76	25	25	0.067	1	6	79	4	31	13	11	3.0	0.2
									2	2	132	57	76	66	13	2.0	4.1
									3	1	16	-	-	-	-	-	-
130	2752	11	161	1	161	15	11	0.059	1	8	111	1	41	14	13	4.0	0.8
									2	2	36	13	24	18	8	2.0	1.3
									3	1	14	-	-	-	-	-	-
131	1218	4	79	5	32	20	12	0.065	1	3	47	5	24	16	10	3.0	0.5
									2	1	32	-	-	-	-	-	-
3	177557	556	12739	0.45	722	23	42	0.072	1	429	6290	0.45	76	15	12	4.6	0.5
									2	95	2991	1	118	32	27	3.8	0.4
									3	25	1983	5	279	79	82	4.2	0.6
									4	6	753	10	211	126	74	6.0	0.2
									5	1	722	-	-	-	-	-	-
89	17106	62	1268	0.63	216	21	29	0.074	1	50	721	0.63	64	14	13	4.6	0.5
									2	11	331	0.89	53	30	17	11.0	0.1
									3	1	216	-	-	-	-	-	-
122	43041	133	3052	0.63	136	23	24	0.071	1	100	1651	0.63	78	17	15	4.0	0.5
									2	25	842	3	106	34	25	6.3	0.7
									3	5	227	9	104	45	37	2.0	0.5
									4	2	196	78	118	98	28	2.0	0.7
									5	1	136	-	-	-	-	-	-

characterize valley network development and describes the degree to which a surface is dissected. Terrestrial drainage densities reflect the interaction between geology and climate, specifically, the influence of relief, slope, lithology, infiltration, total annual precipitation, the ratio of precipitation to evaporation, and vegetation cover [Horton, 1932, 1945; Strahler, 1952, 1957, 1958; Gregory and Walling, 1973; Ritter et al., 1995; Tucker and Bras, 1998; Vogt et al., 2003]. Ritter et al. [1995] also noted that drainage density generally reflects relationships between geology and climate from region to region. For example, in areas with either humid or arid climates, low drainage densities can be achieved if the surface materials are resistant to erosion or have high infiltration capacities; conversely, high drainage densities can be obtained under either climatic condition as resistance decreases or permeability decreases. From the above influences, all but vegetation cover are applicable to Mars, but only relief and slope can currently be measured with any degree of accuracy (the Mars Exploration Rovers Spirit and Opportunity may be able to provide data in which to estimate infiltration capacity) and lithology can be determined in relative terms (i.e., thick versus thin layers of an inferred type). Geologic mapping in Tyrrhena Terra has attempted to constrain the lithology of the terrain in which the valley networks are incised [Mest and Crown, 2004a].

Drainage densities, shown in Tables 4.6a and b, for the thirteen basins examined, range from 0.004 km^{-1} (basin #74) to 0.097 km^{-1} (basin #107) for mapped valleys (average = 0.04 km^{-1}) and 0.039 km^{-1} (basin #131) to 0.085 km^{-1} (basin #107) for modeled valleys (average = 0.067 km^{-1}). As mentioned earlier, the Arc/Info model uses the DEM to delineate valleys within a watershed based purely on topography. Thus the drainage densities (and other parameters to be discussed) calculated from the modeled valleys can be considered to be the ideal densities for these basins, reflecting mature systems in idealized watersheds. This is effectively shown in Figure 4.12a as a function of drainage basin area. The fact that the densities for the mapped valleys are comparable suggests that the model is at least calculating networks comparable in scale to the mapped networks. Similarly in Figure 4.12b, stream lengths as a function of basin area show linear relationships for modeled streams but are more scattered for mapped streams. Similarities of mean values suggest that the modeling approach is useful. The generally similar ranges and similar maximum values help to characterize network-forming processes and suggest that one valley-forming process is dominant in this part of the martian highlands.

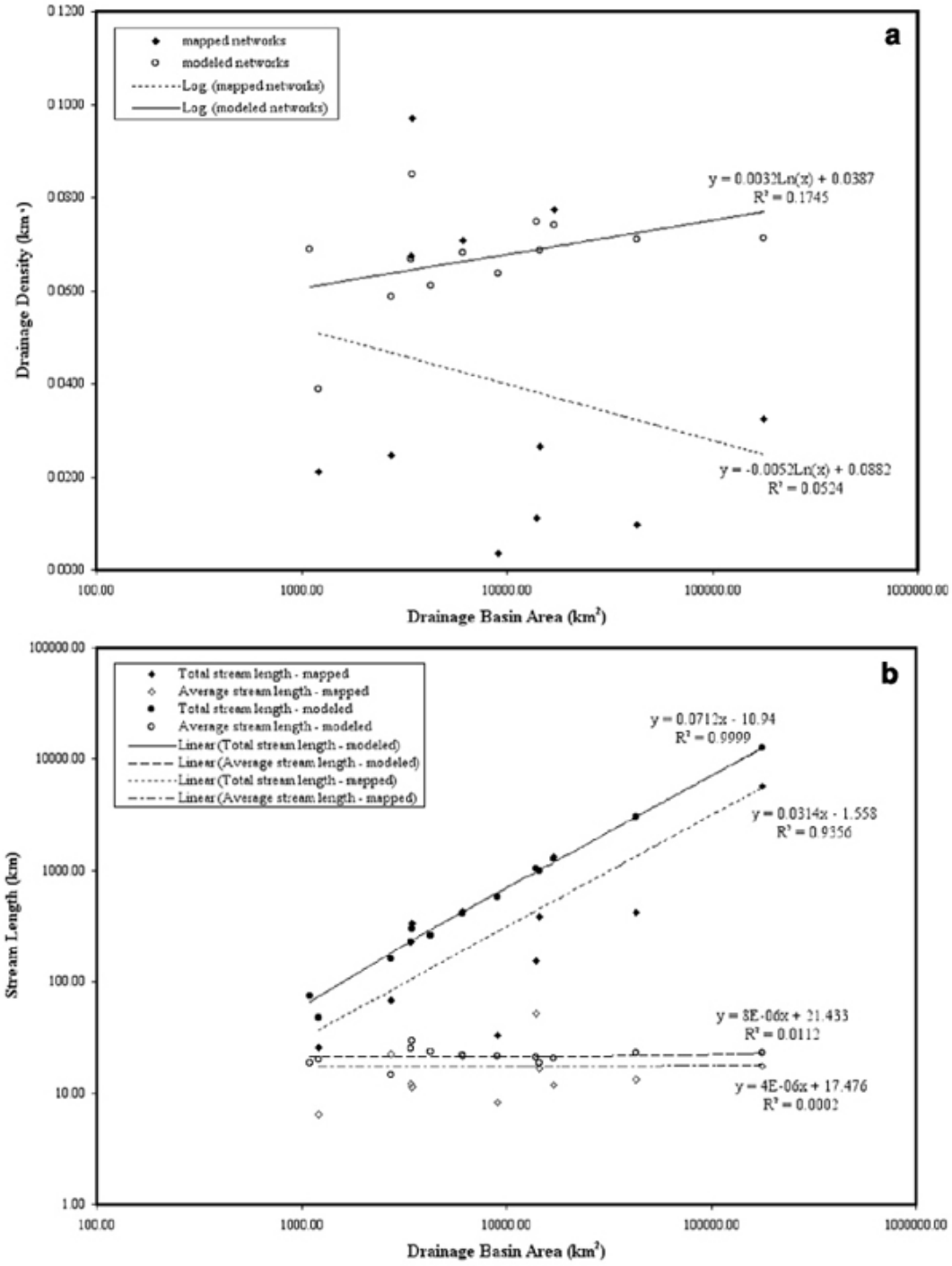

Figure 4.12. Plots of drainage basin area as functions of drainage density (a) and stream length (b). For these data, modeled densities and stream lengths (total and average) tend to plot closer to a straight line than mapped data, especially for drainage density. This is most likely due to the model's inherent nature to attempt to delineate the most ideal networks based on the given digital elevation model, thus generating the most ideal characteristics for those networks.

Martian drainage densities were initially described by the Mars Channel Working Group [1983] as "low" and decreasing toward higher latitudes. Baker and Partridge [1986] showed for sixteen small highland networks, densities ranged from 0.2 km^{-1} to 0.3 km^{-1}, and Cabrol and Grin [2001b] showed that 71 valley networks (including Vichada Valles) mapped at the 1:2M scale had comparable drainage densities, ranging from 0.03 to 0.22 km^{-1}. However, according to Carr [1995, 1996], at the 1:2M scale the most densely dissected areas of the Martian highlands yielded drainage densities of only 0.001 to 0.01 km^{-1}. In a study by Carr and Chuang [1997], Martian and terrestrial networks were mapped at similar scales (1:2M) as a means of providing a better comparison. Terrestrial values at this scale ranged between 0.07 and 0.21 km^{-1}, whereas Martian values were found to be 0.0032 km^{-1} for Noachian units, 0.00047 km^{-1} for Hesperian units, and 0.00007 km^{-1} for Amazonian units. Only the most heavily dissected flanks of several Martian volcanoes were found to be similar to the terrestrial values, ranging from 0.3-2.3 km^{-1} [Gulick and Baker, 1990]. Grant [2000] and Grant and Parker [2002] mapped valley networks in the Margaritifer Sinus region of Mars (1:500K) and found drainage densities to range from 0.03 to 0.11 km^{-1}. Drainage densities ranging from 0.20 to 0.34 km^{-1} were determined by Irwin and Howard [2002] for drainage basins in Terra Cimmeria; however this range is the "maximum" density based on defined areas and does not represent the total areas of their representative drainage basins. Drainage densities calculated in this study and by the above-mentioned authors are much lower than most terrestrial values (>2 km^{-1}) [Schumm, 1956; Smith, 1958; Gregory and Walling, 1973; Morisawa, 1962; Gregory, 1976; Wohl, 2000], but are comparable to values reported for some parts of the United States at 1:1M scale (0.149 for Arizona; 0.079 for Nebraska; 0.206 for New York; 0.119 for Texas; 0.209 for Washington) [Carr and Chuang, 1997], which include a wide range of climates (arid to temperate) and different geologic settings.

4.7.3 Stream Order and Bifurcation Ratio

Stream orders were determined for mapped and modeled valleys using the Strahler ordering system [Strahler, 1964] and are defined by the following rules: fingertip tributaries are designated order 1, and the junction of two streams of the same order (u) forms a channel

segment of the next higher order (u+1). According to Strahler [1964], the ordering system of streams is useful because in general, order number is directly proportional to the size of the contributing watershed, channel dimensions, and discharge anywhere within the network. Terrestrial steam orders, using the Strahler ordering system, are generally low and range from 2 to 6 for mountain networks and 3 to 6 for lowland networks [Wohl, 2000] The bifurcation ratio (R_b) is defined as the ratio of number of streams of a given order (N_u) to the number of streams of the next higher order (N_{u+1}), and can be used to estimate the number of streams of any given order and the total number of streams within a basin [Horton, 1945; Strahler, 1964; Ritter et al., 1995]. Strahler [1964] noted that bifurcation ratios range between 3.0 and 5.0 for watersheds in which the geology (lithology, structure, etc.) is relatively homogeneous, and that rarely is the theoretical minimum value of 2.0 approached under natural conditions. Geologic homogeneity within a basin would tend to form drainage systems that display morphometric and geometric similarities [Strahler, 1964].

Mapped networks in Tyrrhena Terra were found to range from second to fourth order and modeled networks range from second to fifth order (Table 4.6a and b, respectively). In general, stream orders and the numbers of streams (as a basin total and as a function of stream order) are higher for modeled streams (basins #89, 107 and 111 contain more than twice the number of mapped streams). Nevertheless, a difference in one stream order between mapped and modeled streams is not significant and shows the two datasets are comparable in terms of the relative numbers of streams produced naturally or by the model's interpretation of the topography. Stream orders and the log of the number of streams (summed for all 13 basins) plot as a straight line for both mapped and modeled streams (Figure 4.13a), which is typical of terrestrial drainage systems, and numerous authors [e.g., Schumm, 1956; Chorley, 1957; Morisawa, 1962; Strahler, 1964] have verified the close relationship between these two parameters. The data show that Arc/Info is delineating more streams of all orders than are identifiable in the image datasets. This results in greater chances for streams of the same order to intersect and therefore higher order networks to be modeled, which is supported by consistent basin-to-basin bifurcation ratios for the modeled streams (Tables 4.6a and b). One of the main differences between the mapped and modeled networks is that although the modeled drainage divides adequately enclose the mapped networks, there are several mapped valleys within the 13_that are not connected to the "main"

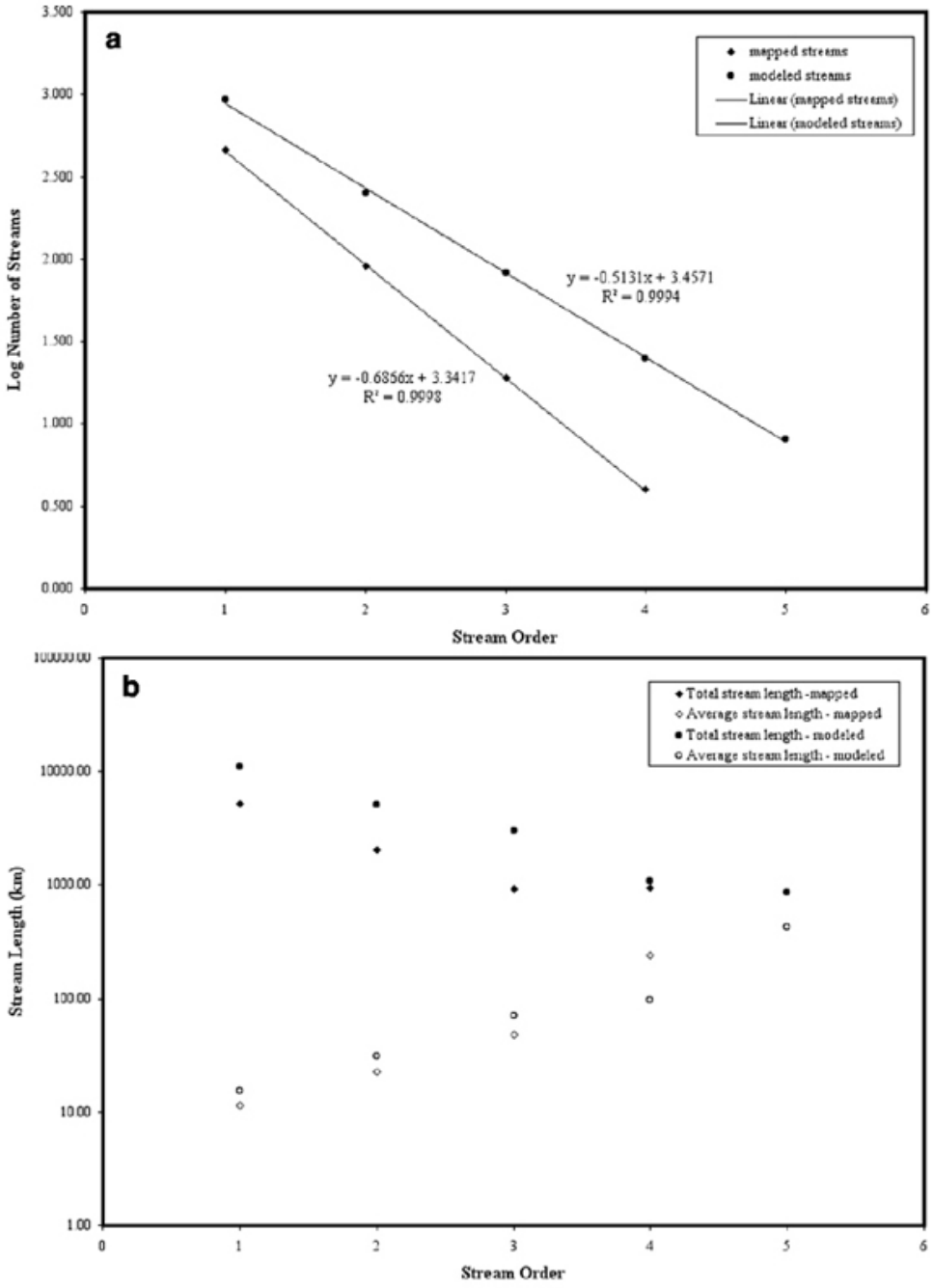

Figure 4.13. Plots of stream order as a function of the number of streams (a) and stream length (b). The numbers of mapped streams show a slightly steeper slope than for modeled streams in (a), but both data sets plot along a straight line. In plot (b), the lengths of both mapped and modeled streams plot fairly close to straight lines and show typical inverse correlations for total (negative) and average (positive) stream lengths as a function of stream order. The relationships in plots (a) and (b) are typical of terrestrial drainage systems [e.g., Schumm, 1956; Chorley, 1957; Morisawa, 1962; Strahler, 1964].

systems within those basins. For example, basin #89 (Figure 4.10) shows several first and second order mapped streams dissecting the crater that forms part of its divide as well as several streams that flow into and terminate along the rim of a buried impact crater. The model does not identify all of these first- and second-order valleys, and those that are identified by the model are connected to a single system. This partially accounts for overall lower orders for mapped networks and the differences in bifurcation ratios. Previous researchers found that martian valley networks mapped at 1:2M and 1:500K scales using Viking Orbiter images were no greater than fourth-order [Carr, 1995, 1996; Grant, 2000; Grant and Parker, 2002]. Several bifurcation ratios for modeled streams in Tyrrhena Terra approach Strahler's theoretical minimum of 2.0, whereas all but one mapped network (basin #130) approaches 2.0. This suggests that because the model only accounts for topography and not geology of the study area, Arc/Info is misrepresenting the effects of geology on valley formation by delineating features with "significant" topographic expressions (such as graben, the edges of or coalescing ejecta blankets, or closely spaced craters) as valleys. This indicates that modeling alone can not be used to characterize the hydrology of the martian surface, but such characterizations require detailed geologic and geomorphic mapping to constrain the materials that occur at and just below the surface.

Stream order plotted against elevation (Figure 4.14; binned in 500 m increments) shows the distribution of first, second and third order stream segments are skewed toward elevations lower than the means (2000 m for modeled streams and 1500 m for mapped streams), but appear distributed over most elevations. Most fourth and fifth order stream segments appear to be located within elevations close to the means for both data sets. Obviously these relationships are dependent on the elevation at which streams of the same order join to form a stream of the next higher order. In addition to stream distributions, Figure 4.14b also shows the onsets of streams of any given order. For example, third and fourth order streams for both datasets are forming at the same elevation, 2500 m and 2000 m, respectively, suggesting valley formation appears to have been relatively efficient at higher elevations within the study area.

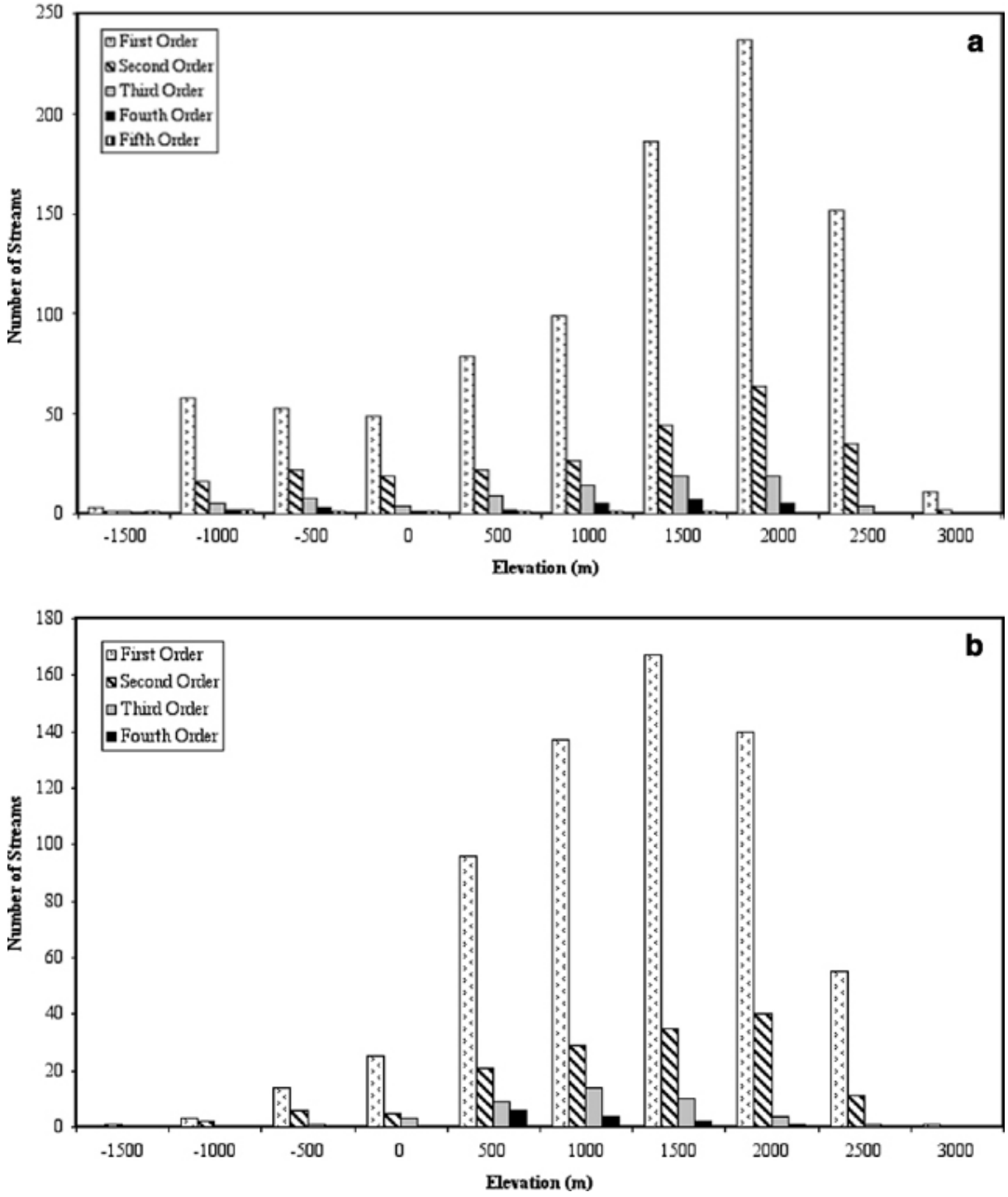

Figure 4.14. Numbers of streams per stream order as a function of elevation range (bins = 500 m) for modeled (a) and mapped (b) streams.

4.7.4 Length Ratio

The length ratio (R_L) is defined as the ratio of the length of streams of a given order (N_u) to the length of streams of the next higher order (N_{u+1}) [Horton, 1945; Strahler, 1964], and can be used to estimate the unmeasured lengths of streams of a given order and their total length within a basin [Ritter et al., 1995]. Length ratios range from 0.14 to 4.12 for modeled networks and 0.10 to 4.86 for mapped networks. In a study by Baker and Partridge [1986], sixteen Martian highland networks were mapped at 1:2M scale and length ratios were found to range from 1.17 to 3.82. For individual basins (Tables 4.6a and b), there is a consistent trend of decreasing total and increasing average stream lengths for higher orders for most basins; however, there appears to be no trend among fourth and fifth order networks. Similar to the bifurcation ratio, the log of stream lengths (summed for all 13 basins) as a function of order will plot as a straight line (Figure 4.13b) showing a close relationship between these parameters [Schumm, 1956; Chorley, 1957; Morisawa, 1962; Strahler, 1964], which for this study is positive for average stream lengths and negative for total stream lengths for both mapped and modeled streams. Figure 4.13b also shows modeled stream lengths plot closer to a straight line than mapped stream lengths.

4.7.5 Relief Morphometry

Relief characteristics, including relief ratio and ruggedness number, provide information about the overall steepness of a drainage basin and indicate the intensity of fluvial erosion operating on basin slopes [Strahler, 1964; Ritter et al., 1995]. Measuring the relief of a drainage basin defines a slope value that provides an indication of runoff [Ritter et al., 1995] and the potential energy of a drainage system [Strahler, 1964]. Maximum basin relief (H) is defined as the elevation difference between the highest point on the basin divide and the mouth of the trunk valley [Strahler, 1964]. The relief ratio (R_h) is the maximum basin relief (H) divided by the horizontal distance (L_b) along the longest dimension of the basin parallel to the principal drainage line

Table 4.7. Relief morphometric data for modeled and mapped watersheds.

Basin ID	(L_b) (km)	Max basin elev. (m)	Min basin elev. (m)	H (m)	R_h	R modeled	R mapped
34	85.35	2807.15	1430.14	1377.01	0.016	0.084	x[1]
36	129.18	3756.78	1275.57	2481.21	0.019	0.186	0.027
46	156.12	2973.13	961.58	2011.55	0.013	0.137	0.143
51	267.96	2371.30	252.22	2119.08	0.008	0.146	0.057
74	141.54	3351.15	1460.54	1890.61	0.013	0.121	0.008
105	51.10	1172.97	-303.43	1476.40	0.029	0.102	x[1]
107	107.49	2524.29	686.87	1837.42	0.017	0.156	0.178
111	137.77	2344.46	-584.07	2928.53	0.021	0.196	0.199
130	99.74	357.66	-1229.39	1587.05	0.016	0.094	0.040
131	66.59	2115.94	355.07	1760.87	0.026	0.063	0.037
3	1014.69	3745.23	-822.08	4567.31	0.005	0.324	0.146
89	274.44	3384.74	234.10	3150.64	0.011	0.233	0.243
122	379.21	3440.68	-1441.59	4882.27	0.013	0.347	0.049

[1]Basin #'s 34 and 105 do not contain mapped valleys; R can not be calculated.
Note: Double line separating basin #'s 3, 89 and 122 indicates most impact craters (D>10 km) in these basins are post-fluvial.

[Schumm, 1956]. The ruggedness number (R) is the product of the maximum basin relief (H) and the drainage density (D_d) [Melton, 1957; Strahler, 1958, 1964].

Maximum basin relief (Table 4.7) determined for the basins identified in this study ranges from 1377 m for basin #34 to 4882 m for basin #122 (mean for 13 basins = 2467 km). Relief ratios for these basins (Table 4.7) range from 0.005 (basin #3) to 0.029 (basin #105) with an average = 0.02. Ruggedness numbers ranged from 0.008 to 0.243 for mapped (average = 0.102) and 0.063 to 0.347 for modeled (average = 0.168) networks. The only other studies to calculate relief ratios and ruggedness numbers for martian drainage basins - Grant [2000] and Grant and Parker [2002] - found that these values ranged from 0.001-0.13 and 0.005-0.086, respectively, for basins in Margaritifer Sinus, and were based on Earth-based radar-derived topography. Typical relief ratios for terrestrial basins range from 0.015 to 6.8 for mountain basins and 0.0004 to 0.01 for lowland basins; in general, $R_h \geq 0.02$ indicates mountain systems and $R_h \leq 0.02$ indicates lowland systems [Wohl, 2000]. Relief ratios calculated here are found to be slightly lower than those for Margaritifer Sinus [Grant, 2000; Grant and Parker, 2002], and comparable to terrestrial lowland networks [Wohl, 2000]. According to Wohl [2000; Table 2.3], terrestrial networks with R_h = 0.004-0.007 formed in humid temperate climates and in glacial sediments, or sedimentary or limestone bedrock, and networks R_h = 0.01-0.017 formed in semiarid climates or in clay shale substrate. Ruggedness numbers on the other hand, were higher for both mapped and modeled networks than determined for Margaritifer Sinus [Grant, 2000; Grant and Parker, 2002] and within the range (on the lower end) for terrestrial examples (0.03-10.9) [Strahler, 1964; Grant, 2000]. Low martian ruggedness numbers (relative to terrestrial systems) have been attributed to the influence of the low martian drainage densities, and imply that erosion by runoff may be inefficient due to surface and near-surface materials with high infiltration capacities and the ability to store large quantities of water [Ritter et al., 1995; Grant, 2000]. In addition, Strahler [1958; 1964] noted that in order to obtain extremely high values of the ruggedness number, both H and D_d must be large, that is the maximum basin relief must not only reflect slopes that are steep (producing high D_d) but are also long.

4.8 CONCLUSIONS

Geologic and geomorphic mapping in the highlands of Tyrrhena Terra has revealed numerous well-incised systems of valleys within degraded intercrater plains and impact craters that record a variety of preservation states, and are interpreted to have formed by fluvial processes. Valleys have been mapped down to MOC resolution and all are shown in this study on the ~1:5M scale Viking photomosaic (Figure 4.1). The valleys that compose these networks display degraded and pristine morphologies and a variety of cross-cutting and superposition relationships with impact craters. Morphologic observations, crater/valley relationships, and impact crater distributions, have been used to determine that valleys in Tyrrhena Terra are old, most likely Noachian in age. Formation of gullies along the interior walls of many craters in the area, most of which head at or near crater rims, unlike the gullies of Malin and Edgett [2000] that originate at specific layers, may represent some of the youngest activity and extend into the Amazonian Period [Mest and Crown, 2004a,b]. The morphologies of valleys and networks and the fact that many gullies head at or near crater rims suggests that a significant part of valley formation involved surface runoff, although some component of groundwater sapping can not be ruled out. Fluvial valleys and impact craters eroded by gullies and filled with flat-lying deposits are distributed not only within the Tyrrhena Terra study area, but throughout the highlands indicating the processs(es) of fluvial erosion was widespread in the highlands as well.

GIS-based hydrologic modeling has been conducted in the highlands of Tyrrhena Terra. The model was run on a low-resolution (16 pixels/degree) and a high-resolution MOLA DEMs to determine the effects of resolution on the model. This study showed that although the low-resolution DEM may be adequate to model features with significant relief, such as drainage divides and high-order streams, the low-resolution DEM did not accurately predict low-order streams. Therefore it was determined that the highest resolution DEM available, here 128 pixels/degree, was most adequate to conduct the hydrologic modeling. Drainage divides and networks were delineated as a function of sink-fill depth (SFD). Multiple iterations of the model, using the hydrologic GRID functions described in this study, were conducted to find the optimal SFD from which to derive morphometric data. The optimal SFD (575 m) was determined by overlaying modeled drainage divides on mapped valley networks until they adequately contained

the mapped networks. After determining the SFD and delineating drainage divides, networks were modeled and compared to mapped valleys to further test the accuracy of the model.

Hydrologic modeling results, which assumes the only source of fluids is from precipitation, suggest that large areas of apparently undissected terrain [Carr, 1996] could have been influenced by fluvial processes. However, the modeling results are most certainly affected by the spatial and vertical resolution of the MOLA DEM, 128 pixels/degree (~460 m/pixel) and ~10 m, respectively, used to generate drainage divides and valleys. As a result, the model most accurately predicted valleys greater than half a kilometer wide and 10 meters deep [Smith et al., 2001]. DEM resolution, combined with the nature of Arc/Info to delineate valleys where the topography suggests, whether a fluvial valleys exists or not, may provide some indication for the discrepancies between the numbers and patterns of valley networks produced via modeling and observed in images. Compared to mapped networks, models of the larger-scale valley systems in Terra Tyrrhena accurately represent the locations of higher order valleys, and down to at least second order valleys; many modeled first-order valleys are not visible in Viking, THEMIS or MOC images. All available images were used to identify and map fluvial valleys. If we assume that valleys are not buried, then image data alone suggests fluvial processes were not very efficient in dissecting the highlands, especially by rainfall-fed runoff. It also appears that sapping would not have been efficient either due to discontinuous aquifers resulting from the interlayered nature of the local intercrater plains, or lack of an effective recharge mechanism. However, other researchers have suggested up to a meter or more of dust may mantle the highlands and therefore may obscure smaller tributaries [Craddock and Maxwell, 1993]; the dune-covered floors of Vichada Valles support this. Many more valleys than are visible could have formed, but have subsequently been buried by impact ejecta or eolian materials. Inability to identify valleys in images can be further accentuated by sun angle and incidence angle. Rigorous comparisons of the model results to image data have helped to produce accurate maps of martian drainage basins and their associated valley networks, which have provided critical constraints for valley formation mechanisms. Additional valley segments may be identified using analyses of new (i.e., THEMIS) and future (i.e., HiRISE and CRISM) datasets, in part by comparing mapped and modeled network patterns.

Terrestrial watersheds are generally characterized by a host of morphometric parameters (e.g., drainage density, stream order, bifurcation ratio, length ratio, and relief morphometry) that

can be used to evaluate the geologic, climatic and hydrologic conditions under which they form. These parameters have been calculated for the thirteen basins identified in the Tyrrhena Terra region. Drainage densities for mapped and modeled basins, respectively, have been shown to be consistent with other studies of martian valley networks, but are still much lower than most terrestrial drainage basins. The low martian drainage densities (0.004-0.097 km^{-1}) that have been determined in this and other studies, particularly in the highlands, can be attributed to various combinations of several factors:

- the processes of valley formation (runoff versus groundwater sapping)
- local and regional variations in lithology
- slopes that are low and therefore inadequate to transport material
- the inability to preserve smaller valleys and subdue larger valleys due to destruction by impact craters and burial by eolian deposits
- temporal limitations or immature network development by climate change.

Strahler stream orders are comparable for both data sets, 4th (mapped) and 5th (modeled), as well as for typical terrestrial mountain and lowland watersheds. Bifurcation ratios, being related to stream order, are also comparable for both data sets, despite the rather large number of disconnected first and second order mapped valleys identified in most basins that are not modeled as such, but the martian values are lower than terrestrial values. The low stream orders determined by this and previous studies of martian valley networks suggest (a) the process of formation may have limited tributary development, and (or) (b) climate changes may have caused tributary development to cease. However, it has also been shown in several studies [e.g., Carr, 1996, Carr and Chuang, 1997; Craddock and Howard, 2002; Irwin and Howard, 2002] that the ability of the smallest fingertip tributaries to be identified is inhibited by image resolution. Furthermore, similar to the argument for low drainage densities, eolian materials and competition with impact cratering could have also acted to limit stream orders. Relief ratios suggest that the basins in Tyrrhena Terra most closely resemble terrestrial lowland watersheds that dissect sediments or sedimentary rocks, which is consistent with previous geologic analysis of this terrain [Mest and Crown, 2004a]. As mentioned before, relief parameters are a measure of the overall steepness of a basin and the efficiency of a basin to be eroded. The low ruggedness numbers, which are dependent on drainage densities, calculated for these martian basins suggest

erosion by runoff was not very efficient in most basins due to low gradients or lithology, and (or) that many of the smaller fingertip tributaries have been subsequently buried.

As a first order attempt to identify flow paths on the present martian surface, the hydrological modeling technique used in this study - commonly used by many studies (described throughout this text) for terrestrial watersheds - appears to adequately delineate large-scale networks at least down to second order valleys. The data presented here indicates that GIS hydrologic modeling is also able to accurately delineate drainage divides from high-resolution digital elevation models, but modeling alone is inadequate to accurately identify martian valley networks in detail. The Arc/Info modeling technique has an inherent nature to fill a basin with valleys. Furthermore, sink-fill depth selection is an important factor in determining the accuracy of the predicted valleys compared to mapped valleys, and is a reflection of the scale at which watersheds should be modeled. Refinement of this model, if applied to other regions of Mars, should involve modeling martian watershed on a basin-to-basin basis so as to maximize accuracy in valley delineation. Alternatively, inconsistent coverage by high-resolution images over large areas of Mars may have resulted in incomplete mapping of valleys and therefore networks may be underrepresented in regards to the morphometric parameters described in this study. It therefore seems necessary, given the combination of topographic and imaging data sets that currently exist for Mars, that hydrologic modeling of martian terrains be accompanied by detailed geologic analyses and geomorphic mapping.

This research has also attempted to use geologic mapping and hydrologic modeling to constrain the process(es) by which these and other highland valleys formed. Mapped valley networks form mainly dendritic and sub(parallel) patterns, which are mostly functions of slope. Shallow sloping interlayered sedimentary, volcanic and impact-related materials dominate the study area, incised with valleys that form dendritic patterns, and valleys forming (sub)parallel patterns are found on steeper slopes along the rims of impact craters. Many interior and exterior valleys head at or near the rims of craters, which has been shown by many studies [e.g., Craddock and Maxwell, 1993] to argue against groundwater sapping because establishing a hydrologic head at the rim of a crater adequate enough to sustain sufficient flow to form valleys is extremely difficult. Valleys in Tyrrhena Terra are found over a wide range of elevations suggesting fluid availability was not restricted by to any specific elevation, as would be expected by sapping in which an aquifer typically intersects the surface at a limited range of elevations.

Valley morphologies, such as depths and widths, vary along the lengths of most valleys, and some valleys appear to have eroded laterally in some places, suggesting sustained and generally excessive flow. Morphometric evidence for mapped and modeled networks, specifically drainage density and relief parameters, suggests that the process(es) of valley formation were relatively inefficient, due in part to high infiltration properties of surface materials. If groundwater sapping dominated valley formation in this part of the highlands, recharge of aquifers would have been very efficient and thus the terrain should exhibit more dissection than is currently observed. Given the overall low slopes over much of the study area, and the potential that the lithology is widespread and relatively heterogeneous [Mest and Crown, 2004a] might indicate that surface materials have low resistance to erosion and (or) a low surface permeability. Thus runoff would have been the dominant erosional process, which could have been derived directly by rainfall, or indirectly by snowmelt. Rainfall on ancient Mars would require a climate much different than is observed today, including a thicker and warmer atmosphere and long-lived hydrologic cycle. However, under cold conditions, in which the atmosphere is also wetter than present to provide significant quantities of snow to generate runoff, a shallow permafrost layer would likely exist and effectively stagnate infiltration, as suggested by Irwin and Howard [2002] in Terra Cimmeria, and increase runoff generated by snowmelt. It appears sapping may have only played a secondary role in valley formation in the highlands of Tyrrhena Terra. Therefore, precipitation-fed runoff, either directly by rainfall or by snowmelt, is likely the dominant process of valley formation. Furthermore, based on the spatial and temporal relationships of dissected highland materials and impact craters, erosion by runoff must have been widespread, but relatively short-lived with most activity confined to the Noachian Period, consistent with the low drainage densities in Tyrrhena Terra.

5.0 ANALYSIS OF WATERSHEDS IN THE CIRCUM-HELLAS AND CIRCUM-ISIDIS HIGHLANDS OF MARS

5.1 INTRODUCTION

Hydrologic modeling, using the technique described in Chapter 4.0 for Tyrrhena Terra, has been conducted in the highlands of Promethei Terra (27.5° to 47.5°S, 245° to 270°W) east of Hellas basin, and Libya Montes (5°N to 5°S, 260° to 280°W) south of Isidis Planitia (Figure 5.1). Geologic mapping and geomorphic analyses in Promethei Terra [Crown et al., 1992; Tanaka and Leonard, 1995; Mest, 1998; Price, 1998; Leonard and Tanaka, 2001; Mest and Crown, 2001b, 2002a,b, 2003a; Pierce and Crown, 2003] and Libya Montes [Crumpler, 1997, 1998, 1999; Crumpler and Tanaka, 2003] have revealed complex histories of impact cratering, fluvial erosion and deposition, mass wasting and eolian activity. High-resolution Mars Orbiter Camera (MOC), Thermal Emission Imaging System (THEMIS), and Viking Orbiter images and Mars Orbiter Laser Altimeter (MOLA) topographic data have been used to qualitatively and quantitatively characterize highland fluvial systems and analyze the role of water in the evolution of these study areas. Fluvial features in these areas include small-scale, well-integrated valley networks isolated by massifs and knobs of highland materials, and gullies incised along the rims of impact craters [Mest, 1998; Mest and Crown, 2001a,b, 2002a,b, 2003a; Crumpler, 1998, 1999; Crumpler and Tanaka, 2003]. Arc/Info Geographical Information System (GIS) software has been used in

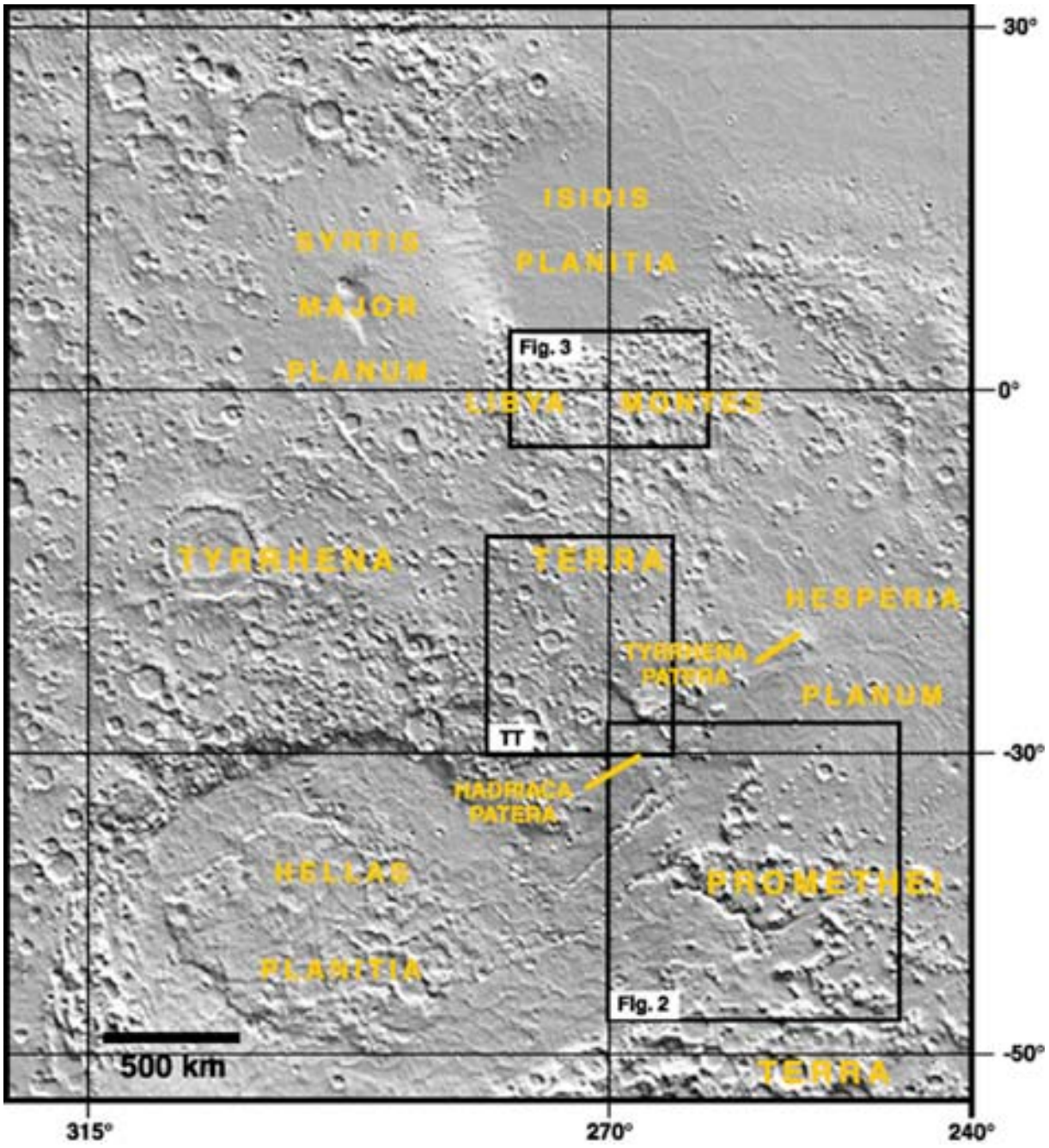

Figure 5.1. MOLA shaded relief map showing the circum-Hellas and -Isidis highlands. The locations of the Promethei Terra (Figure 5.2), Libya Montes (Figure 5.3) and Tyrrhena Terra (TT; Chapter 4.0, Figure 4.1) study areas are indicated. North is to the top in this and all subsequent images unless noted otherwise. DEM resolution is 256 pixels/degree; projection is Mercator; illumination from northeast.

conjunction with MOLA Digital Elevation Models (DEMs) to model drainage basin divides and delineate valley networks, and derive basin and network morphometric parameters to characterize basin "maturity" and the processes involved in watershed development. This study presents the results obtained from modeling watersheds in Promethei Terra and Libya Montes. The modeled networks and the parameters calculated from these data are compared to data derived from fluvial systems mapped by Mest and Crown [2002b, 2003a], Crumpler 1998, 1999] and Crumpler and Tanaka [2003]. The abundance and isolated nature of fluvial features within these study areas, relative to those described in Tyrrhena Terra in Chapter 4.0, have significant implications for past martian environmental conditions. Characterization of fluvial features in Promethei Terra and Libya Montes by mapping and hydrologic modeling is necessary to fully understand the nature of martian fluvial activity and the history of Mars' climate. In addition, data derived from the martian watersheds in Tyrrhena Terra, Promethei Terra and Libya Montes are compared to data from terrestrial drainage basins in order to further constrain the process(es) of martian valley network formation and the climate conditions under which they formed.

5.2 BACKGROUND GEOLOGY

The geology of the highlands of Promethei Terra (Figure 5.2) and Libya Montes (Figure 5.3) have been studied at small scales (1:2M to 1:15M) [e.g., Schaber, 1977; Greeley and Guest, 1987; Tanaka and Leonard, 1995; Mest, 1998; Leonard and Tanaka, 2001; Mest and Crown, 2001b] using predominantly Viking Orbiter image data. Availability of high resolution MOC and THEMIS images allowed larger scale (up to 1:1M) studies [e.g., Crumpler, 1998, 1999; Mest and Crown, 2002b, 2003a; Crumpler and Tanaka, 2003] of these highland terrains to be conducted. The Promethei Terra, Libya Montes and Tyrrhena Terra (discussed in Chapter 4.0) study areas share many similarities. The three areas are located on the rims of large impact

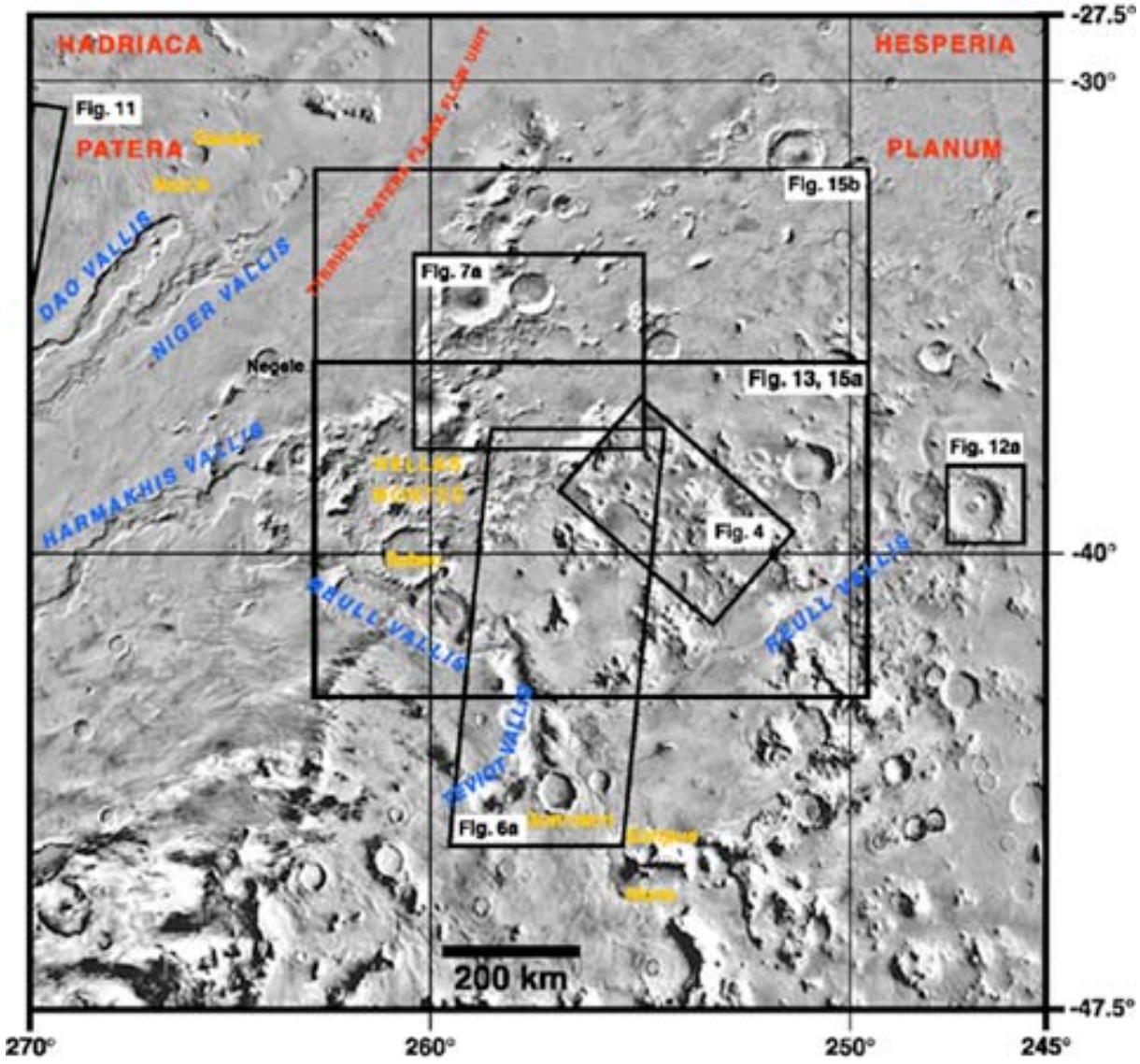

Figure 5.2. Viking MDIM 2.0 photomosaic displaying the rugged highland terrain, volcanic deposits and plains that characterize this part of Promethei Terra. Five large vallis systems (Reull, Teviot, Dao, Niger and Harmakhis Valles), numerous valley networks, sinuous channels, and debris aprons found within this area indicate that volatiles were prevalent in this part of the highlands. The locations of Figures 5.4, 5.6a, 5.7a, 5.11, 5.12a, 5.13 and 5.15a and b are indicated. Photomosaic is composed of Mars Digital Image Mosaics -30247, -35247, -40247, -45247, -30252, -35252, -40252, -45252, -30257, -35257, -40257, -45257, -30262, -35262, -40262, -45262, -30267, -35267, -40267, and -45267; projection is Mercator.

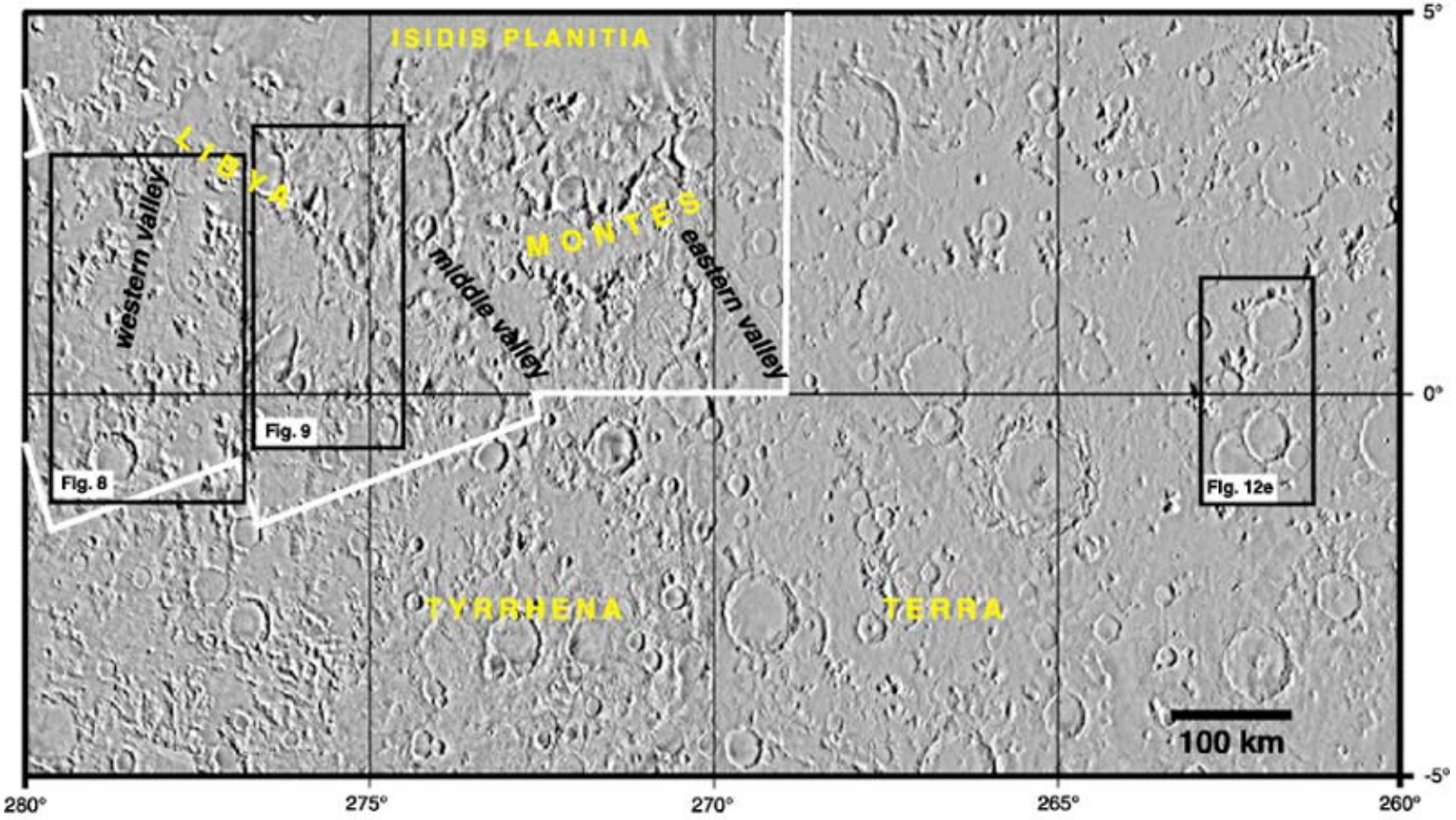

Figure 5.3. Viking MDIM 2.0 photomosaic displaying the rugged highland terrain of the Libya Montes study area. The locations of Figures 5.8, 5.9 and 5.12e are shown. The heavy white line corresponds to the border of the Crumpler and Tanaka [2003] geologic map and the locations of their "western," "middle" and "eastern" valleys are shown. Projection is mercator.

basins (Figure 5.1), suggesting regional slopes and structural patterns that resulted from the impact events may have influenced the geologic and hydrologic histories of these areas over time. MOLA shows regional and local elevations (and relief) are similar for both study areas. Regionally, Promethei Terra ranges from 4.5 km for individual massifs and Hesperia Planum in the northeast to -5.5 km in Hellas basin (~10 km in relief), and Libya Montes ranges from 4.0 km in the highlands along the southern boundary of the study area to -5.0 km in Isidis basin (~9 km in relief). At local scales, such as from the tops of massifs to the floors of valley-incised basins, elevations range from 4 to -2.5 km (~6.5 km in relief) for Promethei Terra and 4 to -3 km (~7 km in relief) for Libya Montes. Lastly, the three areas are each within less than 800 km of a major volcanic site that could have also affected the development of these areas. This section provides a brief summary of the relevant results of some of these previous studies, as they relate to the current study.

5.2.1 Promethei Terra

Geologic mapping of the Promethei Terra region (27.5° to 47.5°S, 245° to 270°W) at the 1:2M [Mest 1998; Mest and Crown, 2001b] and 1:1M scales [Mest and Crown, 2002b, 2003a] has revealed the influence of fluvial activity in the highlands east of the Hellas basin. Regionally, the terrain slopes gradually (~0.4°) to the west-southwest toward Hellas basin. Heavily cratered, Noachian-aged highland materials, which form rugged, mountainous terrains, are the oldest deposits identified in Promethei Terra [Greeley and Guest, 1987; Tanaka and Leonard, 1995; Mest, 1998; Leonard and Tanaka, 2001; Mest and Crown, 2001b]. MOC images show that some massifs of these materials are incised with small valleys (Figure 5.4) that in some instances extend to the crests of the massifs [Crown et al., 1992; Mest and Crown, 2002b, 2003a]. Fluvial and mass wasting processes have degraded highland materials; the eroded sediments were subsequently emplaced in low-lying regions among highland massifs forming isolated, smooth to hummocky deposits of Late Noachian to Early Hesperian-aged intermontane basin fill (Figures 5.4 and 5.5). Many deposits contain well-integrated valley networks and channels [Mest and

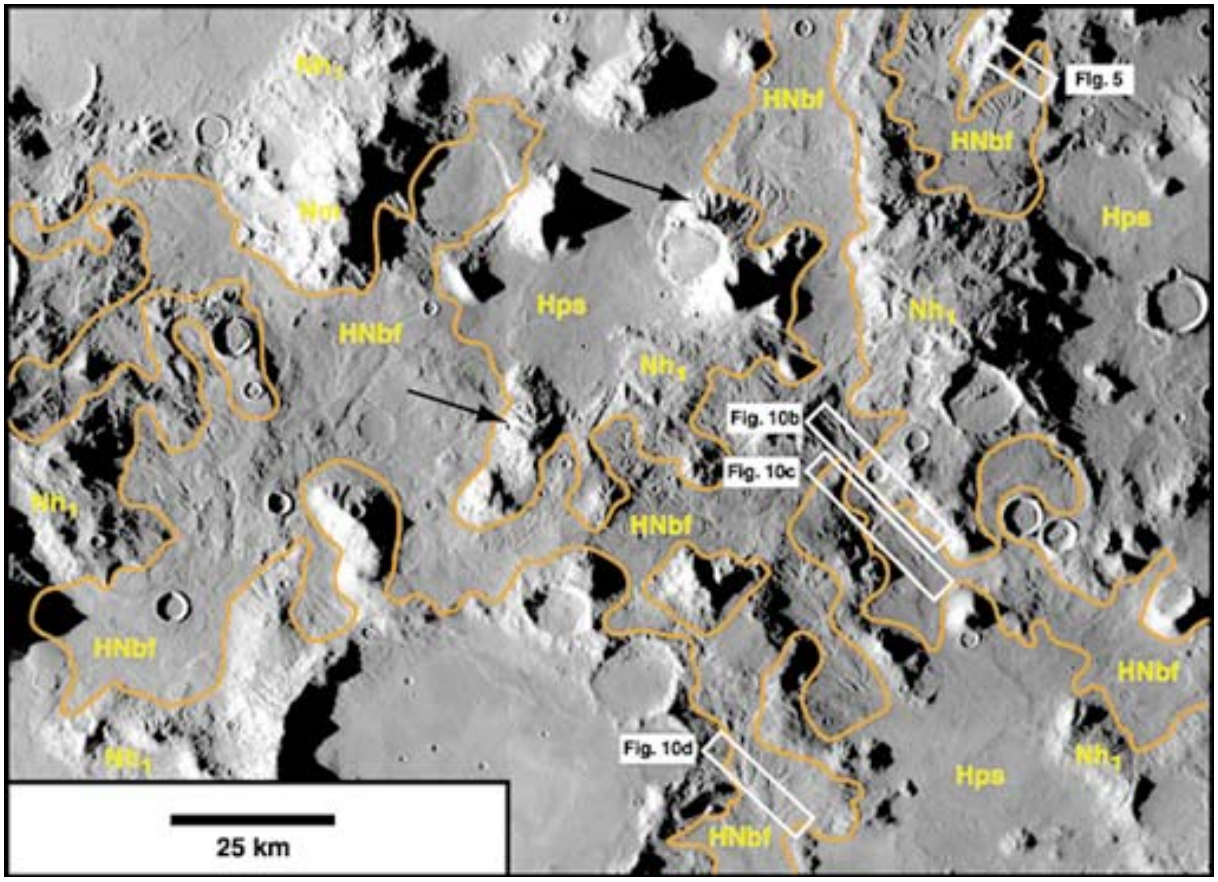

Figure 5.4. Viking Orbiter mosaic of highlands within Promethei Terra. Intermontane basin fill (HNbf) is found in low-lying basins among massifs of mountain material (Nm) and basin-rim material (Nh_1), and is believed to be composed of materials eroded from the adjacent massifs. Smooth plains material (Hps) in this part of the Promethei Terra may consist of sediments eroded from the adjacent highlands by valley networks within intermontane basin fill. (Geologic units and contacts shown in this and other Promethei Terra images are defined in Mest [1998] and Mest and Crown [2001a, 2002b, 2003a]. Locations of contacts (orange lines) shown in images for Promethei Terra and Libya Montes are approximate.) Here intermontane basin fill is characterized by a smooth surface dissected by integrated valley networks. The slopes of some massifs (arrows) are dissected by gullies, some of which head near the massif crests. The locations of Figures 5.5 and 5.10b-d are indicated. Mosaic composed of Viking Orbiter images 411S16, 411S17, 411S18 and 411S19; resolutions = 97 m/pixel. North is to the upper left corner; centered at 39°S, 254°W; illumination from left.

Crown, 2001b, 2002b, 2003a]. The presence of intermontane basin fill provides evidence for a complex sequence of erosional and depositional events within the highlands. Analysis of high-resolution MOC images shows most surfaces, including rugged highland, intermontane basin fill, and even valley floors, are covered by a smooth unit (Figure 5.5) similar to the mantling unit identified by Mustard et al. [2003] that is observed in many mid- to high-latitude highland terrains. This mantling unit tends to be modified by mass wasting more readily on steeper slopes, such as highland massifs, crater rims and interior walls, and valley walls resulting in the formation of lobate features suggestive of flow and accumulation zones at the bases of slopes. This material is also observed to be diverted into adjacent valleys and may likely completely fill smaller valleys, thus obscuring the fluvial record of this part of the highlands.

The Promethei Terra study area is near three major volcanic centers - Hadriaca Patera (29°S, 264°W), Tyrrhena Patera (23°S, 253°W), and Hesperia Planum - that could have had an affect on the hydrologic development of this part of the highlands. Hadriaca Patera is located in the northwest part of Figure 5.2 and Tyrrhena Patera is located just north of the study area [Crown and Greeley, 1990; Greeley and Crown, 1990]. Hadriaca and Tyrrhena Paterae consist of smooth-floored central calderas [Crown et al., 1992] surrounded by flanks that are highly dissected by well-incised, theater-headed, v-shaped and broad, flat-floored troughs that radiate from their summit regions [Gulick and Baker, 1990; Crown et al., 1992; Crown and Greeley, 1993]. Layering is exposed within the volcanoes' flank materials and have been interpreted as zones of welded pyroclastic deposits exposed by erosion [Crown and Greeley, 1993]. The Tyrrhena Patera flank flow unit extends ~1000 km from Tyrrhena Patera's western flank, and is found in the northwest part of the study area. The flank flow unit is composed of numerous lobate flows, leveed channels, collapsed lava tubes, and orthogonal sets of ridges, suggesting the flank flow is composed of lava flows, perhaps basaltic in composition [Crown et al., 1992]. Hadriaca Patera and Tyrrhena Paterae are believed to be late Noachian to early Hesperian in age, whereas the flank flow is believed to be late Hesperian to early Amazonian [Crown et al., 1992].

Hesperia Planum (Figures 5.1) is one of many areally extensive volcanic plains-forming units, known as 'ridged plains materials,' found on Mars [Scott and Tanaka, 1986; Greeley and Guest, 1987]. The ridged plains of Hesperia Planum extend into the northern and eastern parts of the study area (Figure 5.2). Potter [1976] and King [1978] showed that the ridged plains of

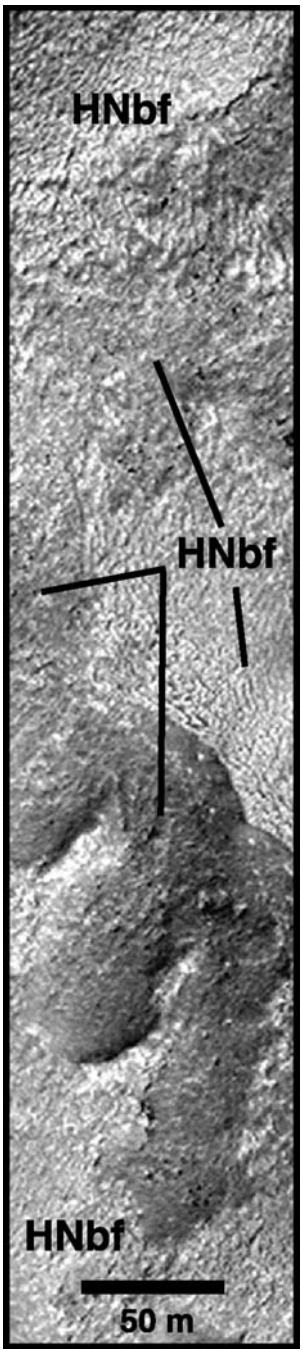

Figure 5.5. MOC image M12-01361 showing the surface of intermontane basin fill (HNbf). Close observation of highland surfaces in this and other MOC images reveals pitted surfaces that resemble mantling deposits found at mid- to high- southern latitudes of Mars [Mustard et al., 2003]. This suggests that many surfaces in Promethei Terra may be mantled with a volatile-rich deposit that has subsequently been removed from some steeper slopes or dissected by fluvial activity. Image centered at 38.74°S, 253.05°W; image width = 1.07 km; resolution = 1.39 m/pixel; illumination from upper left; NASA/JPL/MSSS.

Hesperia Planum embay portions of Tyrrhena Patera and other highland materials, and are interpreted to have been formed by very fluid lavas estimated to be about 1 km thick. The ridged plains of Hesperia Planum were probably emplaced as flood lavas extruded at high rates along fissure systems that spread rapidly among more rugged highland terrains, filling in low-lying regions [Greeley and Spudis, 1981; Greeley and Guest, 1987]. Two orthogonal sets of wrinkle ridges are observed in Hesperia Planum - NE-SW (Hellas-radial) and NW-SE (Hellas-concentric) [King, 1978; Watters and Chadwick, 1989]. Wrinkle ridges in Hesperia Planum are interpreted to be tectonic in origin, most likely by compression of the ridged plains materials [Watters and Chadwick, 1989]. The ridged plains of Hesperia Planum define the base of the Hesperian Epoch [Tanaka, 1986] and is thus early Hesperian in age [Greeley and Guest, 1987].

Highland materials are surrounded and embayed by a Hesperian-aged smooth plains unit (Figures 5.4 and 5.6a), which is interpreted to be composed of flood deposits from Reull Vallis and (or) sediments eroded from adjacent highland massifs via valley networks [Mest and Crown, 2001b, 2002b, 2003a] or by mass wasting [Mest and Crown, 2001b, 2002b, 2003a; Pierce and Crown, 2003]. Highland degradation is also preserved as Amazonian- and Hesperian-aged channeled (Figures 5.6) and dissected (Figure 5.7) plains. These units are characterized by smooth surfaces dissected by narrow, sinuous channels and low-relief scarps. The scoured nature, combined with patches of smooth deposits, of dissected and channeled plains suggests large volumes of water flowed over their surfaces causing localized erosion and redistribution of sediments [Mest and Crown, 2001b, 2002b, 2003a].

Surface and subsurface fluids are believed to have been responsible for the formation of four large mid- to Late Hesperian-aged outflow systems in the eastern Hellas region - Reull, Dao, Niger and Harmakhis Valles (Figures 5.2 and 5.6). The anatomies of the four systems are relatively similar, consisting of theater-headed source basins connected to their main canyons by areas of collapsed and scoured plains [Crown et al. 1992, 2004; Mest 1998; Price 1998; Mest and Crown, 2001b]. Gullies are found along the walls of Dao Vallis and nearby craters [Malin and Edgett, 2000; Crown and Mest, 2001] and are believed to have formed by release of fluids from aquifers and (or) melting of surface snowpacks [Christensen, 2003]. Their presence is consistent with earlier suggestions that groundwater systems may have been active in producing many of the features east of the Hellas basin [Crown et al., 1992; Squyres et al., 1987; Tanaka and Leonard, 1995; and Mest, 1998].

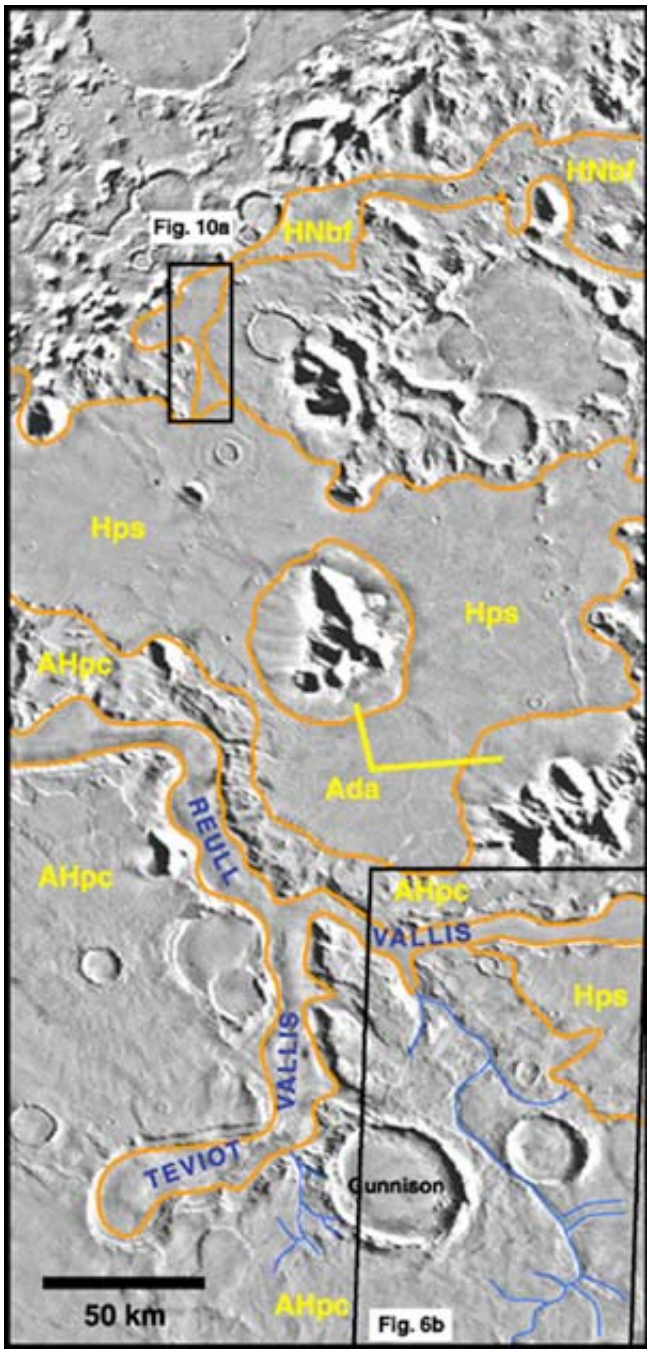

Figure 5.6. (a) Viking MDIM 2.0 photomosaic showing highlands and intermontane basin fill (HNbf) bordered by smooth (Hps) and channeled (AHpc) plains that were emplaced via sedimentary and (or) volcanic processes and subsequently dissected by the Reull and Teviot Valles systems and smaller valley networks [Mest, 1998; Mest and Crown, 2001b, 2002b, 2003a]. Many massifs display large debris aprons (Ada) extending from their bases. The locations of Figures 5.6b and 5.10a are indicated. Centered at 41.5°S, 257°W.

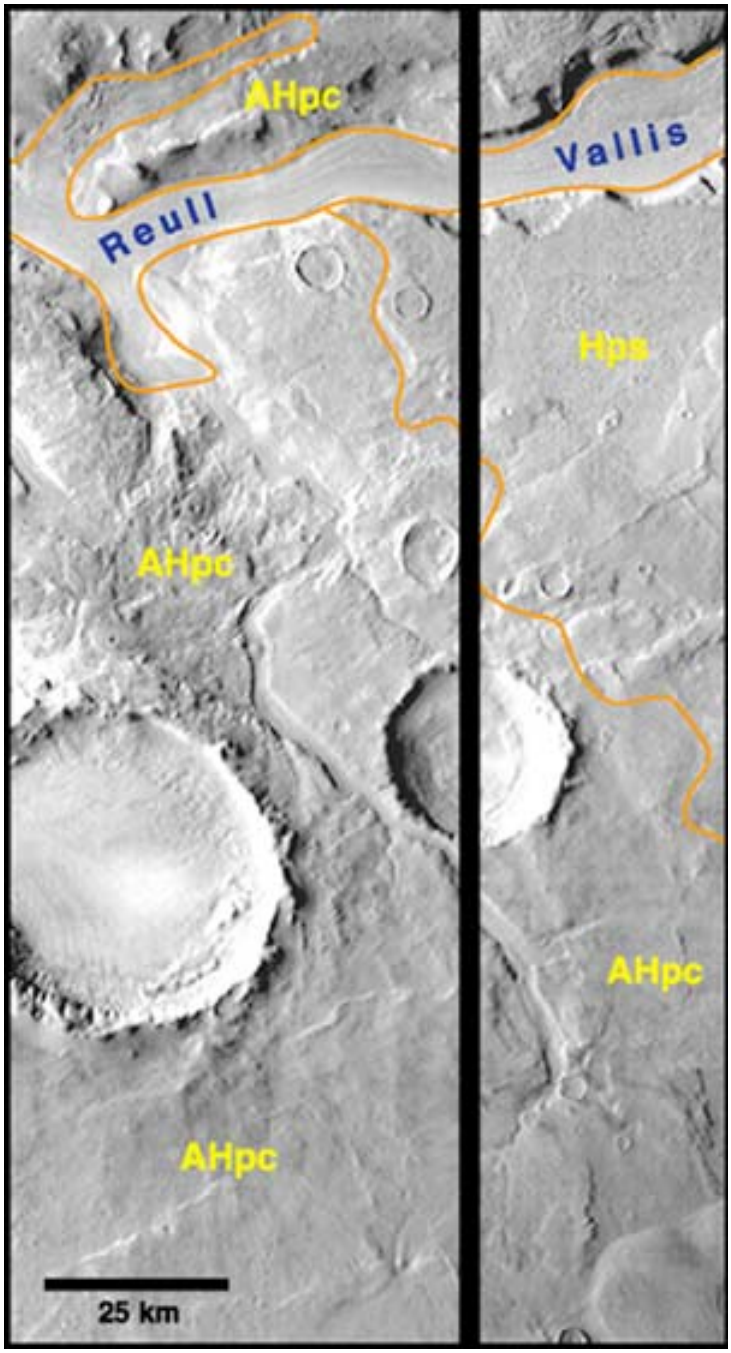

Figure 5.6 (continued). (b) THEMIS daytime infrared image mosaic showing a flat-floored valley (center) and its tributaries dissecting the channeled plains and merging with Reull Vallis. This and other small systems within the channeled plains indicate the role of fluvial activity in modification of this unit [Mest, 1998; Mest and Crown, 2001b, 2002b, 2003a]. Mosaic composed of THEMIS images (left to right) I06688002 (image width = 30.4 km, resolution = 95 m/pixel), I08548002 (image width = 30.1 km, resolution = 94 m/pixel) and I08523003 (image width = 30.4 km, resolution = 95 m/pixel); illumination from upper left; NASA/JPL/ASU.

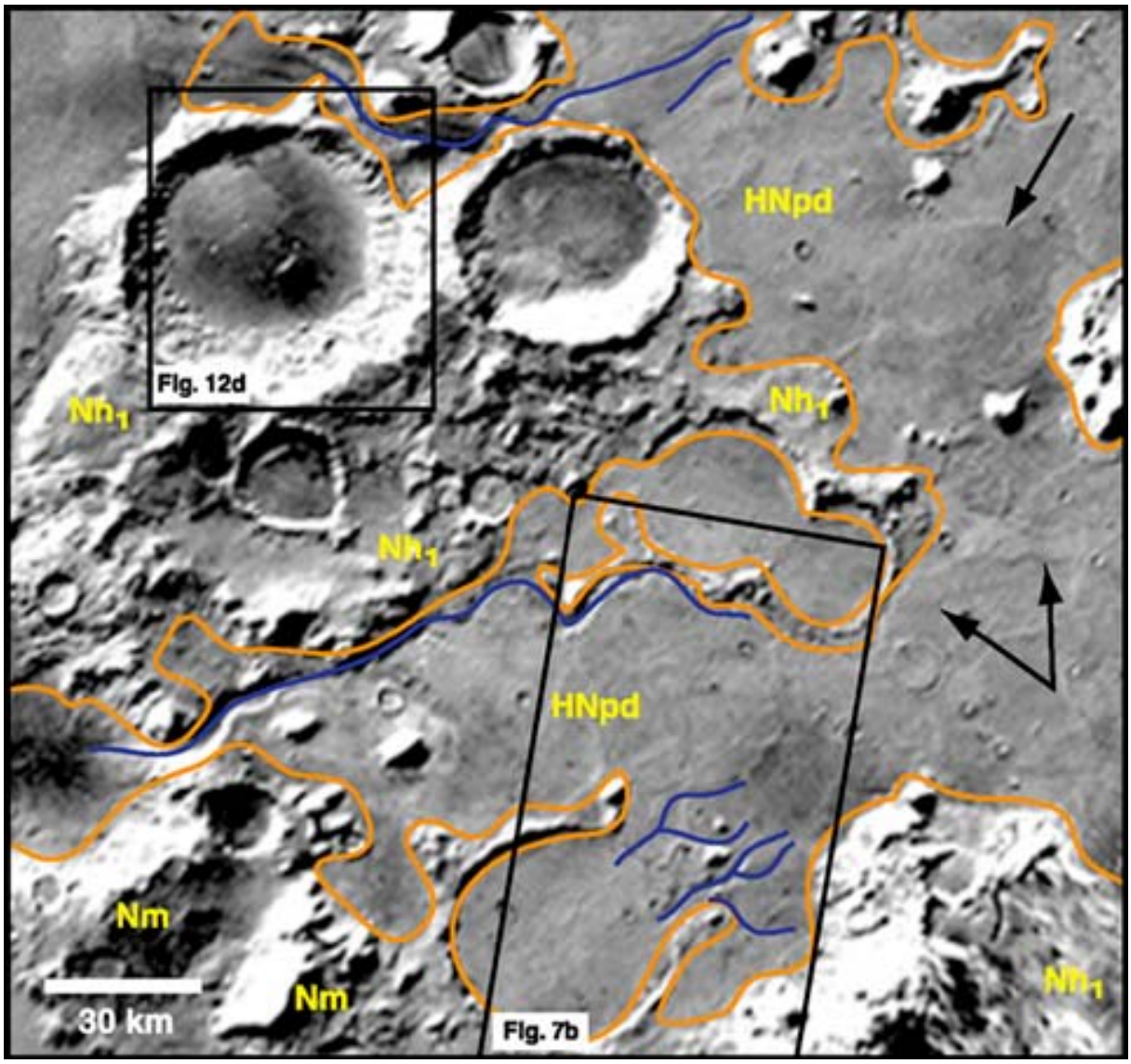

Figure 5.7. (a) Viking MDIM 2.0 photomosaic showing highland materials (mountainous material (Nm) and basin-rim unit (Nh_1)) bordered by dissected plains (HNpd) that were emplaced via sedimentary and (or) volcanic processes and subsequently dissected by small valleys and low-relief scarps (arrows) [Mest, 1998; Mest and Crown, 2001b, 2002b, 2003a]. The locations of Figures 5.7b and 5.12d are indicated. Centered at 36.5°S, 258°W.

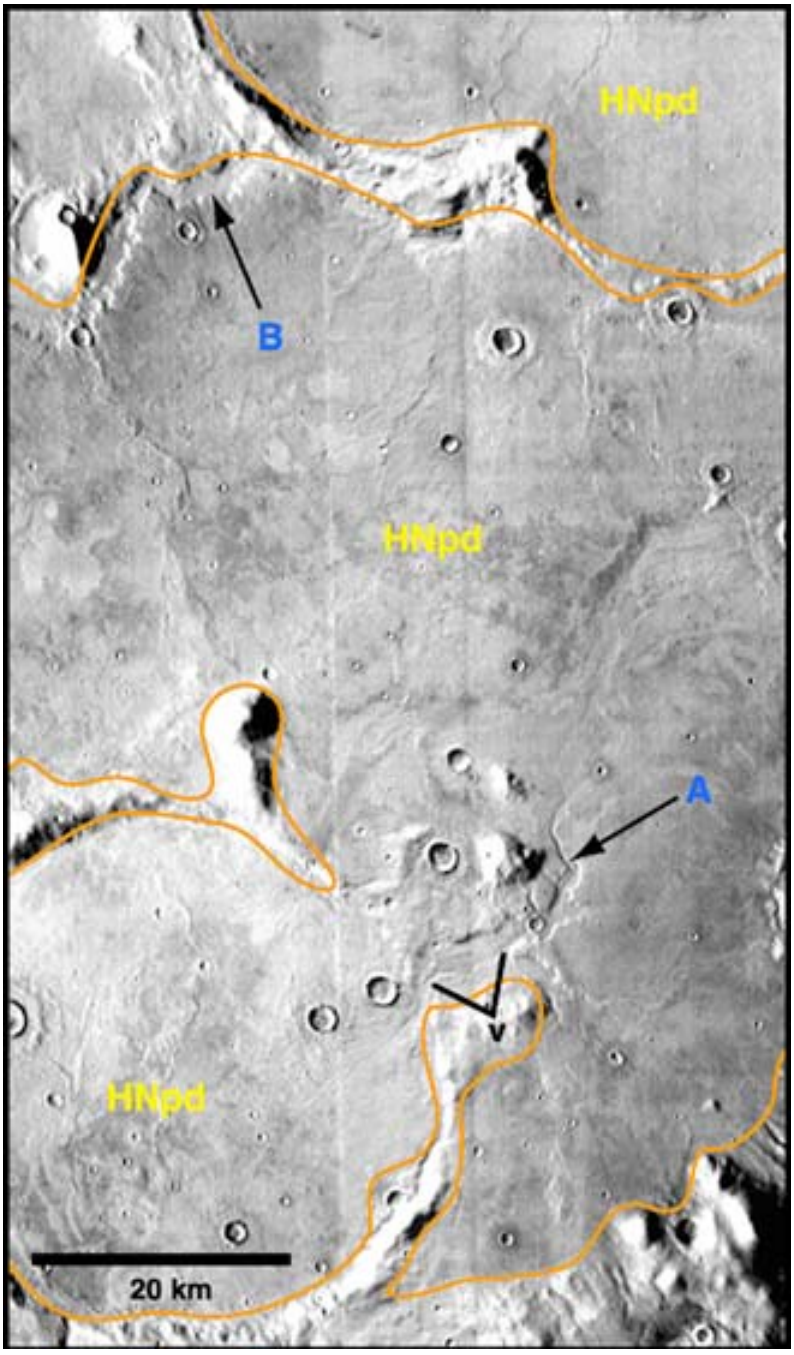

Figure 5.7 (continued). (b) THEMIS daytime infrared image mosaic showing a small network of valleys (A) dissecting the plains; the broader valley appears to contain a narrow channel (c) incised within the valley floor. Another valley (B) is observed along the contact of the plains and impact crater rim materials. Mosaic composed of THEMIS images (left to right) I08211002 (image width = 30.72 km, resolution = 96 m/pixel), I01882002 (image width = 30.72 km, resolution = 96 m/pixel) and I06713002 (image width = 30.4 km, resolution = 95 m/pixel); illumination from left; NASA/JPL/ASU.

Eolian, mass wasting, and fluvial activity appear to have formed some of the youngest (Late Hesperian to Amazonian) deposits in the Promethei Terra study area, including debris aprons and smooth, lineated, and pitted materials that fill craters [Crown et al., 1992; Tanaka and Leonard, 1995; Mest 1998; Price 1998; Leonard and Tanaka, 2001; Mest and Crown, 2001b, 2002b, 2003a; Pierce and Crown, 2003]. Debris aprons (Figure 5.6a) are believed to consist of unconsolidated debris mass-wasted from highland massifs and ice [Squyres and Carr, 1986; Zimbelman et al., 1989; Crown et al., 1992; Pierce and Crown, 2003]. Most large-scale aprons are found at the bases of massifs of ancient highland materials, but others occur along interior crater and vallis walls, and are believed to be Amazonian in age. Crater filling materials cover the floors of most craters in Promethei Terra and range from Hesperian to Amazonian in age; these materials are believed to have had a variety of sources including material eroded from interior crater walls by fluvial processes, lacustrine deposits, coalesced debris aprons, and eolian deposits. Finally, eolian activity, small-scale gully formation, and mass movements on vallis and crater walls, visible in MOC images, are among the youngest geologic processes operating in Promethei Terra.

5.2.2 Libya Montes

The Libya Montes study area (5°N to 5°S, 260° to 280°W) forms the southern rim of the Isidis impact basin (Figure 5.3). Previous mapping studies [e.g., Crumpler, 1998, 1999; Crumpler and Tanaka, 2003] have shown that geologic materials in Libya Montes are similar in type and age, ranging from middle Noachian to late Hesperian, to those previously discussed in Promethei Terra. The Libya Montes study area slopes ~6% (0.6°) [Crumpler and Tanaka, 2003] to the north toward Isidis Planitia. The oldest materials found in Libya Montes, and possibly on Mars [Scott and Tanaka, 1986; Greeley and Guest, 1987], include Noachian-aged massif materials (Figures 5.8 and 5.9)[10] that form rugged mountainous features that are likely the remnants of former

[10]See Figure 2 in Crumpler and Tanaka [2003] for a detailed geologic map of the Libya Montes units discussed in this text.

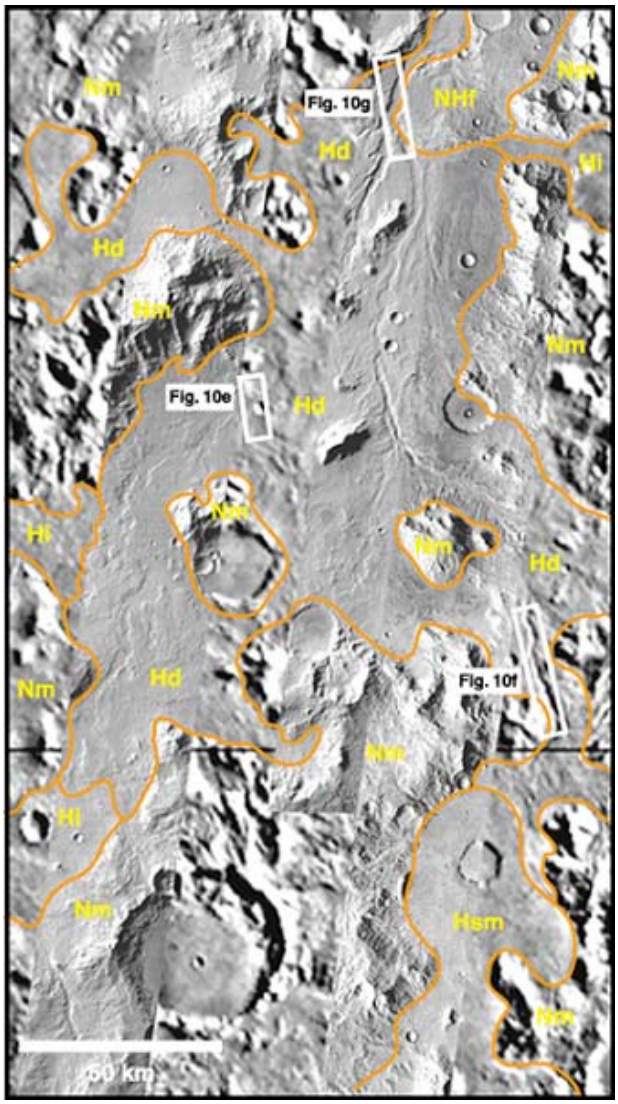

Figure 5.8. Mosaic of THEMIS daytime infrared images and Viking MDIM 2.0 of Libya Montes. Most of the larger valley networks in the Libya Montes study area are incised within the dissected (Hd) and intermontane (Hi) plains materials identified by Crumpler [1997, 1998, 1999] and [Crumpler and Tanaka, 2003]. (Geologic units and contacts shown in this and other Libya Montes images are defined in Crumpler [1997, 1998] and [Crumpler and Tanaka, 2003].) These intermontane basin-filling materials are considered to be similar in origin to the intermontane basin fill in Promethei Terra (Figure 5.4), consisting of sediments eroded from adjacent highland massifs [Crumpler, 1997, 1998; Crumpler and Tanaka, 2003]. Networks within these units tend to form dendritic patterns. Other units shown: Nm = massif material; NHf = fluted and dissected material; Hsm = Syrtis Major flow material. The locations of Figures 5.10e-g are indicated. Centered at 1°N, 278.5°W. THEMIS images (left to right) include: I04441002 (image width = 31.36 km, resolution = 98 m/pixel), I04416005 (image width = 31.68 km, resolution = 99 m/pixel) and I01445005 (image width = 31.68 km, resolution = 99 m/pixel); illumination from upper left; NASA/JPL/ASU.

impact crater rims [Crumpler, 1998, 1999; Crumpler and Tanaka, 2003]. These ancient materials have been heavily modified by local drainage systems and eroded by small-scale valleys incised on the steeper slopes of individual massifs. The Noachian-aged fluted and dissected terrain (Figures 5.8 and 5.9) forms the "foothills" or broad lower slopes of massifs and crater walls. Fluted and dissected terrain is interpreted to consist of Isidis basin impact ejecta or materials shed from adjacent massif materials that were subsequently dissected by numerous local drainage systems and small-scale valleys [Crumpler, 1998, 1999; Crumpler and Tanaka, 2003].

Two Hesperian-aged plains units - intermontane plains material and dissected plains material - fill basins and are interpreted to be sedimentary in nature. Deposits of intermontane plains material and dissected plains material are believed to consist of flood or lacustrine deposits, as well as materials eroded from adjacent Noachian units by fluvial processes (Figures 5.8 and 5.9) [Crumpler, 1998, 1999; Crumpler and Tanaka, 2003]. These plains units are believed to be similar in origin and age to deposits of intermontane basin fill identified in the highlands of Promethei Terra [Mest and Crown, 2001b, 2002b, 2003a]. Exposures of both the intermontane plains and dissected plains materials form deposits in low-lying areas among highland massifs that tend to be isolated or connected by narrow tracts of material between massifs, and most deposits are incised with numerous well-developed valley networks.

The geologic history of Libya Montes and the southern rim of the Isidis basin are relatively similar to the history determined for Promethei Terra, but is simpler at local scales. Following the impact event that formed the Isidis basin, which emplaced Noachian-aged highland materials, extensive valley networks developed early in the Noachian [Crumpler and Tanaka, 2003]. These networks dissected Isidis basin ring structures and modified the highland terrains south of Isidis basin. The materials eroded from adjacent massifs were emplaced in low-lying areas to form localized basin-filling deposits. Valley development on steep slopes and near the summits of small massifs suggest this early period of fluvial activity was driven by runoff from precipitation or meltwater emitted from the base of an ice-rich mantling layer Crumpler and Tanaka [2003]. Short-term paleolakes also existed during this period of fluvial activity, mostly within impact craters whose rims were breached by valleys. Emplacement of lava flows in the western part of the study area (see the Figure 2 in Crumpler and Tanaka [2003]), originating from Syrtis Major Planum, occurred near the end of this early phase of fluvial activity. A second

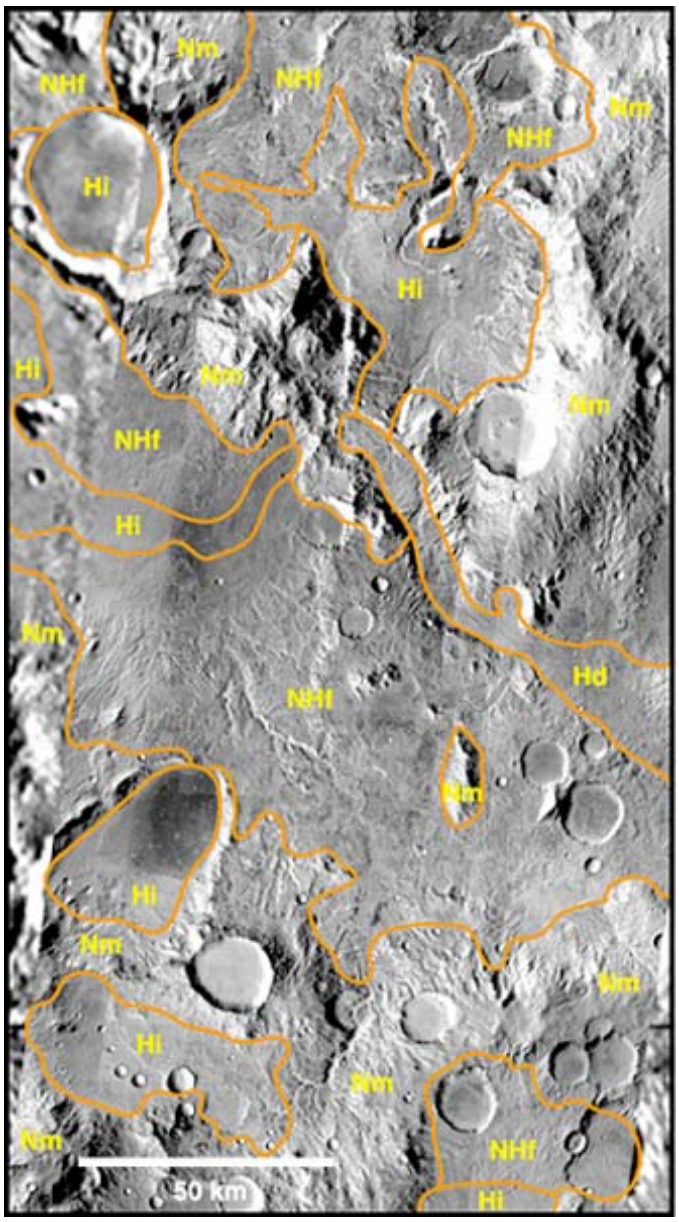

Figure 5.9. Mosaic of THEMIS daytime infrared images and Viking MDIM 2.0 of Libya Montes. Many exposures of the older units identified by Crumpler [1997, 1998, 1999] and [Crumpler and Tanaka, 2003], such as massif (Nm) and fluted and dissected (NHf) materials, are dissected by small networks of valleys. These valleys generally are found on steeper terrain and tend to form parallel patterns. Other units shown: Hd = dissected plains material; Hi = intermontane plains material. Centered at 2°N, 276°W. THEMIS images include (left to right): I03230002 (image width = 31.68 km, resolution = 99 m/pixel), I01058002 (image width = 31.68 km, resolution = 99 m/pixel), I01395005 (image width = 32 km, resolution = 100 m/pixel), I01033002 (image width = 31.68 km, resolution = 99 m/pixel), I01732010 (image width = 32 km, resolution = 100 m/pixel) and I02456002 (image width = 31.04 km, resolution = 97 m/pixel); illumination from upper left; NASA/JPL/ASU.

period of fluvial activity, believed to be the more intense than the first period of activity, followed and produced extensive systems of deeply incised valleys [Crumpler and Tanaka, 2003]. These valleys were incised within the Hesperian-aged basin-filling materials; much of the material eroded from these deposits was emplaced as broad fans at the termini of the larger channels along the highlands-Isidis basin contact. Finally, the most recent evidence for highland modification in Libya Montes exists as thin, sheet-like deposits probably emplaced by mass flows in a colder, dryer climate Crumpler and Tanaka [2003].

5.3 FLUVIAL FEATURES IN PROMETHEI TERRA AND LIBYA MONTES

Evidence for fluvial activity in the Promethei Terra and Libya Montes study areas is found in the forms of valley networks, degraded and in many cases gullied impact craters, and outflow channel systems. This section provides a detailed description of features in the two study areas interpreted to be fluvial in nature, with particular emphasis on the valleys incised within the various geologic materials of the highlands of Promethei Terra and Libya Montes.

5.3.1 Valley Networks

Highland materials in Promethei Terra and Libya Montes exhibit well-developed integrated valley networks and channels, and the flanks of Hadriaca Patera are incised with numerous valleys. Valley forms incised within highland materials, such as mountainous material and the basin rim unit in Promethei Terra and massif material and the fluted and dissected terrain in Libya Montes, occur as parallel valleys on steeper slopes or dendritic on lower slopes (Figures 5.4, 5.8 and 5.9) [Crumpler, 1998, 1999; Mest and Crown, 2001b, 2002b, 2003a; Crumpler and

Tanaka, 2003]. Most of these small-scale valleys terminate at the contacts with basin-filling sedimentary units indicating they are older than these units and may represent an early period of fluvial activity. However, some valleys continue onto the surfaces of these units and may indicate a later stage of fluvial activity that rejuvenated some of these small-scale highland valleys [Mest and Crown, 2001b, 2002b, 2003a; Crumpler and Tanaka, 2003]. Also, many of these valleys in both study areas extend to, or near, the summits of highland massifs and the rims of impact craters, which imply a precipitation-driven process, such as rainfall or snowmelt, as suggested by Mest and Crown [2001a, 2002b, 2003a] and Crumpler and Tanaka [2003].

Well-integrated valley networks are found predominantly within sedimentary materials that form intermontane basin fill in Promethei Terra (Figures 5.4 and 5.10a-d) [Mest and Crown, 2001b, 2002a,b, 2003a], and fluted and dissected terrain, intermontane plains material and dissected plains material in Libya Montes (Figures 5.8, 5.9 and 5.10e-g) [Crumpler, 1998, 1999; Crumpler and Tanaka, 2003]. These sedimentary units occupy the floors of many small, generally interconnected, basins bounded by ridges and massifs of ancient highlands and degraded impact craters. As a result, the valley networks found within these units tend to be confined by the bounding highlands and occur at smaller scales than those found within Tyrrhena Terra discussed in Chapter 4.0. Slopes within individual basins are generally similar to those in Tyrrhena Terra and range from 0.3° to 1.6° in Promethei Terra (average = 0.6°) and 0.2° to 0.6° in Libya Montes (average = 0.4°). These small-scale valley networks exhibit dendritic, (sub)parallel, or rectilinear patterns, which were most likely determined by the local slopes, as well as influenced by faults and fractures within and underlying the dissected deposits; patterns can also vary within a given basin. Some valleys, such as those mentioned above, continue headward into surrounding highland materials, whereas other valleys have theater-shaped heads within the basin-filling deposits. The largest drainage systems in both Promethei Terra and Libya Montes generally consist of multiple basins that are connected by single valleys that appear to have breached their divides [Mest and Crown, 2001b, 2002b, 2003a], which may be indicative of watershed growth. Although the networks in Promethei Terra and Libya Montes are small relative to other highland networks, they are believed to have contributed significant quantities of sediment to plains units where the valleys terminate. For example, several valleys incised within basin-filling materials that debouch from highland terrains have contributed sediments to smooth

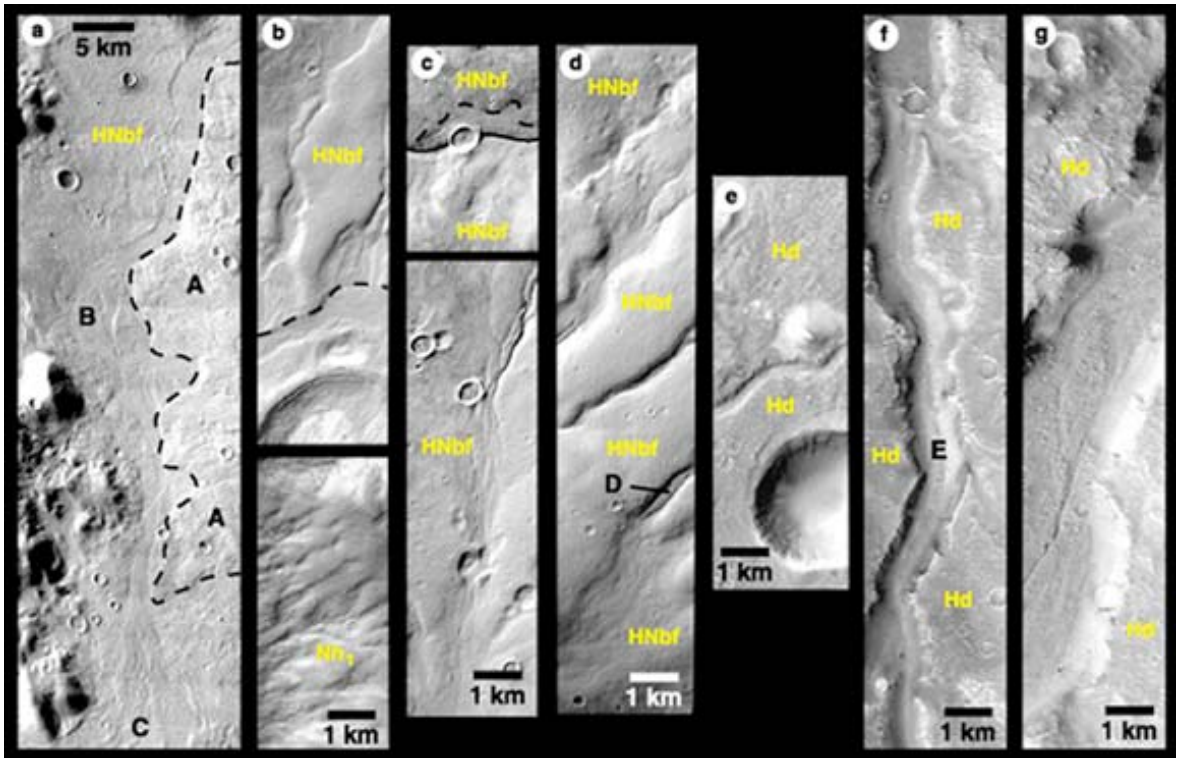

Figure 5.10. THEMIS and MOC views of valleys in Promethei Terra (a-d) and Libya Montes (e-g). (a) A broad valley erodes intermontane basin fill (HNbf) and the distal lobes of an ejecta deposit (A). The valley displays braiding (B) and a depositional fan (C) of material is observed near the bottom of the image. THEMIS visible image V01882003; image width = 17.66 km; resolution = 69 m/pixel; illumination from left; NASA/JPL/ASU. (b) (upper) Valleys dissecting intermontane basin fill are truncated (dashed line) by another valley. Narrow parallel gullies dissect the slopes of a highland massif (Nh_1) in (b) (lower). MOC image M02-02022; image width = 2.85 km; resolution = 2.78 m/pixel. (c) (upper) A valley (solid lines) dissects intermontane basin fill and is bissected by an impact crater; a scarp north of the crater (dashed line), a small notch in the crater's western rim, and lack of an associated ejecta blanket suggests flow within the valley (left to right) was active after the impact event. (c) (lower) Braiding is observed at the convergence of two valleys dissecting intermontane basin fill. Elongated deposits of material are found within the right converging valley, as well as in valley D in image (d), within which further incision has occurred. MOC image M03-02095; image width = 2.85 km; resolution = 5.56 m/pixel. (d) Additional examples of narrow valleys dissecting intermontane basin fill. MOC image R03-01056; image width = 2.99 km; resolution = 5.83 m/pixel. (e) A narrow tributary valley within dissected plains material and the wider trunk valleys in (f) and (g) show steep-walled, flat-floored morphologies. The upstream valley in (f) contains dune features (E) on its floor oriented perpendicular to the valley walls, whereas the valley in (g), located near the mouth of this network, is free of dunes. The valleys shown in (e), (f) and (g) are part of the "western valley" system in Crumpler and Tanaka [2003]. (e) MOC image M02-04206; image width = 2.95 km; resolution = 2.89 m/pixel. (f) MOC image R05-00869; image width = 3.06 km; resolution = 4.55 m/pixel. (g) MOC image R07-01965; image width = 3.12 km; resolution = 3.05 m/pixel. Illumination from upper left in all MOC images; NASA/JPL/MSSS.

plains material in Promethei Terra [Mest and Crown, 2001b, 2002b, 2003a] and terminal plains material that border Libya Montes and Isidis Planitia [Crumpler and Tanaka, 2003]. Debris fans form at the mouths of some valleys in both study areas, indicating rapid deposition of sediments, such as in an alluvial fan [Crumpler and Tanaka, 2003]. However, other valleys continue onto and fade away within these plains units with no apparent debris fans, suggesting flow decreased slowly as slopes shallowed from the highlands to the plains [Mest and Crown, 2001b, 2002b, 2003a; Crumpler and Tanaka, 2003].

Individual valleys in Promethei Terra and Libya Montes are relatively similar in size and morphology. These highland valleys are generally less than 1 km in width, and one to tens of kilometers in length for lower order tributaries and valleys on steep terrain and tens to hundreds of kilometers in length for higher order valleys within basin-filling materials [Mest and Crown, 2001a,b, 2002a,b, 2003a; Crumpler and Tanaka, 2003]. At all image scales (Viking Orbiter, THEMIS and MOC) valleys in Promethei Terra and Libya Montes appear relatively pristine (Figures 5.4 and 5.8-10). The larger valleys, such as those shown in Figure 5.10a, f and g, tend to have fairly steep banks and flat floors, whereas smaller tributaries are v-shaped in profile (Figure 5.10b-e). Most valleys in Promethie Terra and Libya Montes do not contain dune-forming deposits suggesting these valleys may not be infilled to the same degree as the valleys described in Tyrrhena Terra.

The flank materials of Hadriaca Patera are incised with numerous valleys that radiate from the volcano's summit (Figure 5.11). Most valleys are trough-shaped, lack tributaries, and are theater-headed near the summit. Narrow v-shaped channels are observed within some of the broader valley interiors suggesting a contribution by surface runoff; however, their overall morphology indicates that sapping has modified the channels [Gulick and Baker, 1990; Crown et al., 1992].

Valley network formation in Promethei Terra and Libya Montes is believed to have varied temporally among each of the terrains described above. Valley formation on the steeper highland terrains is believed to range from Middle Noachian to Lower Hesperian in age. These valleys contributed sediments to the low-lying parts of the highlands to form the basin-filling units. The more extensive valley networks, which subsequently eroded these basin-filling sedimentary deposits and contributed sediments to plains-forming units, are believed to be

Figure 5.11. The flank materials of Hadriaca Patera are incised with numerous broad valleys, some of which contain narrow v-shaped valleys (v). Fluvial erosion has exposed layering (arrows) within eroded flank material, possibly indicating welded pyroclastic deposits [Crown and Greeley, 1993]. THEMIS daytime infrared image I01146002; centered at 34.6°S, 269.7°W; image width = 30.7 km; resolution = 0.096 m/pixel; illumination from left; NASA/JPL/ASU.

Lower to Upper Hesperian in age [Mest and Crown, 2001b, 2002a,b, 2003a; Crumpler and Tanaka, 2003]. Overall, valley network formation in Promethei Terra and Libya Montes is relatively younger than network formation in Tyrrhena Terra (Upper Noachian to Lower Hesperian) discussed in Chapters 2.0 and 4.0.

5.3.2 Gullied Impact Craters

Several large craters (>10 km in diameter) in the study areas have degraded rims, parallel interior gullies that head near crater rims and terminate on crater floors, dissected or complete lack of ejecta blankets, and smooth floors [Squyres et al., 1987; Crumpler, 1998, 1999; Mest, 1998; Mest and Crown, 2001b, 2002b, 2003a; Crumpler and Tanaka, 2003]. The interior walls of many of these large craters are incised with narrow parallel gullies (Figure 5.12). Most of the gullies observed in Promethei Terra and Libya Montes do not resemble the gullies described by Malin and Edgett [2000] that have alcove heads, typically originate along a particular layer within a given outcrop and have debris fans at their termini. The gullies observed in Promethei Terra and Libya Montes head at various elevations within a given crater and many gullies head at or near the rims of craters. The morphologies of the gullies and the range of crater preservation suggest a combination of fluvial processes and mass wasting are likely responsible for erosion and degradation of craters in the highlands of Promethei Terra and Libya Montes [Craddock and Maxwell, 1993; Malin and Edgett, 2000]. Clearly, gully formation post-dates the impact craters in which the gullies are incised. This suggests gully formation in Promethei Terra and Libya Montes may be Middle Noachian to Upper Hesperian in age, providing some of the youngest evidence for fluvial activity in the two regions [Mest, 1998; Mest and Crown, 2001b, 2002a,b, 2003a; Crumpler and Tanaka, 2003].

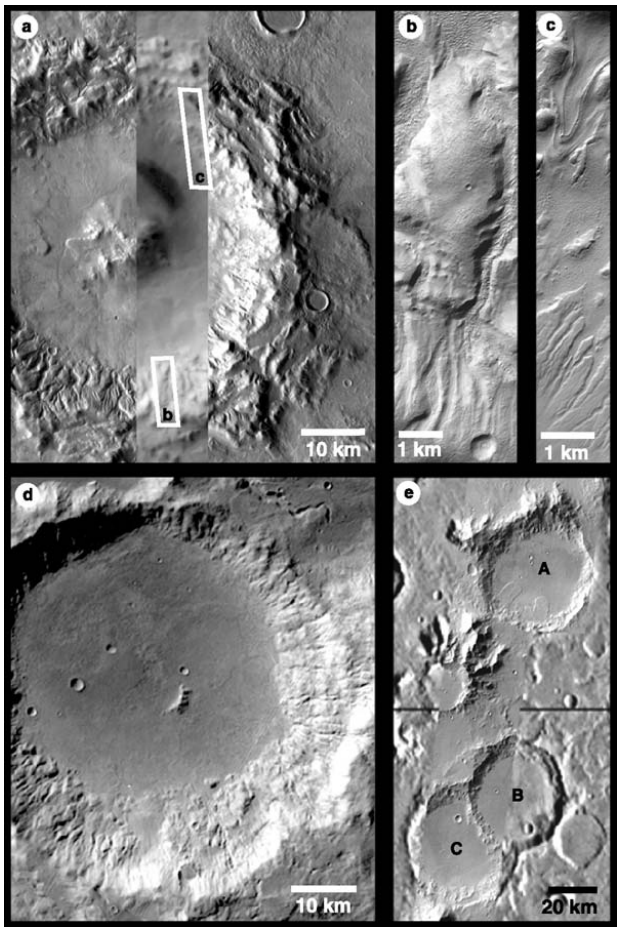

Figure 5.12. Gullies observed along the interior walls of impact craters in Promethei Terra (a-d) and Libya Montes (e), and appear to head near the crater rim crests. (a) Crater contains well-defined gullies in this THEMIS and Viking MDIM 2.0 mosaic. Centered at 39°S, 246.5°W; THEMIS daytime infrared images include (left to right): I06463002 (image width = 30.72 km, resolution = 96 m/pixel) and I07549002 (image width = 30.72 km, resolution = 96 m/pixel); NASA/JPL/ASU. (b) and (c) MOC images suggest mantling material [Mustard et al., 2003] may cover many surfaces in Promethei Terra, including crater walls. (b) Gullies (bottom) head near crater rim crest, and deep gullies (top) erode around a large smooth knob and are filled with debris that has moved down the gullies. MOC image M00-01617; image width = 2.84 km; resolution = 2.77 m/pixel; NASA/JPL/MSSS. (c) gullies along lower slopes of crater wall are parallel and incised within a smooth deposit; smooth material along upper slope has flowed downslope to form a lobate 'tongue'. MOC image M18-00897; image width = 2.67 km; resolution = 4.17 m/pixel; NASA/JPL/MSSS. (d) Parallel gullies in a crater in central Promethei Terra. Mosaic composed of Viking Orbiter images 411S08 and 411S10; resolutions = 97 m/pixel; centered at 35°S, 259°W. (e) THEMIS and Viking MDIM 2.0 mosaic showing gullies along the rims of three craters (diameters are A = 50, B = 45 and C = 50 km). Crater A shows the best examples of mass wasting in Libya Montes in the form of lobate debris aprons. Centered at 0°N, 262°W; THEMIS daytime infrared images include (left to right): I03604002 (image width = 31.68 km, resolution = 99 m/pixel) and I05127008 (image width = 32 km, resolution = 100 m/pixel); NASA/JPL/ASU. Illumination is from left in THEMIS and MOC images.

5.3.3 Outflow Channel Systems

The eastern Hellas region contains five large outflow channel systems - Reull, Teviot, Dao, Niger and Harmakhis Valles (~1200, 150, 230, 800, and 1500 km long, respectively) (Figures 5.2 and 5.6) - believed to be mid- to Late Hesperian in age [Crown et al., 1992, 2004; Tanaka and Leonard, 1995; Mest, 1998; Price, 1998; Crown and Mest, 1997, 2001; Mest and Crown, 2001b, 2002b, 2003a]. Their source areas consist of large steep-walled depressions formed by collapse of volatile-rich plains [Squyres et al., 1987; Crown et al., 1992, 2004; Mest, 1998; Price, 1998; Crown and Mest, 1997, 2001; Mest and Crown, 2001b]. The source areas are connected to their main canyons by areas of collapsed plains, of which portions contain lineations potentially indicative of scour and surface flow. The main canyons are steep-walled, flat-floored troughs with little sinuosity [Crown et al., 1992, 2004; Mest, 1998; Mest and Crown, 2001b, 2002b, 2003a]. The south-facing walls of Dao, Niger and Harmakhis Valles display gully systems (alcoves, channels, and debris fans) believed to have formed by water that emerged from a layer below the canyon rims [Malin and Edgett, 2000; Crown and Mest, 2001; Gilmore and Phillips, 2003]. The valles cut into various highland and plains materials as they extend toward Hellas basin [Greeley and Guest, 1987; Crown et al., 1992, 2004]; Dao and Harmakhis breach the basin rim and terminate on the basin floor. Vallis floor material consists of remnants of the collapsed plains and contributions from wall collapse [Crown et al., 1992, 2004; Mest, 1998; Crown and Mest, 1997, 2001; Mest and Crown, 2001b, 2002b, 2003a]. The valles most likely formed by a combination of collapse and sapping with localized surface flow that eroded the plains [Squyres et al., 1987; Crown et al., 1992, 2004; Mest, 1998; Mest and Crown, 2001b, 2002b, 2003a].

5.4 HYDROLOGIC MODELING IN PROMETHEI TERRA AND LIBYA MONTES

Hydrologic mapping and modeling of valley networks in the Promethei Terra and Libya Montes regions of Mars has been used to derive the hydrologic history of this part of the martian highlands. This section first provides a general description of the image and topographic data sets used in this study and their usage within the Arc/Info Geographical Information System. The hydrologic modeling technique, outlined in detail in Chapter 4.0, is then described as it pertains to these study areas.

5.4.1 Data sets

Preexisting hydrologic maps for the Promethei Terra and Libya Montes study areas were used for analysis. Previous studies by Mest and Crown [2001a, 2002b] for Promethei Terra provided detailed hydrologic maps at the 1:1M scale, adequate for comparison to watersheds generated using automated techniques. Maps produced by Crumpler [1998, 1999] and Crumpler and Tanaka [2003] cover only a portion of the Libya Montes study area and were used to complement mapping of valleys outside of their map area. The above studies used combinations of Viking Orbiter (10-90 m/pixel), THEMIS infrared (day) and visible (~100 and 20 m/pixel, respectively) and MOC narrow angle (1-8 m/pixel) and wide angle (~237 m/pixel) images to identify valleys. Valleys in Promethei Terra (Figure 5.13) and Libya Montes (Figure 5.14) are shown on Mars Mosaicked Digital Image Model (MDIM) version 2.0 base (231 m/pixel). High-resolution MOLA DEMs (128 pixel/degree) of the study areas, generated from MOLA gridded topographic data, were imported into Arc/Info in ascii format and converted to Arc/Info GRIDs. The DEM data layers were projected into sinusoidal coordinate systems using Mars1990 (IAU1990) as the martian spheroid, where the semi-major and semi-minor axes equal 3,393,400 m and 3,375,730 m, respectively (this spheroid is used for all subsequent martian data layers) [Trent Hare, personal communication; 'spheroids.dat' file available by downloading

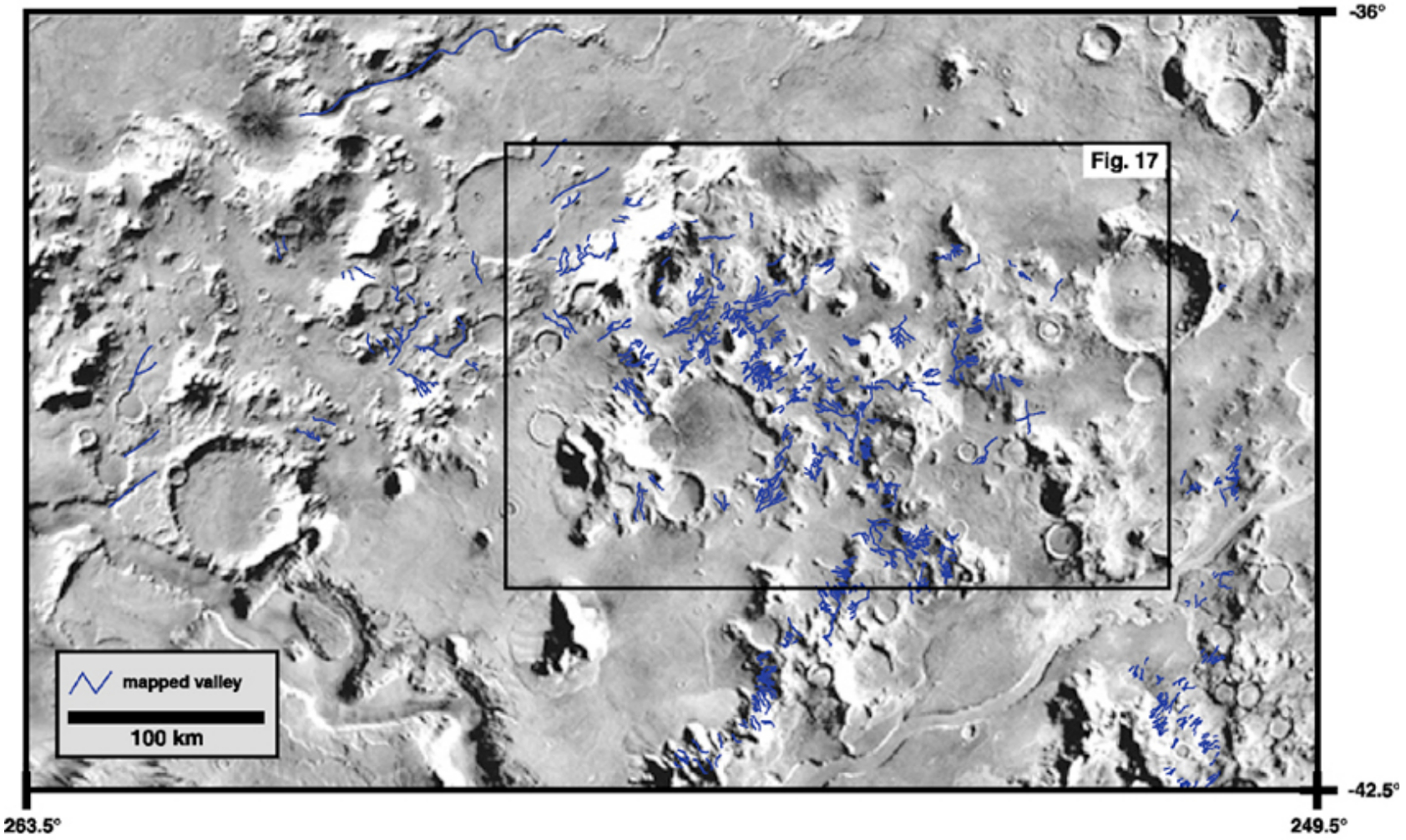

Figure 5.13. Viking MDIM 2.0 photomosaic showing the highest concentration of valley networks mapped within the highlands of Promethei Terra. Location of Figure 5.17 is shown.

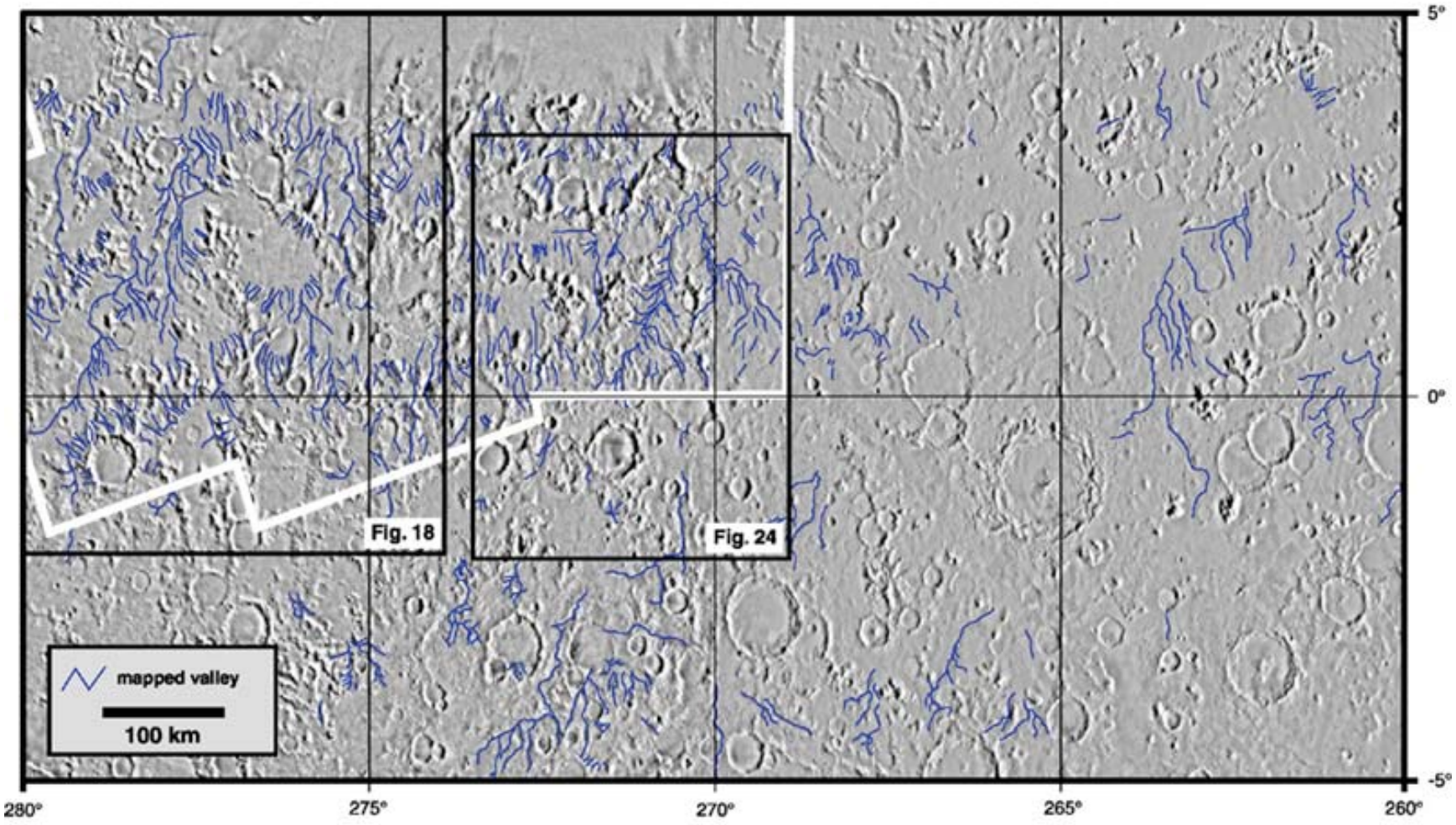

Figure 5.14. Viking MDIM 2.0 photomosaic showing the distribution of valley networks mapped within the highlands of Libya Montes. Heavy white line indicates part of the map area of Crumpler and Tanaka [2003]. Location of Figures 5.18 and 5.24 are shown.

'planetary_projection4_1.zip' from ftp://ftpflag.wr.usgs.gov/dist/pigpen/arcview_extensions/]. Sinusoidal projection was used because it is adequate for small-scale usage and for low- to mid-latitude regions, and it is an equal-area projection, appropriate for calculation of parameters such as drainage basin area [Snyder, 1982].

5.4.2 Methodology

Drainage divides and valley networks were modeled with standard techniques that have been successfully used to model terrestrial drainage networks [e.g., O'Callaghan and Mark, 1984; Jenson, 1991; Tarboton et al., 1991; Thieken et al., 1999; Turcotte, et al., 2001; Vogt et al., 2003] using the methodology described in Chapter 4.0. The model extracts divides and networks using four Arc/Info GRID functions - FILL, FLOWDIRECTION, WATERSHED and FLOWACCUMULATION - from high-resolution MOLA DEMs (128 pixel/degree = 0.0078125 degree/pixel) of the Promethei Terra and Libya Montes study areas. A drainage basin is defined here as the area surrounded by a continuous topographic divide within which all water (surface and subsurface) flows downslope to a point where the water crosses the divide.

One of the most critical aspects in the modeling was to determine the sink-fill depth (FILL function - see Chapter 4.0) that generated drainage divides containing the networks observed in image data sets and produced stream systems that approximated the positions of individual valleys and the scales of the networks observed. Using the MOLA DEMs for Promethei Terra (PT) and Libya Montes (LM), the SINK function was run on the data sets to identify sinks, and histograms were produced to observe the distribution of sinks versus sink-fill depth. As discussed in Chapter 4.0, a standard procedure was used for the first few iterations of the model and includes running the FILL function for SFDs equal to the 0 (zero) m, the mean sink depth, and ± one-half the mean sink depth. For the PT and LM 128 pixels/degree MOLA DEMs, the first iterations of the model used SFD's equal to 0.0 (zero) m, the mean sink depths (PT, 826.3 m; LM, 1102 m), and 413 m and 1240 m (PT, ± one-half the mean) and 551 m and 1653 m (LM, ± one-half the mean). The resulting watershed and network GRIDs were overlain on the network maps described above to compare the accuracy of the modeled watersheds. As in

Chapter 4.0, two criteria were used to determine which model iteration(s) most closely approximated the mapped networks. (1) Do the number of drainage basins approximate the number of mapped networks and do the drainage divides enclose the mapped networks? And (2) are the locations and numbers of the modeled valleys roughly equivalent to the mapped valleys? Analyses of these criteria determined whether additional iterations should be run.

Multiple iterations of the model were run for both Promethei Terra and Libya Montes using sink-fill depths that spanned the ranges of 0 m to the mean SFD in each DEM (see 'Results'). Unlike the large-scale networks analyzed in Tyrrhena Terra in Chapter 4.0, these iterations did not provide "ideal" SFDs that delineated drainage divides that adequately enclosed mapped networks **and** extracted networks that accurately approximated the positions of most of the mapped valleys. Over the course of all of the iterations run for both areas, it was observed that modeled valleys match the best for larger, higher order valleys observed in the image data sets, whereas smaller valleys, such as higher order tributaries and closely spaced small-scale valleys, show the most discrepancies. Therefore, data from two sample iterations for both Promethei Terra (SFD = 30 m and 100 m) and Libya Montes (SFD = 180 m and 300 m) are shown in this study. Selection of these iterations is based on the following criteria: sink-fill depths show clear separation, the modeled data display obvious changes in the numbers and sizes of drainage basins identified, and given the above caveat, modeled valleys reasonably approximate the locations of valleys observed in image data sets.

It is important to note here that a combination of the small-scale of the watersheds being analyzed and close spacing of narrow valleys relative to DEM resolution greatly affect the ability of Arc/Info to accurately predict the locations of valleys visible in the image data sets. Impact craters are abundant in a wide range of sizes and states of preservation in Promethei Terra and Libya Montes, and impact crater rims commonly form parts of drainage divides. Furthermore, using any given SFD, impact craters are frequently delineated as individual drainage basins. It was shown in Chapter 4.0 that as SFD increased the number of drainage basins decreased as basins merged; however, as the "ideal" SFD was approached, rarely were impact craters incorporated as parts of drainage basins. For PT and LM this is not the case; given the small scale of watersheds in these areas, which occur at the same scales as impact craters, altering the SFD readily incorporates impact craters into watersheds. In some cases, image data shows evidence for breached crater rims and these mergers of watersheds and craters is justified, but in

most cases the craters are not breached, but are simply as deep as the SFD applied and are therefore "flooded" by the model and incorporated with adjacent basins. Flooding and incorporation of unbreached craters into drainage basins then results in inaccurate extraction of valley networks, typically involving extension (mouthward or headward) of valleys into these craters. In addition, many valleys observed in PT and LM are narrow and closely spaced on steep highland slopes. The 128 pixels/degree DEMs used in this study contain much interpolation between MOLA tracks; this interpolation is greatest at the equator where MOLA tracks are spaced ~1 km apart on average and decreases toward the poles as MOLA tracks converge [Craddock and Irwin, 2004]. This interpolation could affect the ability of Arc/Info to accurately extract those narrow closely spaced valleys regardless of the SFD selected.

Terrestrial drainage basins are generally delineated by divides that include ridges formed tectonically, volcanically, or by continued erosion. These features also commonly form drainage divides on Mars, but in the highlands of Promethei Terra and Libya Montes there is also an abundance of impact craters whose rims form parts of drainage divides delineated by the model. Impact craters make effective divides by collecting and distributing water and sediment to crater floors, but they are also observed to disrupt drainage paths, or they form closed watersheds either adjacent to or within other drainage basins. Various techniques to identify martian drainage divides, including stereo pairs [Boothroyd and Grant, 1985; Grant, 2000] and the most headward extension of tributaries [Kochel et al., 1985; Baker and Partridge, 1986].

Unlike Tyrrhena Terra, there are very few pre-fluvial craters observed in drainage basins in both Promethei Terra and Libya Montes that could have disrupted valley formation, and very few post-fluvial craters to affect modeling results. In Libya Montes, according to the Crumpler and Tanaka [2003] map, only 3 craters are shown with ejecta deposits and they are located within Isidis Planitia north of the limits of this study area. The Crumpler and Tanaka [2003] map shows no ejecta materials within Libya Montes, which suggests that there are no craters with clearly defined ejecta deposits, at least within their map area. Analysis of Libya Montes outside of the Crumpler and Tanaka [2003] map area, using their crater morphology as a guide, showed very few large, young craters within the study area that could have disrupted valley formation or affected the model results. In both study areas, most fresh craters that occur within basins are smaller (D<2-3 km) than what is necessary to adequately disrupt valley development influence the locations of extracted valleys. Similar to Promethei Terra, image analysis shows that most

young. Thus it can be stated that the geologic and hydrologic scenarios, in the context of the temporal relationships between impact crater formation and valley network development, in Promethei Terra and Libya Montes are similar to that observed in Tyrrhena Terra (Chapters 2.0 to 4.0). In PT and LM, the model does not appear to be affected by large-diameter (D>3 km) post-fluvial impact craters because they are not present in these areas, and the topographic effects from small-diameter (D<3 km) craters are negligible. This is reasonably consistent with the "younger" ages of network formation determined for Promethei Terra [Mest and Crown, 2002b, 2003a] and Libya Montes [Crumpler, 1998, 1999; Crumpler and Tanaka, 2003] relative to Tyrrhena Terra, that is most valley formation occurred after formation of large craters.

5.5 RESULTS

Hydrologic morphometric parameters, listed in Table 4.4, were calculated for drainage basins and valley networks modeled in Promethei Terra and Libya Montes. This section discusses the morphometric data - including drainage density, stream orders, bifurcation and length ratios, and relief morphometry - extracted from applications of the model (described in Chapter 4.0) on MOLA DEMs of the Promethei Terra and Libya Montes study areas. In addition, comparisons of these data are made to data extracted for mapped and modeled drainage basins and valley networks in Tyrrhena Terra, as well as several terrestrial examples.

The following results are based on basin divides and networks modeled using sink-fill depths equal to 30 m and 100 m (PT) and 180 m and 300 m (LM). These sink filling corrections identified 2104 pixels (93%) and 573 pixels (98%), respectively, in the Promethei Terra DEM, and 339 pixels (97%) and 212 pixels (98%), respectively, in the Libya Montes DEM as sinks relative to the total pixels in these scenes (PT = ~5.1 million pixels; LM = ~3.3 million pixels). These percentages are comparable to corrections made to terrestrial DEMs that contain 0.9 to 4.7% percent of cells that are sinks [Tarboton et al., 1991]. Hydrologic modeling at SFDs of 30

m and 100 m for Promethei Terra yielded 2189 and 601 drainage basins, respectively, and at SFDs of 180 m and 300 m for Libya Montes yielded 352 and 224 drainage basins, respectively. Because the model automatically extracts networks to the edge of each DEM, numerous networks were delineated with no associated divides that presumably extend beyond the limits of the DEMs. Image analyses show that drainage divides in both study areas consist of impact crater rims and ridges associated with upland terrains. In Promethei Terra, 456 basins (21%; SFD = 30 m) and 294 basins (49%; SFD = 100 m) correspond to impact craters, whereas in Libya Montes, 194 basins (55%; SFD = 30 m) and 151 basins (67%; SFD = 100 m) correspond to impact craters. The results discussed in the following sections focus on 29 (SFD = 30 m) and 10 (SFD = 100 m) drainage basins in central Promethei Terra that encompass the majority of fluvial networks mapped in Mest and Crown [2001a, 2002b, 2003a] (Figures 5.15a and b), and 37 (SFD = 180 m) and 20 (SFD = 300 m) drainage basins in Libya Montes (Figure 5.16a and b).

5.5.1 Drainage Basin Morphology

Comparison of mapped and modeled watersheds for the representative basins selected in Promethei Terra and Libya Montes show significant inconsistencies for both the locations of valleys and the amounts of dissection produced by the model. The highest order valleys (fourth and fifth order) modeled at all sink-fill depths in both areas show the best matches with the location of mapped valleys, but accuracy of the locations and numbers of modeled valleys significantly decreases for lower order streams for the reasons stated previously regarding DEM resolution versus valley size and spacing. Regional differences between mapped and modeled networks can be seen in Figures 5.13 and 5.15 for Promethei Terra and Figures 5.14 and 5.16 for Libya Montes. A closer look at some of the more "highly dissected" terrains within the study areas (Figures 5.17 and 5.18) provides a more detailed view of the inconsistencies between mapped valleys observed in the image data sets compared to valleys derived from the topography. In Promethei Terra and Libya Montes, numerous mapped valleys are observed to cross drainage divides at the sink-fill depths shown for both areas, as well as for most of the

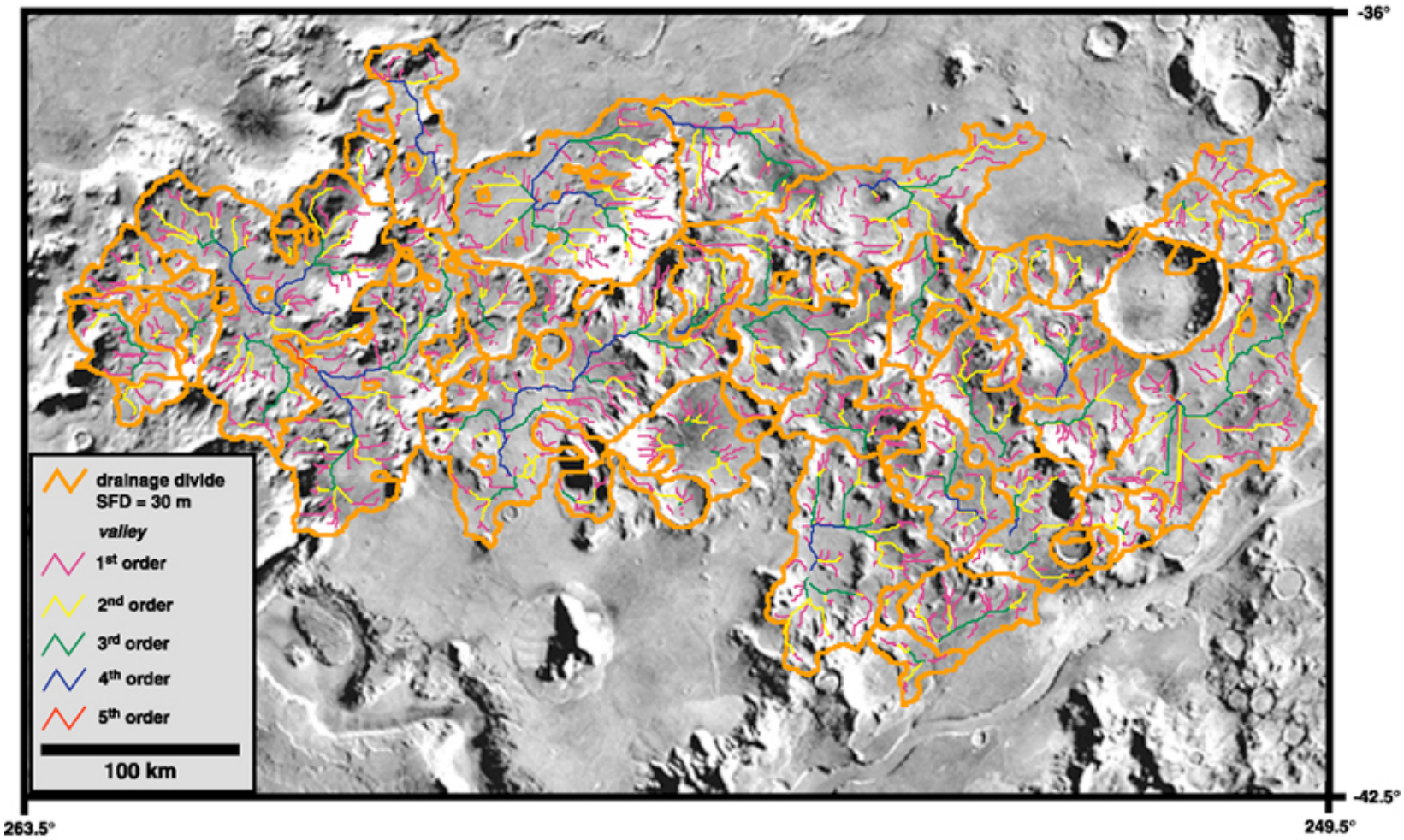

Figure 5.15. Selected drainage basin divides and valley networks in Promethei Terra extracted from Arc/Info using sink-fill depths of (a) 30 m and (b) 100 m (following page). These basins cover the area in Figure 5.13 that contains the highest concentrations of mapped valleys. Viking MDIM 2.0 base.

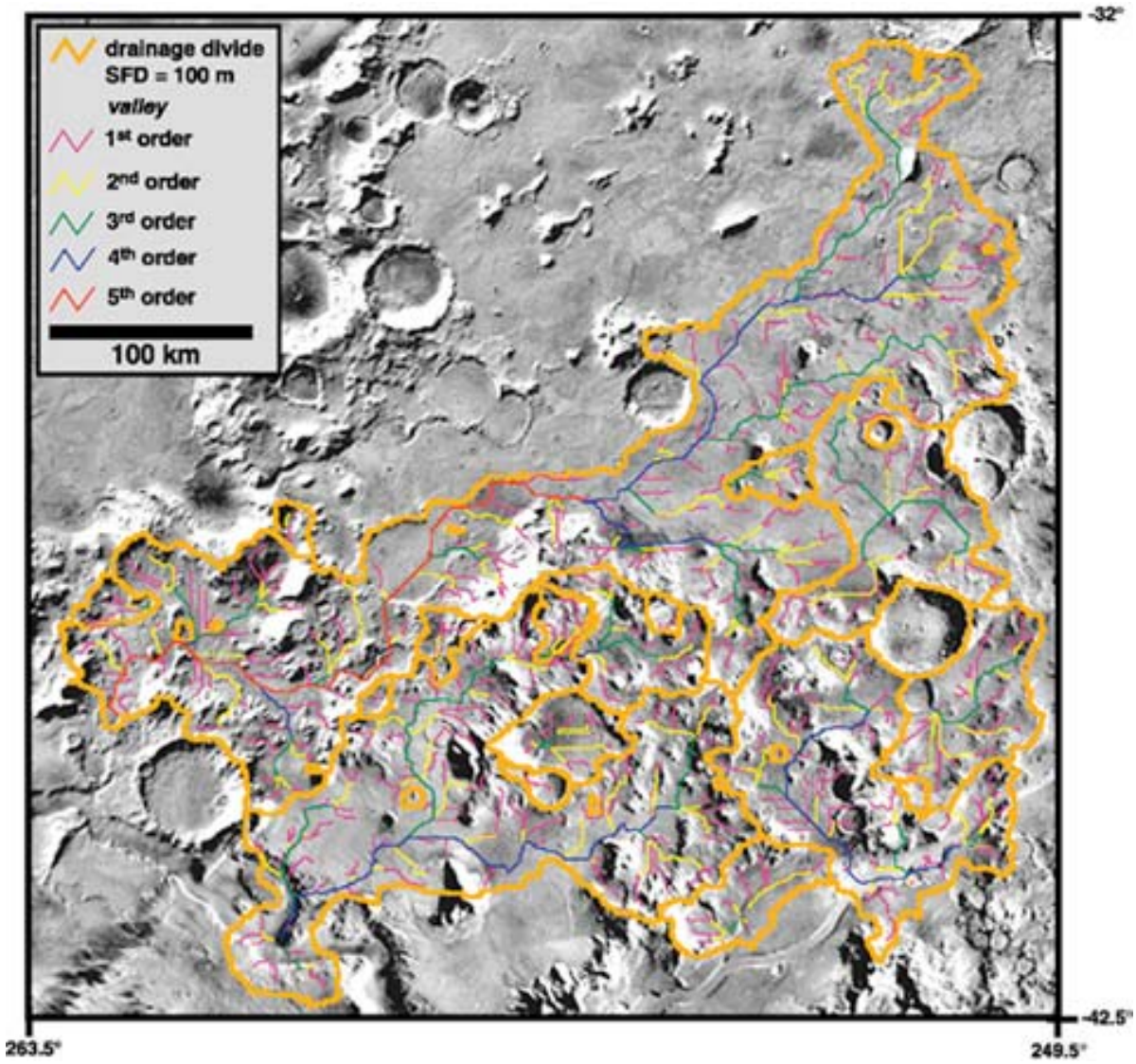

Figure 5.15 (continued). (b) SFD = 100 m.

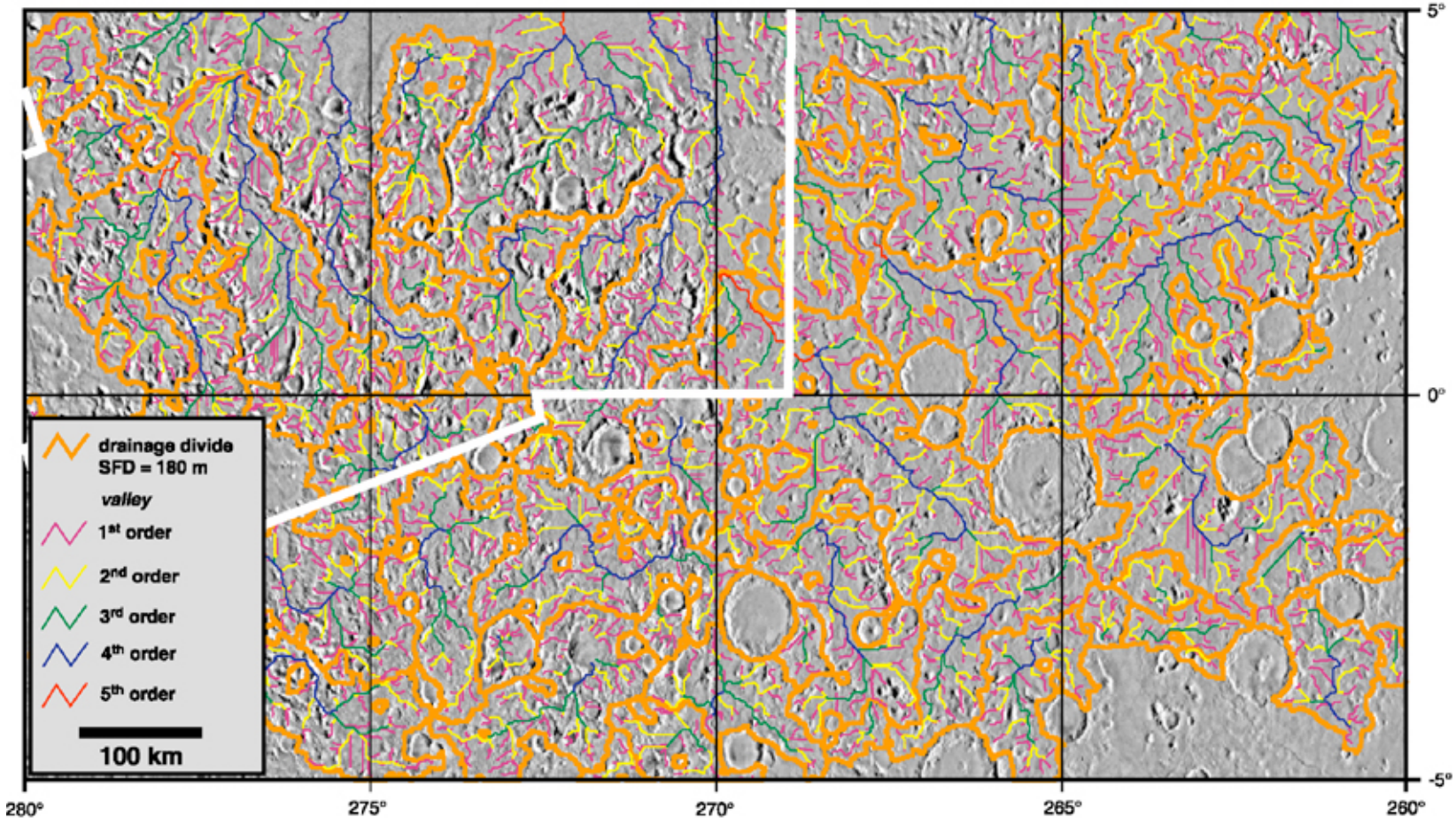

Figure 5.16. Selected drainage basin divides and valley networks in Libya Montes extracted from Arc/Info using sink-fill depths of (a) 180 m and (b) 300 m (following page). Heavy white line indicates part of the map area of Crumpler and Tanaka [2003]. Viking MDIM 2.0 photomosaic is base.

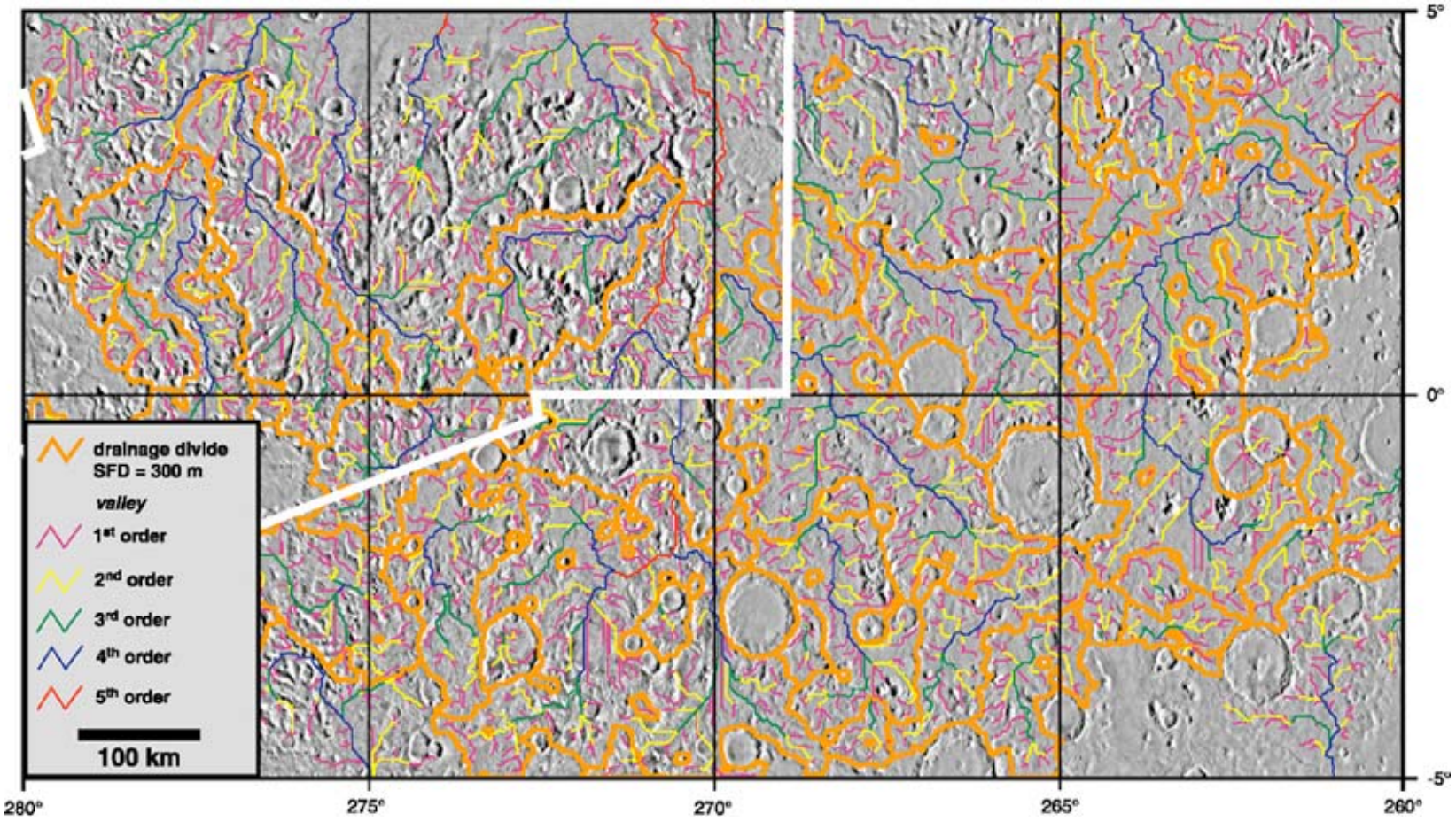

Figure 5.16 (continued). (b) SFD = 300 m.

additional model runs. For example, one of the "larger" continuous networks in Libya Montes (Figure 5.18), the "western valley" in Crumpler and Tanaka [2003], is split among several drainage basins along its course for both sink-fill depths shown. This might reflect actual subbasins, such as in the case of basins 113 (SFD = 180 m; Figure 5.18a) and 71 (SFD = 300 m; Figure 5.18b). This may also indicate the inability of the model to accurately delineate watersheds over a large area where the topography tends to vary greatly over short distances such as in Libya Montes and Promethei Terra. The mapped examples from Promethei Terra and Libya Montes also show a large number of individual single and second order systems found on steeper slopes, such as on massifs of highland materials or impact crater rims. These systems tend to terminate at the bases of their host massif or crater rim and are unconnected to other larger systems. However, Figures 5.17 and 5.18 show that the modeled steeper-slope valleys are connected to larger systems and don't accurately reflect the terminations observed in images.

Disagreements between mapped and modeled valley networks are observed in both regions for all of the sink-fill depths used to model valleys, including the four examples shown here. These disagreements are due partly to the technique used to extract them, as discussed earlier, but could also be due to differences in the processes and ages of valley formation within each region. Even though many mapped and modeled valleys show disagreement, the morphometric parameters discussed in this and following sections can still be valuable for providing insights into network development. Two episodes of valley formation have been proposed for Promethei Terra [Mest and Crown, 2001b, 2002b, 2003a] and Libya Montes [Crumpler and Tanaka, 2003]. The first episode eroded massifs of highland materials and many impact crater rims, and deposited sediments in low-lying areas. A second episode subsequently dissected the basin-filling materials and contributed sediments to adjacent plains-forming units. Most small-scale valleys incised within highland massifs, and gullies incised along interior crater walls are truncated by basin-filling materials and therefore predate emplacement of these deposits. Although much of the episode 1 fluvial activity that formed these features also resulted in deposition of most of the basin-filling deposits, truncation of valleys and gullies suggests an intermediate period of deposition by minor fluvial, mass wasting and eolian processes may have occurred. In Promethei Terra, this intermediate period may have also involved emplacement of a mantling deposit similar to that identified by Mustard et al. [2003]. The second episode of fluvial

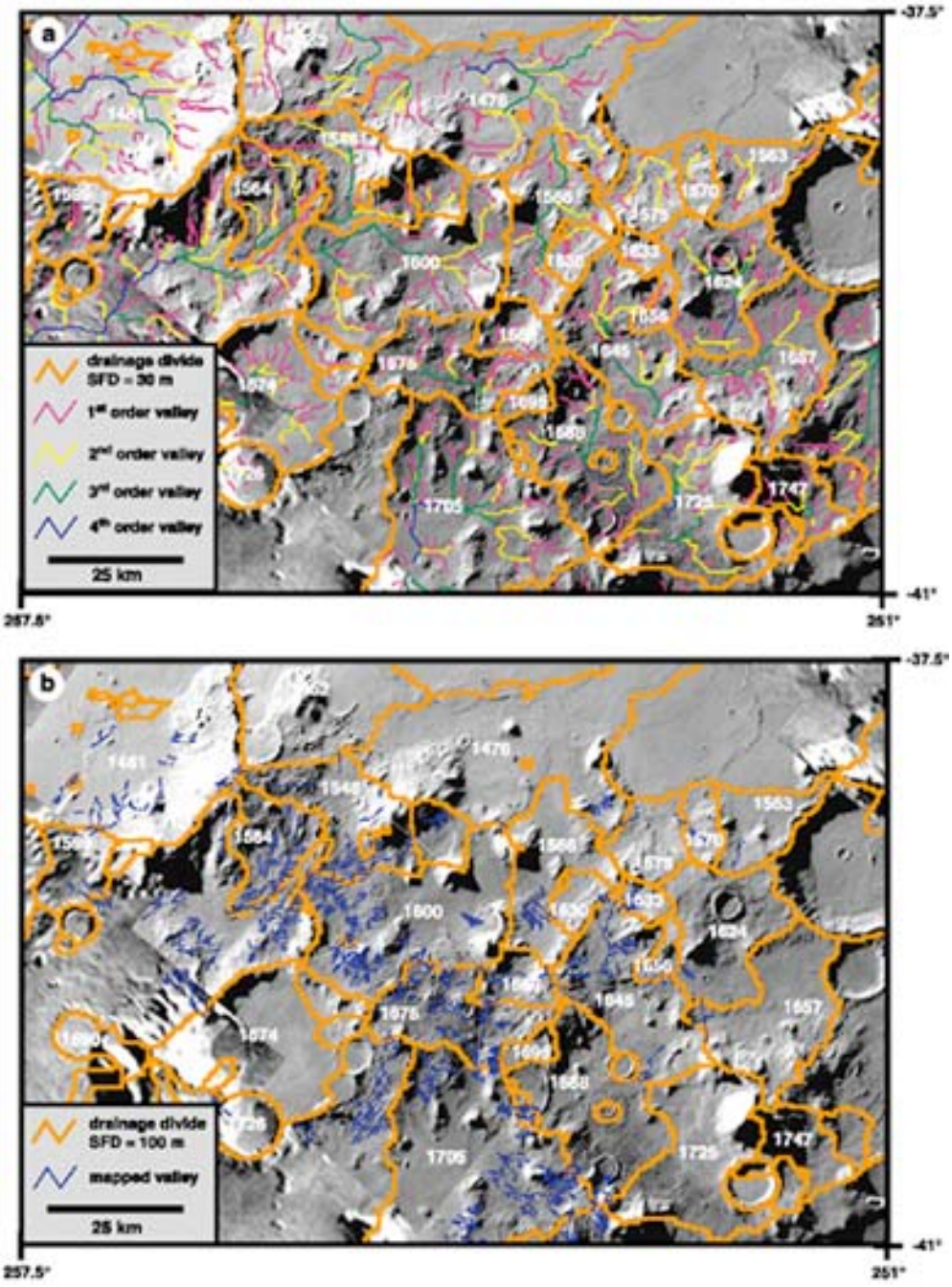

Figure 5.17. (a) Close-up view of modeled drainage basin divides and valley networks in Promethei Terra extracted from Arc/Info using a sink-fill depths of 30 m. (b) Distribution of mapped valley networks overlain on modeled drainage divides corresponding to a sink-fill depth of 30 m. Note the large number of mapped valleys that extend to and commonly cross the extracted basin divides for both sink-fill depths. Mosaic composed of Viking MDIM 2.0 photomosaic and Viking Orbiter images 411S14, 411S15, 411S16, 411S17, 411S18, 411S19, 411S20 and 411S21; resolution = 97 m/pixel.

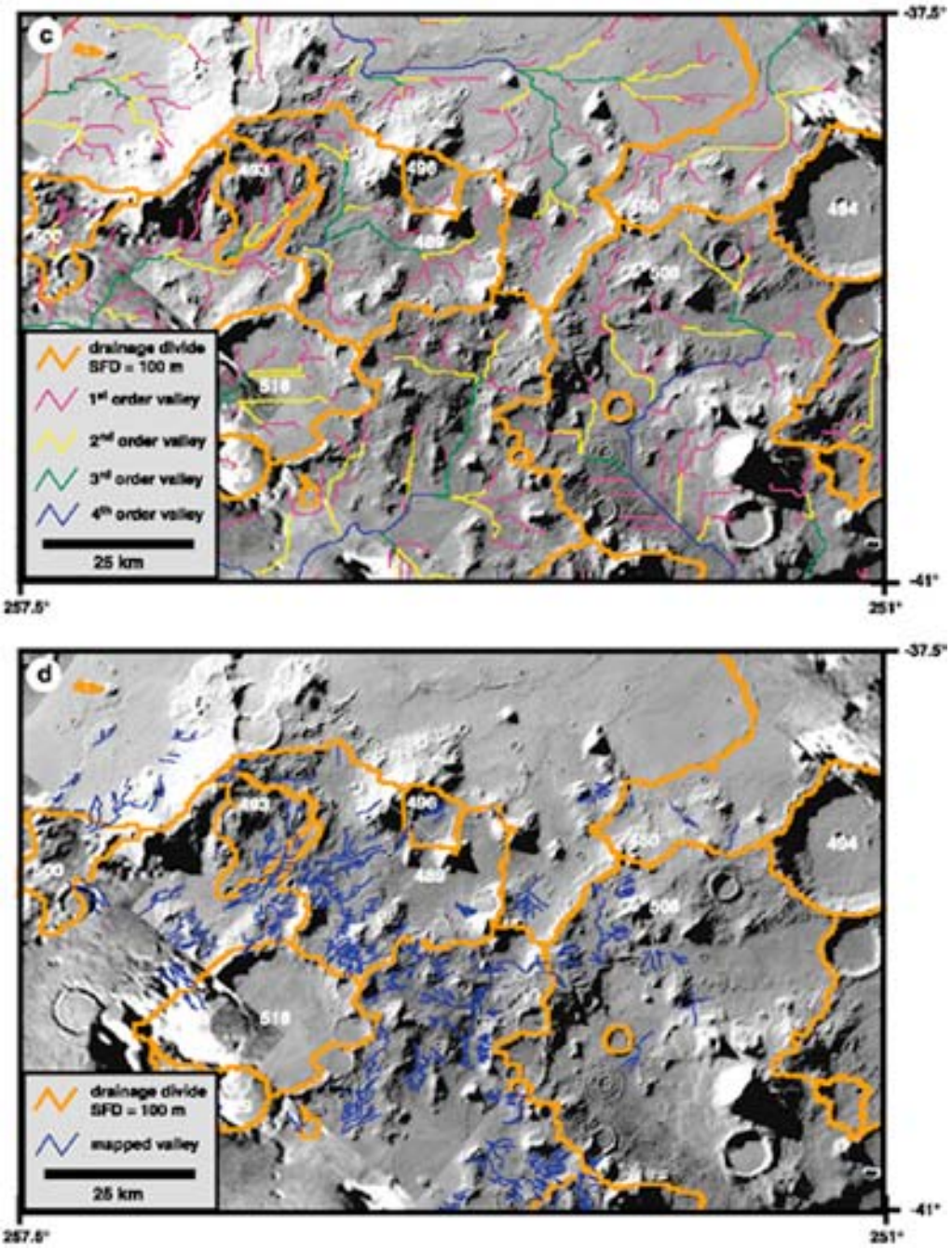

Figure 5.17 (continued). (c) Close-up view of modeled drainage basin divides and valley networks in Promethei Terra extracted from Arc/Info using a sink-fill depths of 30 m. (d) Distribution of mapped valley networks overlain on modeled drainage divides corresponding to a sink-fill depth of 30 m. Note the large number of mapped valleys that extend to and commonly cross the extracted basin divides for both sink-fill depths. Mosaic composed of Viking MDIM 2.0 photomosaic and Viking Orbiter images 411S14, 411S15, 411S16, 411S17, 411S18, 411S19, 411S20 and 411S21; resolution = 97 m/pixel.

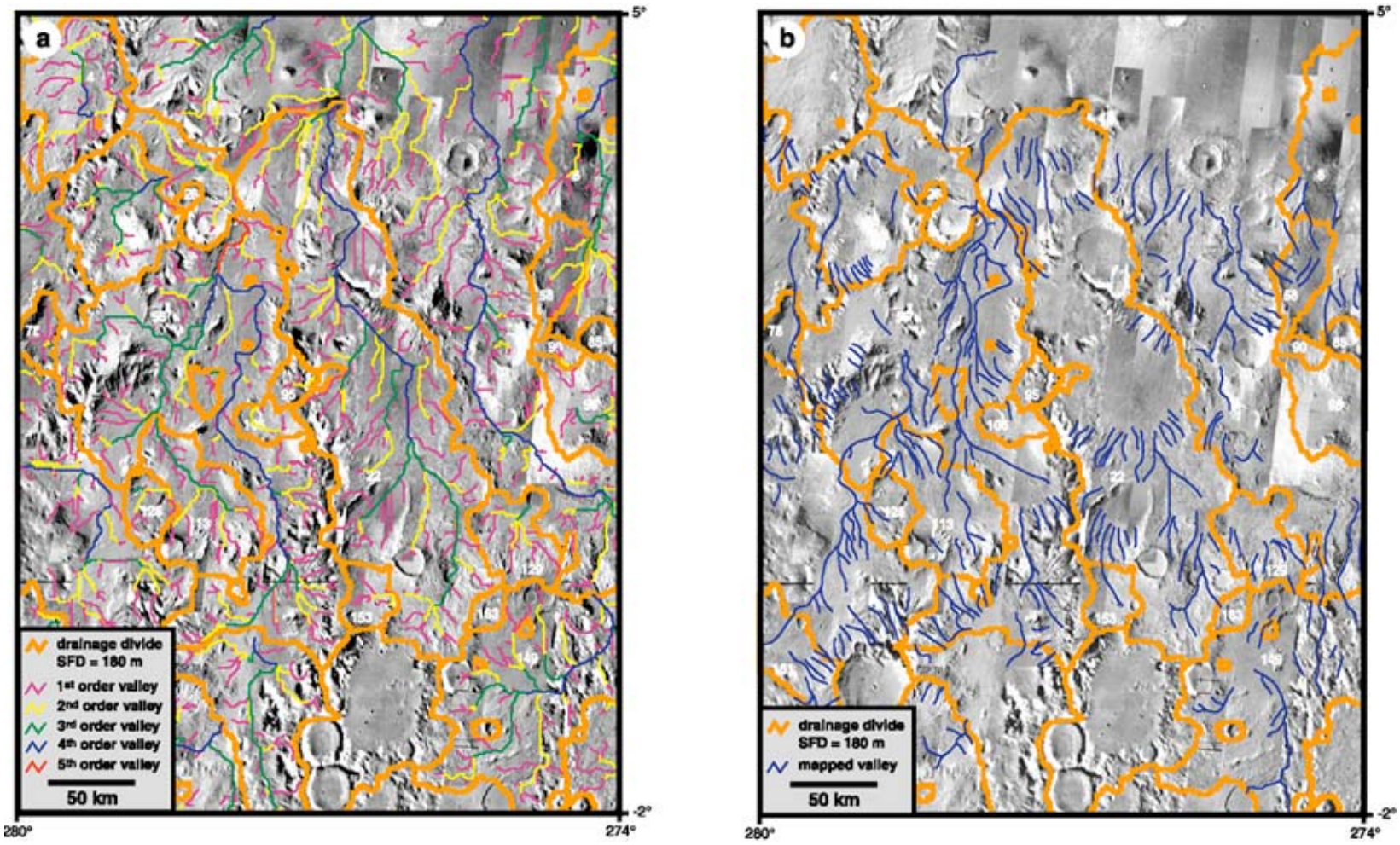

Figure 5.18. (a) Close-up view of modeled drainage basin divides and valley networks in Libya Montes extracted from Arc/Info using a sink-fill depth of 180 m. (b) Distribution of mapped valley networks overlain on modeled drainage divides corresponding to a sink-fill depth of 180 m. Note the large number of mapped valleys that extend to and often cross the extracted basin divides for both sink-fill depths. Viking MDIM 2.0 photomosaic is base.

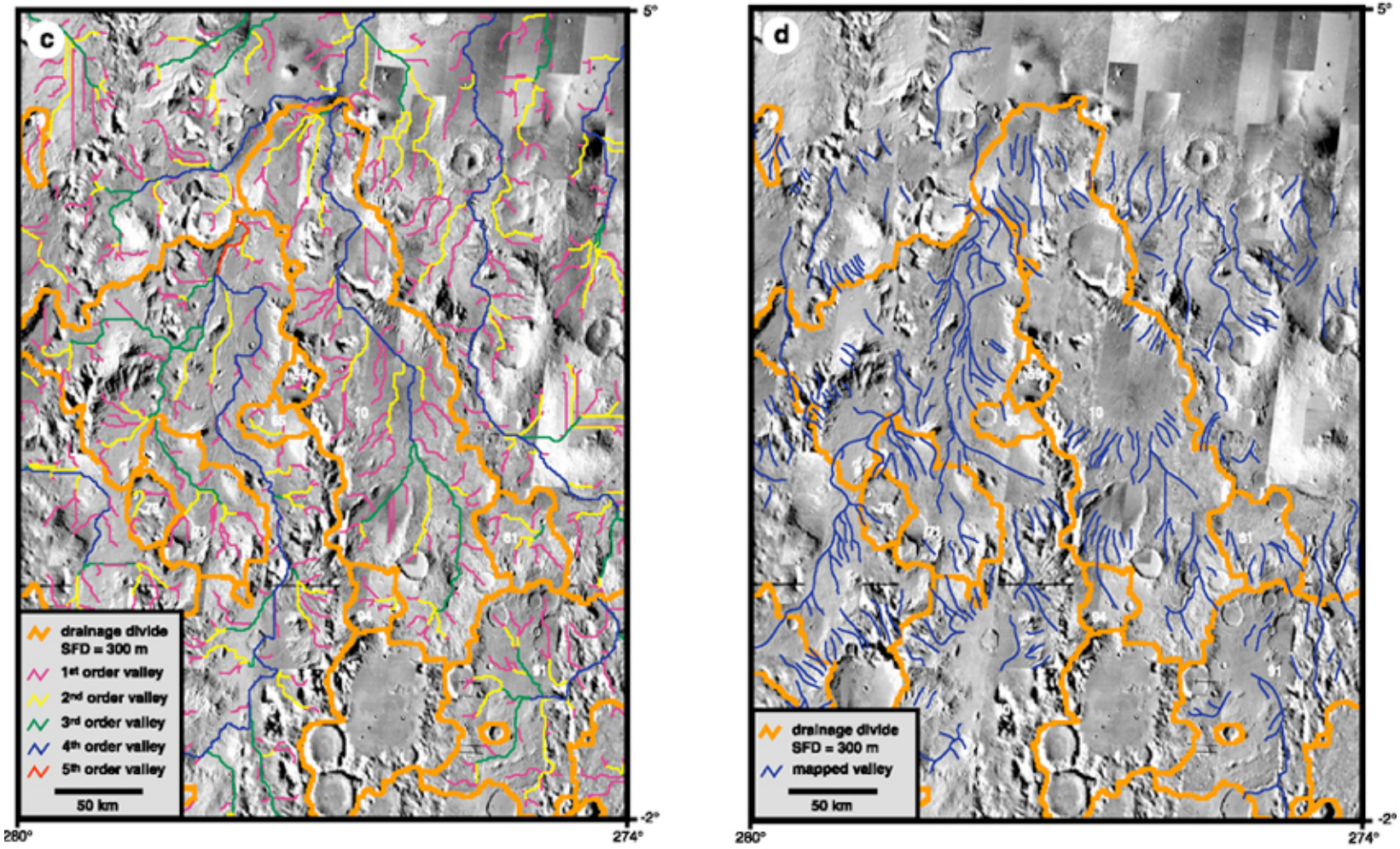

Figure 5.18 (continued). (c) Close-up view of modeled drainage basin divides and valley networks in Libya Montes extracted from Arc/Info using a sink-fill depth of 180 m. (d) Distribution of mapped valley networks overlain on modeled drainage divides corresponding to a sink-fill depth of 180 m. Note the large number of mapped valleys that extend to and often cross the extracted basin divides for both sink-fill depths. Viking MDIM 2.0 photomosaic is base.

activity is highlighted by dissection of large-scale valleys in basin-filling materials; some tributaries extend up the slopes of massifs suggesting some episode 1 valleys may have been reactivated. The disagreements between mapped and modeled networks could be reflecting the episodic fluvial erosion that modified highland terrains in Promethei Terra and Libya Montes. The model does not identify a great number of the small-scale episode 1 valleys and interior crater gullies. This discrepancy could be due in part to DEM resolution and technique, as discussed before, but could also be due to the fact that many of these valleys terminate at the base of the massif in which they are incised. The later phase of valley formation, which formed deeply incised valleys, appear to be better represented by the model.

Drainage basin areas, not including impact craters delineated as basins, in Promethei Terra and Libya Montes (Tables 5.1a and b) are one to two orders of magnitude smaller than basins delineated in Tyrrhena Terra (1,000-180,000 km^2 (mean = 23,000 km^2)). In general, most of the Libya Montes basin areas for both sink-fill depths and Promethei Terra basin areas for SFD = 100 m tend to be comparable to the mean basin areas of Tyrrhena Terra. However, most of the Promethei Terra basin areas for SFD = 30 m are comparable to and smaller than the smallest Tyrrhena Terra and Libya Montes basins. Drainage basin shapes and valley network patterns appear to reflect both local and regional slopes in Promethei Terra and Libya Montes. Valleys on steeper slopes tend to form parallel patterns, whereas valleys incised within basin-forming materials form locally dendritic patterns, as noted by Crumpler and Tanaka [2003]. The patterns of extracted networks tend to follow these trends as well. Most of the modeled drainage basins in Libya Montes, and to a lesser extent in Promethei Terra, are elongated in a direction roughly parallel to the regional slope (e.g., LM basins 10 and 30, SFD = 300 m (Figure 5.18)). The effects of regional slope relative to drainage pattern can best be viewed in the regional view of Libya Montes (Figure 5.16). Here an overall sub(parallel) pattern is observed in both the mapped and modeled data sets in which the elongated orientation of the drainage pattern is oriented roughly parallel to the north-south direction of regional slope. Other drainage basins, especially in Promethei Terra, form irregular to circular shapes and appear to be influenced more by local topography, such as from the configurations of impact crater rims and highland massifs. Nevertheless, plots of basin length versus area (Figure 5.19a) for the basins selected in Promethei

Table 5.1a. Length and area morphometric data for modeled watersheds in Promethei Terra.

Sink-fill depth = 100 m

Basin ID	A (km^2)	N	Total L (km)	Min L (km)	Max L (km)	Mean L (km)	D_d (km^{-1})	u	N_u	Total L_u (km)	Min L_u (km)	Max L_u (km)	Mean L_u (km)	R_b	R_L
365	69736	378	6166	0.4	461	16	0.088	1	292	3079	0.4	48	11	4.4	0.5
								2	67	1413	0.6	79	21	4.8	0.4
								3	14	750	1.8	211	54	3.5	0.5
								4	4	464	9.6	297	116	4.0	0.3
								5	1	461	460.5	461	461		
460	11452	50	850	1.2	87	17	0.074	1	38	461	1.2	45	12	4.8	0.5
								2	8	181	8.7	64	23	2.7	0.3
								3	3	205	37.3	87	68	3.0	20.4
								4	1	3	3.3	3	3		
489	4751	28	376	0.6	45	13	0.079	1	18	188	0.6	28	10	2.6	0.8
								2	7	90	2.9	25	13	3.5	0.3
								3	2	80	35.1	45	40	2.0	2.1
								4	1	19	18.8	19	19		
493	1008	9	153	4.9	30	17	0.152	1	6	104	4.9	30	17	3.0	0.9
								2	2	40	13.3	27	20	2.0	2.2
								3	1	9	9.2	9	9		
495	34553	186	3003	0.4	340	16	0.087	1	147	1627	0.4	38	11	4.6	0.5
								2	32	663	0.8	47	21	5.3	0.3
								3	6	374	6.4	183	62	6.0	0.2
								4	1	340	339.9	340	340		
498	6972	48	646	0.4	89	13	0.093	1	35	363	0.4	49	10	3.5	0.6
								2	10	187	1.2	47	19	5.0	0.4
								3	2	91	1.8	89	45	2.0	8.6
								4	1	5	5.3	5	5		
500	1027	8	77	1.8	23	10	0.075	1	7	58	1.8	23	8	7.0	0.4
								2	1	19	19.0	19	19		
508	17457	105	1522	0.6	242	14	0.087	1	78	831	0.6	43	11	3.9	0.6
								2	20	338	0.6	47	17	3.3	0.9
								3	6	113	2.9	44	19	6.0	0.1
								4	1	242	241.5	242	242		
515	336	2	10	0.8	9	5	0.030	1	2	10	0.8	9	5		
529	633	3	26	1.6	23	9	0.041	1	2	24	1.6	23	12	2.0	7.3
								2	1	2	1.7	2	2		

Table 5.1a (continued).

Sink-fill depth = 30 m

Basin ID	A (km^2)	N	Total L (km)	Min L (km)	Max L (km)	Mean L (km)	D_d (km^{-1})	u	N_u	Total L_u (km)	Min L_u (km)	Max L_u (km)	Mean L_u (km)	R_b	R_L
1461	6563	123	1119	0.4	49	9	0.171	1	86	590	0.4	22	7	3.3	0.6
								2	26	305	0.6	33	12	3.3	0.7
								3	8	136	6.2	35	17	4.0	0.4
								4	2	86	37.4	49	43	2.0	23.5
								5	1	2	1.8	2	2		
1523	8078	143	1265	0.4	64	9	0.157	1	105	664	0.4	22	6	4.0	0.5
								2	26	356	0.4	57	14	3.3	0.7
								3	8	150	4.4	64	19	2.7	0.6
								4	3	95	3.6	46	32	3.0	53.8
								5	1	1	0.6	1	1		
1548	1533	26	228	0.4	40	9	0.149	1	20	115	0.4	27	6	4.0	0.4
								2	5	73	3.6	25	15	5.0	0.4
								3	1	40	39.7	40	40		
1551	6821	122	1086	0.6	73	9	0.159	1	95	599	0.6	24	6	4.8	0.5
								2	20	269	1.2	38	13	5.0	0.5
								3	4	115	1.8	73	29	2.0	0.7
								4	2	77	34.5	43	39	2.0	1.4
								5	1	27	26.9	27	27		
1563	877	12	87	2.9	18	7	0.100	1	10	59	2.9	13	6	5.0	0.4
								2	2	28	9.8	18	14		
1564	1008	23	243	0.4	33	11	0.241	1	15	126	0.4	33	8	3.0	0.6
								2	5	68	0.8	28	14	2.5	0.7
								3	2	40	13.3	27	20	2.0	2.2
								4	1	9	9.2	9	9		
1566	1464	27	224	0.6	66	8	0.153	1	20	109	0.6	19	5	3.3	0.7
								2	6	48	1.8	20	8	6.0	0.1
								3	1	66	66.4	66	66		
1570	373	9	33	0.6	13	4	0.088	1	6	15	0.6	8	2	3.0	0.3
								2	2	15	2.2	13	8	2.0	2.8
								3	1	3	2.7	3	3		
1575	728	14	95	0.6	28	7	0.130	1	12	46	0.6	8	4	6.0	0.2
								2	2	48	20.6	28	24		
1577	7838	130	1203	0.4	127	9	0.153	1	97	627	0.4	31	6	3.7	0.5
								2	26	314	1.2	24	12	4.3	0.5
								3	6	136	13.1	31	23	6.0	0.2
								4	1	127	127.1	127	127		

Table 5.1a (continued).

Sink-fill depth = 30 m

1582	423	12	43	0.4	9	4	0.101	1	8	25	1.2	6	3	2.7	0.6
								2	3	15	0.4	9	5	3.0	2.1
								3	1	2	2.4	2	2		
1586	1164	21	123	0.8	21	6	0.106	1	17	74	0.8	11	4	5.7	0.5
								2	3	27	5.8	15	9	3.0	0.4
								3	1	21	21.4	21	21		
1592	6910	116	1122	0.4	90	10	0.162	1	87	613	0.4	37	7	4.1	0.4
								2	21	342	0.4	53	16	4.2	0.5
								3	5	156	1.2	90	31	2.5	13.1
								4	2	5	1.8	3	2	2.0	0.5
								5	1	5	5.3	5	5		
1599	704	12	85	0.6	17	7	0.120	1	9	74	0.6	17	8	4.5	3.3
								2	2	5	1.0	4	3	2.0	0.4
								3	1	6	5.8	6	6		
1600	3116	47	410	0.4	53	9	0.132	1	39	232	0.4	21	6	6.5	0.3
								2	6	114	1.4	41	19	3.0	0.6
								3	2	65	11.5	53	32		
1624	1739	37	266	0.4	20	7	0.153	1	25	138	0.6	18	6	2.8	0.6
								2	9	77	0.4	20	9	4.5	0.5
								3	2	34	16.0	18	17	2.0	1.0
								4	1	17	17.2	17	17		
1630	350	6	39	0.4	10	7	0.113	1	5	30	0.4	10	6	5.0	0.6
								2	1	9	9.4	9	9		
1633	222	5	22	1.2	9	4	0.098	1	4	20	1.2	9	5	4.0	3.6
								2	1	1	1.4	1	1		
1638	333	6	32	1.6	13	5	0.096	1	5	19	1.6	10	4	5.0	0.3
								2	1	13	13.4	13	13		
1645	2031	33	300	0.4	51	9	0.148	1	27	163	0.4	15	6	5.4	0.3
								2	5	86	13.1	24	17	5.0	0.3
								3	1	51	50.9	51	51		
1656	213	2	2	1.0	1	1	0.009	1	2	2	1.0	1	1	0.4	0.1
								2	5	66	3.3	22	13	5.0	0.3
								3	1	38	37.9	38	38		
1669	495	9	51	0.6	15	6	0.104	1	7	45	3.1	15	6	3.5	2.1
								2	2	6	0.6	5	3		
1675	1483	21	227	1.2	38	11	0.153	1	16	159	1.2	28	10	4.0	1.3
								2	4	30	2.1	12	7	4.0	0.2
								3	1	38	37.5	38	38		

Table 5.1a (continued).

Sink-fill depth = 30 m

1676	282	3	18	0.8	16	6	0.065	1	3	18	0.8	16	6		
1688	2185	46	336	0.6	28	7	0.154	1	32	186	0.6	26	6	3.2	0.7
								2	10	79	0.6	23	8	3.3	0.6
								3	3	43	1.2	24	14	3.0	0.5
								4	1	28	28.4	28	28		
1695	203	3	23	6.3	9	8	0.114	1	3	23	6.3	9	8		
1705	5313	98	751	0.4	42	8	0.141	1	72	390	0.4	26	5	3.8	0.5
								2	19	193	0.6	35	10	3.2	0.5
								3	6	126	10.7	29	21	6.0	0.5
								4	1	42	42.2	42	42		
1786	1900	35	313	0.6	41	9	0.165	1	29	214	0.8	20	7	5.8	0.6
								2	5	58	0.6	25	12	5.0	0.3
								3	1	41	40.8	41	41		

Table 5.1b. Length and area morphometric data for modeled watersheds in Libya Montes.

Sink-fill depth = 300 m

Basin ID	A (km^2)	N	Total L (km)	Min L (km)	Max L (km)	Mean L (km)	D_d (km^{-1})	*u*	N_u	Total L_u (km)	Min L_u (km)	Max L_u (km)	Mean L_u (km)	R_b	R_L
10	19499	107	1926	0.7	235	18	0.099	1	84	1119	0.7	41	13	4.4	0.6
								2	19	395	0.7	49	21	6.3	0.4
								3	3	177	9.2	111	59	3.0	0.3
								4	1	235	235.3	235	235		
16	44917	253	4016	0.7	542	16	0.089	1	195	1813	0.7	45	9	4.2	0.4
								2	46	1137	0.7	116	25	4.2	0.5
								3	11	523	4.7	109	48	11.0	0.1
								4	1	542	542.5	542	542		
30	33928	211	2958	0.5	395	14	0.087	1	163	1332	0.5	39	8	4.9	0.4
								2	33	649	1.3	93	20	2.8	0.5
								3	12	507	0.7	137	42	6.0	0.2
								4	2	426	30.6	395	213	2.0	4.8
								5	1	44	44.0	44	44		
36	14356	102	1397	0.5	231	14	0.097	1	75	730	0.5	63	10	3.6	0.7
								2	21	279	1.3	34	13	4.2	0.4
								3	5	156	4.6	66	31	5.0	0.1
								4	1	231	231.2	231	231		
39	4899	27	339	0.5	102	13	0.069	1	22	188	0.5	29	9	5.5	0.7
								2	4	49	3.0	31	12	4.0	0.1
								3	1	102	102.3	102	102		
42	5291	31	440	0.5	76	14	0.083	1	25	222	0.5	55	9	5.0	0.3
								2	5	141	16.0	42	28	5.0	0.4
								3	1	76	76.4	76	76		
54	15964	101	1518	0.7	176	15	0.095	1	79	784	0.7	36	10	4.6	0.4
								2	17	413	2.2	55	24	4.3	0.7
								3	4	145	13.0	60	36	4.0	0.2
								4	1	176	176.3	176	176		
67	31778	204	2969	0.5	358	15	0.093	1	149	1381	0.5	41	9	3.5	0.5
								2	42	779	1.6	50	19	3.5	0.5
								3	12	451	1.3	108	38	12.0	0.1
								4	1	358	358.1	358	358		
81	1921	15	160	1.3	27	11	0.083	1	11	101	1.3	26	9	3.7	0.6
								2	3	49	7.4	27	16	3.0	1.6
								3	1	10	10.4	10	10		
91	11735	73	996	0.5	98	14	0.085	1	55	529	0.5	37	10	4.2	0.6
								2	13	220	0.7	72	17	3.3	0.5
								3	4	149	19.3	57	37	4.0	0.4
								4	1	98	97.9	98	98		

Table 5.1b (continued).

Sink-fill depth = 300 m

98	2583	16	200	1.9	99	13	0.078	1	14	87	1.9	13	6	7.0	0.1
								2	2	113	14.2	99	57		
103	2345	16	175	0.7	44	11	0.075	1	11	70	0.7	16	6	2.8	0.4
								2	4	70	2.9	44	18	4.0	0.5
								3	1	35	34.6	35	35		
113	12363	83	1102	0.5	87	13	0.089	1	62	556	0.5	32	9	4.1	0.5
								2	15	289	2.0	54	19	3.0	0.6
								3	5	170	2.5	61	34	5.0	0.4
								4	1	87	86.9	87	87		
117	40909	228	3878	0.5	140	17	0.095	1	173	2076	0.5	60	12	4.0	0.6
								2	43	937	0.7	64	22	5.4	0.4
								3	8	447	15.7	100	56	2.7	0.6
								4	3	303	60.4	140	101	3.0	0.9
								5	1	115	115.5	115	115		
135	13701	84	1332	0.5	146	16	0.097	1	64	706	0.5	45	11	4.3	0.5
								2	15	349	0.7	62	23	3.8	0.7
								3	4	131	9.8	67	33	4.0	0.2
								4	1	146	145.5	146	146		
137	12214	75	1160	0.5	104	15	0.095	1	57	691	0.5	57	12	4.4	0.6
								2	13	277	5.7	50	21	3.3	0.5
								3	4	178	11.7	104	45	4.0	3.0
								4	1	15	14.6	15	15		
148	11125	71	993	0.7	92	14	0.089	1	55	497	0.7	30	9	4.2	0.4
								2	13	317	0.7	50	24	6.5	0.6
								3	2	87	22.2	65	43	2.0	0.5
								4	1	92	92.3	92	92		
173	6009	46	627	0.5	60	14	0.104	1	33	342	0.5	33	10	3.7	0.7
								2	9	129	3.4	26	14	3.0	0.4
								3	3	96	10.9	47	32	3.0	0.5
								4	1	60	60.4	60	60		
179	7967	48	697	0.5	123	15	0.087	1	38	383	0.5	36	10	4.2	0.5
								2	9	191	1.8	55	21	9.0	0.2
								3	1	123	122.9	123	123		
205	1851	13	186	0.5	36	14	0.101	1	10	119	0.5	36	12	5.0	0.6
								2	2	38	14.9	23	19	2.0	0.7
								3	1	29	28.7	29	29		

Table Ib (continued).

Sink-fill depth = 180 m

Basin ID	A (km^2)	N	Total L (km)	Min L (km)	Max L (km)	Mean L (km)	D_d (km^{-1})	*u*	N_u	Total L_u (km)	Min L_u (km)	Max L_u (km)	Mean L_u (km)	R_b	R_L
2	5907	64	675	0.7	118	11	0.114	1	48	344	0.7	32	7	3.4	0.3
								2	14	307	0.7	118	22	7.0	1.9
								3	2	24	11.7	12	12	2.0	0.4
								4	1	29	29.2	29	29		
4	3777	40	439	0.5	32	11	0.116	1	29	289	0.5	32	10	3.6	0.8
								2	8	98	0.7	28	12	4.0	1.1
								3	2	22	0.7	22	11	1.0	0.4
								4	2	51	6.7	44	25		
8	8405	88	921	0.5	81	10	0.110	1	63	439	0.5	19	7	3.5	0.4
								2	18	322	1.1	46	18	3.6	0.8
								3	5	108	2.0	81	22	5.0	1.1
								4	1	20	20.4	20	20		
10	3167	33	330	0.7	44	10	0.104	1	24	152	0.7	14	6	4.0	0.4
								2	6	108	1.6	44	18	3.0	0.7
								3	2	50	10.5	40	25	2.0	0.7
								4	1	37	36.9	37	37		
13	4353	45	507	0.5	52	11	0.117	1	33	282	0.5	39	9	3.7	0.6
								2	9	123	0.7	28	14	4.5	0.4
								3	2	65	12.5	52	32	2.0	0.5
								4	1	72	71.7	72	72		
19	5647	57	658	0.7	72	12	0.117	1	42	410	0.9	29	10	4.2	0.7
								2	10	140	0.7	35	14	2.5	1.5
								3	4	37	1.3	15	9	4.0	0.0
								4	1	235	235.3	235	235		
22	19377	169	2389	0.5	235	14	0.123	1	130	1277	0.5	36	10	4.2	0.5
								2	31	601	0.7	69	19	4.4	0.5
								3	7	276	2.0	111	39	7.0	0.2
								4	1	208	208.0	208	208		
25	18158	166	2035	0.5	208	12	0.112	1	126	1129	0.5	46	9	4.1	0.7
								2	31	419	0.7	42	14	3.9	0.4
								3	8	279	17.3	109	35		
26	2133	27	249	0.5	50	9	0.117	1	20	126	0.7	24	6	4.0	0.3
								2	5	114	0.5	50	23	2.5	5.2
								3	2	9	3.1	6	4		

Table 5.1b (continued).
Sink-fill depth = 180 m

33	3777	46	429	0.5	43	9	0.113	1	31	216	0.5	24	7	2.8	0.8
								2	11	97	1.3	31	9	3.7	0.3
								3	3	96	22.9	43	32	3.0	1.6
								4	1	20	20.4	20	20		
34	6205	55	658	0.7	146	12	0.106	1	42	310	0.7	18	7	4.2	0.4
								2	10	190	5.9	36	19	5.0	0.3
								3	2	151	4.7	146	75	2.0	10.8
								4	1	7	7.0	7	7		
53	3317	25	357	0.7	81	14	0.108	1	21	175	0.7	45	8	7.0	0.2
								2	3	101	10.3	69	34	3.0	0.4
								3	1	81	80.6	81	81		
56	18052	170	2124	0.5	227	12	0.118	1	133	1077	0.5	30	8	4.8	0.5
								2	28	447	0.7	44	16	4.7	0.3
								3	6	298	7.2	105	50	3.0	0.4
								4	2	258	30.6	227	129	2.0	2.9
								5	1	44	44.0	44	44		
57	1245	12	130	1.4	25	11	0.104	1	8	87	1.4	22	11	2.7	1.1
								2	3	30	2.0	25	10	3.0	0.8
								3	1	13	12.7	13	13		
58	1280	14	196	1.9	46	14	0.153	1	9	78	1.9	23	9	2.3	0.3
								2	4	102	15.6	46	25	4.0	1.6
								3	1	16	16.3	16	16		
65	6029	64	684	0.5	123	11	0.113	1	48	344	0.5	21	7	4.0	0.5
								2	12	170	1.6	33	14	4.0	0.9
								3	3	47	0.7	43	16	3.0	0.1
								4	1	123	123.2	123	123		
69	4899	41	484	2.2	102	12	0.099	1	33	282	2.2	19	9	4.7	0.6
								2	7	100	7.2	31	14	7.0	0.1
								3	1	102	102.3	102	102		
74	19165	169	2175	0.5	160	13	0.114	1	132	1011	0.5	36	8	4.6	0.4
								2	29	603	0.7	69	21	5.8	0.3
								3	5	353	14.2	123	71	2.5	0.7
								4	2	195	34.5	160	97	2.0	7.4
								5	1	13	13.1	13	13		
80	1585	18	166	1.3	46	9	0.105	1	14	99	1.3	18	7	4.7	1.0
								2	3	21	2.0	15	7	3.0	0.2
								3	1	46	46.0	46	46		

Table 5.1b (continued).

Sink-fill depth = 180 m

81	8305	89	1033	0.7	91	12	0.124	1	63	544	0.7	40	9	3.3	0.6
								2	19	280	0.7	33	15	3.2	0.8
								3	6	118	4.6	41	20	6.0	0.2
								4	1	91	90.8	91	91		
88	15900	141	1775	0.7	200	13	0.112	1	107	912	0.7	37	9	4.3	0.5
								2	25	455	1.1	61	18	4.2	0.6
								3	6	183	7.2	69	31	3.0	0.3
								4	2	202	2.2	200	101	2.0	4.5
								5	1	22	22.4	22	22		
109	30570	284	3448	0.5	267	12	0.113	1	211	1594	0.5	32	8	3.8	0.4
								2	56	990	0.5	50	18	4.0	0.5
								3	14	455	1.3	126	32	7.0	0.2
								4	2	282	14.7	267	141	2.0	1.1
								5	1	128	128.1	128	128		
113	3431	32	448	0.7	79	14	0.131	1	26	286	1.3	27	11	5.2	0.7
								2	5	83	0.7	29	17	5.0	0.2
								3	1	79	79.4	79	79		
149	11286	106	1217	0.7	98	11	0.108	1	81	607	0.7	33	7	4.3	0.4
								2	19	336	0.7	72	18	3.8	0.5
								3	5	176	16.3	57	35	5.0	0.4
								4	1	98	97.9	98	98		
165	15622	125	1683	0.5	149	13	0.108	1	102	940	0.5	42	9	5.7	0.3
								2	18	489	2.6	118	27	4.5	1.0
								3	4	105	12.1	59	26	4.0	0.2
								4	1	149	149.4	149	149		
175	1360	12	154	1.1	39	13	0.113	1	9	74	1.1	29	8	4.5	0.2
								2	2	72	33.3	39	36	2.0	4.7
								3	1	8	7.7	8	8		
192	12363	121	1367	0.5	87	11	0.111	1	91	673	0.5	37	7	3.8	0.5
								2	24	384	1.1	73	16	4.8	0.4
								3	5	223	25.8	61	45	5.0	0.5
								4	1	87	86.9	87	87		
193	6496	67	686	0.7	80	10	0.106	1	52	312	0.7	15	6	5.2	0.3
								2	10	187	0.7	80	19	2.5	0.5
								3	4	149	24.2	52	37	4.0	1.0
								4	1	37	37.1	37	37		
197	14883	143	1599	0.5	215	11	0.107	1	111	824	0.5	29	7	4.3	0.5
								2	26	418	0.7	75	16	5.2	0.6
								3	5	143	13.3	53	29	5.0	0.1
								4	1	215	214.7	215	215		

Table 5.1b (continued).

Sink-fill depth = 180 m

203	1184	14	117	0.5	17	8	0.099	1	12	94	0.5	17	8	6.0	0.7
								2	2	23	7.7	15	11		
222	13478	118	1590	0.5	146	13	0.118	1	90	866	0.5	40	10	4.1	0.5
								2	22	421	1.4	62	19	4.4	0.6
								3	5	158	9.8	67	32	5.0	0.2
								4	1	146	145.5	146	146		
224	12106	117	1392	0.5	119	12	0.115	1	84	809	0.5	45	10	3.5	0.8
								2	24	300	2.0	41	12	3.4	0.5
								3	7	161	5.7	87	23	3.5	0.4
								4	2	124	4.9	119	62		
235	10862	101	1140	0.7	92	11	0.105	1	77	569	0.7	26	7	4.5	0.4
								2	17	311	0.7	47	18	2.8	0.7
								3	6	167	6.9	65	28	6.0	0.3
								4	1	92	92.3	92	92		
272	6009	58	743	1.1	60	13	0.124	1	42	419	1.1	25	10	3.5	0.8
								2	12	154	2.3	26	13	4.0	0.4
								3	3	109	10.9	59	36	3.0	0.6
								4	1	60	60.4	60	60		
276	12712	109	1319	0.7	102	12	0.104	1	83	776	0.7	45	9	4.0	0.6
								2	21	340	0.9	46	16	5.3	0.4
								3	4	166	9.0	102	42	4.0	1.2
								4	1	36	35.8	36	36		
279	7967	78	847	0.5	72	11	0.106	1	58	439	0.5	27	8	4.1	0.4
								2	14	238	1.8	42	17	2.8	0.7
								3	5	118	0.9	72	24	5.0	0.5
								4	1	51	51.4	51	51		
282	7777	73	788	0.5	93	11	0.101	1	54	351	0.5	23	7	3.9	0.4
								2	14	230	1.3	48	16	3.5	0.4
								3	4	179	23.4	93	45	4.0	1.6
								4	1	27	27.2	27	27		

Terra (29 (SFD = 30 m) and 10 (SFD = 100 m) basins) and Libya Montes (37 (SFD = 180 m) and 20 (SFD = 300 m) basins) show fairly linear relationships.

5.5.2 Drainage Density

Drainage density (D_d), defined as the total length of streams in a drainage basin divided by the area of the basin [Horton, 1945], is one of the most important morphometric parameters used to characterize valley network development and describes the degree to which a surface is dissected. Studies of terrestrial watersheds have shown that drainage density reflects the interactions between a number of variables, including relief, slope, lithology, infiltration, total annual precipitation, the ratio of precipitation to evaporation, and vegetation cover [Horton, 1932, 1945; Strahler, 1952, 1957, 1958; Gregory and Walling, 1973; Ritter et al., 1995; Tucker and Bras, 1998; Vogt et al., 2003]. Drainage density has also been shown to reflect relationships between geology and climate [Ritter et al., 1995]. With the exception of vegetation, all of the above variables are applicable to Mars, and only relief and slope can currently be measured accurately, and lithology can be determined in relative terms (i.e., thick versus thin layers of an inferred type). In the future, properties of the near-surface environment, such as lithology, infiltration capacity, porosity, and permeability, may be estimated using new datasets such as from the Mars Exploration Rovers.

Drainage densities calculated from modeled basin and network data, shown in Tables 5.1a and b, for the basins examined in Promethei Terra and Libya Montes are similar in both study areas and to those calculated in Tyrrhena Terra (see Chapter 4.0). As mentioned in Chapter 4.0, the Arc/Info model uses the DEM to delineate valleys within a watershed based on topography. Thus drainage densities (and other parameters) calculated from modeled data can be considered ideal densities for these basins, reflecting mature systems in idealized watersheds. The relationship between drainage density and drainage basin area (Figure 5.19b) shows that the slopes of the martian data are shallower than the terrestrial example shown. However, stream lengths as a function of basin area (Figure 5.19c) show fairly well-defined linear relationships for

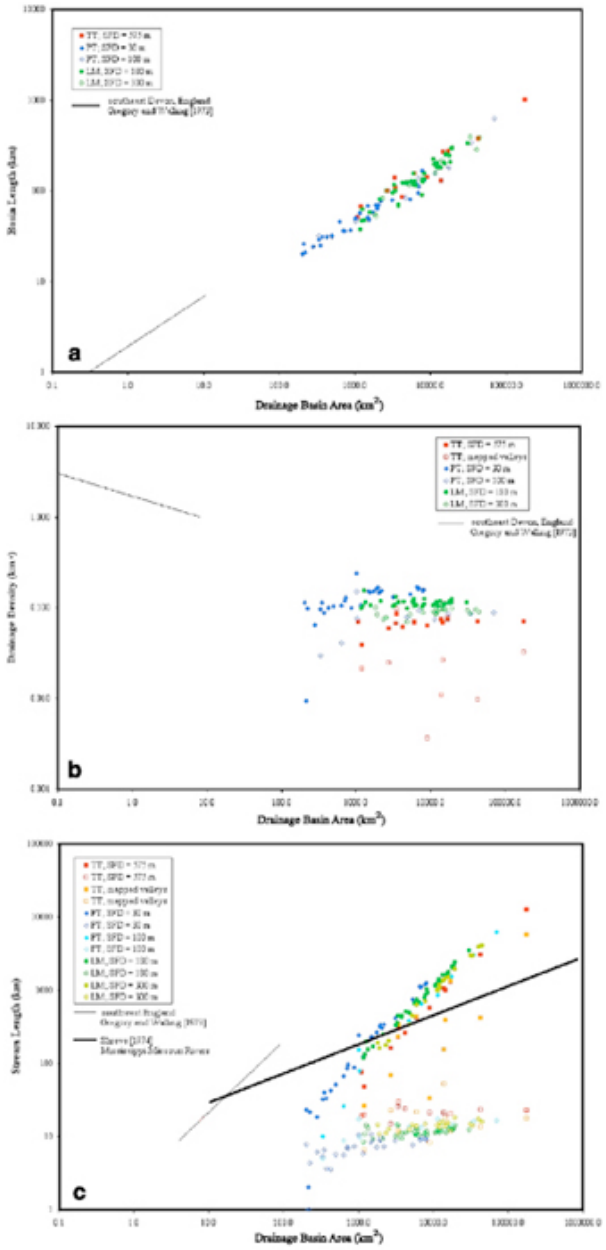

Figure 5.19. Plots of drainage basin area as functions of (a) basin length, (b) drainage density, and (c) stream length for Promethei Terra, Libya Montes and Tyrrhena Terra (data from Chapter 4.0). Basin length data plot close together despite the irregular shapes of drainage basins. Drainage densities (b) and stream lengths (c; closed symbols = total stream length and open symbols = average stream length) plot closer to a straight line than mapped data from Tyrrhena Terra, especially for drainage density. This is most likely due to the model's attempt to delineate the most ideal networks based on the given DEM, thus generating the most ideal characteristics for those networks. In (a)-(c), the data for the three martian sites display similar slopes despite scale differences, and similar slopes to terrestrial data, which exhibit areas that are smaller [Gregory and Walling, 1973] and comparable to [Shreve, 1974] the martian data. In (c), Gregory and Walling [1973] data is total stream length and Shreve [1974] data is average stream length.

modeled streams in both study areas, but are slightly more scattered for the average lengths of Promethei Terra valleys at both sink-fill depths. Chapter 4.0 contains a detailed discussion about martian and terrestrial drainage densities obtained by previous researchers, and this discussion will present these data with more brevity. Drainage densities calculated in Promethei Terra range from 0.009-0.241 km^{-1} (mean = 0.130 km^{-1}) for SFD = 30 m and 0.074-0.152 km^{-1} (mean = 0.081 km^{-1}) for SFD = 100 m, and in Libya Montes range from 0.099-0.153 km^{-1} (mean = 0.113 km^{-1}) for SFD = 180 m and 0.069-0.107 km^{-1} (mean = 0.090 km^{-1}) for SFD = 300 m. These data are comparable to most drainage density analyses of martian networks - 0.001-0.34 km^{-1} [Baker and Partridge, 1986; Carr, 1995, 1996; Grant, 2000; Cabrol and Grin, 2001b; Grant and Parker, 2002; Irwin and Howard, 2002] - and terrestrial networks mapped at 1:2M (0.07-0.21 km^{-1}) [Carr and Chuang, 1997] and 1:1M (Arizona = 0.149 km^{-1}; Nebraska = 0.079 km^{-1}; New York = 0.206 km^{-1}; Texas = 0.119 km^{-1}; Washington = 0.209 km^{-1}) [Carr and Chuang, 1997]. However, these data are lower than networks found on martian volcanoes (0.3-2.3 km^{-1}) [Gulick and Baker,1990], and much lower than most terrestrial densities (>2 km^{-1}) [Schumm, 1956; Smith, 1958; Gregory and Walling, 1973; Morisawa, 1962; Gregory, 1976; Wohl, 2000].

5.5.3 Stream Order and Bifurcation Ratio

Stream orders were determined for modeled valleys in Promethei Terra and Libya Montes using the Strahler ordering system [Strahler, 1964] and are defined by the rules described in Chapter 4.0. Stream ordering is useful because order number is directly proportional to the size of the contributing watershed, channel dimensions, and discharge anywhere within the network [Strahler, 1964]. Terrestrial steam orders generally range from 2 to 6 for mountain networks and 3 to 6 for lowland networks [Wohl, 2000]. The bifurcation ratio (R_b) is defined as the ratio of number of streams of a given order (N_u) to the number of streams of the next higher order (N_{u+1}). The bifurcation ratio can be used to estimate the number of streams of any given order and the total number of streams within a basin [Horton, 1945; Strahler, 1964; Ritter et al., 1995]. Bifurcation ratios range between 3.0 and 5.0 for watersheds in which the geology (lithology, structure, etc.) is relatively homogeneous, and that rarely is the theoretical minimum value of 2.0

approached under natural conditions. Geologic homogeneity within a basin would tend to form drainage systems that display morphometric and geometric similarities [Strahler, 1964].

Networks in Promethei Terra and Libya Montes were found to range from second to fifth order for modeled networks, and appear to range from first to fourth order for mapped networks. Accurate order assignments were difficult due to the high number of valleys that are “disconnected” from the main systems, as shown in the mapping studies of Mest and Crown [2001a, 2002b], Crumpler [1998, 1999] and Crumpler and Tanaka [2003]. Therefore, only modeled data are considered here. For modeled networks, stream orders and the log of the number of streams show linear trends for both study areas (Figure 5.20a). Six examples of terrestrial drainage systems of similar magnitude (fourth and fifth order networks) to the martian data are shown for comparison. These examples show that the modeled martian networks and mapped networks in Tyrrhena Terra exhibit similar trends and slopes as the terrestrial drainage systems. This result does not suggest that drainage systems in Promethei Terra and Libya Montes formed tributaries in a manner similar to terrestrial drainages, but shows that based on the topography, Arc/Info is delineating pathways on the surface by which water might have traveled. Several bifurcation ratios for modeled valleys in Promethei Terra and Libya Montes approach Strahler's theoretical minimum of 2.0. As mentioned in Chapter 4.0, the model only accounts for topography and not geology. As a result, the modeled networks misrepresent the effects of geology on valley formation by delineating features with "significant" topographic expressions (such as graben, the edges of or coalescing ejecta blankets or debris aprons, or closely spaced craters) as valleys. Reiterating the concern from Chapter 4.0, modeling alone cannot be used to characterize the hydrology of the martian surface, but such characterizations require detailed geologic and geomorphic mapping to constrain the materials and structures that occur at and just below the surface that might influence the theoretical pathways of water.

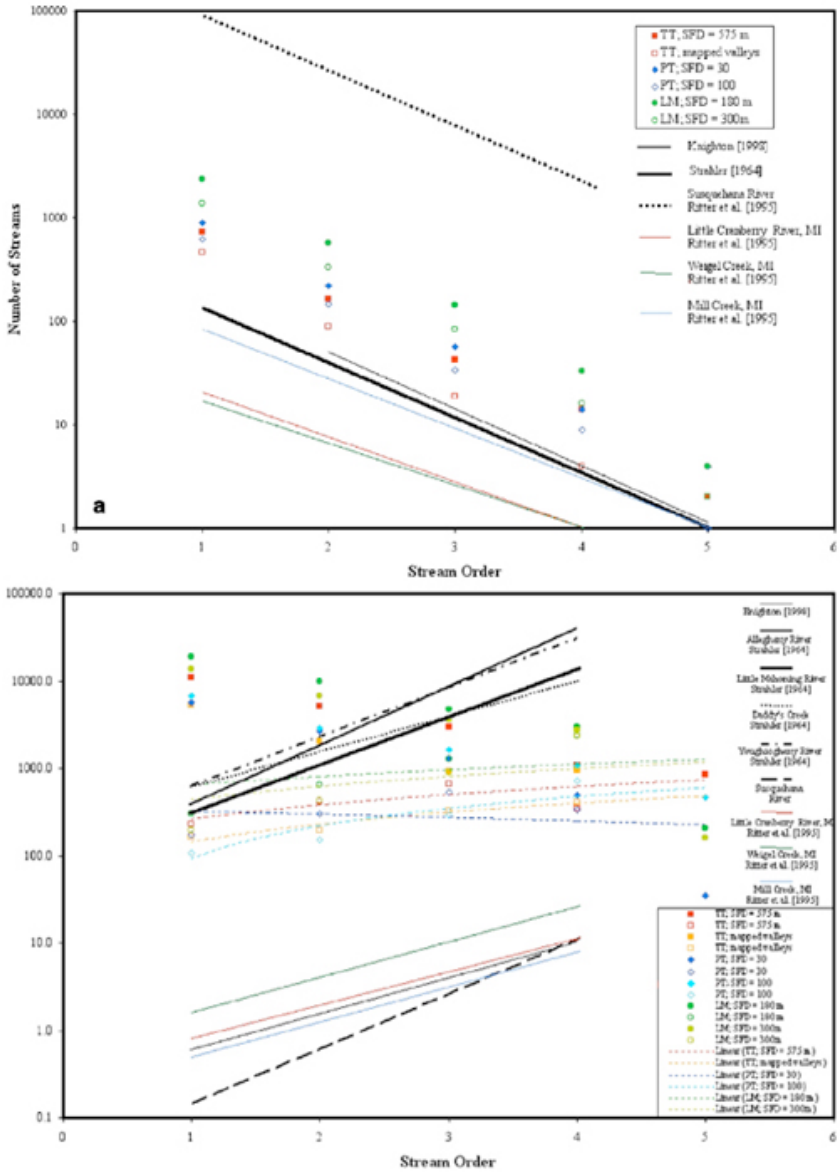

Figure 5.20. Plots of stream order as a function of (a) the number of streams and (b) stream length for Promethei Terra, Libya Montes and Tyrrhena Terra (data from Chapter 4.0). In plot (a), the numbers of mapped streams in Tyrrhena Terra show a slightly steeper slope than for modeled streams, but all martian data sets tend to show linear trends. In plot (b), the lengths of both mapped and modeled streams in each study area show linear trends and exhibit inverse correlations for total (closed symbols) and average (open symbols) stream lengths as a function of stream order. The slopes of the number of streams and stream length for the martian data, with the exception of average stream length for SFD = 30 m for Promethei Terra, appear fairly similar. The relationships in (a) and (b) are typical of terrestrial drainage systems [e.g., Schumm, 1956; Chorley, 1957; Morisawa, 1962; Strahler, 1964]. The terrestrial data in (a) shows slopes that are similar to the martian data, but the slopes of the average stream lengths for terrestrial sites (all terrestrial data in (c) are average stream length) are steeper than the martian data.

5.5.4 Length Ratio

The length ratio (R_L), defined as the ratio of the length of streams of a given order (N_u) to the length of streams of the next higher order (N_{u+1}) [Horton, 1945; Strahler, 1964], provides an estimate of the unmeasured lengths of streams of a given order and their total length within a basin [Ritter et al., 1995]. Length ratios for modeled valleys range from 0.08 to 53.85 for SFD = 30 m and 0.08 to 20.40 for SFD = 100 m in Promethei Terra, and 0.04 to 10.81 for SFD = 180 m and 0.09 to 4.83 for SFD = 300 m in Libya Montes. For comparison, as noted in Chapter 4.0, length ratios were found to range from 1.17 to 3.82 for sixteen martian highland networks mapped at 1:2M scale [Baker and Partridge, 1986]. Similar to trends observed in Tyrrhena Terra, for individual basins in Promethei Terra and Libya Montes (Tables 5.1a and b), there is a consistent trend of decreasing total and increasing average stream lengths for higher orders for most basins. There are a few exceptions among fourth and fifth order networks in both study areas where the total and average lengths of the highest order valleys are significantly smaller than of valleys of the next lower order, which results in the large ranges of length ratios. Disregarding these high values provides ranges comparable to those observed in Tyrrhena Terra for both mapped and modeled valleys, and by Baker and Partridge [1986].

Similar to the bifurcation ratio, the log of total and average stream lengths as a function of stream order plots as straight lines (Figure 5.20b). This plot shows close positive relationships for average stream lengths and negative relationships for total stream lengths for all sink-fill depths modeled in both study areas. These strong linear relationships are typical of terrestrial drainages [Schumm, 1956; Chorley, 1957; Morisawa, 1962; Strahler, 1964; Ritter et al., 1995; Knighton, 1998], of which some examples of average stream length are shown in Figure 5.20b. Four of the terrestrial examples - Allegheny River, Little Mahoning River, Daddy's Creek and Youghiogheny River [Strahler, 1964] - plot above, but close to, the martian data, whereas the other terrestrial examples plot well below the martian data. This might suggest that the martian valleys are more comparable in scale to the previous four terrestrial networks than to the latter. However, lack of detailed information (such as drainage basin area, stream lengths, etc.) provided by the sources from which these data were obtained limits the analysis that can be made. In addition, the slopes of the martian average stream lengths are much shallower than the

slopes of the terrestrial data shown. If the modeled martian valleys bear any resemblance to terrestrial streams, this would suggest that martian valleys, at least in Promethei Terra and Libya Montes, did not grow with the same efficiency as terrestrial streams. That is to say terrestrial drainages attempt to reach equilibrium between inflow and outflow to the system, and is accomplished by adjusting both the number and lengths of steams in order to accommodate the volume of water flowing through the system. The slopes of the numbers of valleys versus stream order (Figure 5.20b) are comparable to the terrestrial examples. The fact that the valley lengths are not comparable suggests that the volumes of water moving through these martian systems formed just enough valleys to move the water through the system but did not promote additional valley growth. This stagnation in valley growth could have been process-related, in that water supplied by sapping or precipitation could have been limited by aquifer size, lack of recharge, climate change, or short-lived precipitation events that yielded minimal volumes of water.

5.5.5 Relief Morphometry

Relief characteristics, including relief ratio and ruggedness number, provide information about the overall steepness of a drainage basin and indicate the intensity of fluvial erosion operating on basin slopes [Strahler, 1964; Ritter et al., 1995]. Measuring the relief of a drainage basin defines a slope value that provides an indication of runoff [Ritter et al., 1995] and the potential energy of a drainage system [Strahler, 1964]. Maximum basin relief (H) is defined as the elevation difference between the highest point on the basin divide and the mouth of the trunk valley [Strahler, 1964]. The relief ratio (R_h) is the maximum basin relief divided by the basin length (L_b), which is the horizontal distance along the longest dimension of the basin parallel to the principal drainage line [Schumm, 1956]. The ruggedness number (R) is the product of the maximum basin relief (H) and the drainage density (D_d) [Melton, 1957; Strahler, 1958, 1964].

Maximum basin relief (Table 5.2a and b) determined for the basins identified in Promethei Terra and Libya Montes range from 802 m to 5146 m (SFD = 30 m) and 1315 m to 7074 m (SFD = 100 m), and 1821 m to 6744 m (SFD = 180 m) and 1808 m to 6068 m (SFD =

Table 5.2a. Relief morphometric data for modeled watersheds in Promethei Terra.

Sink-fill depth = 100 m

Basin ID	(L_b) (km)	Max basin elev. (m)	Min basin elev. (m)	H (m)	R_h	R modeled
365	624	4530	-1369	5899	0.009	0.522
460	156	4752	790	3962	0.025	0.294
489	84	3624	483	3141	0.037	0.249
493	50	3694	-165	3859	0.077	0.586
495	339	4530	-2544	7074	0.021	0.615
498	140	2839	-51	2890	0.021	0.268
500	46	4462	-525	4987	0.108	0.376
508	180	2866	-82	2948	0.016	0.257
515	32	887	-428	1315	0.041	0.039
529	46	2599	-127	2726	0.059	0.112

Sink-fill depth = 30 m

Basin ID	(L_b) (km)	Max basin elev. (m)	Min basin elev. (m)	H (m)	R_b	R modeled
1461	121	4530	-24	4554	0.038	0.777
1523	130	3564	-1115	4679	0.036	0.733
1548	48	3670	804	2866	0.060	0.426
1551	94	3255	-1041	4296	0.046	0.684
1563	37	2469	844	1625	0.044	0.162
1564	49	3694	-165	3859	0.079	0.931
1566	68	2747	720	2027	0.030	0.310
1570	31	2280	903	1377	0.044	0.121
1575	36	2374	893	1481	0.041	0.193
1577	166	4530	-616	5146	0.031	0.790
1582	31	3083	912	2171	0.070	0.219
1586	57	918	-490	1408	0.025	0.149
1592	112	2831	-54	2885	0.026	0.468
1599	36	1271	-180	1451	0.040	0.174
1600	79	2924	606	2318	0.029	0.305
1624	58	2280	504	1776	0.031	0.272
1630	25	1766	964	802	0.032	0.090
1633	21	2192	1320	872	0.042	0.085
1638	29	887	-465	1352	0.047	0.130
1645	70	2729	195	2534	0.036	0.374
1656	26	2189	655	1534	0.059	0.014
1669	32	2768	1085	1683	0.053	0.174
1675	51	1930	185	1745	0.034	0.267
1676	24	1819	326	1493	0.062	0.096
1688	77	2223	69	2154	0.028	0.332
1695	20	2223	617	1606	0.080	0.184
1705	80	1935	-324	2259	0.028	0.319
1726	46	2599	-129	2728	0.059	0.289
1786	69	2272	-146	2418	0.035	0.398

Table 5.2b. Relief morphometric data for modeled watersheds in Libya Montes.

Sink-fill depth = 300 m

Basin ID	(L_b) (km)	Max basin elev. (m)	Min basin elev. (m)	H (m)	R_h	R modeled
10	290.55	2406	-3662	6068	0.021	0.599
16	386.19	1835	-664	2499	0.006	0.223
30	392.84	2594	-683	3277	0.008	0.286
36	216.32	1539	-2210	3749	0.017	0.365
39	120.05	1958	-725	2683	0.022	0.186
42	115.17	2171	-1978	4149	0.036	0.345
54	251.11	2097	-1725	3822	0.015	0.363
67	335.04	3864	-1730	5594	0.017	0.523
81	52.25	2794	-279	3073	0.059	0.256
91	157.67	2660	452	2208	0.014	0.187
98	99.53	2923	-350	3273	0.033	0.254
103	81.7	3138	352	2786	0.034	0.208
113	201.25	2749	656	2093	0.010	0.187
117	284.43	2686	-520	3206	0.011	0.304
135	179.34	2972	-511	3483	0.019	0.339
137	183.39	2780	972	1808	0.010	0.172
148	223.94	3140	157	2983	0.013	0.266
173	125.33	2970	998	1972	0.016	0.206
179	134.37	3163	363	2800	0.021	0.245
205	54.73	3000	785	2215	0.040	0.223

Table 5.2b (continued).

Sink-fill depth = 180 m

Basin ID	(L_b) (km)	Max basin elev. (m)	Min basin elev. (m)	H (m)	R_h	R modeled
2	124.07	1815	-1547	3362	0.027	0.384
4	67.64	1561	-1236	2797	0.041	0.325
8	153.5	1292	-4002	5294	0.034	0.580
10	94.44	2295	-2068	4363	0.046	0.455
13	121.97	3004	-1081	4085	0.033	0.476
19	127.45	2725	-1178	3903	0.031	0.455
22	295.37	3100	-3644	6744	0.023	0.832
25	206.64	2853	-2326	5179	0.025	0.580
26	80.2	1115	-2421	3536	0.044	0.413
33	70.37	1561	-873	2434	0.035	0.276
34	125.84	773	-1093	1866	0.015	0.198
53	114.95	1515	-1516	3031	0.026	0.326
56	244.65	3451	-2251	5702	0.023	0.671
57	46.57	2092	-682	2774	0.060	0.289
58	62.1	1680	-3118	4798	0.077	0.736
65	153.51	2141	-2203	4344	0.028	0.493
69	125.49	1929	-725	2654	0.021	0.262
74	290.25	3911	-581	4492	0.015	0.510
80	57.98	2968	-621	3589	0.062	0.377
81	134.42	2141	-1654	3795	0.028	0.472
88	249.87	2097	-1725	3822	0.015	0.427
109	332.39	3864	-1738	5602	0.017	0.632
113	99.61	2557	-720	3277	0.033	0.428
149	196.89	2687	256	2431	0.012	0.262
165	199.12	3120	686	2434	0.012	0.262
175	47.6	2336	-90	2426	0.051	0.275
192	201.62	2782	580	2202	0.011	0.244
193	114.6	3099	556	2543	0.022	0.268
197	204.1	2386	289	2097	0.010	0.225
203	37.21	1903	-541	2444	0.066	0.242
222	182.32	3095	-511	3606	0.020	0.426
224	183.79	2793	972	1821	0.010	0.209
235	223.81	3100	166	2934	0.013	0.308
272	115.12	2970	998	1972	0.017	0.244
276	180.33	2638	566	2072	0.011	0.215
279	125.13	3100	363	2737	0.022	0.291
282	89.28	3206	608	2598	0.029	0.263

300 m), respectively. Relief ratios for Promethei Terra (Table 5.2a) basins show ranges of 0.025-0.080 (average = 0.044) (SFD = 30 m) and 0.009-0.108 (average = 0.042) (SFD = 100 m), and Libya Montes (Table 5.2b) basins show ranges of 0.010-0.077 (average = 0.029) (SFD = 180 m) and 0.006-0.059 (average = 0.021) (SFD = 100 m). Ruggedness numbers were found to range from 0.014 to 0.931 (average = 0.330) (SFD = 30 m) and 0.039 to 0.615 (average = 0.332) (SFD = 100 m) for Promethei Terra networks, and, range from 0.198 to 0.832 (average = 0.387) (SFD = 180 m) and 0.172 to 0.599 (average = 0.287) (SFD = 300 m) for Libya Montes networks.

As mentioned in Chapter 4.0, martian relief ratios calculated for watersheds in Margaritifer Sinus show a range of 0.001-0.013 [Grant, 2000; Grant and Parker, 2002]. Typical relief ratios for terrestrial basins range from 0.015 to 6.8 for mountain basins and 0.0004 to 0.01 for lowland basins; in general, $R_h \geq 0.02$ indicates mountain systems and $R_h \leq 0.02$ indicates lowland systems [Wohl, 2000]. Relief ratios calculated here for modeled networks are found to be slightly higher than those for Margaritifer Sinus [Grant, 2000; Grant and Parker, 2002] and Tyrrhena Terra (0.005-0.029), and comparable to the lower limit of terrestrial mountain basins [Wohl, 2000]. These relationships are reasonable between Promethei Terra and Libya Montes and both Tyrrhena Terra and the terrestrial values. The drainage basins within the two study areas analyzed here are situated among highland terrains where elevation changes rapidly over short distances, hence relief ratios comparable to terrestrial drainage basins and higher maximum basin relief (1400-4900 m) and relief ratio values relative to Tyrrhena Terra basins and Margaritifer Sinus. In Tyrrhena Terra and Margaritifer Sinus, networks tend to be incised within terrains that have overall lower local slopes and elevation changes in drainage basins occur over longer distances. According to Wohl [2000; Table 2.3], terrestrial networks with R_h = 0.004-0.007 formed in humid temperate climates, glacial sediments, or sedimentary or limestone bedrock, and networks with R_h = 0.01-0.017 formed in semiarid climates or clay shale substrate. The relief ratios calculated here for Promethei Terra and Libya Montes basins seem to suggest that these networks may have formed in mountainous terrains within a semiarid climate and (or) in materials with relatively high infiltration.

Ruggedness numbers typically range from 0.03 to 10.9 for terrestrial drainage basins [Strahler, 1964; Grant, 2000], and have been calculated to be 0.005-0.086 for basins in Margaritifer Sinus [Grant, 2000; Grant and Parker, 2002]. Ruggedness numbers calculated for drainage basins in Promethei Terra and Libya Montes are comparable to slightly higher than in

Tyrrhena Terra (0.063-0.347 (modeled) and 0.008-0.243 (mapped)) and Margaritifer Sinus, and within the range (on the lower end) of terrestrial drainage basins. As discussed in Chapter 4.0, the low martian ruggedness numbers exhibited in Promethei Terra and Libya Montes (and elsewhere on Mars), relative to terrestrial systems, have been attributed to the influence of low martian drainage densities. This implies that runoff-driven erosion may be inefficient due to surface and near-surface materials with high infiltration capacities and their ability to store large quantities of water [Ritter et al., 1995; Grant, 2000]. In addition, Strahler [1958; 1964] noted that in order to obtain extremely high values of the ruggedness number, both H and D_d must be large. That is the maximum basin relief must not only reflect slopes that are steep (producing high D_d) but are also long, which is not the case in Promethei Terra and Libya Montes.

5.6 SINK-FILL DEPTH AND SMALL-SCALE BASINS: THE CASE FOR WATERSHED GROWTH ON MARS

This and other studies have shown that watershed development on Mars was affected by such factors as competition with impact craters or climate change. Although not observed at the same magnitude as other parts of the martian highlands (e.g., Tyrrhena Terra [Chapters 2.0 and 4.0; Mest and Crown, 2004a] and Terra Cimmeria [Irwin and Howard, 2002], valley formation may have been in competition with impact craters. Small-diameter impact craters emplaced along the course of a valley could temporarily disrupt the system, whereas large-diameter craters could completely terminate a drainage system from developing downstream because the topographic barrier that is the crater rim could not be overcome. Furthermore, rapid changes in topography by formation of impact craters, perhaps near an existing drainage divide, could raise the divide, thus increasing the amount of work the system must accomplish in order to erode down to the newly developed base-level. Second, climate change would have influenced the availability of volatiles, as well as their form, which would have affected the amount of erosion acting on the surface and

thus the amount of sediment that could be generated. For example, a warm and wet climate would produce large amounts of erosion via precipitation-driven runoff generating large volumes of sediment to be deposited in low-lying areas. Conversely, lack of atmospheric volatiles in a cold and dry climate would produce little to no erosion by runoff. If surface temperatures on Mars were similar to those observed today (daytime ≈ 210 K (~63°C)) a thick permafrost layer might exist and therefore not even groundwater sapping would occur. In this scenario, continuous topographic steepening by impact craters and tectonism might dominate, as well as distribution of surface materials by the wind. However, if climate changes on Mars were episodic and moderate, a scenario could exist where abundant atmospheric volatiles produced a period of erosion to form extensive networks of valleys and sediment-filled basins. A shift toward a drier climate would result in deposition of eolian materials and possibly topographic steepening. Reversion to a wetter climate would result in increased erosion and burial of older systems, as well as dissection of the basin-filling deposits.

The methodology, described in this chapter and in detail in Chapter 4.0, by which martian drainage divides have been delineated and valley networks extracted is largely dependant on the sink-fill depth. As described earlier, the Arc/Info GRID FILL function simply floods pixel sinks in order to eliminate areas where ponding of water might occur, and to promote continuous pathways of water within a basin. For the larger drainage basins identified in Tyrrhena Terra, where relief varied only a few kilometers among the thirteen basins analyzed, adjustment of the sink-fill depth by values greater than a few tens of meters was required to make significant changes in the placement of drainage divides. However, in Promethei Terra and Libya Montes, where drainage basins are orders of magnitude smaller and relief changes rapidly over short distances, adjustments in the sink-fill depth by tens of meters or less have been shown to greatly affect the positions of drainage divides and thus drainage basin areas and the networks extracted within the basins. It has been shown in this and other studies that as more sinks are filled (i.e., sink-fill depth increases), the number of drainage basins delineated decreases; that is, drainage divides are removed and basins are merged. The results presented here indicate that basin development in the Promethei Terra and Libya Montes study areas may have been more complex than in Terra Tyrrhena. It is suggested here that a systematic adjustment of the sink-fill depth to promote merging of drainage basins might serve as a tool to determine sequences of

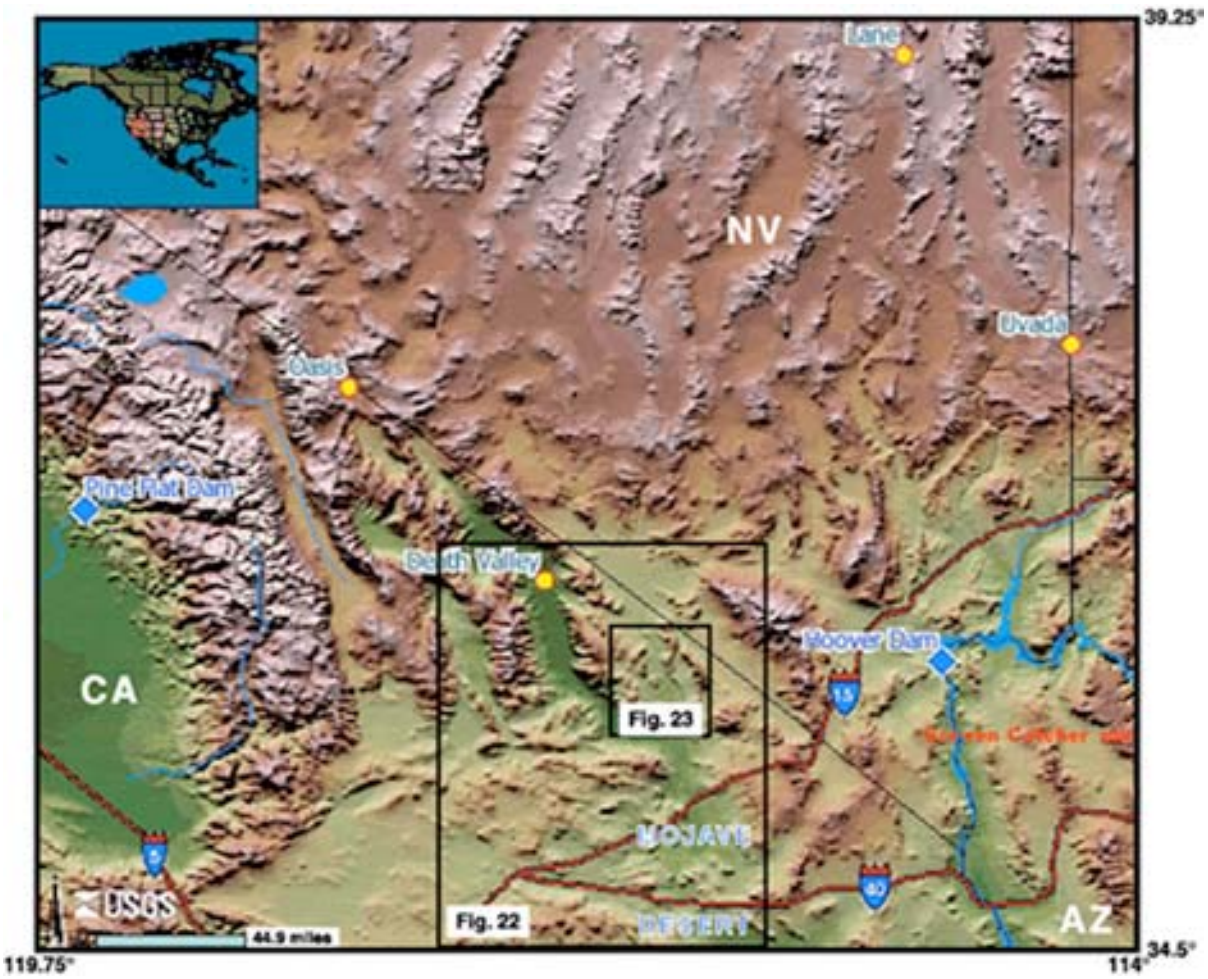

Figure 5.21. Topographic map covering the California and Nevada portions of the Basin and Range Province in the southwestern United States. Death Valley is located in the center of the map, and the approximate locations of Figures 5.22 and 5.23 are indicated. Map acquired from the United States Geological Survey's National Map Viewer (http://nationalmap.gov/).

watershed growth within the highlands of Mars. The highlands of Promethei Terra and the Libya Montes may record a history of drainage basin growth by channels that form either by (a) headward growth into another basin, or (b) one basin overtopping its divide and draining into a topographically lower basin. Additional analysis of MOC and THEMIS images and MOLA topography may be able to provide a sequence of this basin growth and thus help to constrain the timing of fluvial activity in the highlands. Watershed development may also be able to be determined in the context provided in the opening discussion to this section in which fluvial processes were in competition with impact crater formation and climate changes.

Watershed growth, or basin capture is not uncommon on Earth, and was especially prevalent during the Quaternary in the Basin and Range Province of the western United States [e.g., Blackwelder, 1954; Butler, 1981; Wells et al., 1987; Morrison, 1991; Anderson et al., 1998]. Here, large-scale topography is shaped by a long history of northeast-southwest extensional tectonism resulting in a series of horst and graben structures that extend approximately 140 km (~90 miles) from the western Sierra Nevada Mountains in southern California to southwestern Nevada just southwest of Las Vegas (Figure 5.21). These structures form linear, relatively parallel sedimentary basins elongated northwest-southeast that are separated by resistant volcanic ridges [e.g., Hunt et al., 1966; Dohrenwood et al., 1991; Dettinger and Schaefer, 1996], most notable of which is Death Valley. Prior to the drying of this part of the United States, climatic conditions were such that many of the basins in the Basin and Range contained lakes [Smith and Street-Perrott, 1983; Benson and Mifflin, 1986; Dorn et al., 1990; Grasso, 1996; Reheis and Morrison, 1997; Reheis, 1999], such as Lake Lahonton [Benson et al., 1990; Blair, 1999], Lake Mojave [Ore and Warren, 1971; Enzel et al., 1989; 1992; Wells et al., 1994], and Searless Lake [Smith et al., 1983; Smith, 1973, 1979], some of which may have been interconnected. Evidence also exists indicating that a few lakes may have overtopped their divides thereby increasing their drainage area. For example, two lakes in particular - Lake Manix and Lake Tecopa - are believed to have overtopped their divides. Lake Manix (Figures 5.22), fed by the Mojave River, is believed to have drained initially east-southeast through a valley extending from the Troy Bay arm of the lake toward Amboy, CA [Sharp and Glazner, 1999]. Evidence indicates that ~15,000 years ago either lava flows or movement on the Pisgah fault blocked the Troy outlet. As a result, Lake Manix filled and overtopped its eastern rim to carve

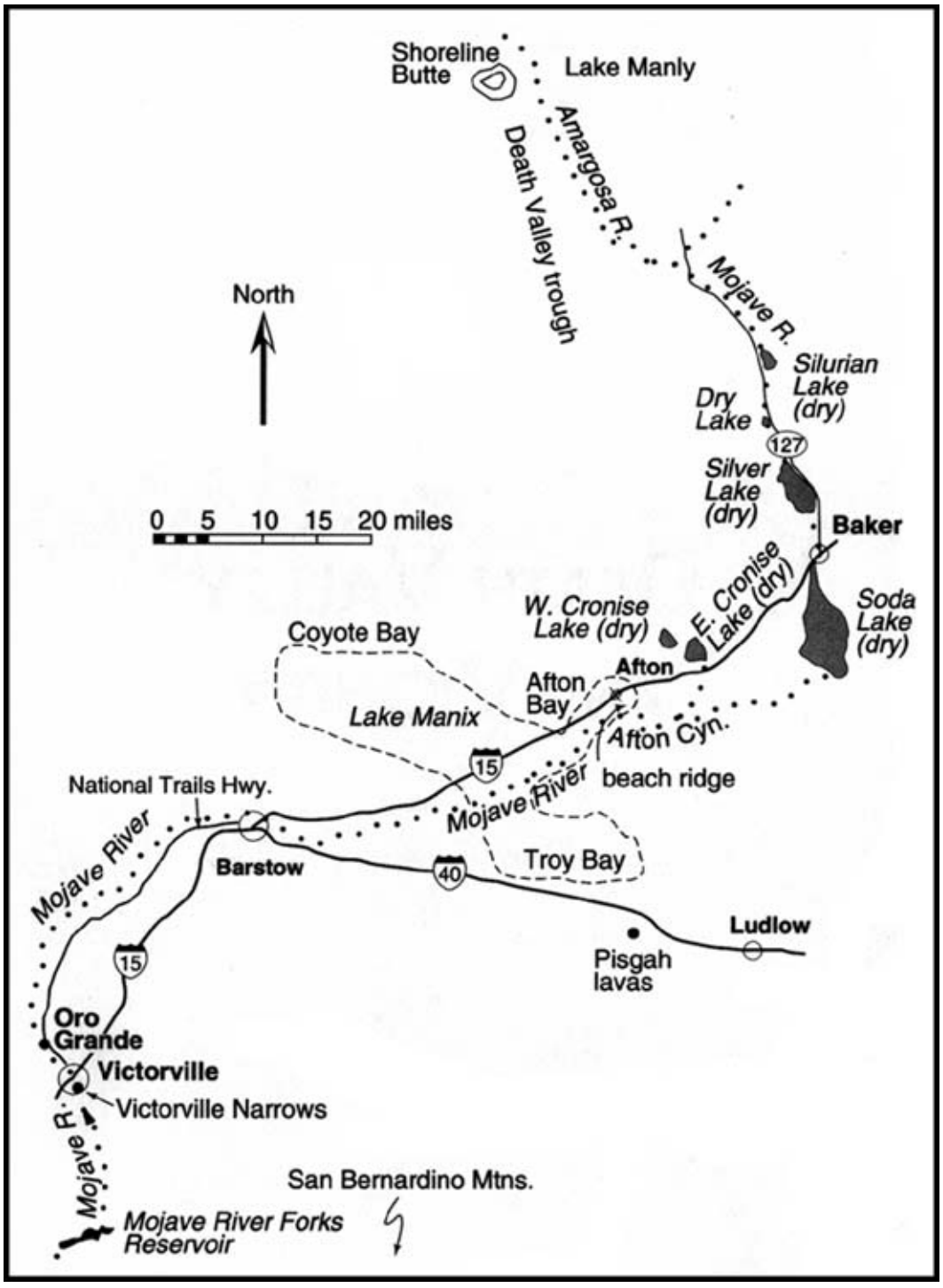

Figure 5.22. Sketch map of the Death Valley / Mojave Desert area showing the locations of present paleolakes, such as Lake Mannix, and the courses of the Mojave and Amargosa Rivers. Map is reproduced from Sharp and Glazner [1999].

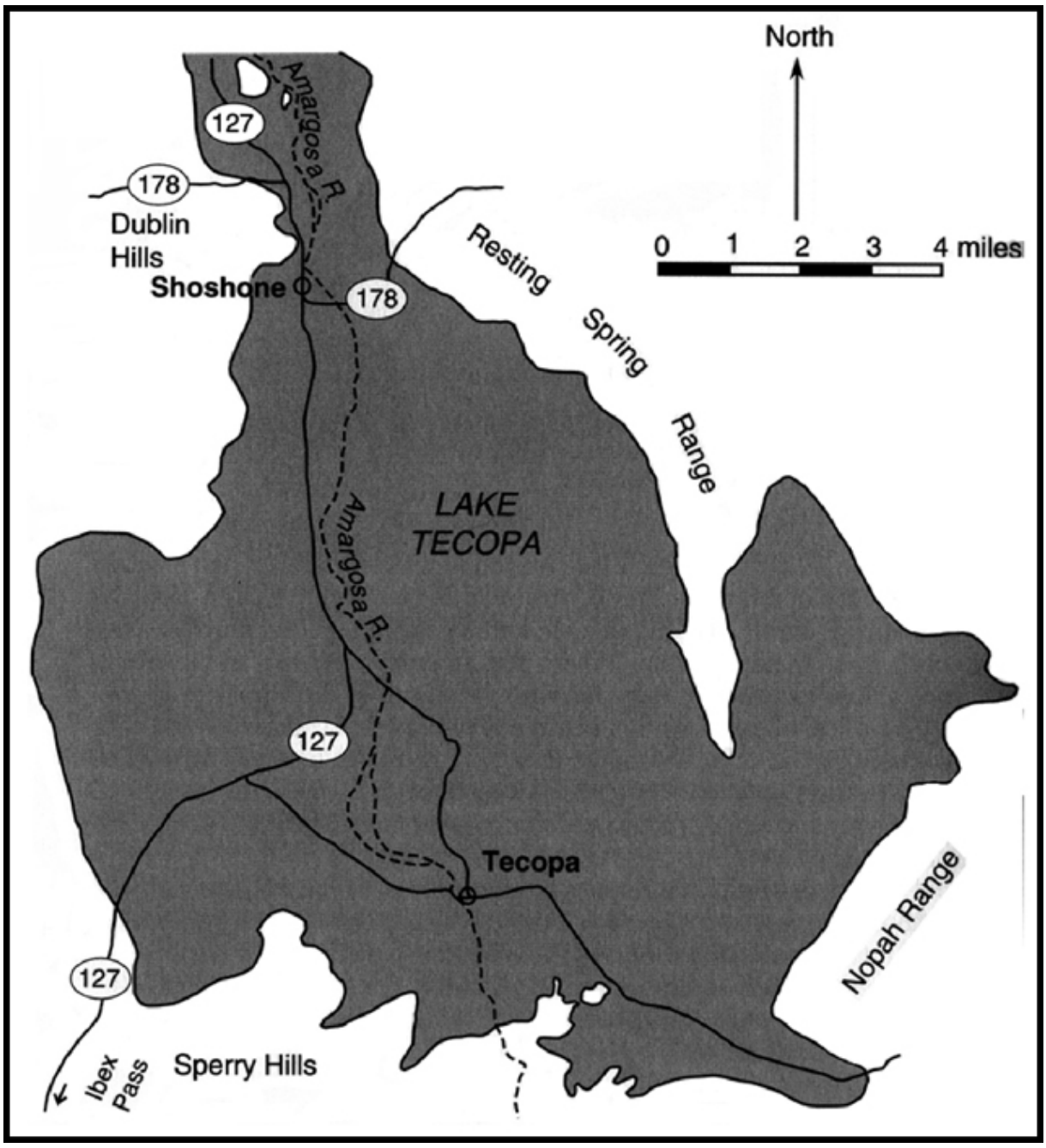

Figure 5.23. Sketch map showing the extent of paleolake Tecopa during the Pleistocene. Map is reproduced from Sharp and Glazner [1999].

Afton Canyon and a new course for the Mojave River, which today typically only contains water during heavy rain events [Meek, 1989; Wells and Enzel, 1994; Sharp and Glazner, 1999]. Lake Tecopa (Figures 5.23), located approximately where the towns of Tecopa and Shoshone now stand, was over 400 feet deep and covered ~85 square miles. The lake was located at the terminus of south-flowing Pleistocene-aged paleo-Amargosa River [Starkey and Blackmon, 1979; Hillhouse, 1987; Morrison, 1999; Sharp and Glazner, 1999]. Presumably, the Amargosa River flowed southward until faulting within coarse, gravelly deposits (fanglomerates formed by emplacement of alluvial fans) dammed the river and formed Lake Tecopa [Mason, 1948; Butler, 1984; Hillhouse, 1987; Anderson et al., 1994; Morrison, 1999; Sharp and Glazner, 1999]. It is believed that ~500,000 years ago, increased discharge into Lake Tecopa coupled with an increased sediment load to the lake caused Lake Tecopa to rise, overtop the southern divide composed of the faulted fanglomerates, and downcut into these deposits. Lake Tecopa drained rapidly, but still retained lower lake levels up until ~16,000 years ago as climate in this region shifted to higher aridity [Butler, 1984; Hillhouse, 1987; Morrison, 1999; Sharp and Glazner, 1999]. As with Lake Manix and Lake Tecopa, and other paleolakes mentioned previously, with climate in the southwest United States changing toward higher aridity, water levels in many of these Basin and Range lakes could not be maintained by the ephemeral streams and groundwater seeps that fed them.

Although the nature of these terrestrial basins and the basins identified in Promethei Terra and Libya Montes may be quite different, analysis of the modeled drainage basins prompted the idea that overtopping of drainage divides or watershed piracy might have also been common on Mars. If so, adjustment of the sink-fill depth and analysis of the locations of divides might yield a chronology of watershed growth. Figure 5.24 shows one example of watershed growth in the upper reaches of the system identified by Crumpler and Tanaka [2003] as the "eastern valley" in Libya Montes. Clearly in Viking MDIM 2.0 mosaic (Figure 5.24a), which shows mapped valleys in blue, and an accompanying MOC image M07-03660 (Figure 5.24b), a tributary valley of the "eastern valley" breaches the northwest rim of a degraded, flat-floored impact crater. Several small valleys breaching the southwest rim of this crater suggests it may have at one time contained a standing body of water and its flat floor resulted in deposition of sediments eroded from the adjacent highlands. The morphology of this crater further suggests

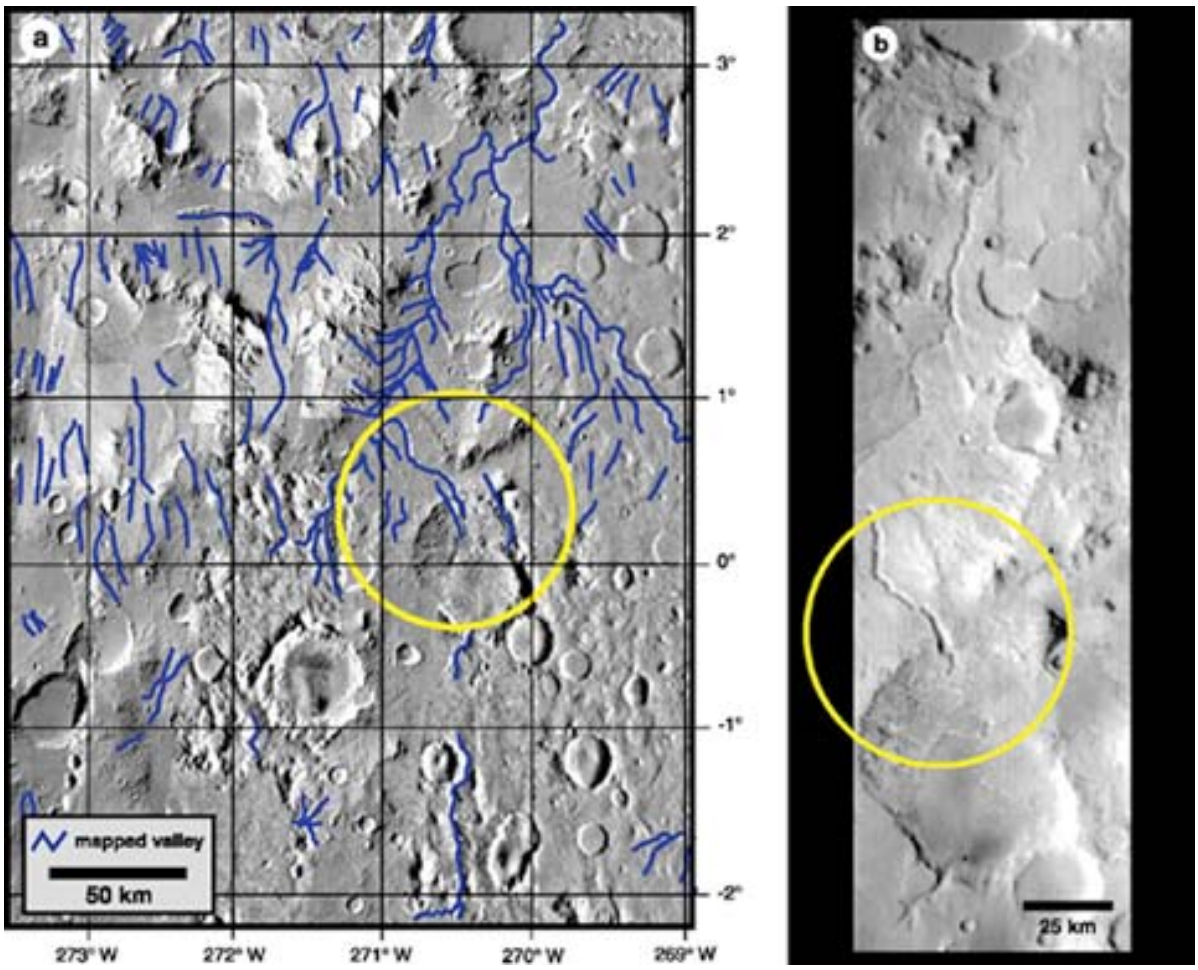

Figure 5.24. Altering the sink-fill depth in the model might enable sequences of drainage basin growth by either basin capture by headward growth of valleys or basin mergers by paleolakes overtopping drainage divides. The circled area in (a-d) shows one example where drainage basins merged by a valley breaching a topographic divide. (a) shows mapped valleys in Libya Montes and the location of (b), which is MOC wide-angle image M07-03660, showing the south rim breached by an inlet valley and the northwest rim breached by an outlet valley. Viking MDIM 2.0 photomosaic is base for (a); M07-03660 centered at 1.2°N, 270.7°W; image width = 61.8 km; resolution = 241.6 m/pixel; NASA/JPL/MSSS.

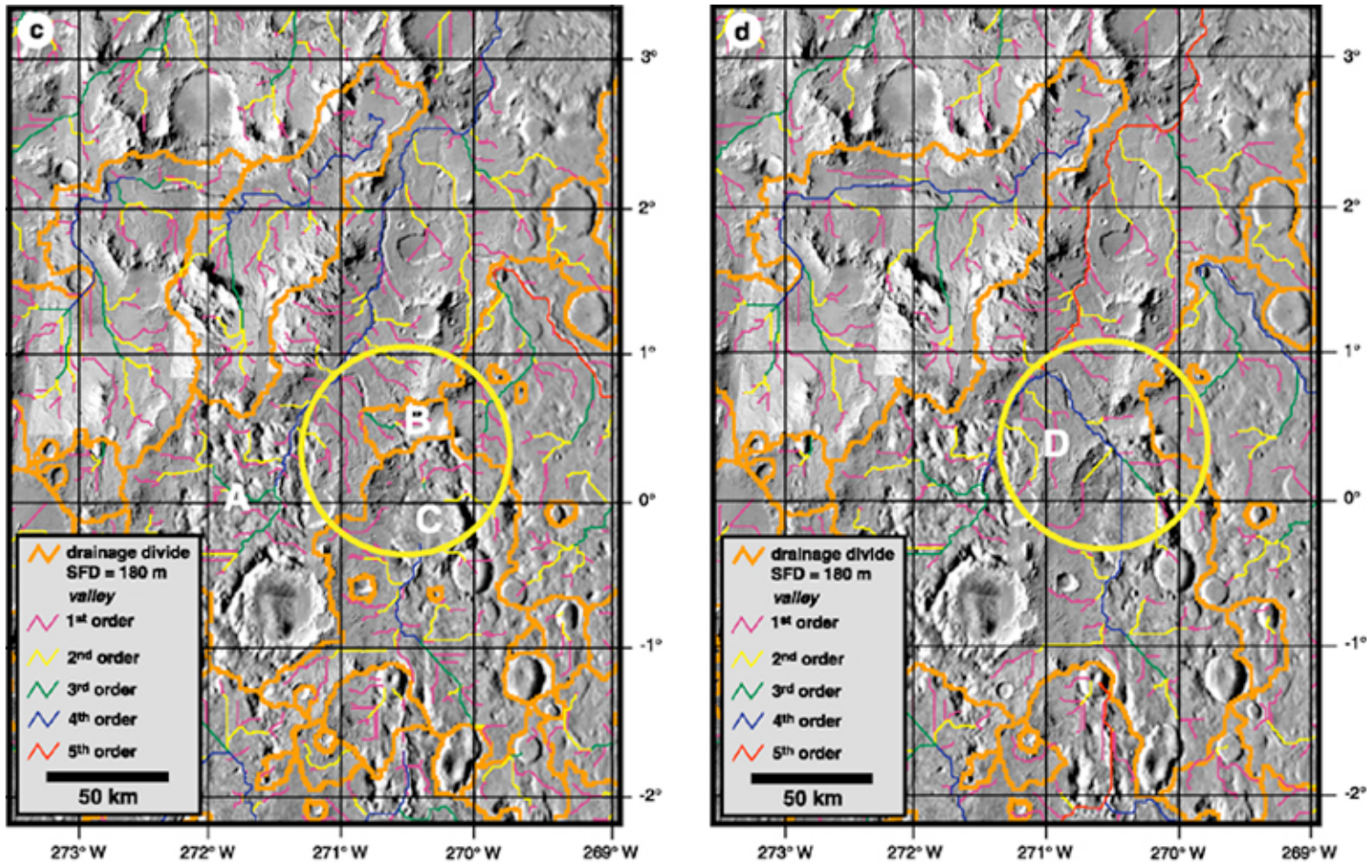

Figure 5.24 (continued). (c) and (d) Close-up views of drainage basin divides and valley networks in Libya Montes extracted from Arc/Info using sink-fill depths of 180 m (c) and 300 m (d). At SFD = 180 m (c), network A is fourth order and drains north toward Isidis Planitia, drainage B is 3rd order, and drainage C consists of several second, third and fourth order networks that drain into two nested impact craters offset to the north of this basin. At SFD = 300 m (d), drainages A, B and C (and several other small basins) are merged and a new drainage system (D) has been delineated within the larger area. In (b), the locations of the valleys are approximately similar to those in (a), and the new network is now a higher order (5th order) network. Viking MDIM 2.0 photomosaic is base for (c) and (d).

that the southwest breach and infilling of the crater occurred prior to the northwest breach, and therefore it is reasonable to assume that at one time the rim of this crater served as a drainage divide.

Hydrologic modeling of Libya Montes at several sink-fill depths has enabled the merging of the "eastern valley" basin and this crater-defined basin (#144; SFD = 180 m) to be identified. Figure 5.24c shows the model results of this area for SFD = 180 m in which a basin divide has been delineated along the northwestern part of the impact crater rim, and bisecting the clearly incised breaching valley. However, in Figure 5.24d (SFD = 300 m), the divide is no longer present and the "eastern valley" basin has been merged with basin #144. Furthermore, a tributary of the "eastern valley", determined to be 4^{th} order, now occupies the valley that breaches the crater rim. Although the definite critical sink-fill depth at which these two basins merged was not identified, the depth of the crater - ~600 m - suggests approximately that depth of water would be required to fill the crater and overtop the northwest part of the crater rim. If steady inflow of water into this crater was available, downcutting of the rim could have continued until the breach valley merged with the "eastern valley." Alternatively, headward growth of an "eastern valley" tributary could have resulted in breaching of the crater rim and therefore piracy of basin #144. Either scenario is possible, but based on previous morphometric analyses regarding the lack of significant valley growth, as well as the short lengths of the valleys breaching the southwest rim of the crater, suggests that the latter scenario is most likely.

5.7 CONCLUSIONS

Previous geologic and geomorphic mapping studies [e.g., Crumpler, 1998, 1999; Mest and Crown, 2001b, 2002b, 2003a; Crumpler and Tanaka, 2003] have revealed the presence of numerous systems of valleys within the highlands of Promethei Terra and Libya Montes. This research has attempted to use these maps in conjunction with GIS-based hydrologic modeling to

constrain the process(es) by which these highland valleys formed. These valley networks are orders of magnitude smaller than networks found in Tyrrhena Terra and other parts of the martian highlands, and are incised within sedimentary materials that fill low-lying basins as well as adjacent massifs of ancient crustal materials and degraded impact crater rims that form most drainage divides. Drainage patterns, which are mostly functions of slope, of the mapped networks in both areas are locally dendritic within the shallow-sloping basin-filling materials and parallel along the steep slopes of highland massifs and crater rims, and are sub(parallel) across the entire region of Libya Montes. The valleys that compose these networks display relatively pristine morphologies at high-resolution Viking, MOC and THEMIS scales, and are observed to widen downstream, which is typical of runoff-derived valleys. Some valleys appear to have eroded laterally in some places, such as around small impact craters, suggesting flow must have been persistent enough in some valleys to have adjusted their courses around these obstacles.

Many highland massifs and impact crater walls are incised with morphologically simple, parallel valleys and gullies, respectively, that typically head at or near the crests of the massifs and crater rims. These features generally terminate at the bases of these steeper terrains, but some are observed to continue onto the surfaces of low-lying sedimentary deposits. The morphologies of these fluvial features suggests a portion of their formation involved surface runoff rather than expulsion of subsurface water. Many of the interior crater gullies observed in Promethei Terra and Libya Montes are unlike the gullies identified by Malin and Edgett [2000], which head at the base of distinct layers, have associated head alcoves and distal debris fans, and are believed to have formed by slow seepage or rapid outbursts of water. Cross-cutting relationships, valley and gully morphologies, crater/valley relationships, and impact crater distributions observed in Promethei Terra [Mest, 1998; Mest and Crown, 2001b, 2002b, 2003a] and Libya Montes [Crumpler, 1998, 1999; Crumpler and Tanaka, 2003] show fluvial activity in the two regions is temporally consistent. Formation of small-scale valleys on steep highland massifs and gullies along the interior walls of some impact craters are believed to be part of an early phase of fluvial activity, possibly Middle Noachian in age, because they are typically truncated by Late Noachian and Hesperian-aged sedimentary basin-filling materials. The valley networks that dissect these basin-filling sedimentary deposits and some reactivated small-scale highland valleys represent a second episode of fluvial activity that is believed to be Early to Late Hesperian in age in both study areas [Mest and Crown, 2001b, 2002a,b, 2003a; Crumpler and

Tanaka, 2003]. Compared to network formation discussed in Chapters 2.0 and 4.0 for Tyrrhena Terra, which was found to range from Upper Noachian to Lower Hesperian, the small-scale Promethei Terra and Libya Montes networks are relatively younger. Small-scale gully formation, with associated alcoves and debris fans, along the walls of the valles in Promethei Terra and the interior walls of some impact craters may provide evidence for some of the youngest fluvial activity in the study areas, possibly as young as Amazonian in age [Mest, 1998; Mest and Crown, 2001b, 2002a,b, 2003a; Crumpler and Tanaka, 2003]. The occurrence and ages of highland valley networks in Promethei Terra, combined with the presence of five Hesperian-aged outflow systems and numerous Amazonian-aged debris aprons, neither of which are found in Libya Montes or Tyrrhena Terra, suggests that volatile distribution and the duration of volatile-related activity varied greatly between these three study areas.

Arc/Info GRID-based hydrologic modeling has been conducted in the highlands of Promethei Terra and Libya Montes using a high-resolution 128 pixels/degree MOLA DEM using the methodology described in Chapter 4.0. The sink-fill depth (SFD) was adjusted in each region over multiple iterations of the model in order to delineate drainage divides and networks that most accurately approximated the locations of observed valleys, from which standard hydrologic morphometric parameters were derived. The hydrologic modeling results presented here, as in Chapter 4.0, assume the only source of fluids is from precipitation. Over several iterations of the model in both study areas, it was found that unlike Tyrrhena Terra, there was no ideal combination of drainage divides and valley networks that best approximated the numbers and locations of valley networks observed in the image data sets. Despite the high spatial and vertical resolution (~460 m/pixel and ~10 m, respectively) of the MOLA DEM, there are a large number of closely-spaced low order valleys visible in the image data sets. These valleys, which include small-scale valleys found on highland massifs and gullies incised along interior crater walls, are largely missed by the model partly because their spacing is smaller than the DEM resolution, but also because at latitudes closer to the equator, the amount of interpolation within the DEM increases. In addition to DEM resolution, Arc/Info inherently delineates valleys where the topography suggests in order to identify pathways by which water may move out of the drainage system, as discussed in Chapter 4.0. As a result, the modeled valleys, especially in Promethei Terra, are observed to be inaccurately delineated along the edges of debris aprons or impact ejecta, and the high numbers of modeled valleys do not accurately represent the overall low

numbers of valleys that have been previously mapped [Crumpler, 1998, 1999; Mest and Crown, 2001b, 2002b, 2003a; Crumpler and Tanaka, 2003]. Image data alone suggests fluvial processes in Promethei Terra and Libya Montes were relatively efficient in dissecting the highland and basin-filling materials. However, overall network morphometry (e.g., large numbers of first order valleys disconnected from the main systems) reflects the immaturity of these watersheds and further suggests that the fluvial processes that eroded these parts of the highlands may have been short-lived. In addition, subsequent processes, such as groundwater sapping, mass wasting and eolian infilling could have extensively modified valleys in Promethei Terra and Libya Montes.

The hydrologic morphometric parameters presented in this study (drainage density, stream order, bifurcation ratio, length ratio, and relief morphometry) for modeled watersheds in Promethei Terra and Libya Montes are typical descriptors of terrestrial watersheds. In general, most of the parameters described for Promethei Terra and Libya Montes are comparable to terrestrial values, with the exception of drainage density, which is still orders of magnitude lower than most terrestrial systems. Several statements can be made regarding drainage densities observed in this study relative to Tyrrhena Terra. (1) Slopes in Tyrrhena Terra are fairly low and consistent from basin to basin, whereas slopes in Promethei Terra and Libya Montes are steep along the highland massifs and lower within the basins. If the Promethei Terra and Libya Montes systems were dominated by precipitation, storm events producing large volumes of runoff on steeper surfaces could have choked low-lying valleys with increased sediment load. The work of the system would have involved channeling the increased sediment load into the larger basin-floor valleys rather than development of new tributaries. Increased sediment into the low-lying valleys could have also filled many of the smaller low order valleys as the processes of deposition and erosion competed. (2) Unlike Tyrrhena Terra, the lithology of basin-filling materials in Promethei Terra and Libya Montes is presumably fairly homogeneous, which should help to promote tributary growth, but is not observed in image data sets. (3) The dominant valley-forming processes may be greatly different between the three study areas, which is supported by the spatial variations in volatile distribution, and would affect the ability of tributaries to develop. (4) Similar to Tyrrhena Terra, climate change on Mars could have resulted in shutting down the hydrologic cycle in Promethei Terra and Libya Montes, thereby leaving relatively immature networks.

Strahler stream orders are comparable for both study areas, as well as for Tyrrhena Terra watersheds and typical terrestrial mountain watersheds. Bifurcation ratios are also comparable for both Promethei Terra and Libya Montes, and to the lower end of terrestrial values, despite the large number of disconnected first and second order mapped valleys identified in most basins that are not modeled as such. The low stream orders determined by this and previous studies of martian valley networks suggest (a) the process of formation may have limited tributary development, and (or) (b) climate changes may have caused tributary development to cease. Unlike Tyrrhena Terra, significant eolian infilling is not observed in Promethei Terra or Libya Montes and may not be responsible for burial of valleys, however, mass wasting from the steeper slopes of adjacent highland massifs could have buried many of the low order tributaries.

Relief ratios suggest that the basins in Promethei Terra and Libya Montes most closely resemble terrestrial mountain watersheds that dissect sediments or sedimentary rock, which is consistent with previous geologic analyses of these terrains [Crumpler, 1998, 1999; Mest and Crown, 2001b, 2002b, 2003a; Crumpler and Tanaka, 2003], and perhaps formed within an arid environment. Relief parameters are a measure of the overall steepness of a basin and the efficiency of a basin to be eroded. The relatively high ruggedness numbers, which are dependent on drainage densities, calculated for these martian basins suggest erosion by runoff should have been quite efficient in most basins due to high local gradients and homogeneous lithology.

Caution has been taken in interpretation of these data since the modeled networks bear little resemblance to those observed in image data sets. Although the data presented here indicate that GIS hydrologic modeling is capable of accurately delineating drainage divides from high-resolution digital elevation models, analyses of watersheds comparable in scale to those in Promethei Terra and Libya Montes should be made on a basin-to-basin basis after carefully checking the image data sets. Furthermore, sink-fill depth selection is an important factor in determining the accuracy of the predicted valleys compared to mapped valleys, and is a reflection of the scale at which watersheds should be modeled. Clearly the interpolation involved in creating the DEM has affected the ability to accurately identify narrow, closely-spaced valleys within the smaller scale watersheds observed here. The mapping study of Crumpler and Tanaka [2003] used many of the available high-resolution MOC and THEMIS images to identify valleys in Libya Montes, which is covered well by these data sets due to its previous high-priority status as a potential landing site. The Promethei Terra study area is not covered well by MOC and

THEMIS visible images, which were not available at the time this area was mapped by Mest [1998] and Mest and Crown [2001a, 2002b, 2003a]. All images that were available for this area were studied, but no additional valleys were identified that greatly changed previous hydrologic maps; however, it is still possible that many valleys remain to be identified due to inconsistent high-resolution coverage of this area. Given the problems with both the modeling and image analyses of small-scale drainage basins in Promethei Terra and Libya Montes, it seems necessary that hydrologic analyses of these martian terrains involve both methods in order to present the most accurate hydrologic scenario.

Morphometric evidence for modeled networks, specifically drainage density and relief parameters, suggests that the process(es) of valley formation were relatively inefficient, most likely due to the rapid changes in slope and infiltration between highland massifs and basin-filling materials. The low infiltration but steeper slopes of highland materials would promote runoff to form small-scale valleys and gullies, but the lack of fluvial features on every massif and crater rim might suggest these materials are somewhat resistant to erosion. Similarly, the basin-filling materials should be more dissected than observed, which supports the scenario mentioned earlier in which high sediment loads derived by high runoff events or mass wasting could have promoted rapid channeling into the larger low-lying valleys rather than tributary development. Alternatively, high infiltration rates within basin-filling materials could have also hindered tributary development within these units. It appears likely that rainfall- or snowmelt-derived runoff would have been the dominant erosional process over groundwater sapping, especially along the steeper slopes of massifs and crater rims where high hydrologic heads would have been required. Valleys incised within basin-filling materials may have had a larger sapping component, where recharge could have been more efficient, but the theater-head and box-like canyon morphologies are not observed in images. Nevertheless, precipitation was required to drive the Promethei Terra and Libya Montes systems, which would require a climate much different than is observed today. Based on the spatial and temporal relationships of dissected highland massifs, impact craters and basin-filling materials, fluvial activity must have been widespread across Promethei Terra and Libya Montes. Fluvial activity appears to span a long period of martian highland history, which is not reflected by the maturity of the networks, suggesting that cyclical shifts in the climate could have caused periods of high fluvial activity and erosion alternating with periods of stagnation. Finally, it is also possible that an early

episode of widespread fluvial activity occurred under more temperate climatic conditions and these episode 1 volatiles were then stored in the subsurface. These volatiles were later remobilized by lessor climatic changes to produce a less intense episode of fluvial erosion and deposition dominated by subsurface migration of volatiles with localized zones of surface accumulation and dissection of surface materials.

6.0 CONCLUSIONS

The martian highlands contain abundant evidence that fluvial activity was widespread and possibly pervasive in some areas. Fluvial features - including well-developed valley networks, single valleys on low slopes, and high densities of gullies on steeper slopes - appear well-preserved at many resolutions in the image data sets available. Some features appear degraded and modified by subsequent processes (eolian and mass wasting) at higher resolutions. This study uses multiple data sets, including Viking Orbiter, THEMIS and MOC images, MOLA topographic data, and TES data to characterize many of the fluvial features and the geology of the terrains in which they are incised in order to better understand the processes that were active in forming valleys and the processes that modified them when flow ceased.

Geologic, geomorphic and hydrologic mapping in three areas of the martian highlands - Tyrrhena Terra, Promethei Terra and Libya Montes - have revealed surfaces that have undergone significant amounts of degradation and modification by impact, fluvial and eolian processes. Most of the materials mapped in Tyrrhena Terra (Chapter 2.0) are very old, ranging from Middle Noachian to Early Hesperian in age, whereas materials in Promethei Terra and Libya Montes (Chapter 4.0), especially those containing fluvial features, are younger, ranging from Late Noachian to Late Hesperian in age [Crumpler, 1998, 1999; Mest, 1998; Mest and Crown, 2001a, 2002b, 2003 Crumpler and Tanaka, 2003]. Among the three study areas, only surficial deposits - such as dune-forming materials, talus, and debris aprons - and small-scale gullies [see Malin and Edgett, 2000] along valles and crater walls show evidence for activity in the Amazonian Period. Localized geologic mapping of crater Millochau in the highlands of Tyrrhena Terra has revealed a suite of intriguing geological units and features, and shown that the crater interior has undergone a complex history of post-emplacement modification that may have included collapse, erosion, and redistribution of fine-grained sediments by the wind. Stratigraphic and cross-cutting

relationships, combined with crater size-frequency distributions, have been used to constrain the relative stratigraphic positions of the units identified in Tyrrhena Terra and within Millochau.

The geologic histories of Tyrrhena Terra, Promethei Terra and Libya Montes can be summarized as follows:

- Hellas and Isidis impact events early in Mars' history established regional gradients and emplaced widespread ejecta deposits across the southern highlands.

- Widespread intercrater plains formed in Tyrrhena Terra by accumulation of sedimentary, volcanic, and impact-related materials during the Early and Middle Noachian Epochs.

- Heavy bombardment during the Noachian Period produced numerous large (D>10 km) impact craters within the three study areas, including crater Millochau in Tyrrhena Terra. Fluvial processes eroded the intercrater plains of Tyrrhena Terra and the highland massifs of Promethei Terra and Libya Montes, forming valley networks, such as Vichada Vallis, on the plains, highland surfaces and ejecta deposits of older craters.

- During the Late Noachian and Early Hesperian Epochs in Promethei Terra and Libya Montes, low-lying basins were filled with sediments shed from adjacent highland massifs, truncating many small valleys and gullies near the bases of the massifs and crater walls in which they are incised. As fluvial activity waned in Tyrrhena Terra, impact events continued, truncating and (or) burying some valley segments.

- Degradation of impact craters occurred during the Noachian and Hesperian Periods in the three regions. Many craters display eroded ejecta blankets and rims, interior walls incised with high densities of parallel gullies, and floor containing deposits of relatively smooth fill material.

- Crater Millochau is one example of an Early to Middle Noachian-aged crater displaying complex sequences of Late Noachian to Hesperian-aged deposition and erosion in which a detailed analysis of the floor deposits could be conducted:

- A 23-km-diameter crater in western Millochau displays a fairly unmodified ejecta blanket with relatively large area; crater size-frequency distributions for this ejecta provide upper age constraints (mid- to Late Hesperian) on the emplacement and erosion of Millochau's interior deposits.

- Deposition of sediments within Millochau appears to be related in part to erosion of the interior crater rim by numerous gullies and mass wasting during the Middle Noachian to Early Hesperian Epoch, but may also include contributions from younger eolian and lacustrine activity.

- Emplacement and erosion of pitted and rugged materials occurred during the Middle Noachian to Late Hesperian, prior to formation of the 23-km-diameter crater. Pitted material is confined to a plateau that stands ~400 m above the surrounding floor materials, and rugged material is observed to embay portions of the plateau. Both are believed to consist of sedimentary and impact-related materials, but pitted material may also have a volcanic component.

- Collapse of pitted and rugged material occurred during the Hesperian Period forming depressions that define the northern and eastern plateau boundaries. The collapse zones exposed layers along portions of the plateau's scarp boundary that consist of thin, relatively horizontal stratigraphically lower layers and thicker, more massive upper layers. Post-collapse erosion and redistribution of sediments (mid- to Late Hesperian to present) formed exposures of etched material.

- Several sapping-type valleys incised along the edges of the plateau indicate water was released from the layered deposits that compose the plateau, possibly initiated following the formation of the collapse zones.

- Eolian deposition of sediments in low-lying areas to form dune fields, and mass wasting of crater wall material to form talus deposits constitute the most recent activity

within Millochau, most likely in the Early to Middle Amazonian and Late Hesperian to Middle Amazonian Epochs, respectively.

- The Late Noachian and Early Hesperian Periods also involved deposition and remobilization of valley floor material within Vichada Valles.

- A later stage of fluvial activity occurred during the Early to Late Hesperian in Promethei Terra and Libya Montes. This stage produced small-scale valley networks in basin-filling materials and may have reactivated some highland gullies. Also during this time, the five large valles - Dao, Niger, Harmakhis, Reull and Teviot Valles - formed in Promethei Terra along the eastern rim of Hellas basin; these features are unique among the three areas studied and presumably delineate zones of high volatile abundance in the Martian subsurface.

- The most recent activity identified in the three areas includes emplacement of Late Hesperian- to Amazonian-aged talus deposits and debris aprons, formation of small-scale Amazonian-aged gullies along valles and interior crater walls, and eolian modification, which is ongoing.

Characterization of drainage basin and valley network morphometry, and valley morphology has been used in this study to constrain the processes of valley formation. Valley networks observed in Tyrrhena Terra, Promethei Terra and Libya Montes display mainly dendritic and sub(parallel) patterns, which are primarily functions of slope. Shallow sloping interlayered sedimentary, volcanic and impact-related materials dominate Tyrrhena Terra, and are incised with valleys that form dendritic patterns, and valleys forming (sub)parallel patterns are found on steeper slopes along the rims of impact craters. Drainage patterns of networks in Promethei Terra and Libya Montes are locally dendritic within the shallow-sloping basin-filling materials and parallel along the steep slopes of highland massifs and crater rims, and are sub(parallel) across the entire region of Libya Montes. Valley networks in Promethei Terra and Libya Montes are orders of magnitude smaller than networks found in Tyrrhena Terra and other parts of the martian highlands. These networks are incised within sedimentary materials that fill low-lying basins as well as adjacent massifs of ancient crustal materials and degraded impact

crater rims that form most drainage divides. The exterior rims and interior walls of many impact craters in the three areas are incised with high densities of parallel networks and gullies, respectively, that generally head at or near the rims of craters. This suggests groundwater sapping may not have been prevalent in forming these features because establishing a hydrologic head at the rim of a crater adequate enough to sustain sufficient flow to form valleys is extremely difficult, as indicated in previous studies [e.g., Craddock and Maxwell, 1993; Craddock and Howard, 2002].

Most gullies in Tyrrhena Terra, Promethei Terra and Libya Montes are unlike the gullies identified by Malin and Edgett [2000], which head at the base of distinct layers and have associated head alcoves and distal debris fans. The valleys that compose the networks analyzed in this study display relatively pristine morphologies at high-resolution Viking, MOC and THEMIS scales. Depths and widths vary along the lengths of most valleys, but most are observed to widen downstream, which is typical of runoff-derived valleys. Some valleys appear to have eroded laterally in some places, such as around small impact craters, suggesting flow must have been sustained, and possibly generally excessive, in some valleys to have adjusted their courses around obstacles.

Investigation of highland degradation and modification by fluvial processes in Tyrrhena Terra, Promethei Terra and Libya Montes provides important insights into the variability of geologic processes and climatic conditions among these areas. Geologic mapping in Promethei Terra [Crown et al., 1992; Mest, 1998; Mest and Crown, 2001a, 2002b, 2003] and Libya Montes [Crumpler, 1998, 1999; Crumpler and Tanaka, 2003] has shown that much of the fluvial activity in the latter two regions is younger relative to Tyrrhena Terra. Valley networks in the highlands of Promethei Terra and Libya Montes are an order of magnitude smaller in scale than those in Tyrrhena Terra and tend to be confined to low-lying areas among highland massifs. The large events that formed the eastern Hellas valles also most likely occurred in the Hesperian Period. In addition, the highlands east of Hellas contain numerous Amazonian-aged debris aprons interpreted to result from downslope movement of volatile-rich material (Crown and others, 1992; Crown and Stewart, 1995; Mest and Crown, 2001, 2002, 2003; Pierce and Crown, 2003). These features are not observed in the Tyrrhena Terra or Libya Montes study areas. The significant differences between the ages, scales and morphologies of fluvially-produced features in the three areas studied here suggests (a) the climate histories of the three regions differ

significantly, (b) the distribution of volatiles in the highlands varies greatly, and (or) (c) the effects of fluvial processes on these landscape were greatly dissimilar.

This research has also conducted Arc/Info GRID-based hydrologic modeling in the highlands of Tyrrhena Terra, Promethei Terra and Libya Montes, in conjunction with the mapping studies outlined above and described in this document, to constrain the process(es) by which most highland valleys formed. The GRID-based model presented in this study assumes the only source of fluids is from precipitation. The model was tested on low-resolution (16 pixels/degree) and high-resolution (128 m/pixel) MOLA DEMs of the Tyrrhena Terra study area to determine the effects of resolution on the model. This showed that although the low-resolution DEM may be adequate to model features with significant relief, such as drainage divides and high-order streams, the low-resolution DEM did not accurately predict low-order streams. Drainage divides and networks were delineated in this analysis for all study areas as a function of sink-fill depth (SFD). Multiple iterations of the model, using the hydrologic GRID functions FILL, FLOWDIRECTION, WATERSHED and FLOWACCUMULATION (Chapter 3.0) were conducted to find the optimal sink-fill depth from which to derive drainage divides and valley networks and thus extract morphometric data. Optimal sink-fill depths were determined by overlaying modeled drainage divides on mapped valley networks until they adequately contained the mapped networks. Although the highest resolution DEM available was used, the modeling results are most certainly affected by the spatial and vertical resolution of the MOLA DEM, 128 pixels/degree (~460 m/pixel) and ~10 m, respectively.

Compared to mapped networks, models of the larger-scale valley systems in Terra Tyrrhena accurately represent the locations of higher order valleys, and down to at least second order; many modeled first-order valleys are not visible in Viking, THEMIS or MOC images. Assuming that valleys in Tyrrhena Terra are not buried, then image data would suggest that rainfall-fed runoff was not very efficient in dissecting the highlands. However, it also appears that sapping would not have been efficient either due to discontinuous aquifers resulting from the interlayered nature of the intercrater plains, or lack of an effective recharge mechanism. Many more valleys could have formed in Tyrrhena Terra, but have subsequently been buried by impact ejecta or eolian materials. The ability to identify valleys in images can be further hindered by valley orientation and depth versus sun angle and incidence angle. Unlike Tyrrhena Terra, there was no ideal combination of drainage divides and valley networks that best approximated the

numbers and locations of valley networks observed in Promethei Terra and Libya Montes. Despite the high spatial and vertical resolution of the MOLA DEMs, there remained a large number of closely-spaced low order valleys visible in the image data sets that were not identified in the topography by the model. Image data alone suggests fluvial processes in Promethei Terra and Libya Montes were relatively efficient in dissecting the highland and basin-filling materials. However, overall network morphometry (e.g., large numbers of first order valleys disconnected from the main systems) reflects the immaturity of these watersheds and further suggests that the fluvial processes that eroded these parts of the highlands may have been short-lived. In addition, subsequent processes, such as groundwater sapping, mass wasting and eolian infilling could have modified valleys in Promethei Terra and Libya Montes, thus affecting ability of the model to extract valleys.

Terrestrial watersheds are characterized by morphometric parameters (e.g., drainage density, stream order, bifurcation ratio, length ratio, and relief morphometry) that can be used to evaluate the geologic, climatic and hydrologic conditions under which they form. These parameters have been calculated for selected basins in the Tyrrhena Terra, Promethei Terra and Libya Montes study areas. Drainage densities for mapped watersheds in Tyrrhena Terra and modeled watersheds in all three areas (0.004-0.171 km^{-1}) have been shown to be consistent with other studies of martian valley networks, but are still much lower than most terrestrial drainage basins. In addition, drainage densities for modeled watersheds in Promethei Terra and Libya Montes are slightly higher than those calculated in Tyrrhena Terra. The low martian drainage densities that have been determined in this study, as well as the differences among the three areas, can be attributed to various combinations of several factors:

- Availability of volatiles / volatile distribution. The variety of volatile-related features produced in Promethei Terra compared to the just valley networks observed in Tyrrhena Terra and Libya Montes suggests distribution of volatiles varied between the three study areas. The distribution and availability of volatiles (including their form - precipitation versus sapping) would affect watershed development in the three study areas, especially the ability of these volatiles to dissect the surface.

- Variations in lithology. Tyrrhena Terra, which is believed to consist mostly of bedrock of interlayered sedimentary, volcanic and impact materials, displays large areas of undissected terrain. Basin-filling materials in Promethei Terra and Libya Montes are believed to consist of unconsolidated or poorly consolidated sediments, which should have helped to promote tributary growth, but the networks dissecting these deposits do not display the density of small tributaries that would be expected in these deposits.

- Local slopes: Slopes in Tyrrhena Terra were fairly low and consistent from basin to basin, whereas slopes in Promethei Terra and Libya Montes are steep along the highland massifs and lower within the basins. If precipitation dominated, storm events could produce large volumes of runoff on steeper surfaces resulting in sediment-choked valleys downstream. Increased sediment load could have been rapidly channeled into the larger basin-floor valleys instead of development of new tributaries. Increased sediment into the low-lying valleys could have also filled many of the smaller low order valleys as the processes of deposition and erosion competed.

- The inability to preserve small valleys and subdue large valleys due to destruction by impact craters and burial by eolian deposits.

- Temporal limitations or immature network development by climate change: Climate change on Mars could have resulted in shutting down the hydrologic cycle in all study areas, thereby leaving relatively immature networks.

Strahler stream orders are comparable for all study areas, as high as 5th order for mapped and modeled watersheds, as well as for typical terrestrial mountain and lowland watersheds. Bifurcation ratios, being related to stream order, are also comparable for all data sets, despite the large number of disconnected first and second order mapped valleys identified in most basins that are not modeled as such, but the martian values are lower than terrestrial values. Low stream orders determined in this study suggests (a) the process(es) of formation may have limited tributary development, and (or) (b) climate changes may have caused tributary development to cease. However, it has also been shown in several studies [e.g., Carr, 1996, Carr and Chuang,

1997; Craddock and Howard, 2002; Irwin and Howard, 2002] that the ability of the smallest fingertip tributaries to be identified is inhibited by image resolution. Furthermore, similar to the argument for low drainage densities, eolian materials and competition with impact cratering could have also acted to limit stream orders.

Relief ratios determined for Tyrrhena Terra, Promethei Terra and Libya Montes are shown to be comparable to terrestrial values. Relief ratios for basins in Tyrrhena Terra indicate they most closely resemble terrestrial lowland watersheds that dissect sediments or sedimentary rocks, which is consistent with the geologic analysis of this terrain discussed in Chapter 2.0. Conversely, relief ratios suggest that the basins in Promethei Terra and Libya Montes most closely resemble terrestrial mountain watersheds that dissect sediments or sedimentary rock, perhaps formed within an arid environment, which is consistent with previous geologic analyses of these terrains [Crumpler, 1998, 1999; Mest and Crown, 2001a, 2002b, 2003; Crumpler and Tanaka, 2003]. Relief parameters are a measure of the overall steepness of a basin and the efficiency of a basin to be eroded. Ruggedness numbers, which are dependent on drainage densities, are relatively low for Tyrrhena Terra basins and high for Promethei Terra and Libya Montes basins. This suggests erosion by runoff was not very efficient in most basins in Tyrrhena Terra due to low gradients or lithology, and (or) that many of the smaller fingertip tributaries have been subsequently buried, but should have been quite efficient in most basins in Promethei Terra and Libya Montes due to high local gradients and homogeneous lithology.

Hydrologic modeling shown in this study, obtained using a technique common to many terrestrial and martian studies, represent a first order attempt to identify flow paths on the present martian surface. The hydrologic modeling results appear to adequately delineate the large-scale watersheds in Tyrrhena Terra, at least down to second order valleys, but inaccuracy tends to increase toward smaller-scale watersheds in Promethei Terra and Libya Montes. Sink-fill depth selection is an important factor in determining the accuracy of the predicted valleys compared to mapped valleys, and is a reflection of the scale at which watersheds should be modeled. For small-scale watersheds, it has been shown that analyses should be made on a basin-to-basin basis after carefully checking the image data sets. The data presented here indicate that GIS-based hydrologic modeling is also able to accurately delineate drainage divides from high-resolution digital elevation models, but modeling alone is inadequate to accurately identify martian valley networks in detail. It therefore seems necessary, given the combination of topographic and

imaging data sets that currently exist for Mars, that hydrologic modeling of martian terrains be accompanied by detailed geologic analyses and geomorphic mapping in order to present the most accurate hydrologic scenario.

The nature of the fluvial activity that formed extensive valley networks has been questioned in this and other areas of the highlands (e.g., Craddock and Maxwell, 1993; Carr, 1996, Maxwell and Craddock, 1995; Grant, 2000; Craddock and Howard, 2002; Grant and Parker, 2002). Carr (1995, 1996) attempted to explain most valley formation by groundwater sapping combined with mass wasting induced by surface runoff. The current study has shown that valley (variations in along-stream valley depths and widths and areas where lateral widening has occurred by excessive flow, lack of theater heads) and network (dendritic to (sub)parallel drainage patterns) morphologies in Tyrrhena Terra, Promethei Terra and Libya Montes do not support sapping dominated systems. Furthermore, the fact that many valleys head near crater rim crests, suggest a significant component of surface runoff not derived from groundwater was involved, such as from direct precipitation or water derived from melting snow or ice, which has been proposed for Margaritifer Sinus (Grant, 2000; Grant and Parker, 2002) and other highland terrains (Craddock and Maxwell, 1993; Maxwell and Craddock, 1995; Craddock and Howard, 2002). However, although systems such as Vichada Valles are extensive and apparently well-integrated, and high-resolution imaging datasets have allowed identification of small tributaries not observed earlier (Carr, 1995, 1996), large interfluves appear undissected. Drainage systems the size of Vichada Valles would seem to require either 1) mobilization of volatiles contained within an extensive subsurface reservoir or 2) widespread precipitation. High infiltration rates presumably characterize the surface and near-surface materials of Tyrrhena Terra, and therefore valley formation could includes a combination of sapping and runoff processes, with larger valley segments shaped in run-off dominated phases or as greater volumes of groundwater collected in the surface drainage system. Furthermore, morphometric evidence for mapped and modeled networks in the three areas - specifically drainage density and relief parameters - suggests that the process(es) of valley formation were relatively inefficient, possibly due in part to high infiltration properties of surface materials.

The evidence presented in this study for Tyrrhena Terra, Promethei Terra and Libya Montes suggests sapping may have only played a secondary role in valley formation. Therefore, precipitation-fed runoff, either directly by rainfall or by snowmelt, is likely the dominant process

of valley formation. Furthermore, based on the spatial and temporal relationships of dissected highland materials and impact craters in the three study areas, erosion by runoff must have been widespread, but relatively short-lived with most activity confined to the Noachian Period in Tyrrhena Terra, and existing as at least two episodes in Promethei Terra and Libya Montes.

Future work on this topic would involve incorporating new martian data sets into existing studies to produce accurate geologic and hydrologic maps. The hydrologic modeling technique can also be refined to make finding the "ideal" sink-fill depth less time consuming and computer-intensive. This could be done by comparing histograms of sink-fill depth to impact crater depth for any DEM in order to effectively eliminate the topographic effects of the craters from the DEM leaving only the dissected surface from which to extract basins and valleys. Furthermore, terrestrial analog studies - from field and modeling perspectives - need to be incorporated into martian hydrologic analyses to better understand the value of the morphometric parameters being used to characterize martian watersheds, as well as to constrain the processes of martian valley network formation. Lastly, impact crater and highland degradation analyses also require attention given the abundant data that are now available. The recent availability of high resolution MOC and THEMIS data sets have allowed enigmatic crater interior deposits, similar to those observed in crater Millochau, to be identified. This suggests that these craters may have undergone similar processes of degradation, infilling, and erosion. There is a clear need for detailed analyses of individual highland craters and regional comparisons of the emplacement and modification of crater interior deposits. Detailed analyses of highland craters using the methods described in this study will provide further understanding of impact crater degradation during the early part of Mars' history and of the types and sequences of processes that have shaped Martian highland surfaces.

APPENDIX A

CRATER COUNTING METHODOLOGY:
MTM -20272 AND -25272 QUADRANGLES, TYRRHENA TERRA, MARS

Relative age information for the geologic units in Mars Transverse Mercator (MTM) quadrangles -20272 and -25272 (1:500,000 scale; latitude -17.5 to -27.5°, longitude 270° to 275°) was derived by determining the number and size distribution of superposed impact craters for each geologic unit mapped [Tanaka, 1986]. Unit boundaries were digitized on the MTM quadrangles and unit areas were determined using NIH Image 1.6 software. Individual craters were identified and counted using the MTM photomosaics, a Mars Digital Image Mosaic of VO images (MDIM 2; 231.4 m/pixel; latitude -13° to -30°, longitude 265° to 280°), as well as individual VO frames. Crater diameters were measured (in centimeters) using Adobe Illustrator 9.0 software and converted to kilometers; diameters for larger craters were checked for accuracy using GRIDVIEW software [Roark et al., 2000; Roark and Frey, 2001]. Craters <0.5 km diameter were not counted for all units except talus material and the Millochau floor materials due to the limits of resolution of the VO image products used. The detailed study of crater Millochau by Mest and Crown [2004b] includes counts for all craters >0.050 km for a small part of the map area using VO, MOC, and THEMIS images; these crater size-frequency data are incorporated into this mapping study. Table 2.1 summarizes the crater size-frequency distribution data for N(2), N(5), and N(16) for each geologic unit mapped. N(2), N(5), and N(16) represent the cumulative number of craters with diameters >2, 5, and 16 km/10^6 km^2, respectively (crater size-frequency errors = ± (($N^{1/2}$) / A) × (10^6 km^2)) [Crater Analysis Techniques Working Group, 1978]. The

N(2), N(5), and N(16) data and their associated uncertainties were then compared for each unit; these data were used to determine the appropriate time-stratigraphic epochs.

Determination of Martian ages for the units described in this study is based in part upon crater size-frequency distributions. It was found that a consistent crater-counting methodology could not be applied to all units in the map area due to the limited areal exposure of some units, and the presence of many large-diameter craters with widespread ejecta blankets and the related complicating effects of secondary craters. Below is an explanation of how these issues were dealt with to provide relative age estimates.

The first issue is significant variation in areal exposures of units and the presence of large-diameter impact craters with distinct, widespread ejecta blankets that may superpose these units. Several units identified in this study have small areas, specifically: valley floor material, talus material, mountainous material, and the Millochau floor deposits. Valley floor material forms narrow linear deposits that typically do not show clear relative age relationships to impact crater ejecta. One example of a clear relationship occurs where the trunk valley of Vichada Valles appears to be truncated and buried in parts by the ejecta from several large (D>25 km) craters around 24° S. These craters have ejecta blankets that cover areas up to two times their diameters. In such examples for this unit and the other limited-exposure units mentioned above, these craters were not included in counts for units of small areal extent. To include these large-diameter craters in the counts for valley floor material would also require including the areas of their ejecta blankets in the area of valley floor material. This would imply that large quantities of valley floor material presumably extend to some distance beneath the ejecta deposits, whereas in reality, valley material would only account for a minor fraction of the surface buried by the ejecta. Inclusion of the area of the ejecta deposits with the area of limited-exposure units would greatly increase the areas of those units and therefore provide inaccurate crater statistics and inaccurate relative ages.

For units with larger areas, such as intercrater plains, the method of counting all craters superposed on its surface does not present a problem. The plains are mapped as a widespread unit that has been superposed by a number of large-diameter impact craters. If a crater with widespread ejecta superposes plains material, and that ejecta is even in part surrounded by plains material, it is reasonable to assume that plains material composes a large portion of the surface

underlying the ejecta. In cases such as this, which are typical for large craters in the map area, these craters were counted and their areas were included in the area of the unit of interest.

An additional difficulty in interpreting crater size-frequency distributions was the potential that numerous secondary craters might be included in the crater counts. Definitive identification of secondary craters is difficult if not impossible. There are some clear identifiers of secondary craters, such as closely spaced chains, clusters of small-diameter craters, and elongated forms, which allowed them to be excluded from the counts. Any not-so-obvious individual secondary craters would have been counted and included in crater size-frequency distributions. Due to the inclusion of these craters, relative age estimates could be skewed to older ages. However, it should be noted that, given the presence of numerous, large, fresh-appearing craters, every unit has the potential to contain secondary craters, such that relative ages may be skewed in a fairly uniform manner.

APPENDIX B

DESCRIPTION OF MAP UNITS

[Unit descriptions and interpretations are based on morphology, texture, albedo, and stratigraphic position as observed in VO, THEMIS and MOC images]

SURFICIAL DEPOSITS

AHt **Talus material**--Narrow deposits found along interior crater walls; overlies crater floor material. Featureless in VO images; irregular surface textures and layering visible in high resolution MOC images. *Type area:* 21.4°S., 273.8°W. *Interpretation:* Debris shed from crater rim materials; layering may be due to deposition of material in multiple mass wasting events

VALLEY MATERIALS

HNvf **Valley floor material**--Deposits forming floors of valleys. Appears smooth to pitted in VO images. Dune or ripples visible in high-resolution MOC images; dunes or ripples oriented perpendicular to valley walls. *Type area:* 20.5°S., 272.5°W. *Interpretation:* Sedimentary material derived from surrounding units and deposited within valleys by

a combination of flowing water, mass-wasting, and eolian processes. Dune or ripples indicate movement of material along valley floors by eolian activity

HIGHLAND MATERIALS

Hpl_3 **Smooth plateau unit**--Regional unit described by Greeley and Guest [1987] as forming flat, featureless plains that locally embay other units; faults and flow fronts rare. In map area, small surface area exposed in southeast corner; smooth to hummocky surface characterized by some wrinkle ridges. Moderately cratered. *Type area:* 25.5°S., 270.3°W. *Interpretation:* Interbedded volcanic and sedimentary deposits of fluvial and (or) eolian origin [Greeley and Guest, 1987]

Npi **Intercrater plains material**--Irregularly to heavily pitted surface dissected by well integrated networks of valleys. MOC images show darker material filling low-lying areas among more heavily cratered and pitted plains; darker material exhibits dune features. Northern parts display numerous scarps; dunes are sparse on dark material; heavily cratered. Southern parts (south of 24°S.) exhibit fewer channels and scarps than northern parts; dunes or ripples abundant on dark material and high-standing exposures; moderately cratered. *Type areas:* 20.7°S., 272.3°W. (pitted) and 25.1°S., 270.4°W. (dune-covered). *Interpretation:* Volcanic and (or) sedimentary deposits that have been subjected to impact and fluvial processes. Valleys are believed to be fluvial in origin. Pitted surface results from small (D<1 km) poorly preserved impact craters. Dunes or ripples result from redistribution of sediments within the plains by wind. Pitted materials (concentrated in northern part) previously mapped as hilly and cratered material by Schaber [1977] and dissected plateau material by Greeley and Guest [1987]; smoother materials located in southern part previously mapped as dark

mottled plains material by Schaber [1977] and ridged plains material by Greeley and Guest [1987]

Nm **Mountainous material**--Forms small isolated massifs within younger units. *Type area:* 17.6°S., 273.6°W. *Interpretation:* Ancient crustal material uplifted during formation of impact basins and large craters [Greeley and Guest, 1987]

CRATER MATERIALS

[Impact craters with rim diameters <3 km not shown; crater materials include floor deposits that post-date crater formation]

HNcf **Crater floor material**--Exhibits smooth surfaces on crater floors in VO images and rugged surfaces in MOC images; some deposits display lobate margins against interior crater walls. *Type area:* 19.7°S., 273.4°W. *Interpretation:* Sedimentary materials deposited on crater floors due to erosion of crater rims and eolian activity. Deposits within craters that have been breached; partially derived from materials outside of the crater rim. Floor deposits may be partially lacustrine in origin. Some craters may contain units similar to those mapped in Crater Millochau but lack of high resolution images has not thus far allowed identification

Crater Millochau Floor Deposits

Amd **Millochau dune material**--Forms patches that fill pits, small craters, and depressions within pitted material (unit Nmp), and forms dune fields that cover large areas within etched material on floor of Crater Millochau. Generally darker than underlying materials in MOC images. Consists of long- and short-wavelength (40-170 km and 10-30 km, respectively) dunes or ripples. Long-wavelength dunes or ripples generally oriented east-west (long axis) and span the widths of depressions in which they occur.

Short-wavelength dunes or ripples are shorter and narrower than long-wavelength dunes; dunes oriented parallel and less commonly perpendicular to long-wavelength dunes, and typically oriented perpendicular to slopes of local topographic highs. *Type area:* 21.3°S., 274.4°W. *Interpretation:* Sedimentary material eroded from interior floor deposits of crater Millochau and redistributed within low-lying areas by wind to form dunes or ripples

HNme **Millochau etched material**--Forms surfaces within depressions that border central plateau of Millochau. Displays smooth, lineated, and irregular surface textures, and variations in brightness in MOC and THEMIS images. Comprises layers of different thickness exposed along scarps and knobs. Unit contains few fresh impact craters, and some craters appear to have been exhumed. Found adjacent to units Nmp and HNmr. *Type area:* 21.2°S., 274.5°W. *Interpretation*: Crater floor materials undergoing erosion and redistribution; locally, removal of overlying materials appear to reveal surfaces that once accumulated craters. Deposits consist of interlayered sedimentary, volcanic, and (or) impact materials that have undergone collapse and (or) been eroded by fluvial, eolian and mass wasting processes. Some of deposits derived from adjacent interior deposits. Dune material (unit Amd) forms small patches that cover unit

HNmr **Millochau rugged material**--Consists of deposits covering the floor of Millochau and surrounding the central plateau; extends from the depressions that border the plateau to the base of inner rim of Millochau. Forms an irregular surface that displays numerous degraded craters (D<1 km) and pits, similar to pitted material (unit Nmp). Contains numerous low-relief scarps that appear to act as boundaries between material with different brightness. Locally, layering exposed along scarps that form boundaries of closed depressions. *Type area:* 20.8°S., 274.8°W. *Interpretation:*

Deposits consisting of interlayered sedimentary, volcanic, and impact materials. Sedimentary materials could be composed of materials eroded from interior crater walls, eolian deposits, or are lacustrine in nature. Pits may be collapse features, degraded craters, or wind-modified depressions. Scarps may be erosional (from fluvial and (or) eolian processes) or tectonic (from collapse or faulting) in nature, or possibly the deposit margin

Nmp **Millochau pitted material**--Covers the central plateau of Millochau and exhibits heavily pitted and cratered surface. Most craters and pits have diameters less than ~1 km. Surface exhibits variations in brightness that correspond to different degradational states; dark material is more rugged and contains more pits and small craters than bright material, and craters and pits in dark material are more degraded; dark material is locally a few meters lower in elevation than bright material. Layering is exposed along the scarp that defines the northern and eastern edge of the plateau. *Type area:* 21.3°S., 274.7°W. *Interpretation:* Deposits consisting of interlayered sedimentary, volcanic, and impact materials. Sedimentary materials could be composed of materials eroded from interior crater walls, eolian deposits, or are lacustrine in nature. Pits may be collapse features, degraded craters, or wind-modified depressions. Bright material representative of upper surface of pitted material that is being eroded, exposing dark substrate, lag deposits, or sediments that accumulated in local low-lying areas.

c_3 **Well preserved crater material**--Characterized by pronounced, continuous crater rim elevated relative to surrounding materials and by well defined, continuous ejecta blanket. *Interpretation:* Pristine impact crater material exhibiting little degradation; some crater floors may contain deposits emplaced by mass wasting, eolian activity, and (or) fluvial processes

c_2 **Moderately degraded crater material**--Characterized by a crater rim that may exhibit only minor relief above surrounding materials and by discontinuous, poorly exposed ejecta. *Interpretation:* Impact craters with moderate degree of degradation; most crater floors contain deposits emplaced by mass wasting, eolian activity, and (or) fluvial processes

c_1 **Highly degraded crater material**--Characterized by a degraded crater rim that may be discontinuous and exhibits little relief relative to the surrounding materials; displays no ejecta and contains smooth, featureless crater floors in VO images. *Interpretation:* Highly degraded impact crater material. Ejecta has been completely eroded or mantled by younger materials; rim has been modified by erosion. Most crater floors contain deposits emplaced by mass wasting, eolian activity, and (or) fluvial processes

APPENDIX C

CRATER COUNTING METHODOLOGY: CRATER MILLOCHAU, TYRRHENA TERRA, MARS

Relative age information for the geologic units mapped in crater Millochau was derived by determining the number and size distribution of superposed impact craters for each geologic unit [e.g., Tanaka, 1986]. Unit boundaries were digitized on the photomosaic (Figure 3.2a) and unit areas were determined using NIH Image 1.6 software. Individual craters were identified using the photomosaic, as well as individual Viking Orbiter, THEMIS, and MOC images. Crater diameters were measured (in centimeters) using Adobe Illustrator 9.0 software and converted to kilometers; diameters for larger craters were checked for accuracy using GRIDVIEW [Roark et al., 2000; Roark and Frey, 2001]. Due to the limits of image resolution and for consistency, craters <0.050 km diameter were not counted. Table 3.1 summarizes the crater size-frequency distribution data for N(2), N(5), and N(16) for each geologic unit mapped. N(2), N(5), and N(16) represent the cumulative number of craters with diameters >2, 5, and 16 km/10^6 km^2, respectively (crater size-frequency errors = ± (($N^{1/2}$) / A) × (10^6 km^2)) [Crater Analysis Techniques Working Group, 1978]. The N(2), N(5), and N(16) data were used to determine the time-stratigraphic series ranges.

Designation of martian stratigraphic ages for the units described in this study is based in part upon crater size-frequency distributions and in part upon stratigraphic relationships. A consistent crater-counting methodology could not be applied to all units in the map area due to the limited areal exposure of some units, and the complicating effects of secondary craters from

the 23-km-diameter crater (M-C-23) in western Millochau. However, the presence of M-C-23 was also beneficial in designating relative ages to other units in Millochau. Because ejecta from M-C-23 covers three of the main units identified in Millochau (Millochau rim, pitted and rugged materials), this crater could be used as a stratigraphic referent for the other units. The area of M-C-23 and the craters contained within it (88 craters; D > 0.050 km) were not incorporated into the areas or counts of any other unit. Interpretation of crater size-frequency distributions was complicated by the potential for secondary craters to be included in crater counts for most units mapped in this study. Definitive identification of isolated secondary craters is difficult if not impossible; however, there are some clear indicators of groups of secondary craters, such as closely spaced chains, clusters of small-diameter craters, and elongated forms, which allowed these types of obvious secondary craters to be excluded from the counts. Any not-so-obvious secondary craters would have been counted and included in crater size-frequency distributions. Due to the likely inclusion of secondaries, relative age estimates could be skewed to older ages. However, it should be noted that, given the presence of M-C-23, every unit within Millochau (perhaps with the exception of dune material) has the potential to contain secondary craters, such that relative ages may be skewed in a fairly uniform manner.

It should be noted that in Table 3.1 the areas and numbers of craters for the 'Millochau floor assemblage' (pitted, rugged, etched and dune materials, and knobs) and the totals for the individual units composing the assemblage are different by 87 km^2 and 58 craters, respectively. The 2% difference in area (calculated as error = ((5,217-5,130) / 5,130) x 100) is insignificant given the uncertainties in area estimation. The difference in the numbers of craters counted is due to craters that overlap unit contacts and have therefore been counted for more than one unit. Possible sources of error in area tabulation include the small patches of dune material being included in the area of pitted material and the areas of several smaller craters that superpose multiple units being included in the areas of each of the units they superpose.

APPENDIX D

ARC/INFO DATA DICTIONARY

Coverages:

Each coverage listed below represents a thematic layer registered within the same geographic region for each study area. The following list describes each coverage and feature type. Nomenclature includes LM = Libya Montes, PT = Promethei Terra, TT = Tyrrhena Terra study areas; 16DPP = 16 degrees per pixel DEM.

Arc/Info Coverages:

Coverage	Type	Description
INT71_#	Arc	Modeled streams for TT intersected by elevation; '7' indicates run number corresponding to SFD = 575 m; '1' corresponds to first order streams (2nd, 3rd, 4th and 5th order stream coverages also generated; '#' indicates elevation bin (TT DEM with elevation range = -3500 to 4000 m separated into 16 500-m bins).
LM_ACCGRD_#	Grid	Accumulation grid for LM, '#' in coverage name is place-holder for run numbers; runs represent specific sink-fill depths used in model.
LM_BASINS_#	Grid	Basin grid for LM, '#' in coverage name is place-holder for run numbers; runs represent specific sink-fill depths used in model.
LM_FILL_#	Grid	Sink fill grid for LM, '#' in coverage name is place-holder for run numbers; runs represent specific sink-fill depths used in model.
LM_FLOWD_#	Grid	Flow direction grid for LM, '#' in coverage name is place-holder for run numbers; runs represent specific sink-fill depths used in model.
LM_GEO	Grid	DEM grid of LM; geographic projection.

LM_LENGRD_#	Grid	Stream length grid for LM, '#' in coverage name is place-holder for run numbers; runs represent specific sink-fill depths used in model.
LM_SHEDCO_#	Polygon	Watershed coverage for LM, '#' in coverage name is place-holder for run numbers; runs represent specific sink-fill depths used in model.
LM_SHEDS_#	Grid	Watershed grid for LM, '#' in coverage name is place-holder for run numbers; runs represent specific sink-fill depths used in model.
LM_SIN	Grid	DEM grid of LM; sinusoidal projection.
LM_SINDEP_#	Grid	Sink depth grid for LM, '#' in coverage name is place-holder for run numbers; runs represent specific sink-fill depths used in model.
LM_SINK_#	Grid	Sink identification grid for LM, '#' in coverage name is place-holder for run numbers; runs represent specific sink-fill depths used in model.
LM_SINMAX_#	Grid	Maximum sink depth grid for LM, '#' in coverage name is place-holder for run numbers; runs represent specific sink-fill depths used in model.
LM_SINMIN_#	Grid	Minimum sink depth grid for LM, '#' in coverage name is place-holder for run numbers; runs represent specific sink-fill depths used in model.
LM_STREAM_#	Grid	Stream location grid for LM, '#' in coverage name is place-holder for run numbers; runs represent specific sink-fill depths used in model.
LM_STRECO_#	Arc	Stream coverage for LM, '#' in coverage name is place-holder for run numbers; runs represent specific sink-fill depths used in model.
LM_STR_#	Grid	Stream coverage using Strahler ordering system for LM, '#' in coverage name is place-holder for run numbers; runs represent specific sink-fill depths used in model.
LM_TICCOV	Tic	Tic coverage of LM; unprojected.
LM_TICCOV_GEO	Tic	Tic coverage of LM; geographic projection.
LM_TICCOV_SIN	Tic	Tic coverage of LM; sinusoidal projection.
PT_ACCGRD_#	Grid	Accumulation grid for PT, '#' in coverage name is place-holder for run numbers; runs represent specific sink-fill depths used in model.
PT_BASINS_#	Grid	Basin grid for PT, '#' in coverage name is place-holder for run numbers; runs represent specific sink-fill depths used in model.
PT_FILL_#	Grid	Sink fill grid for PT, '#' in coverage name is place-holder for run numbers; runs represent specific sink-fill depths used in model.

PT_FLOWD_#	Grid	Flow direction grid for PT, '#' in coverage name is place-holder for run numbers; runs represent specific sink-fill depths used in model.
PT_GEO	Grid	DEM grid of PT; geographic projection.
PT_LENGRD_#	Grid	Stream length grid for PT, '#' in coverage name is place-holder for run numbers; runs represent specific sink-fill depths used in model.
PT_SHEDCO_#	Polygon	Watershed coverage for PT, '#' in coverage name is place-holder for run numbers; runs represent specific sink-fill depths used in model.
PT_SHEDS_#	Grid	Watershed grid for PT, '#' in coverage name is place-holder for run numbers; runs represent specific sink-fill depths used in model.
PT_SIN	Grid	DEM grid of PT; sinusoidal projection.
PT_SINDEP_#	Grid	Sink depth grid for PT, '#' in coverage name is place-holder for run numbers; runs represent specific sink-fill depths used in model.
PT_SINK_#	Grid	Sink identification grid for PT, '#' in coverage name is place-holder for run numbers; runs represent specific sink-fill depths used in model.
PT_SINMAX_#	Grid	Maximum sink depth grid for PT, '#' in coverage name is place-holder for run numbers; runs represent specific sink-fill depths used in model.
PT_SINMIN_#	Grid	Minimum sink depth grid for PT, '#' in coverage name is place-holder for run numbers; runs represent specific sink-fill depths used in model.
PT_STREAM_#	Grid	Stream location grid for PT, '#' in coverage name is place-holder for run numbers; runs represent specific sink-fill depths used in model.
PT_STRECO_#	Arc	Stream coverage for PT, '#' in coverage name is place-holder for run numbers; runs represent specific sink-fill depths used in model.
PT_STR_#	Grid	Stream coverage using Strahler ordering system for PT, '#' in coverage name is place-holder for run numbers; runs represent specific sink-fill depths used in model.
PT_TICCOV	Tic	Tic coverage of PT; unprojected.
PT_TICCOV_GEO	Tic	Tic coverage of PT; geographic projection.
PT_TICCOV_SIN	Tic	Tic coverage of PT; sinusoidal projection.
TT_16DPP_ACC	Grid	Accumulation grid for TT.
TT_16DPP_BAS	Grid	Basin grid for TT.
TT_16DPP_FILL	Grid	Sink fill grid for TT.

TT_16DPP_FLD	Grid	Flow direction grid for TT.
TT_16DPP_GEO	Grid	DEM grid of TT; geographic projection.
TT_16DPP_LEN	Grid	Stream length grid for TT.
TT_16DPP_SHED	Grid	Watershed grid for TT.
TT_16DPP_SHEDCO	Polygon	Watershed coverage for TT.
TT_16DPP_SIN	Grid	DEM grid of TT; sinusoidal projection.
TT_16DPP_SIDEP	Grid	Sink depth grid for TT.
TT_16DPP_SINK	Grid	Sink identification grid for TT.
TT_16DPP_SIMAX	Grid	Maximum sink depth grid for TT.
TT_16DPP_SIMIN	Grid	Minimum sink depth grid for TT.
TT_16DPP_STCO	Arc	Stream coverage for TT.
TT_16DPP_STOR	Grid	Stream coverage using Strahler ordering system for TT.
TT_16DPP_STR	Grid	Stream location grid for TT.
TT_1STORD_#	Arc	First order stream coverage in TT, '#' in coverage name is place-holder for run numbers; runs represent specific sink-fill depths used in model; 2nd, 3rd, 4th and 5th order stream coverage also generated.
TT_#	Grid	Grids of elevation range from TT DEM; '#' indicates elevation bin (TT DEM with elevation range = -3500 to 4000 m separated into 16 500-m bins).
TT_#COV	Polygon	Coverage of elevation ranges from TT grids (above) determining area of elevation bin; '#' indicates elevation bin (TT DEM with elevation range = -3500 to 4000 m separated into 16 500-m bins).
TT_ACCGRD_#	Grid	Accumulation grid for TT, '#' in coverage name is place-holder for run numbers; runs represent specific sink-fill depths used in model.
TT_BASE_GEOG	Grid	Viking Orbiter MDIM 2.0 grid of TT; geographic projection.
TT_BASE_GRD	Grid	Viking Orbiter MDIM 2.0 grid of TT; unprojected.
TT_BASE_SIN	Grid	Viking Orbiter MDIM 2.0 grid of TT; sinusoidal projection.
TT_BASINS_#	Grid	Basin grid for TT, '#' in coverage name is place-holder for run numbers; runs represent specific sink-fill depths used in model.
TT_FILL_#	Grid	Sink fill grid for TT, '#' in coverage name is place-holder for run numbers; runs represent specific sink-fill depths used in model.
TT_FLOWD_#	Grid	Flow direction grid for TT, '#' in coverage name is place-holder for run numbers; runs represent specific sink-fill depths used in model.
TT_GEO	Grid	DEM grid of TT; geographic projection.

TT_LENGRD_#	Grid	Stream length grid for TT, '#' in coverage name is place-holder for run numbers; runs represent specific sink-fill depths used in model.
TT_SHEDCO_#	Polygon	Watershed coverage for TT, '#' in coverage name is place-holder for run numbers; runs represent specific sink-fill depths used in model.
TT_SHEDS_#	Grid	Watershed coverage for TT, '#' in coverage name is place-holder for run numbers; runs represent specific sink-fill depths used in model.
TT_SIN	Grid	DEM grid of TT; sinusoidal projection.
TT_SIN_INTGRD	Grid	DEM grid of TT; sinusoidal projection; integer data type.
TT_SINDEP_#	Grid	Sink depth grid for TT, '#' in coverage name is place-holder for run numbers; runs represent specific sink-fill depths used in model.
TT_SINKS_#	Grid	Sink identification grid for PT, '#' in coverage name is place-holder for run numbers; runs represent specific sink-fill depths used in model.
TT_SINMAX_#	Grid	Maximum sink depth grid for TT, '#' in coverage name is place-holder for run numbers; runs represent specific sink-fill depths used in model.
TT_SINMIN_#	Grid	Minimum sink depth grid for TT, '#' in coverage name is place-holder for run numbers; runs represent specific sink-fill depths used in model.
TT_STREAM_#	Grid	Stream location grid for TT, '#' in coverage name is place-holder for run numbers; runs represent specific sink-fill depths used in model.
TT_STRECO_#	Arc	Stream coverage for TT, '#' in coverage name is place-holder for run numbers; runs represent specific sink-fill depths used in model.
TT_STR_#	Grid	Stream coverage using Strahler ordering system for TT, '#' in coverage name is place-holder for run numbers; runs represent specific sink-fill depths used in model.
TT_TICCOV	Tic	Tic coverage of TT; unprojected.
TT_TICCOV_GEO	Tic	Tic coverage of TT; geographic projection.
TT_TICCOV_SIN	Tic	Tic coverage of TT; sinusoidal projection.
TT_VALLGRD	Grid	Mapped valley grid in TT; unprojected.
TT_VALL_GEOG	Arc	Mapped valley grid in TT; geographic projection.
TT_VALL_SIN	Arc	Mapped valley grid in TT; sinusoidal projection.

Study Areas:

The study areas include Tyrrhena Terra (latitude 13°S to 30°S, longitude 265°W to 280°W), Promethei Terra (latitude 27.5°S to 47.5°S, longitude 245°W to 270°W) and Libya Montes (latitude 5°N to 5°S, longitude 260°W to 280°W), Mars.

Data Layers:

To avoid redundancy, only example coverages from the Tyrrhena Terra study area (128 pixels/degree) are shown below. For coverages that have similar names (e.g., INT71_#) one example is shown that provides the coverage's relevant information, such as areal extent and a list of items defined for that example.

Name: INT71_#

Type: Arc/Info Coverage

Description: Modeled streams for TT intersected by elevation; '7' indicates run number corresponding to SFD = 575 m; '1' corresponds to first order streams (2nd, 3rd, 4th and 5th order stream coverages also generated; '#' indicates elevation bin (TT DEM with elevation range = -3500 to 4000 m separated into 16 500-m bins).

Extent: region: North: -903438.386 East: 399376.908
South: -1626725.125 West: -421494.478

Data Types: Arcs

Source: created by Scott Mest

Projection: SINUSOIDAL

Spheroid: Major Axis: 3393399.9023 Minor Axis: 3375729.9805

Coordinate System: Latitude-longitude

Units: meters

Cover Derivation: Coverage was created using the Arc 'intersect' command in **orders_intersect.aml** by intersecting TT_1STORD_# with TT_#COV. This coverage was used to evaluate stream lengths and numbers of streams (by Strahler order) as a function elevation.

Item definitions: int71_0.aat

COLUMN	ITEM NAME	WIDTH	OUTPUT	TYPE	N.DEC	ALTERNATE NAME	INDEXED?
1	FNODE#	4	5	B	-		-
5	TNODE#	4	5	B	-		-
9	LPOLY#	4	5	B	-		-
13	RPOLY#	4	5	B	-		-
17	LENGTH	8	18	F	5		-
25	INT71_0#	4	5	B	-		-
29	INT71_0-ID	4	5	B	-		-
33	TT_1STORD_7#	4	5	B	-		-
37	TT_0COV#	4	5	B	-		-

* *

Name: TT_1STORD_#

Type: Arc/Info Coverage

Description: First order stream coverage in TT, '#' in coverage name is place-holder for run numbers; runs represent specific sink-fill depths used in model; 2nd, 3rd, 4th and 5th order stream coverage also generated.

Extent: region: North: -769901.637 East: 431532.914
South: -1777009.893 West: -431319.924

Data Types: Arcs

Source: created by Scott Mest

Projection: SINUSOIDAL

Spheroid: Major Axis: 3393399.9023 Minor Axis: 3375729.9805

Coordinate System: Latitude-longitude

Units: meters

Cover Derivation: Coverage was created using the Arc 'reselect' command in **orders.aml** by selecting streams of a specified order from TT_STR_#.

Item definitions: tt_1stord_7

COLUMN	ITEM NAME	WIDTH	OUTPUT	TYPE	N.DEC	ALTERNATE NAME	INDEXED?
1	FNODE#	4	5	B	-		-
5	TNODE#	4	5	B	-		-
9	LPOLY#	4	5	B	-		-
13	RPOLY#	4	5	B	-		-
17	LENGTH	8	18	F	5		-
25	TT_1STORD_7#	4	5	B	-		-
29	TT_1STORD_7-ID	4	5	B	-		-
33	GRID-CODE	4	5	B	-		-

* *

Name: TT_#

Type: Arc/Info Grid

Description: Grids of elevation range from TT DEM; '#' indicates elevation bin (TT DEM with elevation range = -3500 to 4000 m separated into 16 500-m bins).

Extent: region: North: -769678.331 East: 433095.957
South: -1777233.086 West: -433329.675

Source: created by Scott Mest

Cell Size: 446.611 meters/pixel

Projection: SINUSOIDAL

Spheroid: Major Axis: 3393399.9023 Minor Axis: 3375729.9805

Coordinate System: Latitude-longitude

Units: meters

Cover Derivation: Grid was created using the GRID 'select' command in **elevrange_gridtopoly.aml** by selecting 500 meter elevation bins from the DEM Grid TT_SIN_INTGRD.

Statistics: Min: 1.000 Mean: 245.790
Max: 499.000 Standard Deviation: 137.746

* *

Name: TT_#COV

Type: Arc/Info Coverage

Description: Coverage of elevation ranges from TT grids (above) determining area of elevation bin; '#' indicates elevation bin (TT DEM with elevation range = -3500 to 4000 m separated into 16 500-m bins).m).

Extent: region: North: -899642.188 East: 402279.781
South: -1777233.125 West: -424397.438

Data Types: Polygons

Source: created by Scott Mest

Projection: unprojected

Spheroid: none defined

Coordinate System: none defined

Units: none defined

Cover Derivation: Coverage was created using the Arc 'gridpoly' command in **elevrange_gridtopoly.aml** by converting equivalent elevation Grid.

Item definitions: tt_0cov

COLUMN	ITEM NAME	WIDTH	OUTPUT	TYPE	N.DEC	ALTERNATE NAME	INDEXED?
1	AREA	4	12	F	3		-
5	PERIMETER	4	12	F	3		-
9	TT_0COV#	4	5	B	-		-
13	TT_0COV-ID	4	5	B	-		-

* *

Name: TT_ACCGRD_#

Type: Arc/Info Grid

Description: Accumulation grid for TT, '#' in coverage name is place-holder for run numbers; runs represent specific sink-fill depths used in model.

Extent: region: North: -769678.331 East: 433095.957
South: -1777233.086 West: -433329.675

Source: created by Scott Mest

Cell Size: 446.611 meters/pixel

Projection: SINUSOIDAL

Spheroid: Major Axis: 3393399.9023 Minor Axis: 3375729.9805

Coordinate System: Latitude-longitude

Units: meters

Cover Derivation: Grid was created using the GRID 'flowaccumulation' command in **sheds.aml** from TT_FLOWD_#.

Statistics: Min: 0.000 Mean: 548.563
Max: 886929.000 Standard Deviation: 14023.291

* *

Name: TT_BASE_GEOG

Type: Arc/Info Grid

Description: Viking Orbiter MDIM 2.0 grid of TT; geographic projection.

Extent: region: North: -12.717 East: 95.088
South: -30.165 West: 79.927

Source: created by Scott Mest

Cell Size: 0.0078 degrees/pixel

Projection: GEOGRAPHIC

Spheroid: Major Axis: 3393399.9023 Minor Axis: 3375729.9805

Coordinate System: Latitude-longitude

Units: DD

Cover Derivation: Grid was created using the Arc 'projectdefine' command to define a projection for TT_BASE_GRD.

Statistics: Min: 37.000 Mean: 169.627
Max: 255.000 Standard Deviation: 47.009

* *

Name: TT_BASE_GRD

Type: Arc/Info Grid

Description: Viking Orbiter MDIM 2.0 grid of TT; unprojected.

Extent: region: North: 0.002 East: 8.498
South: -9.902 West: -0.003

Source: created by Scott Mest

Cell Size: 0.0078 degrees/pixel

Projection: unprojected

Spheroid: none defined

Coordinate System: 8.5 x 11 page

Units: inches

Cover Derivation: Grid was created using the Arc 'imagegrid' command in **tif_convert.aml** by converting a Viking Orbiter MDIM 2.0 photomosaic in TIF format to an Arc/Info GRID.

Statistics: Min: 37.000 Mean: 169.765
Max: 255.000 Standard Deviation: 47.100

* *

Name: TT_BASE_SIN

Type: Arc/Info Grid

Description: Viking Orbiter MDIM 2.0 grid of TT; sinusoidal projection.

Extent: region: North: -753358.756 East: 438479.618
South: -1786574.010 West: -437518.932

Source: created by Scott Mest

Cell Size: 538.413 meters/pixel

Projection: SINUSOIDAL

Spheroid: Major Axis: 3393399.9023 Minor Axis: 3375729.9805

Coordinate System: Latitude-longitude

Units: meters

Cover Derivation: Grid was created using the Arc 'project' command to reproject TT_BASE_GEOG from geographic to sinusoidal projection. Grid is used for display.

Statistics: Min: 37.000 Mean: 169.545
Max: 255.000 Standard Deviation: 47.124

* *

Name: TT_BASINS_#

Type: Arc/Info Grid

Description: Basin grid for TT, '#' in coverage name is place-holder for run numbers; runs represent specific sink-fill depths used in model.

Extent: region: North: -769678.331 East: 433095.957
South: -1777233.086 West: -433329.675

Source: created by Scott Mest

Cell Size: 446.611 meters/pixel

Projection: SINUSOIDAL

Spheroid: Major Axis: 3393399.9023 Minor Axis: 3375729.9805

Coordinate System: Latitude-longitude

Units: meters

Cover Derivation: Grid was created using the GRID 'basin' command in **sheds.aml** from TT_FLOWD_#.

Statistics: Min: 1.000 Mean: 1857.437
Max: 4158.000 Standard Deviation: 718.055

* *

Name: TT_FILL_#

Type: Arc/Info Grid

Description: Sink fill grid for TT, '#' in coverage name is place-holder for run numbers; runs represent specific sink-fill depths used in model.

Extent: region: North: -769678.331 East: 433095.957
South: -1777233.086 West: -433329.675

Source: created by Scott Mest

Cell Size: 446.611 meters/pixel

Projection: SINUSOIDAL

Spheroid: Major Axis: 3393399.9023 Minor Axis: 3375729.9805

Coordinate System: Latitude-longitude

Units: meters

Cover Derivation: Grid was created using the GRID 'fill' command in **sheds.aml** by filling sinks in TT_SIN.

Statistics: Min: -2978.333 Mean: 1095.537
Max: 4242.371 Standard Deviation: 1435.288

* *

Name: TT_FLOWD_#

Type: Arc/Info Grid

Description: Flow direction grid for TT, '#' in coverage name is place-holder for run numbers; runs represent specific sink-fill depths used in model.

Extent: region: North: -769678.331 East: 433095.957
South: -1777233.086 West: -433329.675

Source: created by Scott Mest

Cell Size: 446.611 meters/pixel

Projection: SINUSOIDAL

Spheroid: Major Axis: 3393399.9023 Minor Axis: 3375729.9805

Coordinate System: Latitude-longitude

Units: meters

Cover Derivation: Grid was created using the GRID 'flowdirection' command in **sheds.aml** from TT_FILL_#.

Statistics: Min: 1.000 Mean: 22.314
Max: 255.000 Standard Deviation: 34.521

* *

Name: TT_LENGRD_#

Type: Arc/Info Grid

Description: Stream length grid for TT, '#' in coverage name is place-holder for run numbers; runs represent specific sink-fill depths used in model.

Extent: region: North: -769678.331 East: 433095.957
South: -1777233.086 West: -433329.675

Source: created by Scott Mest

Cell Size: 446.611 meters/pixel

Projection: SINUSOIDAL

Spheroid: Major Axis: 3393399.9023 Minor Axis: 3375729.9805

Coordinate System: Latitude-longitude

Units: meters

Cover Derivation: Grid was created using the GRID 'flowlength' command in **sheds.aml** from a direction Grid (TT_FLOWD_#) to calculate downstream distance along a flow path.

Statistics: Min: 0.000 Mean: 279962.560
Max: 1266250.625 Standard Deviation: 310949.533

* *

Name: TT_SHEDCO_#

Type: Arc/Info Coverage

Description: Watershed coverage for TT, '#' in coverage name is place-holder for run numbers; runs represent specific sink-fill depths used in model.

Extent: region: North: -770124.938 East: 432202.750
South: -1766514.375 West: -413678.781

Data Types: Polygons

Source: created by Scott Mest

Projection: SINUSOIDAL

Spheroid: Major Axis: 3393399.9023 Minor Axis: 3375729.9805

Coordinate System: Latitude-longitude

Units: meters

Cover Derivation: Coverage was created using the GRID 'gridpoly' command in **sheds.aml** by converting TT_SHEDS_#.

Item definitions: tt_shedco_7

COLUMN	ITEM NAME	WIDTH	OUTPUT	TYPE	N.DEC	ALTERNATE NAME	INDEXED?
1	AREA	4	12	F	3		-
5	PERIMETER	4	12	F	3		-
9	TT_SHEDCO_7#	4	5	B	-		-
13	TT_SHEDCO_7-ID	4	5	B	-		-
17	GRID-CODE	4	8	B	-		-

* *

Name: TT_SHEDS_#

Type: Arc/Info Grid

Description: Watershed coverage for TT, '#' in coverage name is place-holder for run numbers; runs represent specific sink-fill depths used in model.

Extent: region: North: -769678.331 East: 433095.957
South: -1777233.086 West: -433329.675

Source: created by Scott Mest

Cell Size: 446.611 meters/pixel

Projection: SINUSOIDAL

Spheroid: Major Axis: 3393399.9023 Minor Axis: 3375729.9805

Coordinate System: Latitude-longitude

Units: meters

Cover Derivation: Grid was created using the GRID 'watershed' command in **sheds.aml** from a direction (TT_FLOWD_#) and source (TT_SINKS_#) Grid.

Statistics: Min: 1.000 Mean: 100.387
Max: 149.000 Standard Deviation: 40.070

* *

Name: TT_SIN

Type: Arc/Info Grid

Description: DEM grid of TT; sinusoidal projection.

Extent: region: North: -769678.331 East: 433095.957
South: -1777233.086 West: -433329.675

Source: created by Scott Mest

Cell Size: 446.611 meters/pixel

Projection: SINUSOIDAL

Spheroid: Major Axis: 3393399.9023 Minor Axis: 3375729.9805

Coordinate System: Latitude-longitude

Units: meters

Cover Derivation: Grid was created using the Arc 'project' command to reproject TT _GEO from geographic to sinusoidal projection. Grid contains topographic information used for hydrologic modeling and is used for display.

Statistics: Min: -3221.050 Mean: 1076.933
Max: 4242.371 Standard Deviation: 1440.197

* *

Name: TT_SIN_INTGRD

Type: Arc/Info Grid

Description: DEM grid of TT; sinusoidal projection; integer data type.

Extent: region: North: -769678.331 East: 433095.957
South: -1777233.086 West: -433329.675

Source: created by Scott Mest

Cell Size: 446.611 meters/pixel

Projection: SINUSOIDAL

Spheroid: Major Axis: 3393399.9023 Minor Axis: 3375729.9805

Coordinate System: Latitude-longitude

Units: meters

Cover Derivation: Grid was created using the GRID 'int' command to redefine the elevation data in TT _SIN from floating point to integer.

Statistics: Min: -3221.000 Mean: 1076.687
Max: 4242.000 Standard Deviation: 1439.838

* *

Name: TT_SINDEP_#

Type: Arc/Info Grid

Description: Sink depth grid for TT, '#' in coverage name is place-holder for run numbers; runs represent specific sink-fill depths used in model.

Extent: region: North: -769678.331 East: 433095.957
South: -1777233.086 West: -433329.675

Source: created by Scott Mest

Cell Size: 446.611 meters/pixel

Projection: SINUSOIDAL

Spheroid: Major Axis: 3393399.9023 Minor Axis: 3375729.9805

Coordinate System: Latitude-longitude

Units: meters

Cover Derivation: Grid was created in **sheds.aml** by calculating the difference between TT_SINMAX_# and TT_SINMIN_#.

Statistics: Min: 728.414 Mean: 3439.428
Max: 6751.005 Standard Deviation: 1281.264

* *

Name: TT_SINKS_#

Type: Arc/Info Grid

Description: Sink identification grid for PT, '#' in coverage name is place-holder for run numbers; runs represent specific sink-fill depths used in model.

Extent: region: North: -769678.331 East: 433095.957
South: -1777233.086 West: -433329.675

Source: created by Scott Mest

Cell Size: 446.611 meters/pixel

Projection: SINUSOIDAL

Spheroid: Major Axis: 3393399.9023
Minor Axis: 3375729.9805

Coordinate System: Latitude-longitude

Units: meters

Cover Derivation: Grid was created using the GRID 'sink' command in **sheds.aml** from TT_FLOWD_#.

Statistics: Min: 1.000 Mean: 76.501
Max: 149.000 Standard Deviation: 40.104

* *

Name: TT_SINMAX_#

Type: Arc/Info Grid

Description: Maximum sink depth grid for TT, '#' in coverage name is place-holder for run numbers; runs represent specific sink-fill depths used in model.

Extent: region: North: -769678.331 East: 433095.957
South: -1777233.086 West: -433329.675

Source: created by Scott Mest

Cell Size: 446.611 meters/pixel

Projection: SINUSOIDAL

Spheroid: Major Axis: 3393399.9023 Minor Axis: 3375729.9805

Coordinate System: Latitude-longitude

Units: meters

Cover Derivation: Grid was created using the GRID 'zonalmax' command in **sheds.aml** from a zone Grid (TT_SHEDS_#) and a value Grid (TT_FILL_#). Grid was used to calculate TT_SINDEP_#.

Statistics: Min: -836.121 Mean: 3100.050
Max: 4242.371 Standard Deviation: 854.400

* *

Name: TT_SINMIN_#

Type: Arc/Info Grid

Description: Minimum sink depth grid for TT, '#' in coverage name is place-holder for run numbers; runs represent specific sink-fill depths used in model.

Extent: region: North: -769678.331 East: 433095.957
South: -1777233.086 West: -433329.675

Source: created by Scott Mest

Cell Size: 446.611 meters/pixel

Projection: SINUSOIDAL

Spheroid: Major Axis: 3393399.9023 Minor Axis: 3375729.9805

Coordinate System: Latitude-longitude

Units: meters

Cover Derivation: Grid was created using the GRID 'zonalmin' command in **sheds.aml** from a zone Grid (TT_SHEDS_#) and a value Grid (TT_FILL_#). Grid was used to calculate TT_SINDEP_#.

Statistics: Min: -2978.333 Mean: -339.378
Max: 2440.997 Standard Deviation: 1168.177

* *

Name: TT_STR_#

Type: Arc/Info Grid

Description: Stream coverage using Strahler ordering system for TT, '#' in coverage name is place-holder for run numbers; runs represent specific sink-fill depths used in model.

Extent: region: North: -769678.331 East: 433095.957
South: -1777233.086 West: -433329.675

Source: created by Scott Mest

Cell Size: 446.611 meters/pixel

Projection: SINUSOIDAL

Spheroid: Major Axis: 3393399.9023 Minor Axis: 3375729.9805

Coordinate System: Latitude-longitude

Units: meters

Cover Derivation: Grid was created using the GRID 'streamorder' command in **streams.aml** from a network Grid (TT_STREAM_#) and a direction Grid (TT_FLOWD_#), and specifying the method of stream ordering (Strahler or Shreve).

Statistics: Min: 1.000 Mean: 1.779
Max: 5.000 Standard Deviation: 1.010

* *

Name: TT_STREAM_#

Type: Arc/Info Grid

Description: Stream location grid for TT, '#' in coverage name is place-holder for run numbers; runs represent specific sink-fill depths used in model.

Extent: region: North: -769678.331 East: 433095.957
South: -1777233.086 West: -433329.675

Source: created by Scott Mest

Cell Size: 446.611 meters/pixel

Projection: SINUSOIDAL

Spheroid: Major Axis: 3393399.9023 Minor Axis: 3375729.9805

Coordinate System: Latitude-longitude

Units: meters

Cover Derivation: Grid was created using the GRID 'con' command in **streams.aml**, which delineates a network of flowpaths from the conditional statement where each cell value in Grid TT_ACCGRD_# is greater than the mean cell value, else the value is 1, which delineates a stream.

Statistics: Min: 1.000 Mean: 1.000
Max: 1.000 Standard Deviation: 0.000

* *

Name: TT_STRECO_#

Type: Arc/Info Coverage

Description: Stream coverage for TT, '#' in coverage name is place-holder for run numbers; runs represent specific sink-fill depths used in model.

Extent: region: North: -769678.331 East: 433095.957
South: -1777233.086 West: -433329.675

Data Types: Arcs

Source: created by Scott Mest

Projection: SINUSOIDAL

Spheroid: Major Axis: 3393399.9023 Minor Axis: 3375729.9805

Coordinate System: Latitude-longitude

Units: meters

Cover Derivation: Coverage was created using the GRID 'streamline' command in **streams.aml** from a network Grid (TT_STREAM_#) and a direction Grid (TT_FLOWD_#).

Item definitions: tt_streco_7

COLUMN	ITEM NAME	WIDTH	OUTPUT	TYPE	N.DEC	ALTERNATE NAME	INDEXED?
1	FNODE#	4	5	B	-		-
5	TNODE#	4	5	B	-		-
9	LPOLY#	4	5	B	-		-
13	RPOLY#	4	5	B	-		-
17	LENGTH	8	18	F	5		-
25	TT_STRECO_7#	4	5	B	-		-
29	TT_STRECO_7-ID	4	5	B	-		-

* *

Name: TT_TICCOV

Type: Arc/Info Coverage

Description: Tic coverage of TT; unprojected.

Extent: region: North: -13.000 East: 95.000
South: -30.000 West: 80.000

Data Types: Tics

Source: created by Scott Mest

Projection: GEOGRAPHIC

Spheroid: Major Axis: 3393399.9023 Minor Axis: 3375729.9805

Coordinate System: Latitude-longitude

Units: DD

Cover Derivation: Coverage was created using the Arc 'generate' command. Coverage was used for warping and projecting subsequent Viking Orbiter MDIM 2.0 photomosaic (TT_BASE_GRD) and MOLA DEM (TT_GRD) Grids.

* *

Name: TT_TICCOV_SIN

Type: Arc/Info Coverage

Description: Tic coverage of TT; sinusoidal projection.

Extent: region: North: -769938.000 East: 432810.312
South: -1776780.000 West: -432810.312

Data Types: Tics

Source: created by Scott Mest

Projection: SINUSOIDAL

Spheroid: Major Axis: 3393399.9023 Minor Axis: 3375729.9805

Coordinate System: Latitude-longitude

Units: meters

Cover Derivation: Coverage was created using the Arc 'generate' command. Coverage was used for warping and projecting subsequent Viking Orbiter MDIM 2.0 photomosaic (TT_BASE_GRD) and MOLA DEM (TT_GRD) Grids.

* *

Name: TT_VALLGRD

Type: Arc/Info Grid

Description: Mapped valley grid in TT; unprojected.

Extent: region: North: 0.002 East: 8.473

South: -9.728 West: -0.003

Source: created by Scott Mest

Cell Size: 0.0078 degrees/pixel

Projection: unprojected

Spheroid: none defined

Coordinate System: 8.5 x 11 page

Units: inches

Cover Derivation: Grid was created using the Arc 'imagegrid' command in **tif_convert.aml** by converting a map of valleys in TIF format to an Arc/Info GRID.

Statistics: Min: 0.000 Mean: 248.937
Max: 255.000 Standard Deviation: 35.583

* *

Name: TT_VALL_GEOG

Type: Arc/Info Coverage

Description: Mapped valley grid in TT; geographic projection.

Extent: region: North: -13.000 East: 95.000
South: -30.000 West: 80.000

Data Types: Arcs

Source: created by Scott Mest

Projection: GEOGRAPHIC

Spheroid: Major Axis: 3393399.9023 Minor Axis: 3375729.9805

Coordinate System: Latitude-longitude

Units: DD

Cover Derivation: Grid was created using the Arc 'projectdefine' command to define a projection for TT_VALL_GRD.

Item definitions: tt_vall_geog

COLUMN	ITEM NAME	WIDTH	OUTPUT	TYPE	N.DEC	ALTERNATE NAME	INDEXED?
1	FNODE#	4	5	B	-		-
5	TNODE#	4	5	B	-		-
9	LPOLY#	4	5	B	-		-
13	RPOLY#	4	5	B	-		-
17	LENGTH	4	12	F	3		-
21	TT_VALL_GEOG#	4	5	B	-		-
25	TT_VALL_GEOG-ID	4	5	B	-		-

* *

Name: TT_VALL_SIN

Type: Arc/Info Coverage

Description: Mapped valley grid in TT; sinusoidal projection.

Extent: region: North: -769938.000 East: 432810.312
South: -1776780.000 West: -432810.312

Data Types: Arc

Source: created by Scott Mest

Projection: SINUSOIDAL

Spheroid: Major Axis: 3393399.9023 Minor Axis: 3375729.9805

Coordinate System: Latitude-longitude

Units: meters

Cover Derivation: Grid was created using the Arc 'project' command to reproject TT_VALL_GEOG from geographic to sinusoidal projection.

Item definitions: tt_vall_sin

COLUMN	ITEM NAME	WIDTH	OUTPUT	TYPE	N.DEC	ALTERNATE NAME	INDEXED?
1	FNODE#	4	5	B	-		-
5	TNODE#	4	5	B	-		-
9	LPOLY#	4	5	B	-		-
13	RPOLY#	4	5	B	-		-
17	LENGTH	4	12	F	3		-
21	TT_VALL_SIN#	4	5	B	-		-
25	TT_VALL_SIN-ID	4	5	B	-		-

Arc Macro Language (AML) files:

asciitogrid.aml

```
asciigrid
asciigrid 30s_13s_80e_95e_txtb tt_grd float
projectdefine
projectdefine grid tt_grd
projection geographic
units dd
parameters 3393399.9023 3375729.9805
generate
generate tt_ticcov
tics
1,80.000,-30.000
2,80.000,-13.000
3,95.000,-13.00
4,95.000,-30.000
end
quit
```

* *

elevrange.aml

```
grid
int
tt_sin_intgrd = int(tt_sin)
quit
additem
additem tt_sin_intgrd.vat tt_sin_intgrd.vat elevrange 5 5 I
info
~
~
ARC
SELECT TT_SIN_INTGRD.VAT
RESELECT VALUE > 4000
CALCULATE ELEVRANGE = 4000
ASELECT
RESELECT VALUE > 3500 AND VALUE < 4000
CALCULATE ELEVRANGE = 3500
ASELECT
RESELECT VALUE > 3000 AND VALUE < 3500
CALCULATE ELEVRANGE = 3000
ASELECT
RESELECT VALUE > 2500 AND VALUE < 3000
CALCULATE ELEVRANGE = 2500
ASELECT
RESELECT VALUE > 2000 AND VALUE < 2500
CALCULATE ELEVRANGE = 2000
ASELECT
RESELECT VALUE > 1500 AND VALUE < 2000
CALCULATE ELEVRANGE = 1500
ASELECT
RESELECT VALUE > 1000 AND VALUE < 1500
CALCULATE ELEVRANGE = 1000
ASELECT
RESELECT VALUE > 500 AND VALUE < 1000
CALCULATE ELEVRANGE = 500
ASELECT
```

```
RESELECT VALUE > 0 AND VALUE < 500
CALCULATE ELEVRANGE = 0
ASELECT
RESELECT VALUE > -500 AND VALUE < 0
CALCULATE ELEVRANGE = -500
ASELECT
RESELECT VALUE > -1000 AND VALUE < -500
CALCULATE ELEVRANGE = -1000
ASELECT
RESELECT VALUE > -1500 AND VALUE < -1000
CALCULATE ELEVRANGE = -1500
ASELECT
RESELECT VALUE > -2000 AND VALUE < -1500
CALCULATE ELEVRANGE = -2000
ASELECT
RESELECT VALUE > -2500 AND VALUE < -2000
CALCULATE ELEVRANGE = -2500
ASELECT
RESELECT VALUE > -3000 AND VALUE < -2500
CALCULATE ELEVRANGE = -3000
ASELECT
RESELECT VALUE > -3500 AND VALUE < -3000
CALCULATE ELEVRANGE = -3500
ASELECT
CALCULATE VALUE = ELEVRANGE
Q STOP
dropitem
dropitem tt_sin_intgrd.vat tt_sin_intgrd.vat ELEVRANGE
gridpoly
gridpoly tt_sin_intgrd tt_sin_intcov
```

* *

elevrange_gridtopoly.aml

```
grid
tt_4000 = select(tt_sin_intgrd, 'value > 4000')
tt_3500 = select(tt_sin_intgrd, 'value > 3500 and value < 4000')
tt_3000 = select(tt_sin_intgrd, 'value > 3000 and value < 3500')
```

```
tt_2500 = select(tt_sin_intgrd, 'value > 2500 and value < 3000')
tt_2000 = select(tt_sin_intgrd, 'value > 2000 and value < 2500')
tt_1500 = select(tt_sin_intgrd, 'value > 1500 and value < 2000')
tt_1000 = select(tt_sin_intgrd, 'value > 1000 and value < 1500')
tt_500 = select(tt_sin_intgrd, 'value > 500 and value < 1000')
tt_0 = select(tt_sin_intgrd, 'value > 0 and value < 500')
tt_neg500 = select(tt_sin_intgrd, 'value > -500 and value < 0')
tt_neg1000 = select(tt_sin_intgrd, 'value > -1000 and value < -500')
tt_neg1500 = select(tt_sin_intgrd, 'value > -1500 and value < -1000')
tt_neg2000 = select(tt_sin_intgrd, 'value > -2000 and value < -1500')
tt_neg2500 = select(tt_sin_intgrd, 'value > -2500 and value < -2000')
tt_neg3000 = select(tt_sin_intgrd, 'value > -3000 and value < -2500')
tt_neg3500 = select(tt_sin_intgrd, 'value > -3500 and value < -3000')
quit
gridpoly tt_4000 tt_4000cov
gridpoly tt_3500 tt_3500cov
gridpoly tt_3000 tt_3000cov
gridpoly tt_2500 tt_2500cov
gridpoly tt_2000 tt_2000cov
gridpoly tt_1500 tt_1500cov
gridpoly tt_1000 tt_1000cov
gridpoly tt_500 tt_500cov
gridpoly tt_0 tt_0cov
gridpoly tt_neg500 tt_ne500cov
gridpoly tt_neg1000 tt_ne1000cov
gridpoly tt_neg1500 tt_ne1500cov
gridpoly tt_neg2000 tt_ne2000cov
gridpoly tt_neg2500 tt_ne2500 ov
gridpoly tt_neg3000 tt_ne3000cov
gridpoly tt_neg3500 tt_ne3500cov
```

* *

orders.aml

```
arcplot
aselect tt_str_7cov line
reselect tt_str_7cov arcs grid-code = 1
writeselect firstorder7.sel
```

```
arc reselect tt_str_7cov tt_1stord_7 line firstorder7.sel line
arc clean tt_1stord_7 tt_1stord_7 # # line
arc build tt_1stord_7 line
aselect tt_str_7cov line
reselect tt_str_7cov arcs grid-code = 2
writeselect secondorder7.sel
arc reselect tt_str_7cov tt_2ndord_7 line secondorder7.sel line
arc clean tt_2ndord_7 tt_2ndord_7 # # line
arc build tt_2ndord_7 line
aselect tt_str_7cov line
reselect tt_str_7cov arcs grid-code = 3
writeselect thirdorder7.sel
arc reselect tt_str_7cov tt_3rdord_7 line thirdorder7.sel line
arc clean tt_3rdord_7 tt_3rdord_7 # # line
arc build tt_3rdord_7 line
aselect tt_str_7cov line
reselect tt_str_7cov arcs grid-code = 4
writeselect fourthorder7.sel
arc reselect tt_str_7cov tt_4thord_7 line fourthorder7.sel line
arc clean tt_4thord_7 tt_4thord_7 # # line
arc build tt_4thord_7 line
aselect tt_str_7cov line
reselect tt_str_7cov arcs grid-code = 5
writeselect fifthorder7.sel
arc reselect tt_str_7cov tt_5thord_7 line fifthorder7.sel line
arc clean tt_5thord_7 tt_5thord_7 # # line
arc build tt_5thord_7 line
quit
```

* *

orders_intersect.aml

```
shapearc tt_ne3500.shp tt_ne3500cov type
clean tt_ne3500cov
shapearc tt_ne3000.shp tt_ne3000cov type
clean tt_ne3000cov
shapearc tt_ne2500.shp tt_ne2500cov type
clean tt_ne2500cov
```

```
shapearc tt_ne2000.shp tt_ne2000cov type
clean tt_ne2000cov
shapearc tt_ne1500.shp tt_ne1500cov type
clean tt_ne1500cov
shapearc tt_ne1000.shp tt_ne1000cov type
clean tt_ne1000cov
shapearc tt_ne500.shp tt_ne500cov type
clean tt_ne500cov
shapearc tt_0.shp tt_0cov type
clean tt_0cov
shapearc tt_500.shp tt_500cov type
clean tt_500cov
shapearc tt_1000.shp tt_1000cov type
clean tt_1000cov
shapearc tt_1500.shp tt_1500cov type
clean tt_1500cov
shapearc tt_2000.shp tt_2000cov type
clean tt_2000cov
shapearc tt_2500.shp tt_2500cov type
clean tt_2500cov
shapearc tt_3000.shp tt_3000cov type
clean tt_ne3000cov
shapearc tt_3500.shp tt_3500cov type
clean tt_3500cov
shapearc tt_4000.shp tt_4000cov type
clean tt_4000cov
intersect tt_1stord_7 tt_ne3500cov int71_n3500 line # nojoin
intersect tt_1stord_7 tt_ne3000cov int71_n3000 line # nojoin
intersect tt_1stord_7 tt_ne2500cov int71_n2500 line # nojoin
intersect tt_1stord_7 tt_ne2000cov int71_n2000 line # nojoin
intersect tt_1stord_7 tt_ne1500cov int71_n1500 line # nojoin
intersect tt_1stord_7 tt_ne1000cov int71_n1000 line # nojoin
intersect tt_1stord_7 tt_ne500cov int71_n500 line # nojoin
intersect tt_1stord_7 tt_0cov int71_0 line # nojoin
intersect tt_1stord_7 tt_500cov int71_500 line # nojoin
intersect tt_1stord_7 tt_1000cov int71_1000 line # nojoin
intersect tt_1stord_7 tt_1500cov int71_1500 line # nojoin
```

intersect tt_1stord_7 tt_2000cov int71_2000 line # nojoin
intersect tt_1stord_7 tt_2500cov int71_2500 line # nojoin
intersect tt_1stord_7 tt_3000cov int71_3000 line # nojoin
intersect tt_1stord_7 tt_3500cov int71_3500 line # nojoin
intersect tt_1stord_7 tt_4000cov int71_4000 line # nojoin
intersect tt_2ndord_7 tt_ne3500cov int72_n3500 line # nojoin
intersect tt_2ndord_7 tt_ne3000cov int72_n3000 line # nojoin
intersect tt_2ndord_7 tt_ne2500cov int72_n2500 line # nojoin
intersect tt_2ndord_7 tt_ne2000cov int72_n2000 line # nojoin
intersect tt_2ndord_7 tt_ne1500cov int72_n1500 line # nojoin
intersect tt_2ndord_7 tt_ne1000cov int72_n1000 line # nojoin
intersect tt_2ndord_7 tt_ne500cov int72_n500 line # nojoin
intersect tt_2ndord_7 tt_0cov int72_0 line # nojoin
intersect tt_2ndord_7 tt_500cov int72_500 line # nojoin
intersect tt_2ndord_7 tt_1000cov int72_1000 line # nojoin
intersect tt_2ndord_7 tt_1500cov int72_1500 line # nojoin
intersect tt_2ndord_7 tt_2000cov int72_2000 line # nojoin
intersect tt_2ndord_7 tt_2500cov int72_2500 line # nojoin
intersect tt_2ndord_7 tt_3000cov int72_3000 line # nojoin
intersect tt_2ndord_7 tt_3500cov int72_3500 line # nojoin
intersect tt_2ndord_7 tt_4000cov int72_4000 line # nojoin
intersect tt_3rdord_7 tt_ne3500cov int73_n3500 line # nojoin
intersect tt_3rdord_7 tt_ne3000cov int73_n3000 line # nojoin
intersect tt_3rdord_7 tt_ne2500cov int73_n2500 line # nojoin
intersect tt_3rdord_7 tt_ne2000cov int73_n2000 line # nojoin
intersect tt_3rdord_7 tt_ne1500cov int73_n1500 line # nojoin
intersect tt_3rdord_7 tt_ne1000cov int73_n1000 line # nojoin
intersect tt_3rdord_7 tt_ne500cov int73_n500 line # nojoin
intersect tt_3rdord_7 tt_0cov int73_0 line # nojoin
intersect tt_3rdord_7 tt_500cov int73_500 line # nojoin
intersect tt_3rdord_7 tt_1000cov int73_1000 line # nojoin
intersect tt_3rdord_7 tt_1500cov int73_1500 line # nojoin
intersect tt_3rdord_7 tt_2000cov int73_2000 line # nojoin
intersect tt_3rdord_7 tt_2500cov int73_2500 line # nojoin
intersect tt_3rdord_7 tt_3000cov int73_3000 line # nojoin
intersect tt_3rdord_7 tt_3500cov int73_3500 line # nojoin
intersect tt_3rdord_7 tt_4000cov int73_4000 line # nojoin

intersect tt_4thord_7 tt_ne3500cov int74_n3500 line # nojoin
intersect tt_4thord_7 tt_ne3000cov int74_n3000 line # nojoin
intersect tt_4thord_7 tt_ne2500cov int74_n2500 line # nojoin
intersect tt_4thord_7 tt_ne2000cov int74_n2000 line # nojoin
intersect tt_4thord_7 tt_ne1500cov int74_n1500 line # nojoin
intersect tt_4thord_7 tt_ne1000cov int74_n1000 line # nojoin
intersect tt_4thord_7 tt_ne500cov int74_n500 line # nojoin
intersect tt_4thord_7 tt_0cov int74_0 line # nojoin
intersect tt_4thord_7 tt_500cov int74_500 line # nojoin
intersect tt_4thord_7 tt_1000cov int74_1000 line # nojoin
intersect tt_4thord_7 tt_1500cov int74_1500 line # nojoin
intersect tt_4thord_7 tt_2000cov int74_2000 line # nojoin
intersect tt_4thord_7 tt_2500cov int74_2500 line # nojoin
intersect tt_4thord_7 tt_3000cov int74_3000 line # nojoin
intersect tt_4thord_7 tt_3500cov int74_3500 line # nojoin
intersect tt_4thord_7 tt_4000cov int74_4000 line # nojoin
intersect tt_5thord_7 tt_ne3500cov int75_n3500 line # nojoin
intersect tt_5thord_7 tt_ne3000cov int75_n3000 line # nojoin
intersect tt_5thord_7 tt_ne2500cov int75_n2500 line # nojoin
intersect tt_5thord_7 tt_ne2000cov int75_n2000 line # nojoin
intersect tt_5thord_7 tt_ne1500cov int75_n1500 line # nojoin
intersect tt_5thord_7 tt_ne1000cov int75_n1000 line # nojoin
intersect tt_5thord_7 tt_ne500cov int75_n500 line # nojoin
intersect tt_5thord_7 tt_0cov int75_0 line # nojoin
intersect tt_5thord_7 tt_500cov int75_500 line # nojoin
intersect tt_5thord_7 tt_1000cov int75_1000 line # nojoin
intersect tt_5thord_7 tt_1500cov int75_1500 line # nojoin
intersect tt_5thord_7 tt_2000cov int75_2000 line # nojoin
intersect tt_5thord_7 tt_2500cov int75_2500 line # nojoin
intersect tt_5thord_7 tt_3000cov int75_3000 line # nojoin
intersect tt_5thord_7 tt_3500cov int75_3500 line # nojoin
intersect tt_5thord_7 tt_4000cov int75_4000 line # nojoin

* *

sheds.aml

grid
fill tt_sin tt_fill_7 sink 575.00
tt_flowd_7 = flowdirection (tt_fill_7)

```
tt_sinks_7 = sink (tt_flowd_7)
tt_sheds_7 = watershed (tt_flowd_7,tt_sinks_7)
tt_sinmin_7 = zonalmin (tt_sheds_7,tt_fill_7)
tt_sinmax_7 = zonalmax (tt_sheds_7,tt_fill_7)
tt_sindep_7 = tt_sinmax_7 - tt_sinmin_7
tt_shedco_7 = gridpoly (tt_sheds_7)
tt_accgrd_7 = flowaccumulation (tt_flowd_7)
tt_basins_7 = basin (tt_flowd_7)
tt_lengrd_7 = flowlength (tt_flowd_7)
quit
```

* *

streams.aml

```
grid
tt_stream_7 = con (tt_accgrd_7 > 548.563,1)
tt_str_7 = streamorder (tt_stream_7,tt_flowd_7,strahler)
tt_streco_7 = streamline (tt_stream_7,tt_flowd_7)
quit
```

* *

tif_convert.aml

```
imagegrid tt_base.tff tt_base_grd
imagegrid tt_valleys.tff tt_valleysgrd
grid
mapextent tt_base_grd
shadedelete all
shadecolorramp 0 255 darkgreen white
gridshades tt_base_grd # linear nowrap
clear
tt_vall_con = con(tt_valleysgrd < 1,1,0)
mapextent tt_valleysgrd
tt_vall_cov = gridline(tt_vall_con)
linecolor blue
arcs tt_vall_cov
quit
```

Arc/Info Commands Used:

Table A.D1. ESRI Arc/Info and Arc/Info Modules Commands Used

ARC	GRID	Arcplot	INFO	AMLs
additem	basin	aselect	ASELECT	asciitogrid.aml
asciigrid	buildvat	reselect	CALCULATE	elevrange.aml
build	con	writeselect	SELECT	elevrange_gridtopoly.aml
clean	fill		RESELECT	orders.aml
dropitem	flowaccumulation		UPDATE	orders_intersect.aml
generate	flowdirection			sheds.aml
gridpoly	flowlength			streams.aml
imagegrid	gridline			tif_convert.aml
intersect	gridpoly			
kill	gridshades			
project	int			
projectdefine	linecolor			
shapearc	mapextent			
	select			
	shadecolorramp			
	shadedelete			
	sink			
	streamline			
	streamorder			
	watershed			
	zonalmax			
	zonalmin			

Arc/Info Commands: Usage

ARC commands

ADDITEM

Usage: ADDITEM <in_info_file> <out_info_file> <item_name> <item_width> <output_width> <item_type> {decimal_places} {start_item}

ASCIIGRID

Usage: ASCIIGRID <in_ascii_file> <out_grid> {INT | FLOAT}

BUILD

Usage: BUILD <cover> {POLY | LINE | POINT | NODE | ANNO.<subclass>}

CLEAN

Usage: CLEAN <in_cover> {out_cover} {dangle_length} {fuzzy_tolerance} {POLY | LINE}

DROPITEM

Usage: DROPITEM <in_info_file> <out_info_file> {item...item}

GENERATE

Usage: GENERATE <cover>

GRIDCLIP

Usage: GRIDCLIP <in_grid> <out_grid> <x1> <y1> <x2> <y2>

IMAGEGRID

Usage: IMAGEGRID <in_image> <out_grid | out_stack> {out_colormap_file} {in_band} {NEAREST | BILINEAR | CUBIC} {DEFAULT | SQUARE}

INTERSECT

Usage: INTERSECT <in_cover> <intersect_cover> <out_cover> {POLY | LINE | POINT} {fuzzy_tolerance} {JOIN | NOJOIN}

KILL

Usage: KILL <geo_dataset> {ARC | INFO | ALL}

PROJECT

Usage: PROJECT <COVER | FILE> <input> <output> {projection_file}

Usage: PROJECT GRID <input> <output> {projection_file} {NEAREST | BILINEAR | CUBIC} {out_cellsize} {x_register} {y_register}

PROJECTDEFINE

Usage: PROJECTDEFINE <COVER | GRID | FILE | TIN> <target>

SHAPEARC

Usage: SHAPEARC <in_shape_file> <out_cover> {out_subclass} {DEFAULT | DEFINE}

GRID commands

BASIN

Usage: (I) BASIN (<dir_grid>)

BUILDVAT

Usage: BUILDVAT <grid>

CON

Usage: (*) CON (<condition>, <true_expression>,
{<condition>, <true_expression>}, ...
{<condition>, <true_expression>}, {false_expression})

FILL

Usage: FILL <in_grid> <out_grid> {SINK | PEAK} {z_limit} {out_dir_grid}

FLOWACCUMULATION

Usage: (F) FLOWACCUMULATION (<dir_grid>, {weight_grid})

FLOWDIRECTION

Usage: (I) FLOWDIRECTION (<surface_grid>, {o_drop_grid}, {NORMAL | FORCE})

FLOWLENGTH

Usage: (F) FLOWLENGTH (<dir_grid>, {weight_grid}, {DOWNSTREAM | UPSTREAM})

GRIDLINE

Usage: (C) GRIDLINE (<in_grid>, {POSITIVE | DATA}, {THIN | NOTHIN}, {NOFILTER | FILTER}, {ROUND | SHARP}, {item}, {thickness}, {dangle}, {weed})

GRIDPOLY

Usage: (C) GRIDPOLY (<in_grid>,{weed_tolerance})

GRIDSHADES

Usage: GRIDSHADES <grid> {item} {IDENTITY | LINEAR | EQUALAREA | remap_table} {WRAP | NOWRAP}

INT

Usage: (I) INT (<grid | scalar | number>)

LINECOLOR

Usage: LINECOLOR <color_spec>

MAPEXTENT

Usage: MAPEXTENT {feature_class} <cover...cover>

Usage: MAPEXTENT <* | xmin ymin xmax ymax>

Usage: MAPEXTENT LAYER <defined_layer...defined_layer>

Usage: MAPEXTENT TILES {library...library}

Usage: MAPEXTENT LIBRARY {library...library}

Usage: MAPEXTENT IMAGE <image...image | image_catalog>

Usage: MAPEXTENT <geo_dataset...geo_dataset>

Usage: MAPEXTENT DXF <dxf...dxf>

SELECT

Usage: (*) SELECT (<grid>, <logical_expression>, {o_value_item})

SHADECOLORRAMP

Usage: SHADECOLORRAMP <start_symbol> <number_of_symbols> <start_color_spec> <end_color_spec> {LINEAR | NONLINEAR}

SHADEDELETE

Usage: SHADEDELETE <symbol | ALL>

SINK

Usage: (I) SINK (<dir_grid>)

STREAMLINE

Usage: (C) STREAMLINE (<net_grid>, <dir_grid>, {out_item}, {weed})

STREAMORDER

Usage: (I) STREAMORDER (<net_grid>, <dir_grid>, {STRAHLER | SHREVE})

WATERSHED

Usage: (I) WATERSHED (<dir_grid>, <source_grid>)

ZONALMAX

Usage: (*) ZONALMAX (<zone_grid>, <value_grid>, {DATA | NODATA})

ZONALMIN

Usage: (*) ZONALMIN (<zone_grid>, <value_grid>, {DATA | NODATA})

Arcplot commands

ASELECT

Usage: ASELECT <cover> <feature_class> {logical_expression}

Usage: ASELECT <cover> <feature_class> ONE <xy | *>

Usage: ASELECT <cover> <feature_class> MANY <xy...xy | *>

Usage: ASELECT <cover> <feature_class> BOX <xmin ymin xmax ymax | *> {PASSTHRU | WITHIN}

Usage: ASELECT <cover> <feature_class> POLYGON <xy...xy | *> {PASSTHRU | WITHIN}

Usage: ASELECT <cover> <feature_class> CIRCLE <xy radius | * {radius}> {PASSTHRU | WITHIN}

Usage: ASELECT <cover> <feature_class> MAPEXTENT

Usage: ASELECT <cover> <feature_class> PARTIAL

Usage: ASELECT <cover> POLY ADJACENT {* | distance}

Usage: ASELECT <cover> <feature_class> KEYFILE <info_key_file> <item> {KEYITEM <key_file_item>}

Usage: ASELECT <cover> <feature_class> KEYFILE <cover> <feature_class> <item> {KEYITEM <key_file_item>}

Usage: ASELECT <cover> <feature_class> OVERLAP <overlap_cover> <overlap_feature> {selection_distance} {PASSTHRU | WITHIN}

Usage: ASELECT <cover> <feature_class> RANDOM <number> {PERCENT} {seed}

Usage: ASELECT <info_file> INFO {logical_expression}

Usage: ASELECT <info_file> INFO KEYFILE <info_key_file> <item> {KEYITEM <key_file_item>}

Usage: ASELECT <info_file> INFO KEYFILE <cover> <feature_class> <item> {KEYITEM <key_file_item>}

Usage: ASELECT <info_file> INFO RANDOM <number> {PERCENT} {seed}

Usage: ASELECT <image_catalog> IMAGE {logical_expression}

Usage: ASELECT <image_catalog> IMAGE ONE <xy | *>

Usage: ASELECT <image_catalog> IMAGE MANY <xy...xy | *>

Usage: ASELECT <image_catalog> IMAGE BOX <xmin ymin xmax ymax | *> {PASSTHRU | WITHIN}

RESELECT

Usage: RESELECT <cover> <feature_class> {logical_expression}

Usage: RESELECT <cover> <feature_class> ONE <xy | *>

Usage: RESELECT <cover> <feature_class> MANY <xy...xy | *>

Usage: RESELECT <cover> <feature_class> BOX <xmin ymin xmax ymax | *> {PASSTHRU | WITHIN}

Usage: RESELECT <cover> <feature_class> POLYGON <xy...xy | *> {PASSTHRU | WITHIN}

Usage: RESELECT <cover> <feature_class> CIRCLE <xy radius | * {radius}> {PASSTHRU | WITHIN}

Usage: RESELECT <cover> <feature_class> MAPEXTENT

Usage: RESELECT <cover> <feature_class> PARTIAL

Usage: RESELECT <cover> <feature_class> KEYFILE <info_key_file> <item> {KEYITEM <key_file_item>}

Usage: RESELECT <cover> <feature_class> KEYFILE <cover> <feature_class> <item> {KEYITEM <key_file_item>}

Usage: RESELECT <cover> <feature_class> OVERLAP <overlap_cover> <overlap_feature> {selection_distance} {PASSTHRU | WITHIN}

Usage: RESELECT <cover> <feature_class> RANDOM <number> {PERCENT} {seed}

Usage: RESELECT <info_file> INFO {logical_expression}

Usage: RESELECT <info_file> INFO KEYFILE <info_key_file> <item> {KEYITEM <key_file_item>}

Usage: RESELECT <info_file> INFO KEYFILE <cover> <feature_class> <item> {KEYITEM <key_file_item>}

Usage: RESELECT <info_file> INFO RANDOM <number> {PERCENT} {seed}

Usage: RESELECT <image_catalog> IMAGE {logical_expression}

Usage: RESELECT <image_catalog> IMAGE ONE <xy | *>

Usage: RESELECT <image_catalog> IMAGE MANY <xy...xy | *>

Usage: RESELECT <image_catalog> IMAGE BOX <xmin ymin xmax ymax | *> {PASSTHRU | WITHIN}

WRITESELECT

Usage: WRITESELECT <selection_file> {<cover> <feature_class>}

Usage: WRITESELECT <selection_file> <info_file> INFO

Usage: WRITESELECT <selection_file> <image_catalog> IMAGE

INFO commands

ASELECT

Usage: ASELECT [FOR] [logical-expression]

CALCULATE

Usage: CALCULATE |DF-item | = arithmetic-expression
|system-item |
|system-variable|

RESELECT

Usage: RESELECT [|BY |] logical-expression
[|FOR|]

SELECT

Usage: SELECT DF-name

UPDATE

Usage: UPDATE [[DF-item-1[,...]] [BY DF-item [ORDERED]] [PROMPT] [[,]S]]

BIBLIOGRAPHY

Anderson, D.E., S.G. Wells, and J. Reynolds, 1994, Preliminary fluvial geomorphic studies of the Amargosa River through Amargosa Canyon, San Bernardino and Inyo counties, California, *in* Abstracts from Proceedings of the 1994 Desert Research Symposium, Redlands, San Bernadino County Museum Association, 41, 19-20.

Anderson, D.E., J. Poths, S.G. and Wells, 1998, *Cosmogenic 3 He age estimates for the terminal highstand of Plio-Pleistocene Lake Tecopa, California–Integration of the upper Amargosa River with the Death Valley drainage basin*, Geol. Soc. of Amer. Abstracts with Programs, Rocky Mountain Section, 50th annual meeting, **30**, 2.

Baker, V.R., and J.B. Partridge, 1986, *Small Martian valleys: Pristine and degraded morphology*, J. Geophys. Res., **91**, 3561-3572.

Banerdt, W.B., and A. Vidal, 2001, *Surface drainage on Mars*, Lunar and Planet. Sci. Conf., XXXII, Abstract **1488**, Lunar and Planetary Institute, Houston (CD-ROM).

Benson, L.V., and M.D. Mifflin, 1986, *Reconnaisance bathymetry of basins occupied by Pleistocene Lake Lahontan, Nevada and California*, U.S. Geol. Surv., Water-Res. Invest. Rpt. 85-4262, 1-14.

Benson, L.V., D.R. Currey, R.I. Dorn, K.R. Lajoie, C.G. Oviatt, S.W. Robinson, G.I. Smith, and S. Stine, 1990, *Chronology of expansion and contraction of four Great Basin lake systems during the past 35,000 years*, Paleogeog., Paleoclim., Paleoecol., **78**, 241-286.

Blackwelder, E., 1954, *Pleistocene lakes and drainage in the Mojave region, southern California*, in Jahns, R.H., ed., Geology of southern California: California Division of Mines Bull. No. 170, 35-40.

Blair, T.C., 1999, *Sedimentology of gravelly Lake Lahontan highstand shoreline deposits, Churchill Butte, Nevada, USA*, Sedimentary Geology, **123**, 199-218.

Boothroyd, J.C., and J.A. Grant, 1985, *Fluvial drainage basins and valley networks: Eastern Margaritifer Sinus*, Reports of the Planetary Geology and Geophysics Program - 1984, NASA Tech. Memo., TM87563, 316-318.

Brakenridge, G.R., H.E. Newsom, and V.R. Baker, 1985, *Ancient hot springs on Mars: Origins and paleoenvironmental significance of small martian valleys*, Geology, **12**, 859-862.

Butler, P.R., 1981, *Evidence for higher stands of Pleistocene Lake Manley, southern Death Valley, California and a possible drainage connection to the Colorado River*, Geol. Soc. of Amer. Abstracts with Programs, **13**, 47.

Butler, P.R., 1984, Fluvial response to on-going tectonism and base-level changes, lower Amargosa River, southern Death Valley, California, *in* Fluvial Sedimentation and Related Tectonic Framework, Western North America, T.H. Nilsen, ed., Sedimentary Geology, **38**, 107-125.

Cabrol, N.A., and E.A. Grin, 1999, *Distribution, classification, and ages of martian impact crater lakes*, Icarus, **142**, 160-172.

Cabrol, N.A., E.A. Grin, 2001a, *The evolution of lacustrine environments on Mars: Is Mars only hydrologically dormant?*, Icarus, **149**, 291-328.

Cabrol, N.A., and E.A. Grin, 2001b, *Composition of the drainage network on early Mars*, Geomorphology, **37**, 269-287.
Cabrol, N.A., E.A. Grin, and G. Davidowicz, 1996, *Ma'adim Vallis revisited through new topographic data: Evidence for an ancient intravalley lake*, Icarus, 123, 269-283.
Carr, M.H., 1973, *Volcanism on Mars*, J. Geophys. Res., 78, 4049-4062.
Carr, M.H., 1995, *The Martian drainage system and the origin of valley networks and fretted channels*, J. Geophys. Res., **100**, 7479-7507.
Carr, M.H., 1996, Water on Mars, Oxford University Press, NY, NY, 229p.
Carr, M.H., and F.C. Chuang, 1997, *Martian drainage densities*, J. Geophys. Res., **102**, 9145-9152.
Carr, M.H., and G.D. Clow, 1981, *Martian channels and valleys: Their characteristics, distribution, and age*, Icarus, **48**, 91-117.
Carr, M.H., and J.W. Head, 2004, *Formation of martian valley networks: Melting of low to mid-latitude snowpacks during periods of high obliquity?*, Lunar and Planet. Sci. Conf., XXXV, Abstract **1183**, Lunar and Planetary Institute, Houston, (CD-ROM).
Carr, M.H., and M.C. Malin, 2000, *Meter-scale characteristics of martian channels and valleys*, Icarus, **146**, 366-386.
Carr, M.H., and G.G. Schaber, 1977, *Martian permafrost features*, J. Geophys. Res. **82**, 4039-4054.
Chorley, R.J., 1957, *Climate and morphometry*, J. Geology, **65**, 628-638.
Christensen, P.R., 2003, *Formation of recent martian gullies through melting of extensive water-rich snow deposits*, Nature, **422**, 45-47.
Christensen, P.R., and 25 colleagues, 2001, *The Mars Global Surveyor Thermal Emission Spectrometer experiment: Investigation description and surface science results*, J. Geophys. Res. **106**, 23,823-23,871.
Clifford, S.M., 1993, *A model for the hydrologic and climatic behavior of water on Mars*, J. Geophys. Res., **98**, 10,973-11,016.
Colaprete, A., and B.M. Jakosky, B.M., 1998, *Ice flow and rock glaciers on Mars*, J. Geophys. Res. 103, 5897–5909.
Collier, M.L., T.F Stepinski, S.M. Clifford, and P.J. McGovern, 2003, *Martian geomorphology from statistics of drainage networks*, Lunar and Planet. Sci. Conf., XXXIV, Abstract 1642, Lunar and Planetary Institute, Houston (CD-ROM).
Craddock, R.A., and A.D. Howard, 2002, *The case for rainfall on a warm, wet early Mars*, J. Geophys. Res., **107**, doi:10.1029/2001-JE001505.
Craddock, R.A., and R.P. Irwin, 2004, *Martian drainage densities: The final word?*, in Mars Valley Networks, Abstract #Craddock_MVN_2004, Smithsonian Institution, Washington, DC (CD-ROM).
Craddock, R.A., and T.A. Maxwell, 1993, *Geomorphic evolution of the Martian highlands through ancient fluvial processes*, J. Geophys. Res., **98**, 3453-3468.
Craddock, R.A., T.A. Maxwell, and A.D. Howard, 1997a, *The early history of Mars as told by degraded highland impact craters*, Conference on Early Mars: Geologic and Hydrologic Evolution, Physical and Chemical Environments, and the Implications for Life, LPI Contrib. No. 916, 20-21.
Craddock, R.A., T.A. Maxwell, and A.D. Howard, 1997b, *Crater morphometry and modification in the Sinus Sabaeus and Margaritifer Sinus region of Mars*, J. Geophys. Res., **102**, 13,321-13,340.
Craddock, R.A., T.A. Maxwell, and A.D. Howard, 1999, *The evidence for climatic variations on early Mars*, Lunar and Planet. Sci. Conf., XXX, Abstract **1977**, Lunar and Planetary Institute, Houston, (CD-ROM).
Craddock, R.A., G.A. Franz, A.C. Cook, and A.D. Howard, 2001a, *High resolution morphometric studies of martian valley networks in the Iapygia region*, Lunar and Planet. Sci. Conf., XXXII, Abstract **1833**, Lunar and Planetary Institute, Houston (CD-ROM).
Craddock, R.A., R.P. Irwin, and A.D. Howard, 2001b, *Martian drainage densities: Analyses from MOLA digital elevation models*, abstract submitted to the Workshop on the Martian Highlands and Mojave Desert Analogs, October 20-27, 2001, Las Vegas, NV and Barstow, CA, Abstract **4016**.

Craddock, R.A., R.P. Irwin, and A.D. Howard, 2003, *Characteristics of martian valley networks and the implications for past climates*, Lunar and Planet. Sci. Conf., XXXIV, Abstract **1888**, Lunar and Planetary Institute, Houston (CD-ROM).

Crater Analysis Techniques Working Group, 1978, *Standard techniques for presentation and analysis of crater size-frequency data*, NASA TM-79730.

Crown, D.A., and R. Greeley, 1990, *Styles of volcanism, tectonic associations, and evidence for magma-water interactions in eastern Hellas, Mars*, Lunar Planet. Sci. Conf., XXI, 250-251.

Crown, D.A., and R. Greeley, 1993, *Volcanic geology of Hadriaca Patera and the eastern Hellas region of Mars*, J. Geophys. Res., **98**, 3431-3451.

Crown, D.A., and R. Greeley, 2004, *Geologic map of MTM quadrangles -30262 and -30267: Hadriaca Patera region of Mars*, U.S. Geol. Surv., scale 1:500K, in review.

Crown, D.A., and S.C. Mest, 1997, *Dao, Harmakhis, and Reull Valles: The role of outflow channels in the degradation of the circum-Hellas highlands of Mars*, Lunar Planet. Sci. Conf., XXVIII, 269-270.

Crown, D.A., and S.C. Mest, 2001, *Circum-Hellas outflow channels: New views from Mars Global Surveyor*, Lunar and Planet. Sci. Conf., XXXII, Abstract **1344**, Lunar and Planetary Institute, Houston (CD-ROM).

Crown, D.A., and K.H. Stewart, 1995, *Debris aprons in the eastern Hellas region of Mars*, Lunar and Planet. Sci. Conf., XXVI, Houston, Lunar and Planetary Institute, 301-302.

Crown, D.A., L.F. Bleamaster III and S.C. Mest, 2004, *Geologic evolution of Dao Vallis*, Mars, Lunar and Planet. Sci. Conf., XXXV, Abstract **1185**, Lunar and Planetary Institute, Houston (CD-ROM).

Crown, D.A., K.H. Price, and R. Greeley, 1992, *Geologic evolution of the east rim of the Hellas basin, Mars*, Icarus, **100**, 1-25.

Crumpler, L.S., 1997, *Syrtis Major-Isidis Planitia transition, Mars: Preliminary evaluation of a potential Mars Surveyor Program landing site*, Lunar and Planet. Sci. Conf., XXVIII, Houston, Lunar and Planetary Institute, 273-274.

Crumpler, L.S., 1998, *Southwestern Isidis Planitia, Mars: A Mars Surveyor landing site at the geologic contact between three units*, Lunar and Planet. Sci. Conf. XXIX, Abstract **1946**, Lunar and Planetary Institute, Houston (CD-ROM).

Crumpler, L.S., 1999, *Highland valley networks and ephemeral lake basins, Libya Montes, SW Isidis basin margin*, Second Mars Surveyor Landing Site Workshop, SUNY Buffalo, Buffalo, NY, 22-24.

Crumpler, L.S., and K.L. Tanaka, 2003, *Geology and MER target site characteristics along the southern rim of Isidis Planitia, Mars*, J. Geophys. Res., doi:10.1029/2002JE002040.

De Hon, R.A., 2002, *Martian sedimentary basins and regional watersheds*, Lunar and Planet. Sci. Conf. XXXIII, Abstract **1915**, Lunar and Planetary Institute, Houston (CD-ROM).

Dettinger, M.D., and D.H. Schaefer, 1996, *Hydrogeology of structurally extended terrain in the eastern Great Basin of Nevada, Utah, and adjacent states from geologic and geophysical models*, U.S. Geol. Surv. Hydrol. Invest. Atlas HA-694-D.

Dohrenwend, J.C., W.B. Bull, L.D. McFadden, G.I. Smith, R.S.U. Smith, and S.G. Wells, 1991, *Quaternary Geology of the Basin and Range Province in California*, in Quaternary Nonglacial Geology: Conterminous U.S., R.B. Morrison, ed., The Geology of North America, **K-2**, Geol. Soc. of Amer., Boulder, CO, 321-352.

Dorn, R.I., A.J.T. Jull, D.J. Donahue, T.W. Linick, and L.J. Toolin, 1990, *Latest Pleistocene lake shorelines and glacial chronology in the western Basin and Range province, U.S.A.: Insights from AMS radiocarbon dating of rock varnish and paleoclimatic implications*, in Paleoclimates: The Record from Lakes, Oceans and Land, P.A. Meyers and L.V. Benson, eds., Paleogeog., Paleoclim., Paleoecol., **78**, 315-331.

Edgett, K.S., 2001a, *Geologic aspects and relations of small eolian dunes and large ripples on Mars*, Lunar and Planet. Sci. Conf., XXXII, Abstract 1181, Lunar and Planetary Institute, Houston (CD-ROM).

Edgett, K.S., 2001b, *Observations regarding small eolian dunes and large ripples on Mars*, Geol. Soc. of Amer. Abstracts with Programs 33, Abstract 19777.

Edgett, K.S., and M.C. Malin, 2000, *Sedimentary geology of Trouvelot Crater and dark intracrater features (or, "splotches") of western Arabia Terra*, Lunar and Planet. Sci. Conf., XXXI, Abstract **1066**, Lunar and Planetary Institute, Houston (CD-ROM).

Enzel, Y., D.R. Cayan, R.Y. Anderson, and S.G. Wells, 1989, *Atmospheric circulation during Holocene lake stands in the Mojave Desert: Evidence of regional climate change*, Nature, **341**, 44-48.

Enzel, Y., W.J. Brown, R.V. Anderson,. L.D. McFadden, and S.G. Wells, 1992, *Short-duration Holocene lakes in the Mojave River drainage basins, southern California*, Quaternary Res., **38**, 60-73.

Fagin, S.W., D.M. Worrall, and W.R. Muehlberger, 1978, *Lunar mare ridges orientations: Implications for lunar tectonic models, in* Proceedings of the Lunar and Planet. Sci. Conf., IX, 3473-3479.

Fairfield, J., and P. Leymarie, 1991, *Drainage networks from grid digital elevation models*, Water Resour. Res., **27**, 709-717.

Fassett, C.I., and J.W. Head, 2004, *Snowmelt and the formation of valley networks on martian volcanoes*, Lunar and Planet. Sci. Conf., XXXV, Abstract **1113**, Lunar and Planetary Institute, Houston, (CD-ROM).

Forsythe, R.D., and C.R. Blackwelder, 1998, *Closed drainage crater basins of the martian highlands: Constraints on the early martian hydrologic cycle*, J. Geophys. Res., **103**, 31421-31431.

Fortezzo, C.M., and J.A. Grant, 2004, *Hypsometric analyses of martian basins: A comparison to terrestrial, lunar and venusian hypsometry*, Lunar and Planet. Sci. Conf., XXXV, Abstract **1647**, Lunar and Planetary Institute, Houston (CD-ROM).

Frey, H., L. Hutchison, S. Sakimoto, and J. Roark, 2000, *A large population of possible buried impact basins on Mars revealed by MOLA topographic data*, Lunar and Planet. Sci. Conf., XXXI, Abstract **1736**, Lunar and Planetary Institute, Houston (CD-ROM).

Garvin, J.B., S.E.H. Sakimoto, S.E.H., J.J. Frawley, 2003, *Craters on Mars: Global geometric properties from gridded MOLA topography*, Sixth International Conference on Mars, Abstract **3277**, Lunar and Planetary Institute, Houston.

Gilmore, M.S. and E.L. Phillips, 2003, *Role of aquicludes in formation of Martian gullies*, Geology, **30**, 1107-1110.

Goldspiel, J.M., and S.W. Squyres, 2000, *Groundwater sapping and valley formation on Mars*, Icarus, **148**, 176-192.

Goldspiel, J.M., S.W. Squyres, and D.G. Jankowski, 1993, *Topography of small Martian valleys*, Icarus, **105**, 479-500.

Grant, J.A., 1999, *Evaluating the evolution of process specific degradation signatures around impact craters*, International Journal of Impact Engineering, **23**, 331-340.

Grant, J.A., 2000, *Valley formation in Margaritifer Sinus, Mars, by precipitation-recharged ground-water sapping*, Geology, **28**, 223-226.

Grant, J.A., and C. Fortezzo, 2003a, *Hypsometric analysis of martian basins*, Lunar and Planet. Sci. Conf. XXXIV, Abstract **1123**, Lunar and Planetary Institute, Houston (CD-ROM).

Grant, J.A, and C.M. Fortezzo, 2003b, *Basin Hypsometry on the Earth, Mars, and the Moon*, Sixth International Conference on Mars, Abstract *3050*, Lunar and Planetary Institute, Houston.

Grant, J.A., and T.J. Parker, 2002, *Drainage evolution in the Margaritifer Sinus region, Mars*, J. Geophys. Res., **107**, doi:10.1029/2001JE001678, 2002

Grant, J.A., and P.H. Schultz, 1990, *Gradational epochs on Mars: Evidence from west-northwest of Isidis Basin and Electris*, Icarus, **84**, 166-195.

Grant, J.A., and P.H. Schultz, 1991a, *The gradational history of southern Ismenius Lacus, Mars*, Lunar and Planet. Sci. Conf., XXII, Houston, Lunar and Planetary Institute, 485-486.

Grant, J.A., and P.H. Schultz, 1991b, *Styles of crater gradation in southern Ismenius Lacus, Mars*, Lunar and Planet. Sci. Conf., XXII, Houston, Lunar and Planetary Institute, 487-488.

Grant, J.A., and P.H. Schultz, 1993, *Degradation of selected terrestrial and Martian impact craters*, J. Geophys. Res., **98**, 11,025-11,042.

Grant, J.A., and P.H. Schultz, 1994, *Early fluvial degradation in Terra Tyrrhena, Mars: Constraints from styles of crater degradation on the Earth*, Lunar and Planet. Sci. Conf., XXV, Houston, Lunar and Planetary Institute, 457-458.

Grasso, D.N., 1996, *Hydrology of modern and late Holocene lakes, Death Valley, California*, U.S. Geol. Surv. Water-Res. Invest. Rpt. 95-4237, 54p.

Greeley, R. and D.A. Crown, 1990, *Volcanic geology of Tyrrhena Patera, Mars*, J. Geophys. Res., **95**, 7133-7149.

Greeley, R., and J.E. Guest, 1987, *Geologic map of the eastern equatorial region of Mars*, U.S. Geol. Surv. Misc. Inv. Ser. Map I-1802B, scale 1:15M.

Greeley, R., and P.D. Spudis, 1981, *Volcanism on Mars*, Rev. Geophys., **19**, 13-41.

Gregg, T.K.P., D.A. Crown, and R. Greeley, 1998, *Geologic map of the Tyrrhena Patera region of Mars (MTM quadrangle -20252)*, U.S. Geol. Surv. Misc. Inv. Ser. Map I-2556, scale 1:500K.

Gregory, K.J., 1976, Drainage networks and climate, *in* Geomorphology and Climate, E. Derbyshire, ed., Wiley-Interscience, Chinchester, pp. 289-315.

Gregory, K.J., and D.E. Walling, 1973, Drainage Basin Form and Process, Halsted Press, New York, 456p.

Grieve, R.A.F., and M.J. Cintala, 1992, *An analysis of differential impact melt-crater scaling and implications for the terrestrial impact record*, Meteoritics, **27**, 526-538.

Grin, E.A., and N.A. Cabrol, 1997, *Limnologic analysis of Gusev Crater paleolake, Mars*, Icarus, **130**, 461-474.

Gulick, V.C., 1998, *Magmatic intrusions and a hydrothermal origin for fluvial valleys on Mars*, J. Geophys. Res., **103**, 19,365–19,387.

Gulick, V.C., 2001, *Origin of the valley networks on Mars: A hydrological perspective*, Geomorphology, **37**, 241–268.

Gulick, V.C., and V.R. Baker, 1990, *Origin and evolution of valleys on Martian volcanoes*, J. Geophys. Res., **95**, 14,325-14,344.

Gulick, V.C., D. Tyler, C.P. McKay, and R.M. Haberle, 1997, *Episodic ocean-induced CO_2 pulses on Mars: Implications for fluvial valley formation*, Icarus, **130**, 68-86.

Gyasi-Agyei, Y., G. Willgoose, and F.P. de Troch, 1995, *Effects of vertical resolution and map scale of digital elevation models on geomorphological parameters used in hydrology*, Hydrol. Process., **9**, 363-382.

Hartmann, W.K., 1971, *Martian cratering III: Theory of crater obliteration*, Icarus, **15**, 410-428.

Hartmann, W.K., and G. Neukum, 2001, *Cratering chronology and the evolution of Mars*, Icarus, **96**, 165-194.

Hillhouse, J.W., 1987, *Late Tertiary and Quaternary geology of the Tecopa basin, southeastern California*, U.S. Geol. Surv. Misc. Invest. Ser. Map I-1728, scale 1:48K.

Horton, R.E., 1932, *Drainage basin characteristics*, Trans. Am. Geophys. Union, **13**, 350-361.

Horton, R.E., 1945, *Erosional development of streams and their drainage basins: Hydrophysical approach to quantitative morphology*, Geol. Soc. of Amer. Bull., **56**, 275-370.

Howard, A.D., 1994, *A detachment-limited model of drainage basin evolution*, Water Resour. Res., **30**, 2261-2285.

Howard, A.D., and R.A. Craddock, 1998, *Simulation of erosion of ancient cratered terrain on Mars*, Lunar and Planet. Sci. Conf., XXIX, Abstract **1323**, Lunar and Planetary Institute, Houston, (CD-ROM).

Hunt, C.B., T.W. Robinson, W.A. Bowles, and A.L. Washburn, 1966, *General geology of Death Valley, California: Hydrologic basin*, U.S. Geol. Surv Prof. Paper 0494-B, 138p.

Hynek, B.M., and R.J. Phillips, 2001, *Evidence for extensive denudation of the martian highlands*, Geology, **29**, 407-410.

Irwin, R.P., and R.A. Craddock, 2001, *Drainage basin integration in the martian highlands*, abstract submitted to the Workshop on the Martian Highlands and Mojave Desert Analogs, October 20-27, 2001, Las Vegas, NV and Barstow, CA, Abstract **4013**.

Irwin, R.P., and A.D. Howard, 2001, *Cratering and fluvial erosion in Noachian Terra Cimmeria, Mars*, Lunar and Planet. Sci. Conf., XXXII, Abstract **1377**, Lunar and Planetary Institute, Houston (CD-ROM).

Irwin, R.P., and A.D. Howard, 2002, *Drainage basin evolution in Noachian Terra Cimmeria, Mars*, J. Geophys. Res., **107**, doi:10.1029/2001JE001818.

Irwin, R.P., and T.A. Maxwell, 2003, *Multiple generations of martian valley networks: reconciling extensive fluvial erosion with immature drainage systems*, Sixth International Conference on Mars, Abstract **3243**, Lunar and Planetary Institute, Houston.

Irwin, R.P., A.D. Howard, T.A. Maxwell, and R.A. Craddock, 2002a, *Drainage basin disruption and re-integration processes in the martian highlands*, Lunar and Planet. Sci. Conf., XXXIII, Abstract **1729**, Lunar and Planetary Institute, Houston (CD-ROM).

Irwin R.P., T.A. Maxwell, A.D. Howard, R.A. Craddock, D.W. Leverington, 2002b, *A large paleolake basin at the head of Ma'adim Vallis, Mars*, Science, **296**, 2209-2212.

Irwin, R.P., A.D. Howard, and T.A. Maxwell, 2004, *Geomorphology and hydraulics of Ma'adim Vallis, Mars, during a Noachian / Hesperian boundary paleoflood*, Lunar and Planet. Sci. Conf., XXXV, Abstract **1852**, Lunar and Planetary Institute, Houston, (CD-ROM).

Jakosky, B.M., M.T. Mellon, H.H. Kieffer, P.R. Christensen, E.S. Varnes, and S.W. Lee, 2000, *The thermal inertia of Mars from the Mars Global Surveyor Thermal Emission Spectrometer*, J. Geophys. Res. **105**, 9,643-9,652.

Jenson, S.K., 1991, *Applications of hydrologic information automatically extracted from digital elevation models*, Hydrol. Process., **5**, 31-44.

Jenson, S.K., and J.O. Domingue, 1988, *Extracting topographic structure from digital elevation data for Geographic Information System analysis*, Photogramm. Eng. Remote Sensing, **54**, 1593-1600.

Kelson, K.I., and S.G. Wells, 1989, *Geologic influence on fluvial hydrology and bedload transport in small mountain watersheds, northern New Mexico*, Earth Surf. Process. and Landforms, **14**, 671-690.

Kenward, T., D.P. Lettenmaier, E.F. Wood, and E. Fielding, 2000, *Effects of digital elevation model accuracy on hydrologic predictions*, Remote Sens. Environ., **74**, 432-444.

King, E.A., 1978, *Geologic map of the Mare Tyrrhenum quadrangle*, U.S. Geol. Surv. Misc. Inv. Ser. Map I-910, scale 1:5M.

Knighton, D., 1998, Fluvial Forms and Processes: A New Perspective, John Wiley & Sons, Inc., New York, New York, 383p.

Kochel, R.C., and J.F. Piper, 1986, *Morphology of large valleys on Hawaii: Evidence for groundwater sapping and comparisons with martian valleys*, J. Geophys. Res., **91**, E175-E192.

Kochel, R.C., A.D. Howard, and C. McLane, 1985, Channel networks developed by groundwater sapping in fine-grained sediments: Analogs to some Martian valleys, *in* Models in Geomorphology, M.J. Woldenberg, ed., Allen and Unwin, Boston, pp. 313-341.

Leonard, G.J., and K.L. Tanaka, 2001, *Geologic map of the Hellas region of Mars*, U.S. Geol. Surv. Geol. Inv. Ser. Map I-2694, scale 1:5M.

Lucchitta, B.K., 1976, *Mare ridges and related highland scarps--Results of vertical tectonism?*, Proceedings of the Lunar and Planet. Sci. Conf., VII, Houston, Lunar and Planetary Institute, 2761-2782.

Lucchitta, B.K., 1977, *Topography, structure, and mare ridges in southern Mare Imbrium and northern Oceanus Procellarum*. Geochim. Cosmochim. Acta, **3**, suppl., 2691-2703.

Lucchitta, B.K., 1984, *Ice and debris in the fretted terrain, Mars*, J. Geophys. Res. Suppl. **89**, B409-B418.

Luo, W., 2000, *Quantifying groundwater-sapping landforms with a hypsometric technique*, J. Geophys. Res., **105**, 1685-1694.

Luo, W., 2001, *Digital elevation model resolution and hypsometric analysis: Implications for MOLA gridded topographic data*, Lunar and Planet. Sci. Conf. XXXII, Abstract **2043**, Lunar and Planetary Institute, Houston (CD-ROM).

Luo, W., 2002, *Hypsometric analysis of Margaritifer Sinus and origin of valley networks*, J. Geophys. Res., **107**, doi:10.1029/2001JE001500.
Malin, M.C., and M.H. Carr, 1999, *Groundwater formation of Martian valleys*, Nature, **397**, 589-591.
Malin, M.C., and K.S. Edgett, 2000, *Evidence for recent groundwater seepage and surface runoff on Mars*, Science, **288**, 2330-2335.
Malin, M.C., and K.S. Edgett, 2003, *Evidence for persistent flow and aqueous sedimentation on early Mars*, Science, **302**, 1931-1934, doi:10.1126/science.1090544.
Mars Channel Working Group, 1983, *Channels and valleys on Mars*, Geol. Soc. of Amer. Bull., **94**, 1035-1054.
Martz, L.W., and J. Garbrecht, 1998, *The treatment of flat areas and depressions in automated drainage analysis of raster digital elevation models*, Hydrol. Process., **12**, 843-855.
Mason, J.F., 1948, *Geology of the Tecopa area, southeastern California*, Geol. Soc. of Amer. Bull., **59**, 333-352.
Masursky, H., 1973, *An overview of geological results from Mariner 9*, J. of Geophys. Res., **78**, 4009-4030.
Maxwell, T.A., and R.A. Craddock, 1995, *Age relations of Martian highland drainage basins*, J. Geophys. Res., **100**, 11,765-11,780.
McCauley, J.F., M.H. Carr, J.A. Cutts, W.K. Hartmann, H. Masursky, D.J. Milton, R.P. Sharp, and D.E. Wilhelms, 1972, *Preliminary Mariner 9 report on the geology of Mars*, Icarus, **17**, 289-327.
Meek, N., 1989, *Geomorphic and hydrologic implications of the rapid incision of Afton Canyon, Mojave Desert, California*, Geology, 17, 7-10.
Mellon, M.T., B.M. Jakosky, H.H. Kieffer, and P.R. Christensen, 2000, *High-resolution thermal inertia mapping from the Mars Global Surveyor Thermal Emission Spectrometer*, Icarus, 148, 437-455.
Melton, M.A., 1957, *An analysis of the relations among elements of climate, surface properties, and geomorphology*, Project NR 389-042, Tech. Rept. 11, Columbia University, Department of Geology, ONR, Geography Branch, New York, 100p.
Mest, S.C., 1998, *Geologic history of the Reull Vallis region, Mars*, M.S. Thesis, University of Pittsburgh, 269p.
Mest, S.C., and D.A. Crown, 2001a, *Fluvial degradation of the circum-Hellas highlands of Mars*, abstract submitted to the Workshop on the Martian Highlands and Mojave Desert Analogs, October 20-27, 2001, Las Vegas, NV and Barstow, CA, Abstract **4014**.
Mest, S.C., and D.A., Crown, 2001b, *Geology of the Reull Vallis Region, Mars*, Icarus, **153**, 89-110.
Mest, S.C., and D.A. Crown, 2002a, *Geology of MTM quadrangles -20272 and -25272, Terra Tyrrhena region of Mars*, Lunar and Planet. Sci. Conf., XXXIII, Abstract **1730**, Lunar and Planetary Institute, Houston (CD-ROM).
Mest, S.C., and D.A. Crown, 2002b, *Geologic map of MTM -40252 and -40257 Quadrangles, Reull Vallis region of Mars*, U.S. Geol. Surv. Geol. Invest. Ser. Map I-2730, scale 1:1M.
Mest, S.C., and D.A., Crown, 2003a, *Geologic map of MTM -45252 and -45257 Quadrangles, Reull Vallis region of Mars*, U.S. Geol. Surv. Geol. Invest. Ser. Map I-2763, scale 1:1M.
Mest, S.C., D.A. Crown, 2003b, *Geology of crater Millochau, Terra Tyrrhena region of Mars*, Lunar and Planet. Sci. Conf., XXXIV, Abstract **1942**, Lunar and Planetary Institute, Houston (CD-ROM).
Mest, S.C., and D.A. Crown, 2004a, *Geologic map of MTM -20272 and -25272 Quadrangles, Tyrrhena Terra region of Mars*, U.S. Geol. Surv., accepted for publication.
Mest, S.C., and D.A. Crown, 2004b, *Crater Millochau, Mars: Hesperian-aged erosion of an ancient highland impact crater*, submitted to Icarus.
Mest, S.C., D.A. Crown and W. Harbert, 2001a, *Highland drainage basins and valley networks in the eastern Hellas region of Mars*, Lunar and Planet. Sci. Conf. XXXII, Abstract **1457**, Lunar and Planetary Institute, Houston (CD-ROM).
Mest, S.C., W. Harbert and D.A. Crown, 2001b, *Application of Geographical Information System Arc/Info grid-based surface hydrologic modeling to the eastern Hellas region, Mars*, EOS Trans. AGU, **82**, Spring Meet. Suppl., Abstract **P31A-05**.

Mest, S.C., D.A. Crown and W. Harbert, 2002, *Fluvial degradation of the highlands: The Terra Tyrrhena region of Mars*, Lunar and Planet. Sci. Conf. XXXIII, Abstract **1892**, Lunar and Planetary Institute, Houston (CD-ROM).

Milton, D.J., 1973, *Water and processes of degradation in the Martian landscape*, J. Geophys. Res., **78**, 4037-4047.

Moore, J.M., and D.E. Wilhelms, 2001, *Hellas as a possible site of ancient ice-covered lakes on Mars*, Icarus, **154**, 258-276.

Morisawa, M.E., 1962, *Quantitative geomorphology of some watersheds in the Appalachian Plateau*, Geol. Soc. of Amer. Bull., **73**, 1025-1046.

Morrison, R.B., 1991, Quaternary stratigraphic, hydrologic, and climatic history of the Great Basin, with emphasis on Lakes Lahonton, Bonneville, and Tecopa, *in* Quaternary nonglacial geology–Conterminous U.S.: The Geology of North America, R.B. Morrison, ed.., Geol. Soc. of Amer., **K-2**, 1-12, 283-320.

Morrison, R.B., 1999, Lake Tecopa: Quaternary geology of Tecopa Valley, California, a mullet-million-year record and its relevance to the proposed nuclear-waste repository at Yucca Mountain, Nevada, *in* Cenozoic Basins of the Death Valley Region, L.A. Wright and B.W. Trowel, eds., Geol. Soc. of Amer. Special Paper 333, 301-344.

Murray, B.C., L.A. Soderblom, R.P. Sharp, and J.A. Cutts, 1971, *The surface of Mars, 1. Cratered terrains*, J. Geophys. Res., **76**, 313-330.

Mustard, J.F., M.A. Kreslavsky, J.W. Head, and R.E. Milliken, 2003, *Correlating meter-scale morphology and kilometer-scale topography: Evidence for a degraded mid-latitude surface layer on Mars*, Lunar and Planet. Sci. Conf., XXXIII, Abstract **1289**, Lunar and Planetary Institute, Houston (CD-ROM).

Newsom, H.E., G.E. Brittelle, C.A. Hibbitts, L.J. Crossey, and A.M. Kudo, 1996, *Impact crater lakes on Mars*, J. Geophys. Res., **101**, 14951-14955.

O'Callaghan, J.F., and D.M. Mark, 1984, *The extraction of drainage networks from digital elevation data*, Comput. Vis. Graph. Image Process., **28**, 323-344.

Ore, H.T., and C.N. Warren, 1971, *Late Pleistocene-early Holocene geomorphic history of Lake Mojave, California*, Geol. Soc. of Amer. Bull., **82**, 2553-2562.

Ori, G.G., L. Marinangeli, and A. Baliva, 2000, *Terraces and Gilbert-type deltas in crater lakes in Ismenius Lacus and Memnonia (Mars)*, J. Geophys. Res., **105**, 17,629-17,641.

Phillips, R.J., and K. Lambeck, 1980, *Gravity fields of the terrestrial planets: Long-wavelength anomalies and tectonics*, Reviews of Geophysics and Space Physics, **18**, 27-76.

Pierce, T.L., and D.A. Crown, 2003, *Morphologic and topographic analyses of debris aprons in the eastern Hellas region, Mars*, Icarus, **163**, 46-65, doi:10.1016/S0019-1035(03)00046-0.

Pieri, D.C., 1976, *Martian channels: Distribution of small channels in the Martian surface*, Icarus, **27**, 25-50.

Pieri, D.C., 1980, *Martian valleys: Morphology, distribution, age, and origin*, Science, **210**, 895-897.

Pike, R.J., and P.A. Davis, 1984, *Toward a topographic model of martian craters from photoclinometry*, Lunar and Planet. Sci. Conf., XV, Lunar and Planetary Institute, Houston, 645-646.

Pike, R.J. and P.d. Spudis, 1987, *Basin-ring spacing on the Moon, Mercury and Mars*, Earth, Moon, and Planets, **39**, 129-194.

Plescia, J.B., and M.P. Golombek, 1986, *Origin of planetary wrinkle ridges based on the study of terrestrial analogs*, Geol. Soc. of Amer. Bull., **97**, 1289-1299.

Potter, D.B., 1976, *Geologic map of the Hellas quadrangle of Mars*, U.S. Geol. Surv. Misc. Inv. Ser. Map I-941, scale 1:5M.

Price, K.H., 1998, *Geologic map of Dao, Harmakhis and Reull Valles region of Mars*, U.S. Geol. Surv. Misc. Invest. Ser. Map I-2557, scale 1:1M.

Putzig, N.E., M.T. Mellon, and R.E. Arvidson, 2003, *Thermophysical properties of the martian south polar region*, Sixth International Conference on Mars, Abstract **3173**, Lunar and Planetary Institute, Houston.

Reheis, M.C., 1999, *Extent of Pleistocene lakes in the western Great Basin*, U.S. Geol. Surv. Misc. Field Studies Map, MF-2323.
Reheis, M.C., and R.B. Morrison, 1997, *High, old, pluvial lakes of western Nevada: Proterozoic to recent stratigraphy, tectonics, and volcanology, Utah, Nevada, southern Idaho and central Mexico*, Geology Studies, **42**, 459-492.
Ritter, D.F., R.C. Kochel, and J.R. Miller, 1995, Process Geomorphology, Wm. C. Brown Publishers, Dubuque, IA, 540p.
Roark, J.H., and H.V. Frey, 2001, *GRIDVIEW: Recent improvements in research and education software for exploring Mars topography*, Lunar and Planet. Sci. Conf., XXXII, Abstract **1618**, Lunar and Planetary Institute, Houston (CD-ROM).
Roark, J.H., H.V. Frey, and S. Sakimoto, 2000, *Interactive graphics tools for analysis of MOLA and other data*, Lunar and Planet. Sci. Conf., XXXI, Abstract **2026**, Lunar and Planetary Institute, Houston (CD-ROM).
Saunders, R.S., and T.E. Gregory, 1980, *Tectonic implications of martian ridged plains*, NASA Tech. Memo 82385, 93-94.
Schaber, G.G., 1977, *Geologic map of the Iapygia Quadrangle, Mars*, U.S. Geol. Surv. Misc. Inv. Ser. Map I-1020, scale 1:5M.
Schultz, P.H., 1976, *Floor-fractured lunar craters*, The Moon, **15**, 241-273.
Schultz, P.H., and H. Glicken, 1979, *Impact crater and basin control of igneous processes on Mars*, J. Geophys. Res., **84**, 8033-8047.
Schumm, S.A., 1956, *The evolution of drainage systems and slopes in badlands at Perth Amboy, New Jersey*, Geol. Soc. of Amer. Bull., **67**, 597-646.
Scott, D.H., and K.L. Tanaka, 1986, *Geologic map of the western equatorial region of Mars*, U.S. Geol. Surv. Misc. Inv. Ser. Map I-1802A, scale 1:15M.
Sharp, R.P., and A.F. Glazner, 1999, Geology Underfoot in Death Valley and Owens Valley, Mountain Press Publishing Company, Missoula, MT, 319p.
Shreve, R.L., 1974, *Variation of mainstream length with basin area in river networks*, Water Resour. Res., **10**, 1167-1177.
Smith, D.E., and 18 others, 1999, *The global topography of Mars and implications for surface evolution*, Science, **284**, 1495-1503.
Smith, D.E., and 20 others, 2001, *Mars Orbiter Laser Altimeter: Experiment summary after the first year of global mapping of Mars*, J. Geophys. Res., **106**, 23,689-23,722.
Smith, G.I., 1973, *Subsurface stratigraphy and composition of saline bodies, Searless Lake, California: A preliminary report*, U.S. Geol. Surv. Open-file Report, 122p.
Smith, G.I., 1979, *Subsurface stratigraphy and geochemistry of late Quaternary evaporites, Searles Lake, California*, U.S. Geol. Surv. Prof. Paper 1043, 130p.
Smith, G.I., and F.A. Street-Perrott, 1983, Pluvial Lakes in the Western United States, in Late Quaternary Environments of the United States, 1, H.E. Wright and S.C. Porter, eds., University of Minnesota Press, Minneapolis, pp. 190-214.
Smith, G.I., V.J. Barczak, G.F. Moulton, and J.C. Liddicoat, 1983, *Core KM-3, a surface-to-bedrock record of late Cenozoic sedimentation in Searles Valley, California*, U.S. Geol. Surv. Prof. Paper 1256, 24p.
Smith, K.G., 1958, *Erosional processes and landforms in Badlands National Monument, South Dakota*, GSA Bull., **69**, 975-1008.
Snyder, J.P., 1982, *Map projections used by the U.S. Geological Survey*, Geol. Surv. Bull. 1532, 313p.
Squyres, S.W., 1978, *Martian fretted terrain: Flow of erosional debris*, Icarus, **34**, 600-613.
Squyres, S.W., and M.H. Carr, 1986, *Geomorphic evidence for the distribution of ground ice on Mars*, Science, **231**, 249-252.
Squyres, S.W., D.E. Wilhelms, and A.C. Moosman, 1987, *Large-scale volcano-ground ice interactions on Mars*, Icarus, **70**, 385-408.

Starkey, H.C., and P.D. Blackmon, 1979, *Clay mineralogy of Pleistocene Lake Tecopa, Inyo County, California*, U.S. Geol. Surv. Prof. Paper P-1061, 34p.

Stepinski, T.F., 2003, *Vertical analysis of martian drainage basins*, Lunar and Planet. Sci. Conf. XXXIV, Abstract **1659**, Lunar and Planetary Institute, Houston (CD-ROM).

Stepinski, T.F., and M.L. Collier, 2003, *Drainage densities of computationally extracted martian drainage basins*, Sixth International Conference on Mars, Abstract **3100**, Lunar and Planetary Institute, Houston.

Stepinksi, T.F., and M.L. Collier, 2004, *Computational analysis of drainage basins on Mars: Appraising the drainage density*, Lunar and Planet. Sci. Conf., XXXV, Abstract **1168**, Lunar and Planetary Institute, Houston, (CD-ROM).

Stepinksi, T.F., and S. Coradetti, 2004, *Systematic differences in topography of martian and terrestrial drainage basins*, Lunar and Planet. Sci. Conf., XXXV, Abstract **1166**, Lunar and Planetary Institute, Houston, (CD-ROM).

Stepinski, T.F., M.M. Marinova, P.J. McGovern, and S.M. Clifford, 2002a, *The fractal characteristics of martian drainage basins: Implications for the timing, intensity, and duration of rainfall*, Lunar and Planet. Sci. Conf. XXXIII, Abstract **1347**, Lunar and Planetary Institute, Houston (CD-ROM).

Stepinksi, T.F., M.M. Marinova, P.J. McGovern, and S.M. Clifford, 2002b, *Fractal analysis of drainage basins on Mars*, Geophys. Res. Lett., **29**, doi:10.1029/2002GL014666.

Stepinski, T.F., R. Vilalta, M. Achari, and P.J. McGovern, 2003, *Algorithmic classification of drainage networks on Mars and its relation to martian geological units*, Lunar and Planet. Sci. Conf. XXXIV, Abstract **1653**, Lunar and Planetary Institute, Houston (CD-ROM).

Strahler, A.N., 1952, *Hypsometric (area-altitude) analysis of erosional topography*, Geol. Soc. of Amer. Bull., **63**, 1,117-1,142.

Strahler, A.N., 1957, *Quantitative analysis of watershed geomorphology*, Am. Geophys. Union Trans., **38**, 913-920.

Strahler, A.N., 1958, *Dimensional Analysis applied to fluvially eroded landforms*, Geol. Soc. of Amer. Bull., **69**, 279-300.

Strahler, A.N., 1964, *Part II.* Quantitative geomorphology of drainage basins and channel networks, *in* Handbook of Applied Hydrology: A Compendium of Water-resource Technology, V.T. Chow, ed., McGraw-Hill, Inc., pp. 39-76.

Strom, R.G., 1972, *Lunar mare ridges, rings, and volcanic ring complexes*, in Moon, IAU Symposium 47, 187-215.

Strom, R.G., S.K. Croft, and N.G. Barlow, 1992, The Martian impact cratering record, *in* Mars, H.H. Kieffer, B.M. Jakosky, C.W. Snyder, and M.S. Matthews, eds., University of Arizona Press, Tucson, AZ, pp. 383-423.

Tanaka, K.L., 1986, *The stratigraphy of Mars*, Proceedings of the Lunar Planet. Sci. Conf., 17, J. Geophys. Res. Suppl., **91**, E139-E158.

Tanaka, K.L., and G.J. Leonard, 1995, *Geology and landscape evolution of the Hellas region of Mars*, J. Geophy. Res., **100**, 5,407-5,432.

Tanaka, K.L., N.K. Isbell, D.H. Scott, R. Greeley, and J.E. Guest, 1988, *The resurfacing history of Mars: A synthesis of digitized, Viking-based geology*, Proceedings of the Lunar and Planet. Sci. Conf., 18, 665-678.

Tanaka, K.L, D.H. Scott, and R. Greeley, 1992, Global stratigraphy, *in* Mars, H.H. Kieffer, B.M. Jakosky, C.W. Snyder, and M.S. Matthews, eds., University of Arizona Press, Tucson, AZ, pp. 345-382.

Tanaka, K.L., J.M. Dohm, J.H. Lias, and T.M. Hare, 1998, *Erosional valleys in the Thaumasia region of Mars: Hydrothermal and seismic origin*, J. Geophys. Res., **103**, 31,407-31,420.

Tarboton, D.G., R.L. Bras, and I. Rodriguez-Iturbe, 1991, *On the extraction of channel networks from digital elevation data*, Hydrol. Process., **5**, 81-100.

Thieken, A.H., A. Lücke, B. Diekkrüger, and O. Richter, 1999, *Scaling input data by GIS for hydrological modeling*, Hydrol. Process., **13**, 611-630.

Tucker, G.E., and R.L. Bras, 1998, *Hillslope proceses, drainage density, and landscape morphology*, Water Resour. Res., **34**, 2571-2564.

Turcotte, R., J.-P. Fortin, A.N. Rousseau, S. Massicotte, J.-P. Villeneuve, 2001, *Determination of the drainage structure of a watershed using a digital elevation model and a digital river and lake network*, J. Hydrol., **240**, 225-242.

Vogt, J.V., R. Colombo, and F.Bertolo, 2003, *Deriving drainage networks and catchment boundaries: A new methodology combining digital elevation data and environmental characteristics*, Geomorphology, **53**, 281-298.

Wang, X., and Z. Yin, 1998, *A comparison of drainage networks derived from digital elevation models at two scales*, J. Hydrol., **210**, 221-241.

Watters, T.R., 1988, *Wrinkle ridge assemblages on the terrestrial planets*, J. Geophys. Res., **93**, 10,236-10,254.

Watters, T.R., 1991, *Origin of periodically spaced wrinkle ridges on the Tharsis plateau of Mars*, J. Geophys. Res., **96**, 15,599-15,616.

Watters, T.R., 1993, *Compressional tectonism on Mars*, J. Geophys. Res., **98**, 17,049-17,060.

Watters, T.R., and D.J. Chadwick, 1989, *Cross-cutting periodically spaced first-order ridges in the ridged plains of Hesperia Planum: Another case for a buckling model*, LPI Tech. Rpt. 89-06, 68-69.

Wells, S.G., and Y. Enzel, 1994, Fluvial geomorphology of the Mojave River in the Afton Canyon area, Eastern California: Implications for the geomorphic evolution of Afton Canyon, *in* Geological Investigations of an Active Margin, S.F. McGill and T.M. Ross, eds., Geol. Soc. of Amer., Cordilleran Section, Annual Meeting, **27**, 177-182.

Wells, S.G., R.Y. Anderson, Y. Enzel, and W. Brown, 1987, *Late Quaternary climatic changes and hydrologic evolution of the Mojave River drainage basin, California*, EOS, **68**, 1270.

Wells, S.G., W.J. Brown, Y. Enzel, R.Y. Anderson, and L.D. McFadden, 1994, A brief summary of the late Quaternary history of pluvial Lake Mojave, eastern California, *in* Geological Investigations of an Active Margin, Geol. Soc. of Amer., Cordilleran Section Fieldtrip Guidebook, 182-188.

Wohl, E., 2000, Mountain Rivers, American Geophysical Union, Washington, D.C., 320p.

Wood, C.A., 1980, *Martian double ring basins: New observations*, Proceedings of the Lunar and Planet. Sci. Conf., 11, Lunar and Planetary Institute, Houston, 2221-2241.

Zimbelman, J.R., S.M. Clifford, and S.H. Williams, 1989, *Concentric crater fill on Mars: An aeolian alternative to ice-rich mass wasting*, Proceedings of the Lunar Planet. Sci. Conf., 19, 397-407.